

# Lunar Domes

## Properties and Formation Processes

Raffaello Lena  
Christian Wöhler  
James Phillips  
Maria Teresa Chiocchetta

---

# Springer Praxis Books

For further volumes:  
<http://www.springer.com/series/4097>

---

Raffaello Lena • Christian Wöhler  
James Phillips • Maria Teresa Chiocchetta

# Lunar Domes

Properties and Formation Processes



Published in association with  
**Praxis Publishing**  
Chichester, UK



Raffaello Lena  
Roma  
Italy

James Phillips  
Charleston  
USA

Christian Wöhler  
Faculty of Electrical Engineering and  
Information Technology  
Image Analysis Group  
TU Dortmund University  
Germany

Maria Teresa Chiocchetta  
Chiavari  
Italy

All figures of the book (including the colour versions) are available at Springer ExtraMaterials (<http://extras.springer.com/978-88-470-2636-0>). The cover images were taken by James Phillips.

ISBN 978-88-470-2636-0

ISBN 978-88-470-2637-7 (eBook)

DOI 10.1007/978-88-470-2637-7

Springer Milan Heidelberg New York Dordrecht London

Library of Congress Control Number: 2012945982

© Springer-Verlag Italia 2013

This work is subject to copyright. All rights are reserved by the Publisher, whether the whole or part of the material is concerned, specifically the rights of translation, reprinting, reuse of illustrations, recitation, broadcasting, reproduction on microfilms or in any other physical way, and transmission or information storage and retrieval, electronic adaptation, computer software, or by similar or dissimilar methodology now known or hereafter developed. Exempted from this legal reservation are brief excerpts in connection with reviews or scholarly analysis or material supplied specifically for the purpose of being entered and executed on a computer system, for exclusive use by the purchaser of the work. Duplication of this publication or parts thereof is permitted only under the provisions of the Copyright Law of the Publisher's location, in its current version, and permission for use must always be obtained from Springer. Permissions for use may be obtained through RightsLink at the Copyright Clearance Center. Violations are liable to prosecution under the respective Copyright Law.

The use of general descriptive names, registered names, trademarks, service marks, etc. in this publication does not imply, even in the absence of a specific statement, that such names are exempt from the relevant protective laws and regulations and therefore free for general use.

While the advice and information in this book are believed to be true and accurate at the date of publication, neither the authors nor the editors nor the publisher can accept any legal responsibility for any errors or omissions that may be made. The publisher makes no warranty, express or implied, with respect to the material contained herein.

Printed on acid-free paper

Springer is part of Springer Science+Business Media ([www.springer.com](http://www.springer.com))



*To all the GLR (Geological Lunar Research Group)  
friends who have worked with us acquiring ima-  
ges to allow for lunar studies and increase of lunar  
knowledge.*

---

## Preface

During the six successful Apollo missions to the Moon, twelve human beings have walked on its surface. These efforts were accompanied by a variety of robotic spacecraft. Nevertheless, the Moon still has retained many of its secrets.

After the last manned mission, Apollo 17, which took place in 1972, and the unmanned Soviet spacecraft Luna 20–24 launched between 1972 and 1976, the next spacecraft was sent towards the Moon no earlier than 1994: Clementine achieved a nearly global multi-spectral mapping with imaging sensors in the visible and near-infrared wavelength range. The Clementine mission and a few years later the Lunar Prospector mission in 1998 have stimulated a broad range of scientific activities dealing with the geology and surface composition of the lunar surface. More recently, these efforts were continued by an international “armada” consisting of the European technology demonstrator Smart-1, the Chinese spacecraft Chang’e, the Japanese orbiter Kaguya (SELENE), the Indian spacecraft Chandrayaan-1, and the US-American Lunar Reconnaissance Orbiter (LRO), which provided high-resolution imagery as well as topographic and hyperspectral data of unprecedented quality.

An important domain of lunar research is the field of lunar volcanism. In this context, lunar domes are the result of volcanic processes on the Moon billions of years ago. Lunar domes are low volcanic edifices that are similar to small and low shield volcanoes on the Earth. Most of them are situated in the lunar mare regions, only few are located in the highlands, most of which are steeper than the lunar mare domes. On top of many lunar domes, summit pits can be observed. These are commonly interpreted as having been formed by the eruption of magma from a central vent. The shapes of a relatively small number of exceptionally low lunar domes suggest a formation by subsurface intrusion of a pressurised magmatic body rather than by lava eruption. This scenario is characterised by the intrusion of pressurised magma between layers of rock, the upper one of which is bent upwards to form a dome-like profile on the surface.

Generally spoken, the morphological development of a volcanic edifice is determined by the properties of the dome-forming lava, such as its viscosity, temperature, and chemical composition, as well as the effusion rate and the duration of the effusion process. The magma temperature and composition govern its viscosity and in turn the steepness of the resulting volcanic edifice. Hence, steeper lunar domes were probably formed by more

viscous lavas of lower temperature and higher crystalline content than lunar domes with low flank slopes. Accordingly, knowledge about the morphometric properties of lunar domes, especially their diameters, heights, and volumes allows to estimate such magma-specific properties. Recent studies about lunar domes are therefore based on the evaluation of their spectral and morphometric properties, rheologic parameters, and their classification.

This book describes these physical differences between lunar domes of different appearance, examines the factors that may have led to a concentration of domes with certain properties in certain lunar regions, and discusses how the variety of observed properties of lunar domes are related to the characteristics of the dome-forming magma. The presentation partially draws upon various previous publications by the authors.

Notably, the detailed study of lunar domes is only possible based on images of the lunar surface acquired under strongly oblique illumination conditions. The Lunar Orbiter images have hardly been acquired under such illumination, while most images of the Clementine spacecraft were taken at high solar illumination, which is the best configuration for spectral studies. LRO provides coverage of the lunar surface at more or less oblique illumination, but not all known lunar domes are favourably imaged. Most lunar domes are discernible in the topographic maps acquired by the laser altimeters LALT and LOLA on board the Kaguya and LRO spacecraft. Hardly, however, they can be unambiguously identified as lunar domes based on such data alone. As a consequence, ground-based images obtained using telescopes and CCD cameras like those commonly used by well-equipped amateur astronomers are still of great value for the morphologic and morphometric analysis of lunar domes in their geological context.

Accordingly, the main goal of this book is to describe the present knowledge about lunar domes and also to encourage dedicated amateur astronomers who are interested in lunar observations and imaging as well as in the geologic processes that formed the lunar surface. All figures of the book (including the colour versions) are available at Springer ExtraMaterials (<http://extras.springer.com/>; 978-88-470-2636-0).

The Authors

---

## Acknowledgments

Special thanks go to KC Pau, Mike Wirths, Stefan Lammel, Paolo Lazzarotti, Carmelo Zannelli, Zac Pujic, George Tarsoudis, Gerardo Sbarufatti and Charlie Kapral, who have worked for decades on lunar studies. Finally, we thank Rick Evans for establishing spectral analyses in the GLR group.

---

# Contents

**Part I Lunar Domes Morphometry, Geophysical Modelling  
and Formation Processes**

<b>1</b>	<b>Volcanism on the Earth and the Moon: Morphometry and Eruption Conditions</b>	<b>3</b>
1.1	Volcanic Processes and Formation of Volcanic Edifices on the Earth and the Moon	3
1.2	Physical Parameters of Dome Formation	6
1.3	Lunar Pyroclastic Deposits	6
1.4	Lunar Cones	8
1.5	Vents of Effusive Lunar Domes	9
1.6	Localization of Lunar Domes	10
1.6.1	Domes in the Maria	10
1.6.2	Domes Inside Craters	10
1.6.3	Domes in Highland Regions	10
1.6.4	Domes Bisected by Rilles	15
1.6.5	Domes with Non-volcanic Hills and Linear Rilles on their Surface	18
1.6.6	Domes with Concentric Craters on their Summit	18
1.6.7	Aligned Lunar Domes, Formation along Crustal Fractures	20
1.6.8	Lunar Intrusive Domes	21
<b>2</b>	<b>Lunar Domes: Morphometric and Rheologic Properties</b>	<b>23</b>
2.1	Observing Lunar Domes	23
2.2	Images Rendered Based on Topographic Data	24
2.3	Image-Based Photogrammetric Measurements	25
2.4	Determination of Morphometric Properties	27
2.4.1	Shadow Length Measurements	27
2.4.2	Photoclinometry and Shape from Shading	29
2.4.3	A Combined DEM Construction Approach	33
2.5	Modelling of Rheologic Properties	34
2.6	Monogenetic and Non-Monogenetic Lunar Effusive Domes	36

2.7	Classification Schemes Based on Qualitative Morphologic Features . . . . .	36
2.7.1	The Classification Scheme by Westfall (1964) . . . . .	36
2.7.2	The Classification Scheme by Head and Gifford (1980) . . . . .	38
2.8	Conclusion . . . . .	38
<b>3</b>	<b>Determination of Spectral Properties . . . . .</b>	<b>39</b>
3.1	Spectral Ratios . . . . .	39
3.2	Diagnostic Spectral Parameters . . . . .	41
3.3	Petrographic Maps . . . . .	44
<b>4</b>	<b>Modelling of Lunar Effusive and Intrusive Domes . . . . .</b>	<b>49</b>
4.1	Modelling of Feeder Dike Dimensions . . . . .	49
4.2	Time Scales Relevant During Dome Formation . . . . .	52
4.3	Laccolith Modelling of Putative Intrusive Domes . . . . .	54
4.3.1	Arguments Against and In Favour of an Intrusive Origin . . . . .	54
4.3.2	Laccolith Modelling . . . . .	55
4.3.3	Comparison with Terrestrial Laccoliths . . . . .	56
<b>5</b>	<b>Lunar Domes Classification Scheme . . . . .</b>	<b>59</b>
5.1	Classification Based on Principal Component Analysis . . . . .	60
5.2	Non-monogenetic Lunar Effusive Domes . . . . .	63
5.3	Classes of Lunar Intrusive Domes . . . . .	63
5.4	Conclusion . . . . .	65
<b>Part II Guide to Observing Lunar Domes on the Moon</b>		
<b>6</b>	<b>Effusive Bisected Lunar Domes . . . . .</b>	<b>69</b>
6.1	The Birt Domes . . . . .	69
6.2	The Domes near the Crater Menelaus . . . . .	72
6.3	The Bisected Dome near Gassendi . . . . .	77
<b>7</b>	<b>Effusive Lunar Domes . . . . .</b>	<b>79</b>
7.1	Effusive Lunar Domes Located from Selenographic Longitude 0° to 90° East . . . . .	79
7.1.1	Mare Tranquillitatis . . . . .	79
7.1.2	Mare Vaporum and Hyginus . . . . .	89
7.1.3	Autolycus . . . . .	90
7.1.4	Meton . . . . .	91
7.1.5	Rupes Altai and Piccolomini . . . . .	95
7.1.6	Fracastorius . . . . .	96
7.1.7	Mare Fecunditatis . . . . .	97
7.1.8	Vendelinus . . . . .	98
7.1.9	Mare Crisium and Yerkes . . . . .	100
7.1.10	Petavius . . . . .	101
7.1.11	Mare Undarum . . . . .	103



---

7.2	Effusive Lunar Domes Located from Selenographic Longitude	
	0° to 90° West . . . . .	105
7.2.1	Palus Putredinis . . . . .	105
7.2.2	Mare Frigoris and Region Around Archytas . . . . .	107
7.2.3	Dome Suite near Hortensius and Domes and Swells Between Milichius and Tobias Mayer, Mare Nubium and Aristarchus . . . . .	108
7.2.4	Capuanus and Palus Epidemiarum . . . . .	116
7.2.5	Region Around C. Herschel in Mare Imbrium and Sinus Iridum . . .	118
7.2.6	The Doppelmayer Region . . . . .	120
7.2.7	Region Around Mee . . . . .	124
7.2.8	Gruithuisen Region . . . . .	125
7.2.9	Mons Hansten . . . . .	127
7.2.10	Marius Hills . . . . .	127
7.2.11	Mons Rümker . . . . .	131
<b>8</b>	<b>Candidate Lunar Intrusive Domes . . . . .</b>	<b>135</b>
<b>9</b>	<b>Conclusion . . . . .</b>	<b>145</b>
	<b>Appendix A: Lunar dome images . . . . .</b>	<b>149</b>
	<b>Appendix B: Further Resources . . . . .</b>	<b>157</b>
	<b>References . . . . .</b>	<b>163</b>
	<b>Index . . . . .</b>	<b>171</b>

---

## **Part I**

# **Lunar Domes Morphometry, Geophysical Modelling and Formation Processes**

---

# Volcanism on the Earth and the Moon: Morphometry and Eruption Conditions

1

---

## Abstract

This chapter provides an overview of terrestrial and lunar volcanic processes. The dependence of the shape of a volcanic construct on the physical and chemical properties of the erupting lava is described. Furthermore, an introduction to lunar pyroclastic deposits, lunar cones and effusive lunar domes and their vents as well as an outline of the occurrence of different types of volcanic constructs on the Moon and the corresponding formation mechanisms is given.

---

## 1.1 Volcanic Processes and Formation of Volcanic Edifices on the Earth and the Moon

According to the currently most commonly accepted hypothesis, the Earth's Moon was formed by the impact of a protoplanet of about the size of Mars into the proto-Earth (Vaniman et al. 1991). It is assumed that both protoplanets had a core largely consisting of iron and a silicate mantle. According to this model, most of the material ejected during the collision was made up of silicates, which explains the fact that the Moon only has a small metallic core and therefore has a significantly lower average density than the Earth. On the Moon, an outer molten layer of silicate material then formed the so-called “magma ocean” reaching down to a depth of 250–1,000 km, where a differentiation occurred in the form that low-density plagioclase-rich material (which nowadays forms the lunar highlands) rose to the surface while minerals of higher density, e.g. pyroxene, olivine, and ilmenite, formed layers at higher depths. After solidification of the plagioclase-rich upper layer, partial melting of the denser lower layers resulted in the occurrence of extended basaltic volcanism on the Moon (Vaniman et al. 1991).

Fluid material rising up from the interior of a planet is termed “magma” as long as it is located inside the planetary interior and “lava” once it reaches the surface. The so-called “volcanic” or “extrusive” magmatic processes lead to the eruption of lava to the surface, which

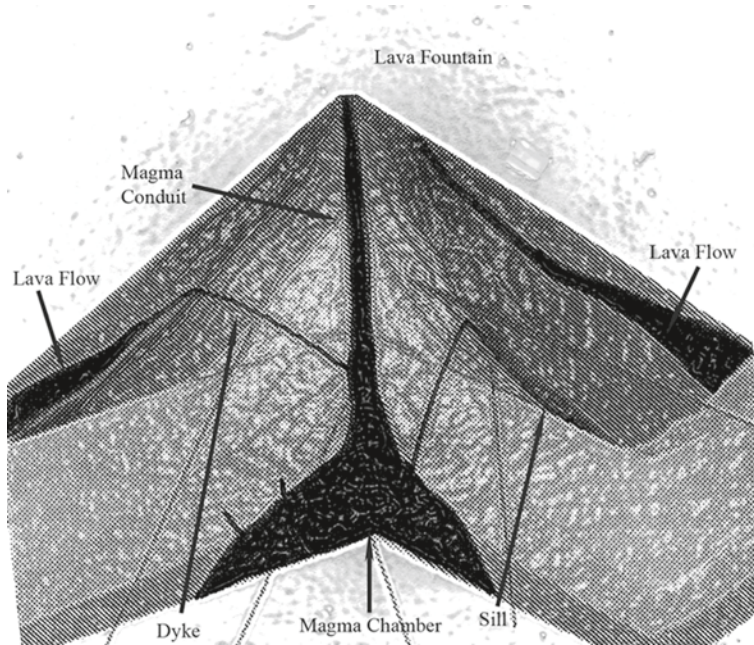


**Fig. 1.1** Scheme of a Strombolian eruption. Magma ascends to the surface through dikes. Illustration following Sémhur ([http://en.wikipedia.org/wiki/File:Strombolian\\_Eruption-numbers.svg](http://en.wikipedia.org/wiki/File:Strombolian_Eruption-numbers.svg)) and Walker (2000)

may occur explosively due to the presence of gases in the magma or in the form of lava flows. Furthermore, pressurised magma that penetrates between layers of solid rock may change the shape of these rocks, e.g. by bending them upwards, and solidifies without erupting to the surface. These magmatic processes are termed “intrusive” processes. Accordingly, terrestrial volcanic edifices may either form by an effusion of lava, e.g. resulting in shield volcanoes, or by an up doming of rock layers caused by magma intrusion below the surface, resulting in laccoliths (Ollier 1988; Rosi et al. 1999; Lipman 2000; Peterson and Tilling 2000).

The magma typically arises from the base of the crust or from the mantle (Head and Wilson 1992; Wilson and Head 1996). If magma erupts from a vent around which the erupted material is distributed in a radial manner to form a volcanic edifice, this procedure is called “central eruption”. Such processes involve the ascent of magma through a conduit, while in contrast the term “fissure eruption” denotes the extrusion of lava through an extended fracture in the crust, as shown in Fig. 1.1 (Ollier 1988; Rosi et al. 1999; Simkin and Siebert 2000).

Magma may be able to ascend through a dike as a consequence of its density being lower than that of the surrounding material, resulting in a positive buoyancy. Furthermore, the magma may be over pressurised due to thermal expansion of the melt at large depth (Wilson and Head 1996). Depending on these influencing quantities and also on the structural properties of the material of the crust, the formation of a dike may stop below the surface, or the magma in the dike may break through to the surface such that an

eruption of lava occurs (Head and Wilson 1996). If the depth below the surface to which the dike ascends is shallow, i.e. 1–2 km, the extensional forces stretching the crust may lead to the formation of a graben (Wilson and Head 1996, 2002). Such mechanisms are common on the Earth and are postulated by Wilson and Head (1996) to have occurred on the Moon as well, as indicated by the presence of extended linear graben systems and rilles.

According to laboratory analyses, the composition of mare rocks is mafic (basaltic) as they contain high fractions of metal oxides such as FeO, MgO, or CaO, while their silica ( $\text{SiO}_2$ ) content is low (BVSP 1981). Murase and McBirney (1970) determine the viscosity of lunar basaltic magma by melting synthetic lunar samples and find it to be very low with values of several Pascal second, i.e. similar to motor oil. In contrast, the viscosities of more feldspathic lavas of higher  $\text{SiO}_2$  content, such as andesitic and rhyolitic lavas, have viscosities which are higher by several orders of magnitudes, where the viscosity increases with increasing  $\text{SiO}_2$  content (BVSP 1981; Rosi et al. 1999). On the Earth, low and flat edifices are formed by basaltic lavas, such as the large Icelandic shield volcanoes, while more viscous lavas tend to build up steep volcanic edifices (Whitford-Stark and Head 1977). On the Moon, the volcanic domes in the mare regions resemble terrestrial shield volcanoes due to their low flank slopes and heights, such that they are commonly assumed to have formed from basaltic lava of low viscosity (Head and Gifford 1980). A few lunar domes, however, such as those located in the regions around Gruithuisen and Mairan, have steeper flank slopes and according to the infrared spectroscopic analysis by Kusuma et al. (2012) consist of material containing a high fraction of  $\text{SiO}_2$ . Hence, these domes are commonly believed to have formed from lavas of high viscosity, where the eruption might have occurred during several subsequent phases (Wilson and Head 2003).

Basaltic minerals, especially pyroxenes, make up the lunar mare regions but also occur in small areas in the highlands. Pyroxenes of high calcium (Ca) content, so-called clinopyroxenes, are abundant in most maria (BVSP 1981). Low-Ca pyroxene (orthopyroxene) primarily occurs in the highland regions, e.g. in the central peaks of some impact craters such as Bullialdus (Tompkins et al. 1994). Other common minerals are olivine, which is commonly observed as a mixture of  $\text{Fe}_2\text{SiO}_4$  (fayalite) and  $\text{Mg}_2\text{SiO}_4$  (forsterite) (King and Ridley 1987), and ilmenite ( $\text{FeTiO}_3$ ). All lunar basalts have a high iron (Fe) content while the titanium (Ti) abundance shows distinct variations on regional scales (BVSP 1981). According to the age estimates of lunar mare surfaces based on crater counts by Hiesinger et al. (2003), most Ti-rich basalts erupted between 3.85 and 3.55 billion years (Ga) ago, while the ages of low-Ti mare basalts are generally in between 3.45 and 3.15 Ga. However, some mare units in Oceanus Procellarum have ages of only 1.2 Ga.

During the early stages of the mare eruptions, the lavas were characterised by low viscosities due to their low Si content but also as a consequence of their high temperatures. Accordingly, the lava flows were only a few tens of metres thick and extended over distances of hundreds of kilometres (Hörz et al. 1991). In the course of time, the magma cooled down, such that its viscosity increased and its effusion rate decreased. As a consequence, flat shields built up around the eruption vents (Head and Gifford 1980). Most lunar effusive domes are characterised by smooth surfaces. Many of them display pits or elongated vents on their summits. Fissures or chains of crater pits can be observed on the surfaces of a

few lunar domes. Lunar domes are usually not associated with sinuous rilles or pyroclastic deposits (Head and Gifford 1980). Sinuous rilles are commonly interpreted as lava channels that transported large volumes of hot lava of low viscosity, while pyroclastic deposits are the result of explosive volcanic eruptions (Hörz et al. 1991).

However, several lunar domes occur in the vicinity of presumable tectonic structures, e.g. the domes near Rupes Cauchy in Mare Tranquillitatis (Head and Gifford 1980). According to the mechanism suggested by Head and Wilson (1996) and Petrycki and Wilson (1999), the ascent of dikes to shallow depth below the surface led to the formation of linear rilles and graben. A prominent example is Rima Hyginus, along which rimless crater pits are aligned which were presumably formed by degassing eruptions (Head and Wilson 1996; Giguere et al. 2010). Comparably steep-sided lunar cones such as Isis and Osiris in Mare Serenitatis are interpreted as having been formed by the eruption of lava (Weitz and Head 1999).

---

## 1.2 Physical Parameters of Dome Formation

The growth and morphology of a volcanic structure depends on various parameters, among which the physical and chemical properties and the gas content of the lava as well as the eruption mode and duration are most important (Simkin and Siebert 2000; Whitford-Stark and Head 1977; Weitz and Head 1999).

The viscosity of the magma depends on its composition and temperature. According to Spera (2000), the  $\text{SiO}_2$  content of the magma has a major influence on its viscosity. The viscosity of pure  $\text{SiO}_2$  melt is high as it is characterised by a tetrahedral molecular structure where each O atom is bound to two nearest-neighbour Si atoms. Metal oxides in the melt result in O atoms being bound to single Si atoms only, the so-called “nonbridging oxygen”. A similar effect is caused by volatiles such as water ( $\text{H}_2\text{O}$ ) or carbon dioxide ( $\text{CO}_2$ ) (Spera 2000). Moreover, the viscosity of magma is influenced by its temperature and strongly decreases with increasing temperature. For example, an increase in temperature from 1,100°C to 1,300°C decreases the viscosity of basaltic lava by one order of magnitude (Spera 2000). A third quantity influencing the magma viscosity is the fraction of crystalline material, which, among other factors, depends on the solidification temperatures of its constituents. Crystallisation of some of the melt constituents due to decreasing temperature leads to an increase of viscosity (Spera 2000).

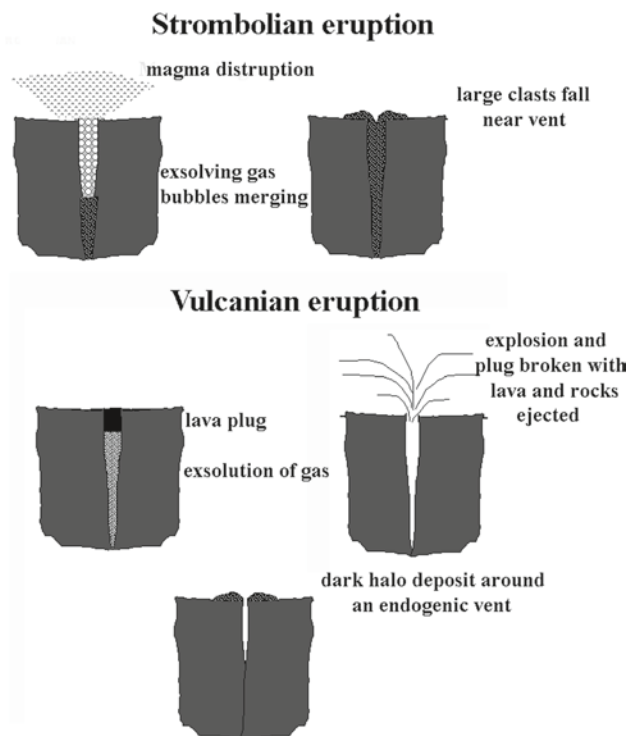
---

## 1.3 Lunar Pyroclastic Deposits

At many places in the lunar mare regions, dark patches occur which are termed “dark mantling deposits” (DMD) or “lunar pyroclastic deposits” (LPD). According to Head and Wilson (1979) and Weitz and Head (1999), the formation of small LPDs is due to vulcanian eruptions during which a plug consisting of solidified lava filling the conduit was removed violently and torn into fragments (Fig. 1.2). For example, several such small LPDs of about 10 km size and smaller can be observed on the floor of the crater Alphonsus.



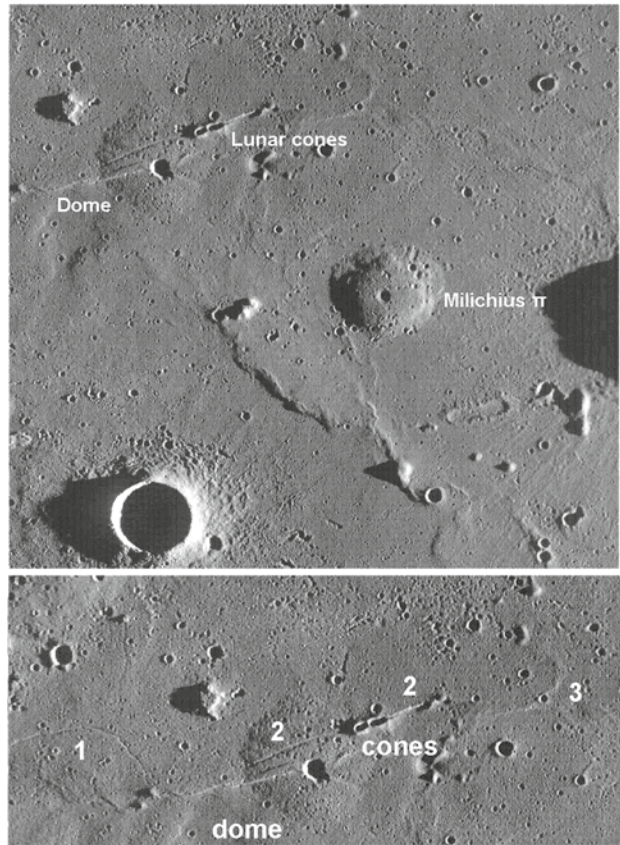
**Fig. 1.2** Scheme of a Strombolian (*top*) and Vulcanian eruption (*bottom*). In a Strombolian eruption, gases are dissolved from the magma during its ascent as the magma pressure decreases. At the surface, the magma droplets are ejected. A Vulcanian eruption may occur when the vent is plugged by solidified lava, such that the pressure of the dissolved gas increases until it reaches a critical value. The lava plug is then removed violently and torn into fragments. (Modified from Wilson and Head 1981)



In contrast, large LPDs may cover areas of thousands of square kilometres, such as those situated on the Aristarchus plateau, in southern Mare Humorum, in the south of Mare Vaporum, and near the crater Sulpicius Gallus at the southwestern border of Mare Serenitatis (Gaddis et al. 2003). The formation of these large LPDs is commonly attributed to fire-fountaining or Strombolian eruptions occurring over more extended periods of time, during which the dark pyroclastic material was broadly distributed across the lunar surface (Gaddis et al. 2003).

The mechanism of the eruptions that formed the large LPDs is such that gases were dissolved from the magma during its ascent as the magma pressure decreased. At the surface, the gases exploded, leading to a fragmentation of the surrounding magma and the ejection of the resulting droplets. As a result, the fragmented material was distributed across the lunar surface around the vent (Gaddis et al. 2003; cf. also Rosi et al. 1999). The size of the particles is assumed to depend on their cooling time, where short cooling times leads to a high fraction of volcanic glasses like those sampled during the Apollo 17 mission, while slower cooling allows for a partial crystallisation of the lava (Gaddis et al. 2003 and references therein). Furthermore, mixing of the pyroclastic material with surrounding rock of non-volcanic origin may occur (Head and Wilson 1979, 1996; Gaddis et al. 2003).

**Fig. 1.3** (*top*) Section of the LROC image WAC M116520385ME (NASA/GSFC/Arizona State University). The eastern dome, Milichius  $\pi$ , is termed M12 in Fig. 1.5a. Two lunar cones (termed MC1 in Fig. 1.5a) are aligned on the flank of another dome bisected by rilles; (*bottom*) Enlarged part of the preceding WAC image, showing several volcanic features: 1 sinuous rille, 2 linear rille traversing the dome, thus providing evidence for the presence of a near-surface dike, 3 lobe-shaped front of a lava flow



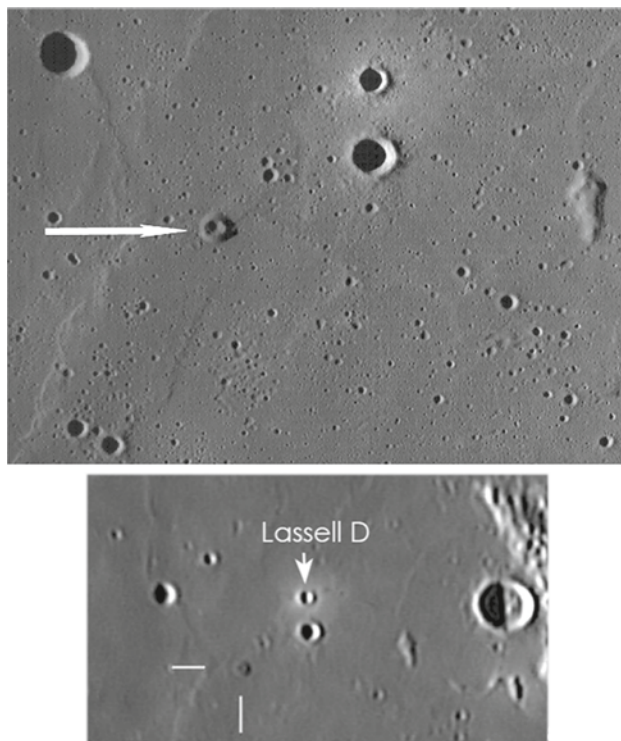
## 1.4 Lunar Cones

The fragmentation of lava due to dissolution of the gases contained therein may lead to eruptions that build up small cone-shaped edifices around the eruption vent (Wood 1979). Head and Wilson (1996) and Weitz and Head (1999) attribute the formation of lunar cones to a similar mechanism based on an explosive eruption of lava as a result of degassing.

Pike and Clow (1981) report the morphometric properties of 18 lunar volcanoes, including five lunar cones. They inferred the cone diameters, heights, and summit crater depths from Lunar Orbiter images and topographic maps constructed from Apollo metric camera images. Weitz and Head (1999) use Clementine UVVIS multispectral image data to study the spectral and compositional properties of the cones Isis and Osiris in Mare Serenitatis, Mons Esam in Mare Tranquillitatis, and the cones located in the Marius Hills region, which display non-circular shapes resembling that of a horseshoe.

Lunar cones have diameters smaller than about 4–5 km. Osiris has a largely circular shape. Its immediate neighbour Isis is characterised by a short sinuous rille on its surface that is commonly interpreted as a lava outflow channel (Masursky et al. 1978; Weitz

**Fig. 1.4** (*top*) Section of the LROC image WAC M117562021ME (NASA/GSFC/Arizona State University). An impressive lunar cone is located southwest of Lassell D and J in Mare Nubium; (*bottom*) Telescopic image of the lunar cone. (Image by Z. Pujic)



and Head 1999). Two small cones near the crater Milichius are aligned along a linear rille (Fig. 1.3). Such a configuration indicates that the intrusive dike reached a shallow depth below the surface (Head and Wilson 1996). Another impressive cone is located near the craters Lassell D and J in Mare Nubium (Fig. 1.4). The observation that lunar cones are typically not associated with LPDs is attributed by Head and Wilson (1996) to a formation by eruptions involving a disruption of the magma into large fragments building up an edifice in the immediate vicinity of the vent, in contrast to the small LPD-forming droplets being distributed across much larger surface areas. According to Wood (1979), the low edifice volumes of small cones when compared to those of large cones indicate lower lava extrusion rates during their construction and the presence of magma chambers located at shallower depths below the surface.

---

## 1.5 Vents of Effusive Lunar Domes

For many lunar domes, the presence of a rimless crater pit on the dome summit suggests a volcanic origin (Head and Gifford 1980; cf. also Wilhelms 1987). These central pits have diameters of no more than a few kilometres. They are commonly interpreted as volcanic vents, where the crater-like appearance is assumed to be the result of magma subsidence or

collapse due to decreasing pressure (Head and Gifford 1980). The depth-to-diameter ratio of the central pits is generally lower than the typical value (about one-fifth as observed e.g. by Pike (1974) and Wood and Andersson (1978)) for small lunar impact craters of similar diameter (Head and Gifford 1980). However, many effusive lunar domes do not display a summit vent at all, indicating that no collapse processes occurred (Head and Gifford 1980).

---

## 1.6 Localization of Lunar Domes

This section provides an overview of different occurrences of lunar domes with their specific characteristics. We present telescopic CCD images along with recently acquired images of the Lunar Reconnaissance Orbiter Wide Angle Camera (LROC WAC) (Robinson et al. 2010) and results derived from the 85-channel hyperspectral image data of the Moon Mineralogy Mapper ( $M^3$ ) carried by the Chandrayaan-1 spacecraft (Pieters et al. 2009).

### 1.6.1 Domes in the Maria

Important clusters of lunar domes are observed in the Hortensius/Milichius/T. Mayer region in Mare Insularum (Fig. 1.5a–c), and in Mare Tranquillitatis around the craters Arago and Cauchy (Fig. 1.5d–f). Furthermore, most lunar nearside maria exhibit single domes (Head and Gifford 1980). The region west of the crater Marius in southern Oceanus Procellarum is the most extensive volcanic region on the Moon and shows a multitude of volcanic domes, cones, and sinuous rilles (Fig. 1.8) (Weitz and Head 1999). In the northern part of Mare Tranquillitatis, eight small domes are aligned in a direction radial to Mare Imbrium (Fig. 1.5g). The small basaltic plain of Mare Undarum displays a group of four impressive domes (Fig. 1.6c). The volcanic complex Mons Rümker in northern Oceanus Procellarum (Fig. 1.6a, b) is of unique morphology. As described by Smith (1974), it is composed of a large number of mare domes, some of which mutually overlap.

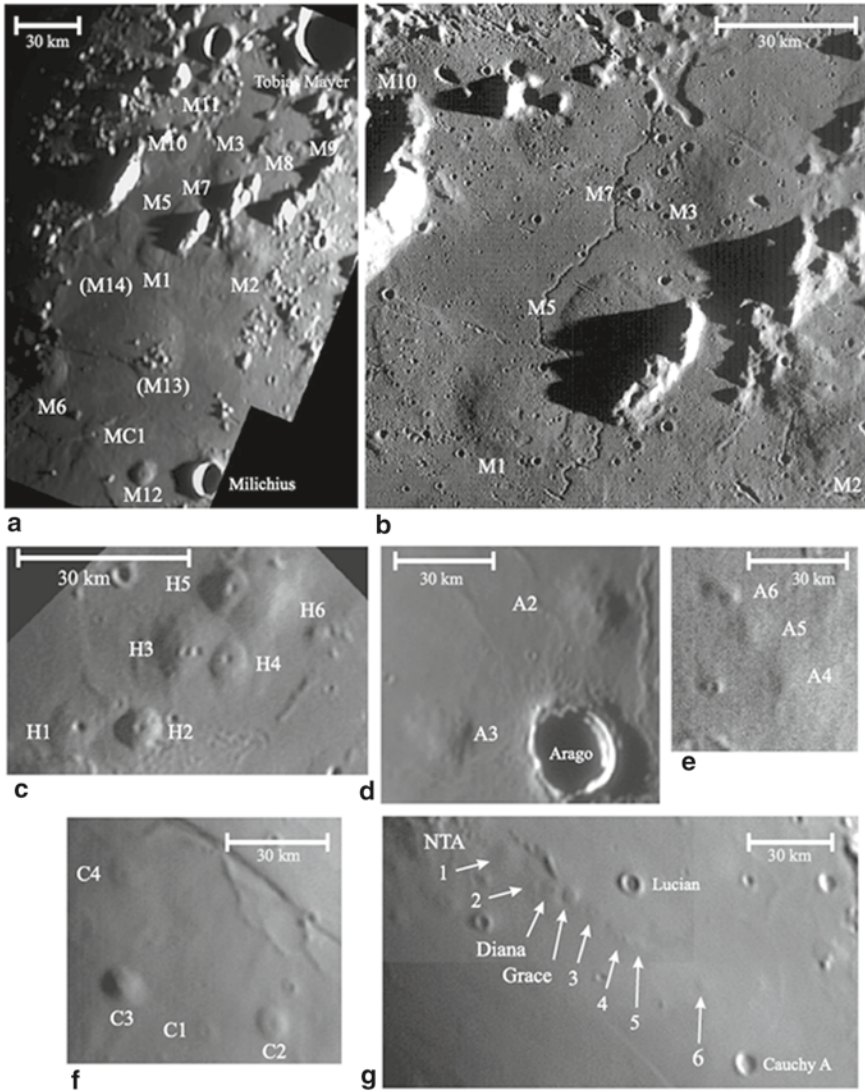
### 1.6.2 Domes Inside Craters

Lunar domes also occur inside some lava-filled craters, such as Capuanus and Petavius (Fig. 1.7a, b), where the lava probably lifted up the crater floor (Wichman and Schultz 1996). The pressurised magma ascended to the surface through dikes and built up domes.

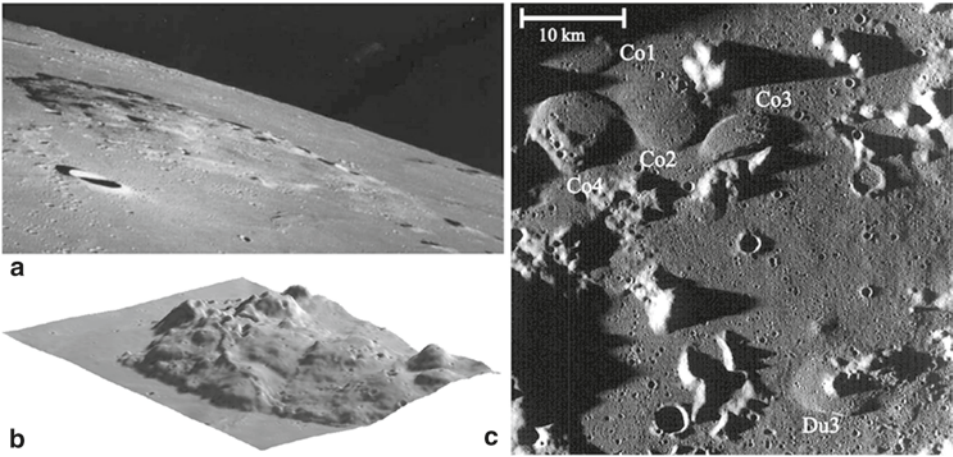
### 1.6.3 Domes in Highland Regions

Unusually steep lunar domes consisting of bright, spectrally red highland-like material can be found in northern Oceanus Procellarum near the craters Gruithuisen (domes Gruithuisen  $\gamma$ ,  $\delta$ , and NW) and Mairan (Wilson and Head 2003). According to Hawke



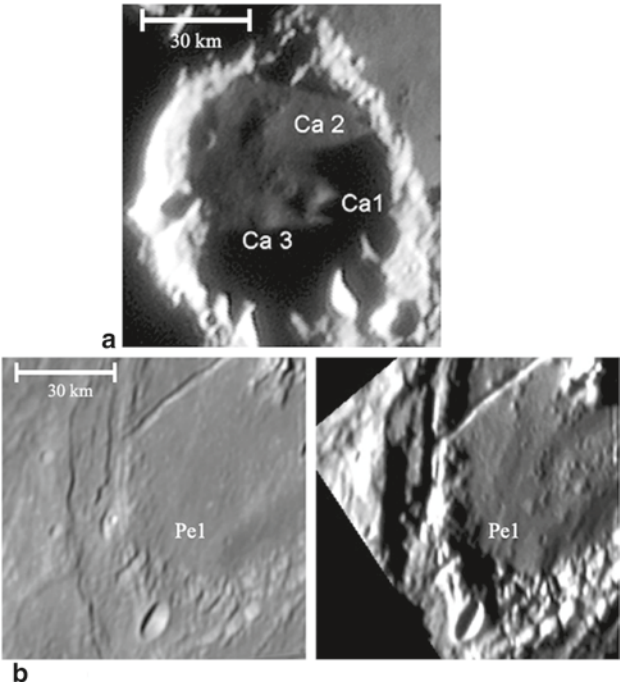


**Fig. 1.5** **a** Telescopic image of the dome field between Milichius and T. Mayer in Mare Insularum. (Image by J. Phillips). **b** Domes southwest of the crater T. Mayer. LROC WAC image M116520385ME (NASA/GSFC/Arizona State University). **c** Telescopic image of the domes north of Hortensius in Mare Insularum. (Image by M. Wirths). **d** Telescopic image of the large domes near Arago in Mare Tranquillitatis. (Image by P. Lazzarotti). **e** Telescopic image of the aligned low domes north of Arago. (Image by C. Wöhler). **f** Telescopic image of the domes south of the crater Cauchy in Mare Tranquillitatis. (Image by P. Lazzarotti). **g** Telescopic image of the Northern Tranquillitatis Alignment (NTA). (Image by C. Wöhler)



**Fig. 1.6** **a** Apollo 15 orbital image AS15-97-13252 (NASA), showing an oblique view of the lunar dome complex Mons Rümker from southern direction (NASA/USGS). **b** Dome complex Mons Rümker. 3D view from southwestern direction, obtained by shape from shading analysis of Smart-1 AMIE image LR3-R01914-00017-00100 (original AMIE image by ESA/J.-L. Josset/B. Grieger). **c** Domes Condorcet 1–4 and Dubiago 3 situated in Mare Undarum. LROC WAC image M117033140ME (NASA/GSFC/Arizona State University)

**Fig. 1.7** **a** Telescopic image of the domes inside the lava-filled crater Capuanus. (Image by S. Lammel). **b** Telescopic images of the dome at the southern rim of Petavius. The dark pyroclastic deposit associated with the dome is apparent in the *left* image. (Images by P. Lazzarotti)





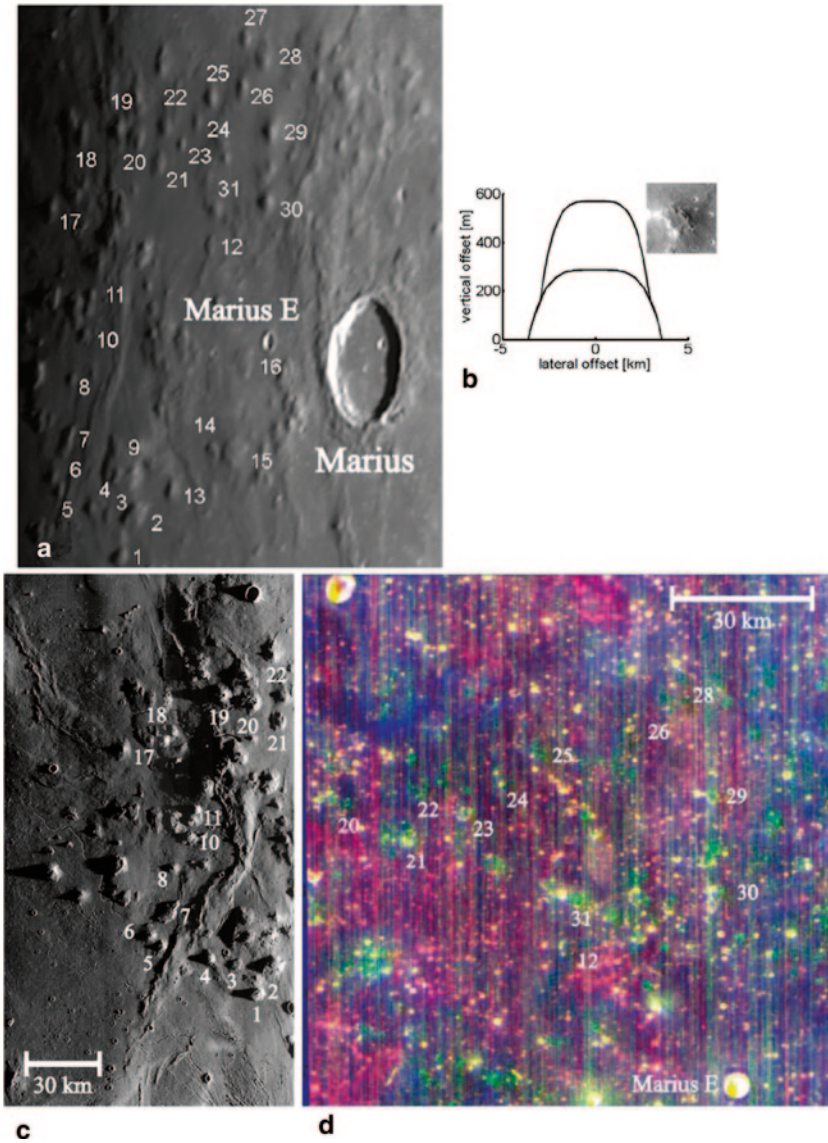


**Fig. 1.8** **a** Telescopic image of the Marius Hills region. The diameter of Marius crater corresponds to 41 km. (Image by J. Phillips). **b** Double-layered model of the dome Ma29 (Chap. 5) with cutout from LROC WAC mosaic (cutout: NASA/GSFC/Arizona State University). **c** Low-sun LROC WAC image M116696805ME of the western Marius Hills region (NASA/GSFC/Arizona State University). **d** Map of the integrated band depths of the 1000 nm absorption (IBD1, red channel) and the 2000 nm absorption (IBD2, green channel) and the LROC WAC radiance (NASA/GSFC/Arizona State University, blue channel). The IBD1 and IBD2 values were inferred from  $M^3$  data. Some of the domes are associated with high IBD2 values and appear as green patches. (This observation has first been reported by Besse et al. (2010), who provide a similar image)

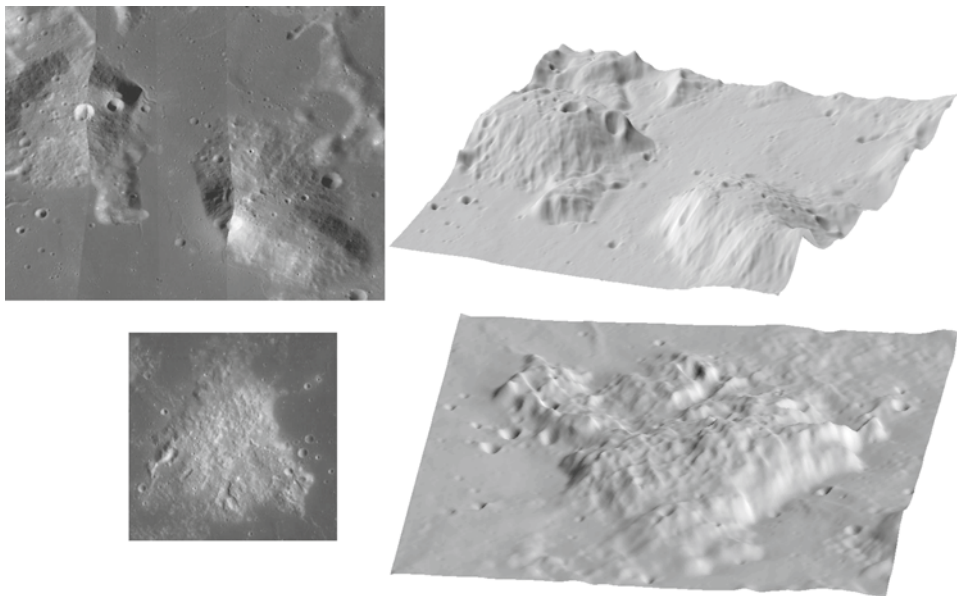


**Fig. 1.9** Global WAC mosaic images (NASA/GSFC/Arizona State University) and refined DEMs of (top) Gruithuisen  $\gamma$  and  $\delta$  and (bottom) Mons Hansteen, obtained using the method by Herbort et al. (2011) based on LOLA and M<sup>3</sup> data. The vertical axis of the DEMs is three times exaggerated. The heights of Gruithuisen  $\gamma$  and  $\delta$  and Mons Hansteen are 1,740, 2,010, and 1,070 m, respectively. (cf. Sect. 2.4.3)

et al. (2003), a similar feature presumably originating from non-mare volcanism is Mons Hansteen in southwestern Oceanus Procellarum (Fig. 1.9). The observed very high reflectance and spectrally red appearance of these so-called “highland domes” has led to the conclusion that their mineralogy is different from that of the lunar mare domes since the FeO and TiO<sub>2</sub> content of the dome material inferred from multispectral image data is much lower. These findings led to the suggestion of an early period of non-basaltic lunar volcanism unrelated to the maria (Chevrel et al. 1999). The rheologic modelling analysis by Wilson and Head (2003) yields high viscosities of the lava that formed the highland domes, which are comparable to those of terrestrial andesitic or rhyolitic lavas. The assumed source region is the lower lunar crust. A recent analysis by Kusuma et al. (2012) indicates an exceptionally high Si content of the material that makes up the highland domes Gruithuisen  $\gamma$  and  $\delta$ , thus supporting their formation by highly viscous lavas.

Some highland areas, such as the Schiller-Schickard basin located southwest of Mare Humorum, display mare basalts covered by a relatively thin layer of impact ejecta which is younger than the mare surface (Schultz and Spudis 1979; Blewett and Hawke 1993). These buried mare regions are termed “cryptomaria” (Head and Wilson 1992). In a few cases, cryptomare areas display effusive domes. Examples include a dome near Piccolomini and a dome near the craters Mee H and Drebbel F. The commonly accepted mechanism to explain the presence of highland components in mare soils and vice versa is “lateral mixing”

as a consequence of impact events as suggested by Li et al. (1997) and modelled in more detail by Li and Mustard (2000). Li and Mustard (2000) infer the respective fractions of mare and highland soil around the borderlines of mare regions based on spectral unmixing of Clementine UVVIS multispectral data. The obtained fractional amounts are explained for a range of distances from the mare-highland border of up to 10 km by the so-called “anomalous diffusion model”. The shapes of the determined curves denoting fractional abundance vs. distance from the border are found to be symmetric. From this observation, Li and Mustard (2000) conclude that the effect of lateral mixing on the surface composition strongly exceeds that of vertical mixing—the latter mechanism is caused by impacts that penetrate the mare basalt layer and bring up basin floor, i.e. highland, material from below the mare basalt onto the surface and distribute it around the impact crater.

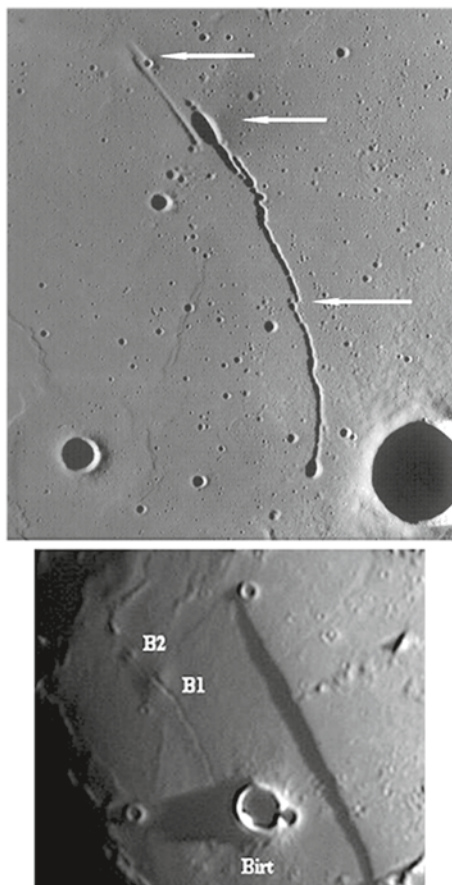
### 1.6.4 Domes Bisected by Rilles

Bisected domes are especially interesting volcanic features of the Moon, which will be described in detail in Chap. 6. According to Head and Wilson (1996), the visible traces of dike emplacement in the crust are depending on the depth below the surface to which the dike penetrates. If the ascent of the top of the dike stops at a large depth below the surface, the magnitude of the resulting stress field will be too small to cause any visible deformation of the surface. For depth values below about 2 km, extensional deformation and eventually graben formation will occur as a result of the stress field. If the dike ascends to depths between 1.5 and 2.0 km, degassing will occur in parallel with graben formation, leading to the formation of explosion craters such as those observed along the Hyginus rille, while intrusion depths in between 2 and 3 km will lead to the formation of similar volcanic structures related to degassing processes without stress-induced graben formation. If a dike ascends to shallow depths of typically some tens of metres and at most about 150 m, the magma may gain access to the surface at some parts of the dike, such that a dome may be formed together with a linear graben (Head and Wilson 1996; cf. also Jackson et al. 1997).

Rima Birt located in Mare Nubium is associated with two bisected domes (Fig. 1.10). It is a slightly curved rille of more than 50 km length and displays an offset in its central section. It is unlikely that such offsets occur in a lava channel or tube produced by flowing lava. Hence, according to the model by Head and Wilson (1996) it is plausible to attribute the formation of the different parts of Rima Birt to the stress field resulting from the ascent of one or several dikes to shallow depth below the surface, where some of the intruded magma reached the surface and formed the low domes B1 and B2 indicated in Fig. 1.10.

As apparent in Fig. 1.11, Rima Menelaus I bisects two dome-like structures which might, however, also be considered mare kipukas, i.e. surface parts surrounded by mare plains of lower age (Howard et al. 1973; cf. also Nichols et al. 1974; Head and Gifford 1980). The composition of a kipuka is usually different from that of the surrounding mare, such that a spectral contrast is observed. A typical example of a lunar kipuka is the formation

**Fig. 1.10** (*top*) LROC WAC image M117555061M of Rima Birt (NASA/GSFC/Arizona State University). The rille has an offset in its central section, which is marked by an *arrow*; (*bottom*) Telescopic image of the two bisected domes B1 and B2 at the northern end of Rima Birt. (Image by C. Wöhler)



Darney  $\chi$  located in the western part of Mare Cognitum, which corresponds to a bright, elevated part of highland surface embayed by darker mare lava (Nichols et al. 1974).

For the Menelaus domes, the dike lengths resulting from rheologic models (Chap. 4) are comparable to the extensions of the linear rilles associated with the domes, which correspond to about 100–150 km, suggesting that the Menelaus rilles may well represent the surface expressions of dome-forming dikes according to the model by Head and Wilson (1996).

The presence of rilles crossing the surface of lunar domes is a common phenomenon. A dome located near the crater Doppelmayer is associated with several linear rilles and an outflow channel or chain of vents (Fig. 1.12). The lava forming this feature appears to have flowed around an elevated part of the highland terrain to its south. According to the dike intrusion mechanisms described by Head and Wilson (1992, 1996), it is plausible to assume that the narrow linear rilles near the dome were formed by dikes that ascended to depths below the surface shallow enough to allow for graben formation (features A and B



**Fig. 1.11** (*top*) Section of LROC WAC image M117386175ME of the Menelaus region (NASA/GSFC/Arizona State University); (*bottom*) Telescopic image of the Menelaus region including two bisected domes inside of Menelaus, termed Menelaus 1 and 2. (Image by J. Phillips)

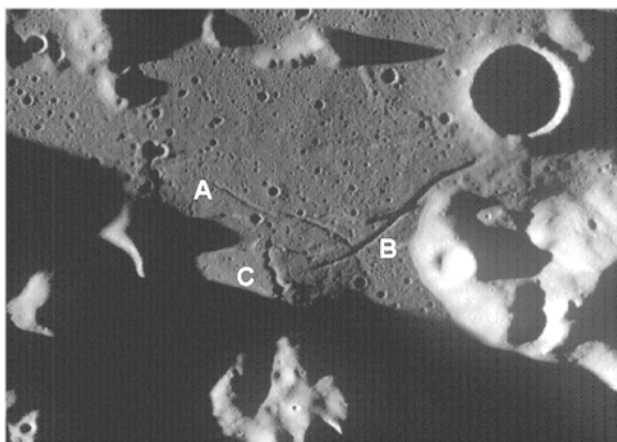
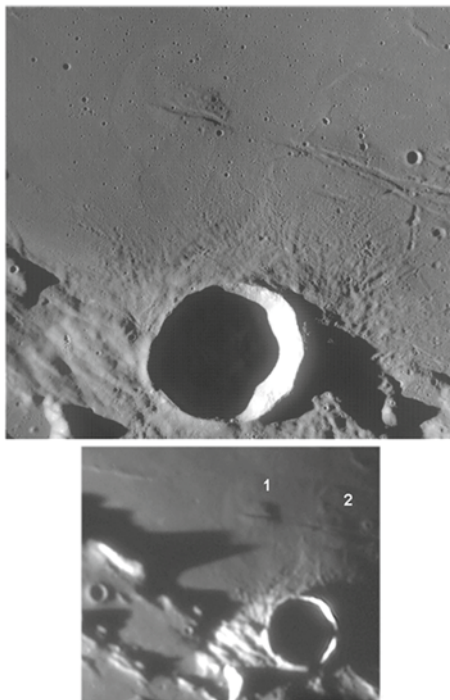
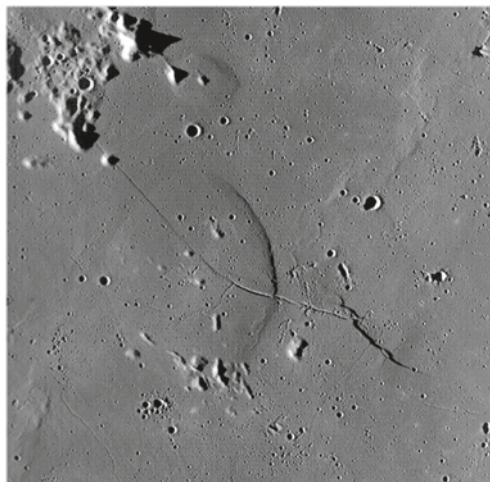


**Fig. 1.12** Section of LROC image WAC M116595799ME (NASA/GSFC/Arizona State University). It shows the presence of several rilles crossing the surface of a dome located near the crater Doppelmayr, termed Doppelmayr 2. The dome appears to have a smooth surface with an outflow channel or chain of vents (feature C) and linear rilles (features A and B) due to tensional stress, probably formed by dike intrusion

**Fig. 1.13** Section of LROC image WAC M117420283ME (NASA/GSFC/Arizona State University). The large and flat dome, unofficially termed “Valentine dome”, and its smaller northern neighbour are associated with faults and rilles. Both show non-volcanic hills on their surface. The large Valentine dome is characterized by the presence of a curvilinear rille traversing the surface



in Fig. 1.12). Some of the magma in the dike gained access to the surface, resulting in an extensive effusion of relatively cool and viscous lava leading to the formation of the dome and the generation of the associated outflow channel or chain of effusive vents (feature C in Fig. 1.12) (Lena et al. 2007).

### 1.6.5 Domes with Non-volcanic Hills and Linear Rilles on their Surface

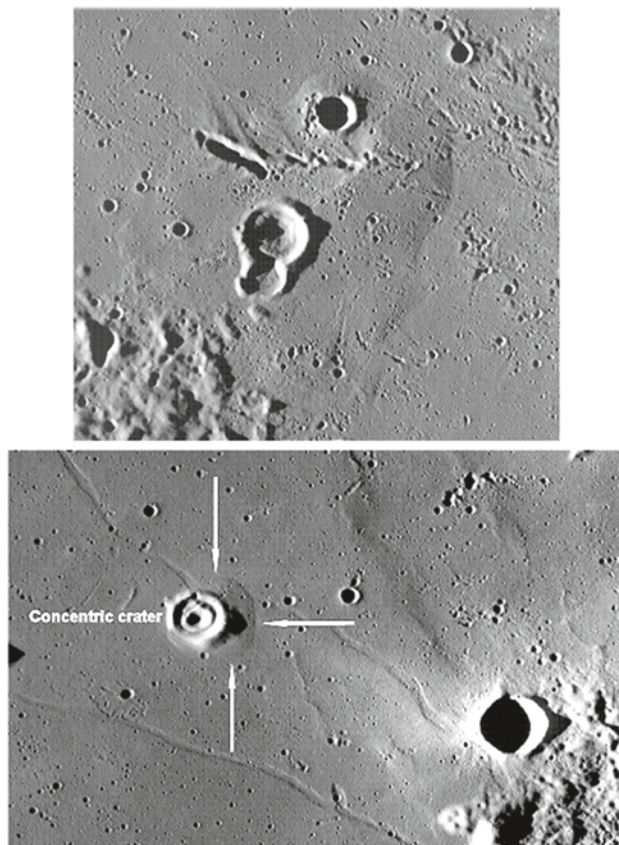
The surfaces of several low domes of elongated shape show small embayed non-volcanic hills on their surface. Examples are the large Valentine dome situated in Mare Serenitatis and its smaller northern neighbour (Fig. 1.13). Presumably, these hills are part of the underlying basin floor below the mare lavas. In some cases, the surface of such low lunar domes are crossed by linear rilles. The association of linear rilles with large and flat domes may suggest a formation mechanism based on magmatic intrusion in a way similar to a terrestrial laccolith. Details of this possible formation mechanism are described in Sect. 1.6.8.

### 1.6.6 Domes with Concentric Craters on their Summit

Some small lunar craters display besides their main rim an additional inner ring, the size of which is about half as large as the size of the crater itself. The average diameter of these “concentric craters” amounts to about 8 km (Wood 1978). The morphology and distribution of 51 concentric craters is examined by Wood (1978), who finds that rather than being randomly distributed, a fraction of 70 % of the catalogued concentric craters are situated in



**Fig. 1.14** (*top*) Section of LROC WAC image M117481923ME (NASA/GSFC/Arizona State University). The concentric crater Archytas G is located on the summit of a low and flat dome; (*bottom*) A crop of the LROC WAC image M116419373ME (NASA/GSFC/Arizona State University). The concentric crater Marth is located on the summit of a low and flat dome, a configuration which has already been noted by Wood (1978). In both images, linear rilles indicating tensional stress are detectable



the close proximity of the borders of mare regions, sometimes also on lava-flooded crater floors or (rarely) in highlands regions.

It is suggested by Wood (1978) that the inner rings of concentric craters were formed by the eruption of high-viscosity lava which ascended to the surface through impact-related fractures. An alternative hypothesis is the formation of concentric craters by impact on a surface characterized by two horizontal superposed layers, where the upper layer is “softer” than the lower layer (Piekutowski 1977; Abels 2004). According to the analysis of terrestrial concentric craters by Abels (2004), the upper layer may e.g. consist of sediments and the lower layer of crystalline material. A third theory suggests that if an impact occurred in an area with ongoing magmatic intrusion, the thinned part of the rock layer on top of the intrusive body was probably unable to resist the pressurised magma, which in turn may have lifted up the crater floor, thus leading to the shallow crater depth. In this line of thought, the inner ring of a concentric crater is a remnant of the original bowl-shaped crater floor (Wöhler and Lena 2009).

Based on morphologic, morphometric, and compositional considerations as well as the spatial distribution of the known concentric craters across the lunar surface, Trang et al.

(2011) arrive at the conclusion that a formation mechanism related to magmatic intrusion is the most plausible one. This finding is supported by the craters Archytas G and Marth—the superposition of the crater Marth on top of a slightly elevated structure is described by Wood (1978). These are two examples of concentric craters situated on top of a low dome of likely intrusive origin (Fig. 1.14).

### 1.6.7 Aligned Lunar Domes, Formation along Crustal Fractures

The strong differences in dome shapes lead to questions about where the source regions of the various dome types are located, about the reasons why certain types of lunar domes are concentrated in certain areas of the lunar surface, why especially domes with gentle flank slopes tend to be aligned, and which differences in the formation conditions led to the observed variety of lunar dome properties.

The low domes in the Milichius/T. Mayer region display elongated summit vents or fissures oriented in parallel, radially with respect to both the Insularum basin (Spudis 1993) and the East Procellarum basin postulated by de Hon (1979) (cf. also Spudis 1993). The locations of four of these domes are forming a linear chain of 210 km length in the same direction. Similarly, the eight low domes situated in northern Mare Tranquillitatis forming a linear chain of 100 km length are aligned radially with respect to the Imbrium basin (Fig. 1.5g). Six of these domes display elongated summit vents oriented in the same direction. Another alignment is represented by the domes Condorcet 1–4 (Fig. 1.6c) in Mare Undarum, radial to the Crisium basin. The explanation proposed for these observations is that the domes were formed along crustal fractures generated by major impact events, hence running radially with respect to basin centres since dikes tend to be extended orthogonal to the direction of lowest compressional stress (Rubin 1993b, 1995). In this context, the elongated summit vents are interpreted to indicate the direction of the dike through which the magma ascended to the lunar surface. Hence, in the line of thought of the model by Rubin (1993b) impact-induced stress fields caused by large impact events, facilitated the ascent of dikes and led to the formation of domes (Wöhler et al. 2007).

Furthermore, Spudis et al. (2011) describe the observation that the most important lunar dome fields (and other volcanic regions primarily characterised by sinuous rilles or lunar cones) are situated on large parts of topographically elevated terrain measuring up to several hundred kilometres across. They put forward the hypothesis that these elevated regions are large shield volcanoes. Their study comprises seven well-known volcanic regions, including Mons Rümker, the Aristarchus and Prinz-Harbinger plateaus, Marius Hills, the region around Kepler, the Hortensius/Milichius/T. Mayer region, and the Cauchy region. Spudis et al. (2011) point out that the diameters and heights of the putative large lunar shields are similar to those observed for shield volcanoes on Venus and Mars.

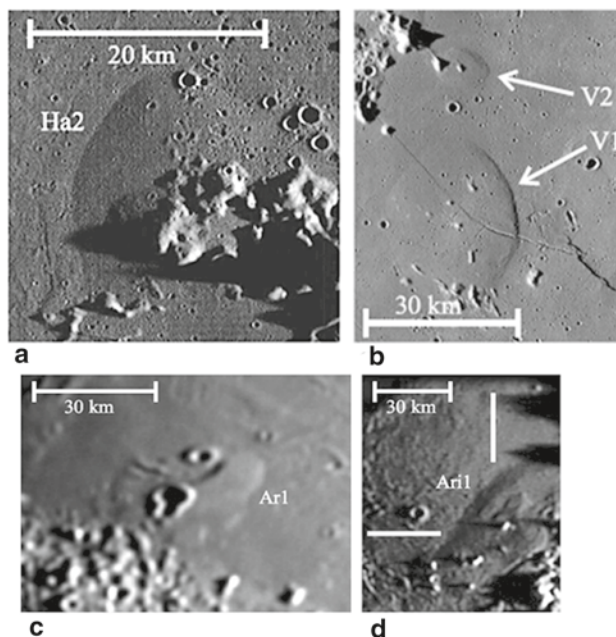


**Fig. 1.15** Candidate lunar intrusive domes. **a** LROC WAC image M116629324ME of Hansteen 2 near Hansteen crater (NASA/GSFC/Arizona State University). **b** LROC WAC image M117420283ME of the Valentine dome V1 with its smaller northern neighbour V2 in western Mare Serenitatis (NASA/GSFC/Arizona State University). **c** Telescopic image of Archytas 1 in Mare Frigoris. (Image by J. Phillips). **d** Telescopic image of Aristillus 1 at the eastern border of Mare Imbrium. For the Valentine dome and Archytas 1 dome see also the high resolution images shown in Figs. 1.13 and 1.14, respectively. (Image by R. Lena)

### 1.6.8 Lunar Intrusive Domes

Head and Gifford (1980) state as a general remark that an intrusive origin of some lunar domes “cannot be established or ruled out on the basis of available data”. Some domes which do not display effusive vents differ morphometrically from the common effusive domes in that they are characterised by very low flank slopes of less than  $0.9^\circ$ , often have larger diameters than effusive lunar domes of 30 km and more, and display non-circular outlines. These domes tend to be associated with tectonic faults or linear rilles, indicating tensional stress, and may suggest a possible, and plausible, intrusive mode of formation (Wöhler and Lena 2009).

On the Earth, the intrusion of a magmatic body often leads to the formation of a laccolith, where pressurised magma penetrates between layers of rock and bends the upper layer upwards (Pollard and Fletcher 2005). Wichman and Schultz (1996) adopt the laccolith formation model by Johnson and Pollard (1973), who postulate that laccolith formation is characterised by three distinct stages. During the first stage, a thin horizontal magma layer

similar to a sill expands laterally. The second stage consists of an expansion of the pressurised magmatic body in vertical direction, leading to flexure of the upper layer. During the third stage of laccolith formation, a “piston-like uplift” of a piece of crustal material surrounded by faults may occur (Wichman and Schultz 1996).

This mechanism is proposed by Carlino et al. (2006) as a mode of formation for the Epomeo mountain on the Italian island of Ischia. Wichman and Schultz (1996) attribute the modification processes observed in floor-fractured lunar craters, such as uplift and fracturing of the crater floor, to the formation and vertical expansion of laccoliths, especially the third (“piston-like uplift”) stage, employing the laccolith model by Johnson and Pollard (1973).

A formation by intrusive processes is supported by the linear or curvilinear rilles associated with many of the candidate intrusive domes, as such features are commonly interpreted as being due to fractural processes (Nichols et al. 1974; Wichman and Schultz 1996). They may thus be formed by the flexural uplift of a laccolith. Furthermore, some of the larger candidate lunar intrusive domes are limited by faults (Fig. 1.15), which may indicate the beginning of the piston-like uplift of a laccolith. Hence, the intrusion of laccoliths appears as a possible and plausible mode of formation. We will present in Chap. 4 arguments against and in favour of an intrusive laccolithic origin of these shallow swell-like lunar structures, providing a comparison with terrestrial laccoliths both qualitatively and in the context of the recent numerical analysis by Michaut (2011).

## Abstract

This chapter describes different methods for determining the morphometric properties (diameter, height, flank slope, volume) of lunar domes, a model to estimate the physical properties of the dome-forming magma, and different classification schemes for lunar domes.

## 2.1 Observing Lunar Domes

The appearance of an “ideal” dome of hemispherical shape located on an even mare surface can be simulated based on image rendering, which provides an artificial image and thus yields the brightness distribution across the dome surface and the shape of the shadow (Fig. 2.1). The dome diameter is given by  $D$  and its height by  $h$ . Domes with a non-circular outline can be described by a major axis  $a$  and a minor axis  $b$ . We then define the dome diameter as the geometric mean  $D = (ab)^{1/2}$  and its so-called circularity by  $c = b/a$ .

Based on this approach, it can be shown according to Lena et al. (2004) that lunar domes with their typically low flank slopes display a significant contrast with respect to the surrounding surface only when the solar elevation angle is lower than 4–5°. As shown in Fig. 2.1b, only slightly different solar elevation angles may result in strong differences in the simulated image of the dome and its shadow. For a dome located on a sloping surface, the shadow is longer than for a dome situated on an even surface when the surrounding surface is inclined away from the sun and is shorter otherwise (Fig. 2.2). If the dome is not hemispherical but has steep flanks and a flat surface, the shape and length of the shadow are different from those shown in Fig. 2.1.

The selenographic coordinates of a lunar dome and its diameter can be computed based on a telescopic CCD image e.g. using the freely available Lunar Terminator Visualization Tool (LTVT) software package by Mosher and Bondo (2012). This software relies on the Unified Lunar Control Network (ULCN) 1994 (Davies et al. 1994) or, in a more recent version, on the ULCN 2005 (Archinal et al. 2006). For each control point in this list, precise

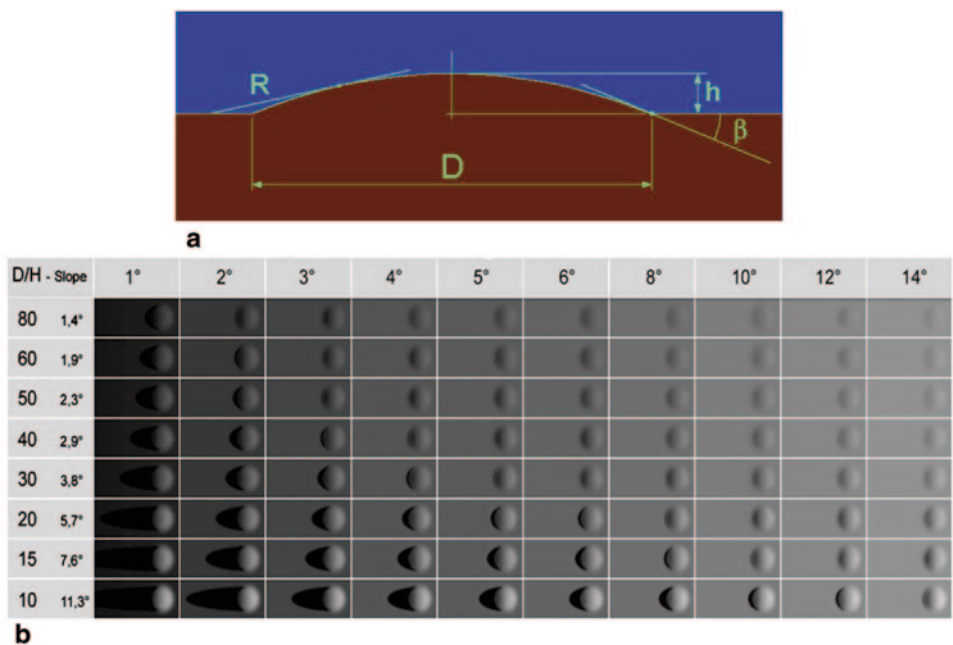


**Fig. 2.1** **a** A lunar dome of diameter  $D$  and height  $h$ . **b** Model of an “ideal” dome with hemispherical cross-section located on a flat mare surface, rendered with the software developed by Lena et al. (2004). The appearance of a dome changes with increasing solar elevation

information about the selenographic coordinates and the elevation with respect to the average lunar radius is available. Marking some of these control points in a CCD image within the LTVT software then allows to read out selenographic coordinates for each image pixel.

## 2.2 Images Rendered Based on Topographic Data

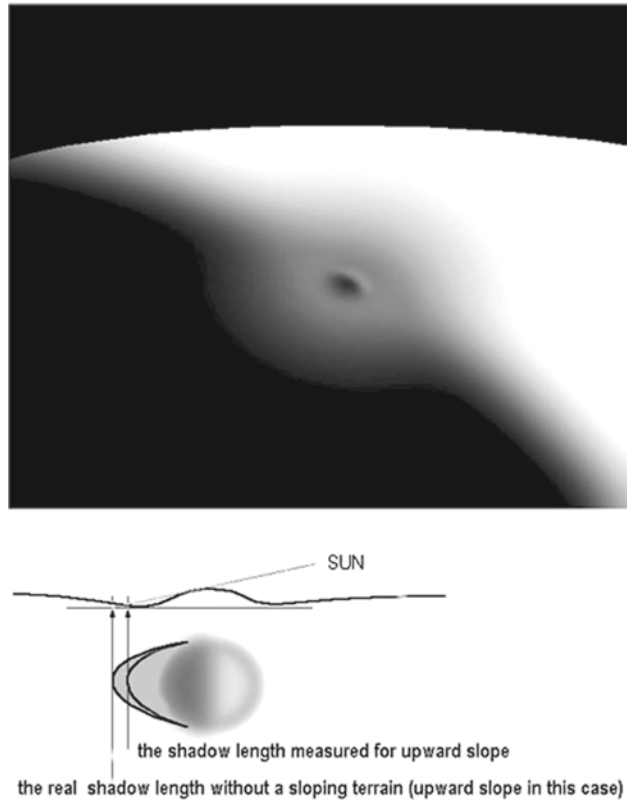
Digital elevation models (DEMs) are of high importance for geologic interpretations. Most DEMs presented in this book were obtained based on an analysis of spacecraft or telescopic CCD images in terms of photoclinometry and shape from shading. These approaches rely on the fact that surface parts inclined towards the sun appear brighter than surface parts inclined away from it. The shape from shading approach aims for deriving the orientation of the surface at each image location by using a model of the reflectance properties of the surface and knowledge of the illumination conditions, finally leading to an elevation value for each image pixel (Horn 1990).

Inversely, a synthetic image of a dome can be generated based on an available DEM as seen from a given direction for lighting from some other specified direction. A global lunar DEM with a grid size of 1/1024 degree, obtained with the Lunar Orbiter Laser Altimeter (LOLA) instrument, has been released.<sup>1</sup> The LOLA instrument measures the distance

<sup>1</sup> <http://pds-geosciences.wustl.edu/missions/lro/lola.htm>.



**Fig. 2.2** The effect produced by a sloping soil on the shadow length: it will be either longer (*downward slope*) or shorter (*upward slope*) than on a flat surface



between the spacecraft and the lunar surface based on the time-of-flight of emitted laser pulses with a nominal accuracy of 0.1 m (Smith et al. 2010). The LTVT software can be used to generate synthetic views of selected parts of the LOLA DEM (Figs. 2.3 and 2.4).

The global LOLA DEM reveals many lunar domes and allows to estimate their diameters, approximate heights, and volumes. However, it is hardly possible to identify lunar domes in LOLA data alone, especially when they are situated on sloped terrain. In these cases, the dome shape and especially its diameter, which together with the height defines the flank slope, is not easily separable from the underlying terrain in the LOLA DEM. Additional images acquired at low solar elevation angles of no more than a few degrees are then required for an unambiguous identification of a dome based on its characteristic morphology.

## 2.3 Image-Based Photogrammetric Measurements

The Lunar Topographic Orthophotomaps, based on images acquired by the Apollo 15, 16, and 17 command modules with modified aerial cameras, were computed based on classical photogrammetric triangulation and represent lunar topographic data with elevation

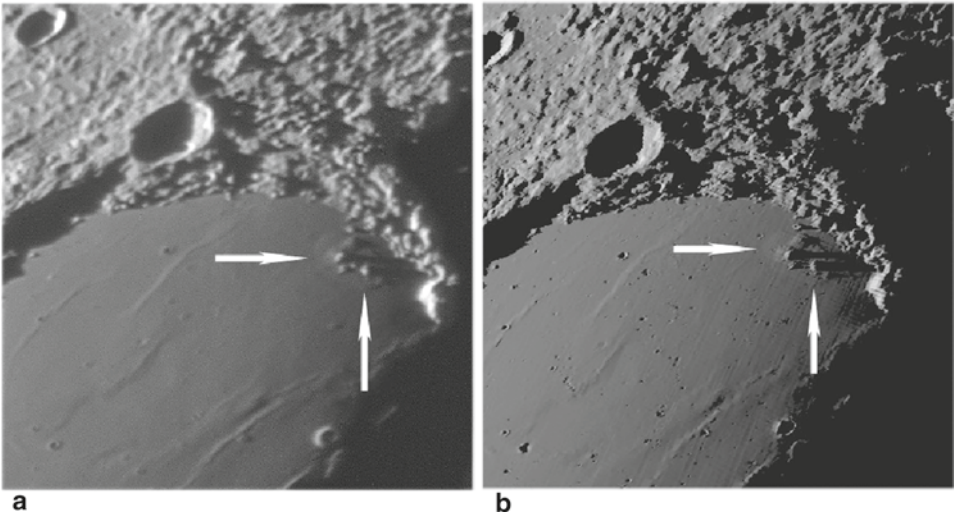


**Fig. 2.3** **a** Telescopic image of a large domical feature in Sinus Iridum with several hills on top of it, image under late evening illumination. (Image by K. C. Pau). **b** Image rendered for the same illumination conditions based on the LOLA DEM

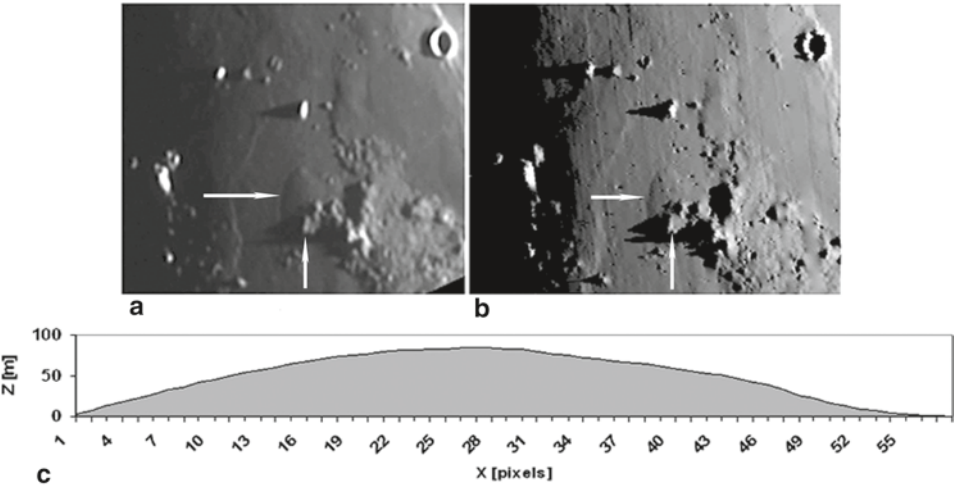


**Fig. 2.4** **a** Telescopic image of a dome located near the crater Hansteen, termed Hansteen 2. (Image by J. Phillips taken under a solar elevation of  $1.56^\circ$ ). **b** Image rendered for the same illumination conditions based on the LOLA DEM. **c** Cross-sectional profile of Hansteen 2 in east-west direction, obtained based on phot clinometry. The vertical axis is 20 times exaggerated. The effective dome height after subtraction of the spherical curvature amounts to  $85 \pm 10$  m



standard errors of 30 m (Wu and Doyle 1990). They only cover a part of the lunar surface, mainly comprising Mare Serenitatis and Mare Tranquillitatis. Arya et al. (2011) present a DEM of one of the Marius Hills domes obtained using Chandrayaan-1 Terrain Mapping Camera (TMC) images. However, no statements are made about the lateral resolution and vertical accuracy of the DEM, and to our knowledge only one local TMC-based dome DEM has been published so far.

## 2.4 Determination of Morphometric Properties

### 2.4.1 Shadow Length Measurements

From the shadow length  $l$  corrected for foreshortening and a local solar elevation angle  $\mu$ , the height  $h$  of a dome is given by

$$h = l \tan \mu. \quad (2.1)$$

The average flank slope angle  $\xi$  is then given by

$$\xi = \arctan \left( \frac{2h}{D} \right) \quad (2.2)$$

where  $D$  is the diameter of the dome and  $h$  its height.

The heights of more than 200 lunar domes were determined by Brungart (1964) based on telescopic lunar photographs by measuring shadow lengths, but his height estimates tend to be systematically too high. A possible reason is that on the high-contrast photographic reproductions of that time true shadows and shading effects could easily be confused. For example, for a dome (entry #30) on the floor of Capuanus crater (Capuanus 1, Fig. 1.7a), Brungart (1964) states a height of 376 m. Our shadow-based measurement yields a height of  $100 \pm 15$  m for the same dome, consistent with the value obtained by the DEM construction approach described in Sect. 2.4.2.

A different shadow-based method for measuring lunar dome heights is introduced by Ashbrook (1961), who shows that the average slope of the dome flank equals the solar elevation angle when the shadow covers one quarter of the dome diameter, assuming a spherical surface of the dome. The observer determines the moment in time (corresponding to a known solar elevation angle  $\xi$ ) for which this condition is met. The dome height is then readily obtained using Eq. 2.1 with  $\mu = \xi$ . The method by Ashbrook (1961) has primarily been devised for visual observations. The assumption of a spherical dome surface, however, represents a significant restriction. For the dome Milichius  $\pi$  (Fig. 2.5), a height of 742 m with an average slope of  $9^\circ$  is reported by Brungart (1964). We estimated the height of this dome with the method by Ashbrook (1961), yielding an average slope angle

**Fig. 2.5** Telescopic image of Milichius  $\pi$  (M12 in Fig. 1.5a) taken by J. Phillips (solar elevation  $2.7^\circ$ ). The Ashbrook method yields a dome height of  $220 \pm 25$  m



**Table 2.1** Dome height and slope values determined using the shadow-based method by Ashbrook (1961) and the shape from shading approach (cf. Fig. 1.5 for identification of the domes)

Dome	Ashbrook		Shape from shading	
	Slope ( $^\circ$ )	Height (m)	Slope ( $^\circ$ )	Height (m)
C11	0.6	60	0.7	75
A2	1.5	310	1.5	330
H7	1.5	100	1.5	100
M11	2.8	150	2.8	150
M12	2.7	220	2.7	220

of  $2.7^\circ$  and a height of 220 m, which is found to be in good agreement with the photoclinometry and shape from shading analysis described in Sect. 2.4.2, resulting in a height of  $220 \pm 25$  m. Slope and height values determined for some domes using the shadow-based method by Ashbrook (1961) and the shape from shading method are listed in Table 2.1.

As described in Sect. 1.6.5, some domes exhibit small embayed non-volcanic hills on their flanks (the dome V2 in Fig. 1.15b). Under sunrise and sunset illumination conditions, the hill on the dome V2 casts a shadow on the dome summit and on the surrounding surface, yielding height values of  $h_1$  and  $h_2$ , respectively (Fig. 2.6). The height  $h$  of the dome is thus given by  $h = h_2 - h_1$ .

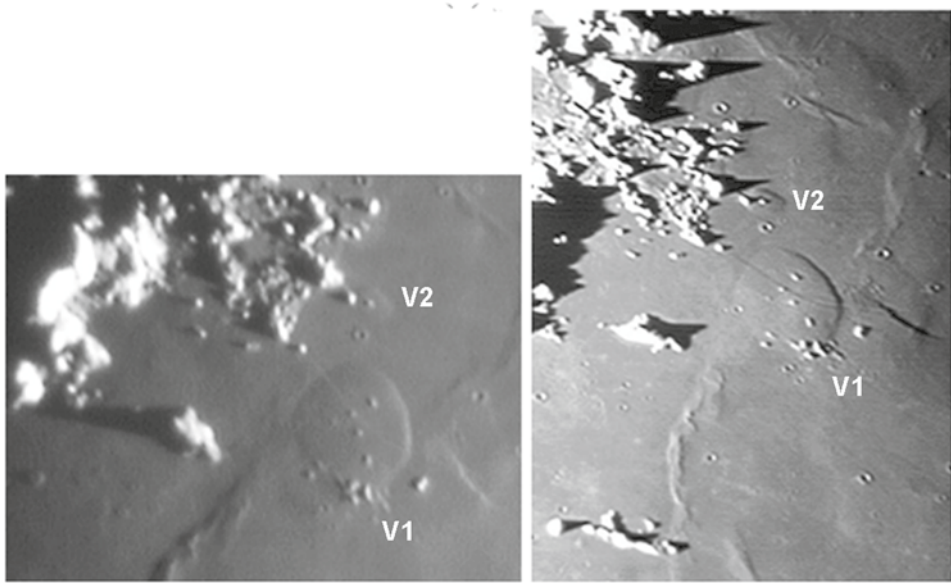


**Fig. 2.6** Telescopic images of the Valentine dome and the dome V2, taken by K. C. Pau under opposite illumination (left image with solar elevation of  $3.4^\circ$  and right image with solar elevation of  $3.2^\circ$ , respectively). A height value of 76 m was derived by bidirectional evaluation of the length of the shadow cast by a hill on the surrounding mare surface under sunrise illumination ( $h_s = 336$  m) and on the dome summit under sunset illumination ( $h_l = 260$  m), respectively, implying a height of 76 m. The shape from shading method yields a dome height of  $80 \pm 10$  m

## 2.4.2 Photoclinometry and Shape from Shading

Photoclinometric and shape from shading techniques have been proven to be suitable for the construction of local DEMs of the lunar surface, especially of low volcanic edifices. Since images acquired under solar illumination angles of less than a few degrees are required to reveal low domes, and because the current spacecraft image archives do not contain many images of this kind, we performed a reconstruction of the DEMs of a large set of lunar domes based on telescopic image data, relying on a combined photoclinometry and shape from shading approach.

The shape from shading method requires accurate knowledge of the reflectance properties of the surface material. The so-called Lambert model assumes perfectly diffuse scattering, implying an intensity  $R_L$  of scattered light according to

$$R_L(\rho, \theta_i) = \rho \cos \theta_i \quad (2.3)$$

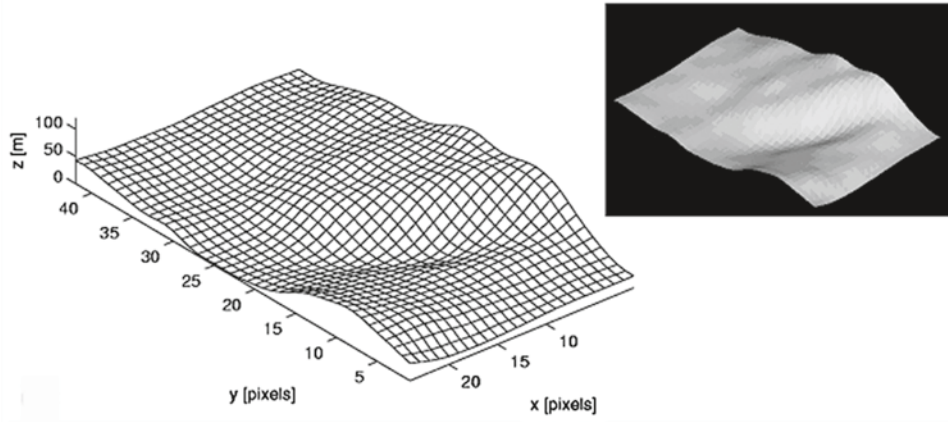


**Fig. 2.7** DEM of the eastern flank of the dome V2 derived from Fig. 2.6 based on the shape from shading method (view from northeastern direction). The dome height corresponds to  $80 \pm 10$  m. The curvature of the lunar surface has been subtracted

with  $\rho$  as the surface albedo and  $\theta_i$  as the incidence angle between the normal vector of the surface and the illumination direction (Horn 1990). However, the Lambert model does not provide an accurate representation of the true scattering behaviour of the lunar surface. A much more appropriate relation is the physically motivated reflectance function by Hapke (1981, 1984, 1986, 2002) that is based on the theory of radiative transfer. It is not straightforward, however, to directly apply that model to 3D reconstruction (McEwen 1991). Therefore, in many remote sensing applications, the empirical lunar-Lambert law by McEwen (1991) is used according to

$$R_{LL}(\rho, \theta_i, \theta_e, \alpha) = \rho \left[ 2L(\alpha) \frac{\cos \theta_i}{\cos \theta_i + \cos \theta_e} + (1 - L(\alpha)) \cos \theta_i \right] \quad (2.4)$$

with  $\theta_e$  as the emission angle between the normal vector of the surface and the viewing direction, and the lunar-Lambert parameter  $L(\alpha)$  as an empirical value depending on the phase angle  $\alpha$  between the illumination and the viewing direction. Given a suitable choice of  $L(\alpha)$ , the lunar-Lambert law fits the true scattering behaviour of a planetary surface similarly well as the Hapke model. Values of  $L(\alpha)$  are given by McEwen (1991) for various kinds of planetary surfaces.

According to the method introduced by Horn (1990), the DEM is constructed by adjusting the gradients of the surface such that the average deviation of the observed and the modelled reflectance is minimised. The illumination direction and the viewing direction are known. An iterative optimisation scheme yields the surface gradient field along with

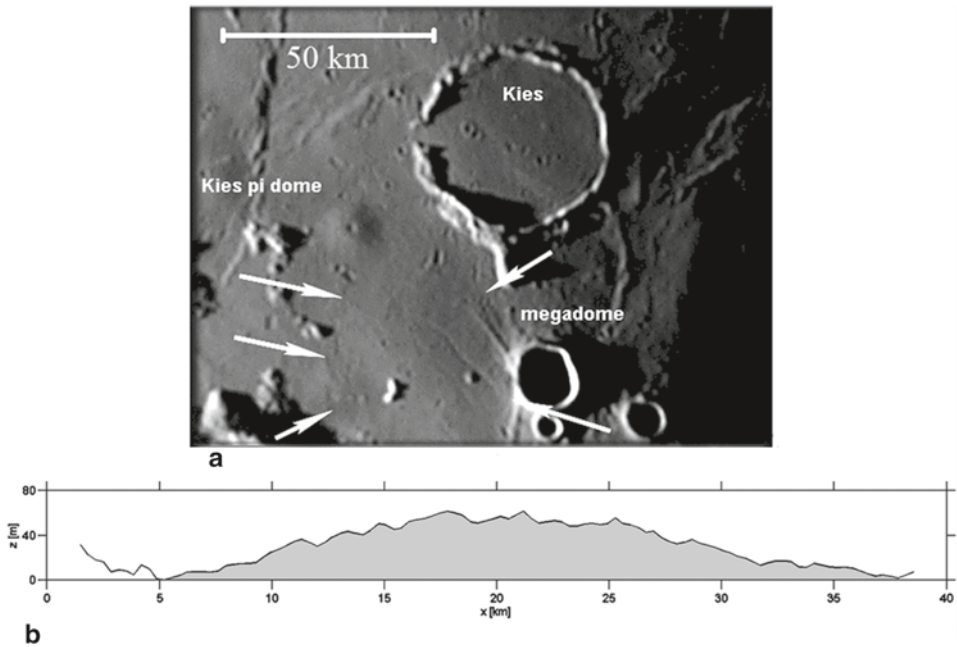


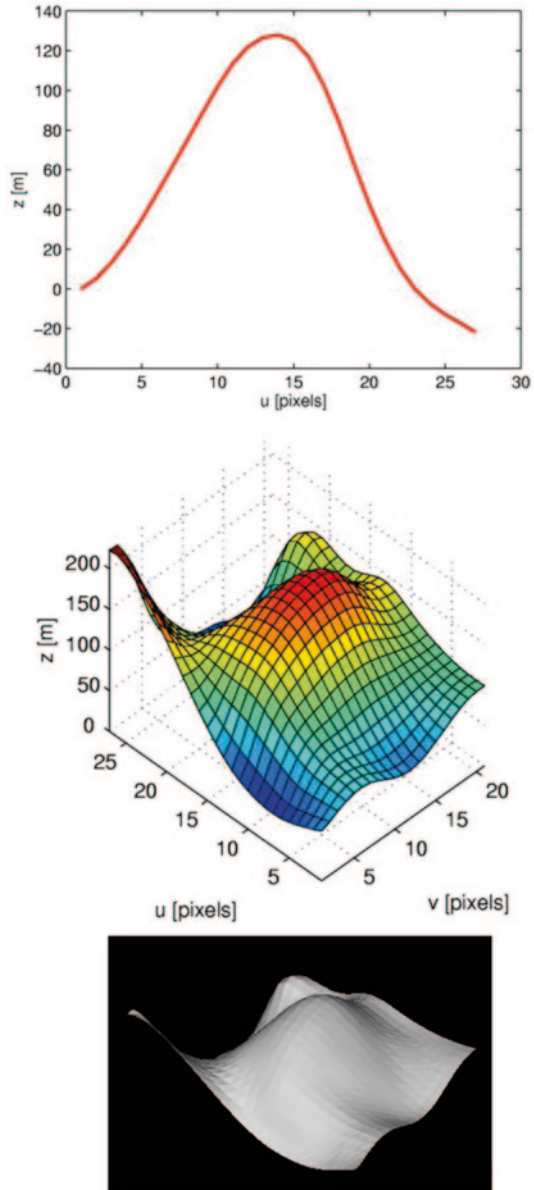
**Fig. 2.8** **a** Telescopic image of the large dome Kies 2, located near the effusive dome Kies  $\pi$ . (Image by J. Phillips). **b** Cross-sectional profile of Kies 2 in east-west direction. The vertical axis is 50 times exaggerated, the curvature of the lunar surface has been subtracted. The height amounts to  $55 \pm 5$  m. The rough shape of the surface is an artefact resulting from the image noise

the corresponding surface (i.e. the DEM) that fits best with the observed pixel intensities (Figs. 2.7 and 2.9).

The height  $h$  of a dome is obtained by measuring the elevation differences in the reconstructed DEM between the dome summit and the surrounding surface, taking into account the curvature of the lunar surface (Figs. 2.7–2.11). The dome volume  $V$  is computed by integrating the DEM over an area corresponding to a circular region of diameter  $D$  around the dome centre. If only a part of the dome surface can be reconstructed, e.g. due to the presence of shadows cast on the dome surfaces by nearby hills, the volume is estimated based on a cross-section in east-west direction through the centre of the dome, assuming rotational symmetry. A rough quantitative measure for the shape of the dome is given by the form factor  $f = V / [h\pi(D/2)^2]$ , where we have  $f = 1/3$  for domes of conical shape,  $f = 1/2$  for parabolic shape,  $f = 1$  for cylindrical shape, and intermediate values for spherical shape.

The typical relative accuracy was found to correspond to 10 % for the dome height  $h$  and of 20 % for the volume  $V$ . A comprehensive catalogue of the morphometric properties of a large set of lunar domes is given by Lena and Wöhler (2011). Our dome height

**Fig. 2.9** DEM of the dome M11 obtained by means of the shape from shading method (Fig. 1.5a). Cross-section through the summit of the dome obtained with the photoclinometric approach (*top*), DEM viewed from the north-west (*middle*), and rendered view derived from the DEM (*bottom*, vertical axis 20 times exaggerated). The dome height amounts to  $135 \pm 20$  m. The curvature of the lunar surface has been subtracted



values and those derived from the LOLA DEM commonly correspond to each other within less than a few percent. The modelling analyses about rheologic properties described in Sect. 2.5 mainly rely on dome heights inferred from low-sun images using the shape from shading technique. An advantage of the shape from shading approach is the fact that the image used for DEM construction can serve simultaneously for an accurate identification of the dome outline, while using the LOLA DEM would require the non-trivial registration of laser altimetry data and low-sun images.

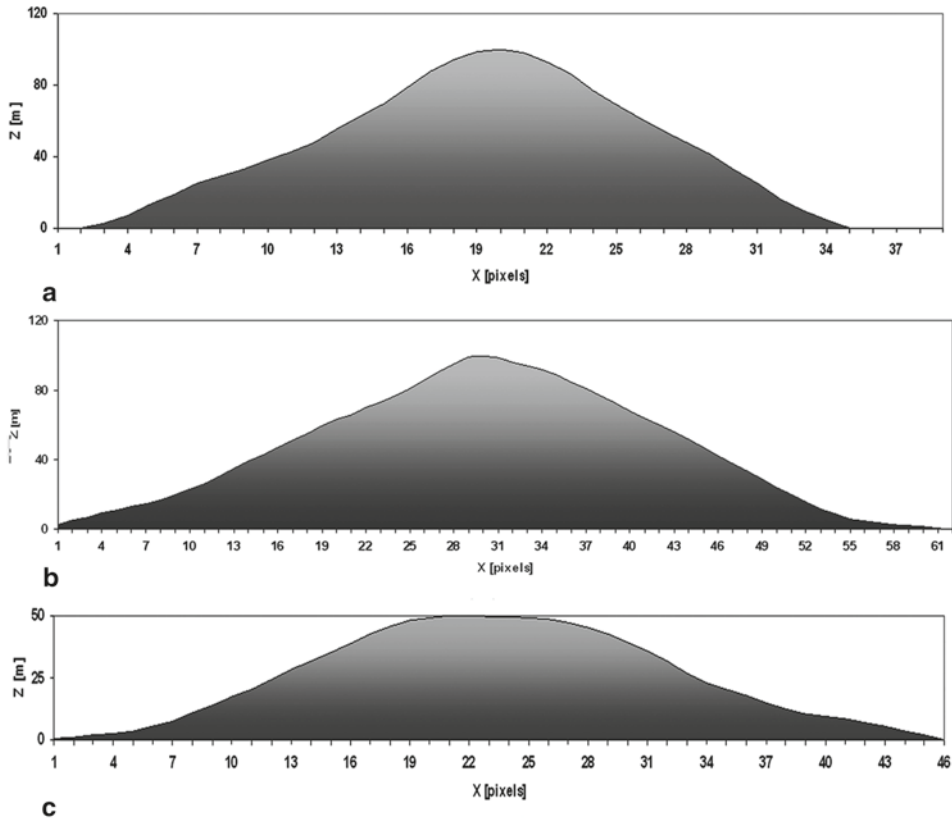


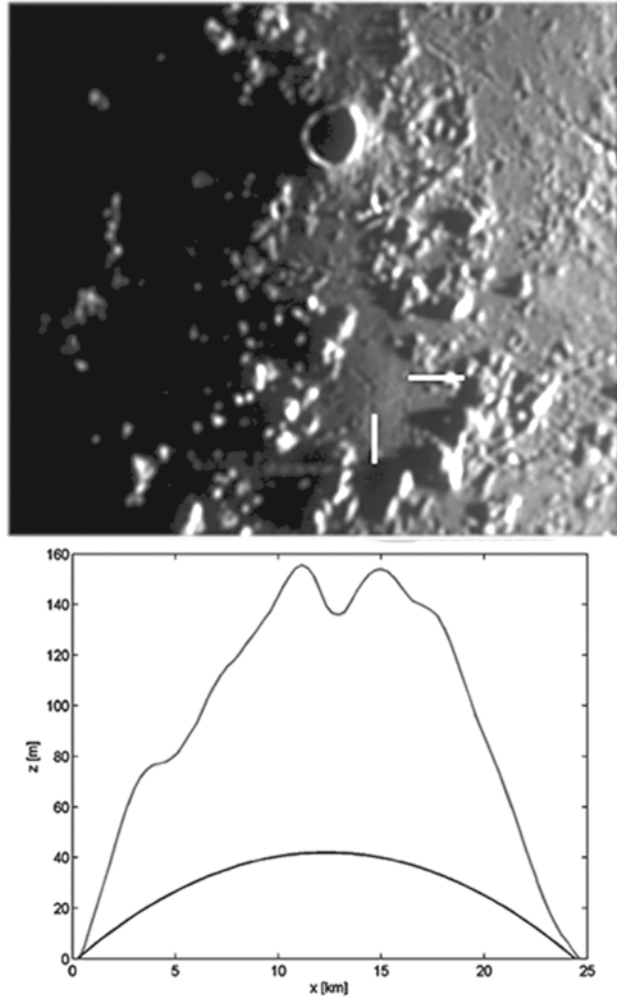
**Fig. 2.10** Cross-sectional profile of the Capuanus domes (Fig. 1.7) in east-west direction. The curvature of the lunar surface has been subtracted. **a** Capuanus 1. **b** Capuanus 2. **c** Capuanus 3. The dome heights obtained by 3D reconstruction correspond to  $100 \pm 10$  m for Capuanus 1 and 2 and  $50 \pm 5$  m for Capuanus 3

### 2.4.3 A Combined DEM Construction Approach

Herbort et al. (2011) propose an algorithm for the integration of surface gradient information obtained by shape from shading with laser altimetry data, making use of the respective advantages. While shape from shading yields dense surface structure information which is reliable on small spatial scales, laser altimetry provides absolute depth data, which are not always dense but reliable on large spatial scales. The algorithm iteratively refines the reconstructed surface in order to obtain a solution which is consistent with both the surface normals and the laser altimetry data, relying on the minimisation of a combined error functional (cf. Fig. 1.9 for two example DEMs).



**Fig. 2.11** (*top*) Telescopic image of a lunar dome located in the Milichius-Hortensius dome field, termed M15. A summit fissure is apparent. (Image by J. Phillips). (*bottom*) Cross-section through the dome summit in an east-west direction (*top curve*). The dome height is obtained by determining elevation differences between the summit of the dome and its surroundings, taking into account the curvature of the lunar surface (*bottom curve*). This leads to a dome height of  $110 \pm 10$  m. The dome volume  $V$  (Sect. 2.4.2) was computed by integrating the reconstructed cross-sectional profile over an area corresponding to a circular region of diameter  $D$  around the dome summit, yielding an edifice volume of  $16.6 \text{ km}^3$



## 2.5 Modelling of Rheologic Properties

Wilson and Head (2003) provide a quantitative treatment of dome-forming eruptions of magma onto a flat plane. This model estimates the yield strength  $\tau$ , i.e. the pressure or stress that must be exceeded to make the lava flow, the plastic viscosity  $\eta$ , yielding a measure for the fluidity of the erupted lava, the effusion rate  $E$ , i.e. the lava volume erupted per second, and the duration  $T_e$  of the effusion process. In the model by Wilson and Head (2003), the magma is treated as a Bingham fluid with a yield strength of

$$\tau = \frac{0.323h^2\rho_0g}{D/2} \quad (2.5)$$

according to Blake (1990). The plastic viscosity  $\eta$  is then estimated by the empirical relation

$$\eta(\tau) = 6 \times 10^{-4} \tau^{2.4} \quad (2.6)$$

where  $\tau$  is expressed in Pascal and  $\eta$  in Pascal second. In Eq. 2.5,  $\rho_0$  denotes the lava density, for which Wilson and Head (2003) apply a value of  $2,000 \text{ kg m}^{-3}$ ,  $g = 1.63 \text{ m s}^{-2}$  the acceleration due to gravity,  $h$  the height of the dome, and  $D$  its diameter.

In their study, Wilson and Head (2003) regard the Gruithuisen and Mairan highland domes, for which they infer a formation from non-basaltic lava of fairly low density, while lunar mare domes are composed of mare basalts, which typically have densities higher than  $2,000 \text{ kg m}^{-3}$  (Wieczorek et al. 2001). However, assuming a higher density will increase the viscosity value merely by a constant factor for all domes. For a magma density of  $2,800 \text{ kg m}^{-3}$ , this factor amounts to 2.2, which is not too significant when regarding the broad range of viscosities of about six orders of magnitude inferred for lunar mare and highland domes (Sect. 5.1). Wilson and Head (2003) make the assumption that the forward movement of the front of a lava flow is limited by cooling once a specific part of the flowing magma has cooled down considerably. Relying on this assumption, they derive a relation for the lava effusion rate  $E$  which is based on the effective flow thickness  $d_f = c_f h$  of the dome, which is not straightforward to determine. As an approximation, Wilson and Head (2003) set the effective flow thickness to the elevation difference between the dome surface and the surrounding surface in the middle between the dome summit and its outer rim. Accordingly, a value of  $c_f = 0.7$  is implied by the parabolic shapes assumed for the Gruithuisen and Mairan highland domes.

The relation for the effusion rate obtained by Wilson and Head (2003) then corresponds to

$$E = \frac{0.323^{1/2} 300 k (D/2)^2}{0.65^{5/2} c_f^2 h} \quad (2.7)$$

Here,  $k \approx 10^{-6} \text{ m}^2 \text{ s}^{-1}$  denotes the thermal diffusivity of the lava. The value of  $c_f$  can easily be extracted from the constructed DEM. Effectively, the effusion rates for lunar mare domes have been computed with  $c_f^2 = 0.72$  ( $c_f = 0.85$ ), which is realistic due to the flattened or pancake-like cross-sectional dome shapes. As it is unknown if the ad-hoc assumption of measuring  $c_f$  half-way between the dome summit and its rim appropriately reflects the effective flow thickness, and as  $E$  depends on the square of  $c_f$ , we assume that the values for the lava effusion rate obtained from Eq. 2.7 may be off by factors of up to about two (Lena et al. 2008).

Hence, these values reflect the order of magnitude of  $E$  but should not be taken to be very accurate. Wilson and Head (2003) point out that the duration  $T_e$  of the lava effusion process amounts to

$$T_e = \frac{V}{E} \quad (2.8)$$

with  $V$  as the edifice volume.

## 2.6 Monogenetic and Non-Monogenetic Lunar Effusive Domes

Presumably, a monogenetic mode of origin can be assumed for nearly all effusive domes of the four examined dome fields, due to their fairly uniform surface texture showing no traces of individual lava flow units or other signs of several subsequent eruption stages. Exceptions are the highly complex edifices in the Marius Hills region (Fig. 1.8), which likely formed during several subsequent eruption events (Head and Gifford 1980; Weitz and Head 1999). A similar formation may be assumed for Arago  $\alpha$  and  $\beta$  (A2 and A3 in Fig. 1.5d). Eqs. 2.5–2.8 are valid for monogenetic domes. Otherwise, the computed values for  $\tau$  and  $\eta$  are upper limits to the respective true values.

## 2.7 Classification Schemes Based on Qualitative Morphologic Features

A catalogue comprising 713 lunar domes was established by the Association of Lunar and Planetary Observers (ALPO) and the British Astronomical Association (BAA) in the 1960s (Jamieson and Phillips 1992). However, the selenographic coordinates in that catalogue tend to be inaccurate, and a significant fraction of structures recorded as domes therein are actually hills of non-volcanic origin or are non-existent. To provide a systematic subdivision of this large number of lunar domes, a classification scheme has been developed by Westfall (1964).

### 2.7.1 The Classification Scheme by Westfall (1964)

Westfall (1964) develops a classification scheme for lunar domes which is based on qualitative morphologic considerations. The definition is repeated here from Westfall (1964):

Dome: A discrete, regular swelling whose ratio of major axis:minor axis, when corrected for foreshortening, does not exceed 2:1, and whose maximum slope, not including secondary features, does not exceed 5°. Under high illumination, domes are indistinguishable from their surroundings. Domes may exhibit secondary features, such as pits, clefts, ridges, and hills, as long as any single such feature does not occupy more than a quarter of the area of the dome.  
Dome Complex: Any object similar to a dome but which has two or more contiguous swellings or an irregularly vertical profile.

Westfall (1964) summarises the properties of a lunar mare dome by the following criteria, which are combined into a string of characters:

Broad Category

D Dome

DC Dome complex

## Surroundings

U Uplands

W Maria

UW Uncertain or intermediate between Uplands or Maria

## Position

Orthogonal absolute Xi and Eta coordinates of the center of the object are given in parentheses, in units of thousandths of the lunar radius, preceded by the Roman numeral of the quadrant of the moon.

## Plan

## Major Axis

1 Less than 5 km

2 5–20 km

3 20–35 km

4 Over 35 km

## Border

a Circular (major:minor axes are between 1.00 and 1.25)

b Elliptical (major:minor axes are between 1.26 and 2.00)

c Polygonal

d Irregular

e Too ill-defined to classify, or variable (i.e., dependent on aperture, etc.)

## Profile

## Maximum Slope

5 Gentle (under 2°)

6 Moderate (2–5°)

## Cross Section

f Hemispherical

g Flat summit (platykurtic)

h Sharp summit (leptokurtic)

i Multiple summit (more than one summit, but of single type; for example, three hemispherical summits)

f' Hemispherical—Asymmetric

g' Flat summit—Asymmetric

h' Sharp summit—Asymmetric

i' Complex summit (more than one summit, of more than one type; for example, one flat and one sharp summit)

## Surface Detail

## Type

7 Depression (pit, craterlet, or saucer)

8 Elevation (hill, ridge, or peak)

9 Cleft or valley

0 No observable surface detail

Position

- j Central
- k Off-center
- m On margin
- n Transversal (linear feature crossing entire dome)
- p More than one such feature

(Westfall 1964).

### **2.7.2 The Classification Scheme by Head and Gifford (1980)**

In the classification scheme by Head and Gifford (1980), the lunar domes are divided into seven classes. Domes of class 1 are characterised by summit vents, circular or elliptical boundaries with diameters between 5.5 and 15 km, and flank slopes lower than  $5^\circ$ . Class 2 domes have flatter cross-sections and slightly larger diameters (6.0–16.0 km) than those of class 1. A majority of the domes of class 2 display summit vents. The lunar domes of class 3 are similarly shaped but lower and commonly display summit vents. Domes of class 4 are less well-defined than the domes of classes 1–3. They commonly occur near mare ridges and are interpreted by Head and Gifford (1980) as the result of intrusive magmatic processes or deformations of the lunar crust. Irregularly shaped domes that appear to have been formed by lava that flowed around highland terrain are assigned to class 5. These domes commonly do not display summit vents, and their diameters are between 5 and 19 km. Domes of class 6 defined by Head and Gifford (1980) are small with diameters of only 3–7 km but comparably steep and represent kipukas, i.e. highland surface embayed by mare material. Class 7 domes have rough shapes and were probably formed during several subsequent eruption events. Examples are the small and steep Marius Hills in Oceanus Procellarum (Weitz and Head 1999).

---

## **2.8 Conclusion**

Both classification schemes described above are mainly based on a qualitative description of dome shape and its geologic setting rather than morphometric quantities. Especially the assignment of a dome to Head and Gifford classes 1, 2, or 3, which denote mare domes not being associated with other volcanic features, will remain ambiguous in many cases. Hence, in Chap. 5 we will describe a classification scheme which subdivides lunar mare domes according to their spectral and morphometric properties in a quantitative way. Furthermore, a classification scheme for lunar domes which are assumed to have formed by magmatic intrusions will be described.

---

## Abstract

This chapter gives an outline of methods for describing the lunar surface in terms of specific spectral parameters inferred from multispectral or hyperspectral image data. These allow for the detection of specific lunar minerals, an estimation of the abundances of important chemical elements, and a mapping of the lunar surface in terms of its basic petrographic constituents.

---

## 3.1 Spectral Ratios

The first analyses of lunar soil types were performed by means of reflectance spectra acquired with earth-based telescopes (Adams and McCord 1970; McCord and Adams 1973; McCord et al. 1972). Burns et al. (1976) provide a discussion of spectral parameters indicating the titanium content of lunar soils. As an example, Charette et al. (1974) show for the Mare Tranquillitatis region based on a comparison between the UV/VIS ratio inferred from telescopic lunar spectra and those of returned lunar samples that the northwestern region of the mare comprises basalts of high  $\text{TiO}_2$  content, while the  $\text{TiO}_2$  abundance is lower in the northern part of Mare Tranquillitatis. They furthermore find the  $\text{TiO}_2$  abundance to decrease further for southwestern and central Mare Serenitatis, respectively. Subsequent studies confirmed these findings for this region (McCord et al. 1976; Melendrez et al. 1994; Pieters 1978).

The Clementine spacecraft provided the first global lunar orbital multispectral image data set of the Moon. The Clementine UVVIS multispectral image data have a lateral resolution of up to 100 m per pixel and were acquired at five wavelengths: 415, 750, 900, 950, and 1,000 nm (Eliason et al. 1999). In this data set, the corresponding UVVIS reflectances are normalised to an incidence angle of  $30^\circ$  and an emission angle of  $0^\circ$ , and calibrated with respect to the laboratory spectrum of Apollo 16 sample 62,231 (Pieters 1999).

The  $\text{TiO}_2$  content of lunar mare soils can be estimated using Clementine data based on the  $R_{415}/R_{750}$  spectral ratio (Lucey et al. 2000). The work by Gillis-Davis et al. (2006), relying



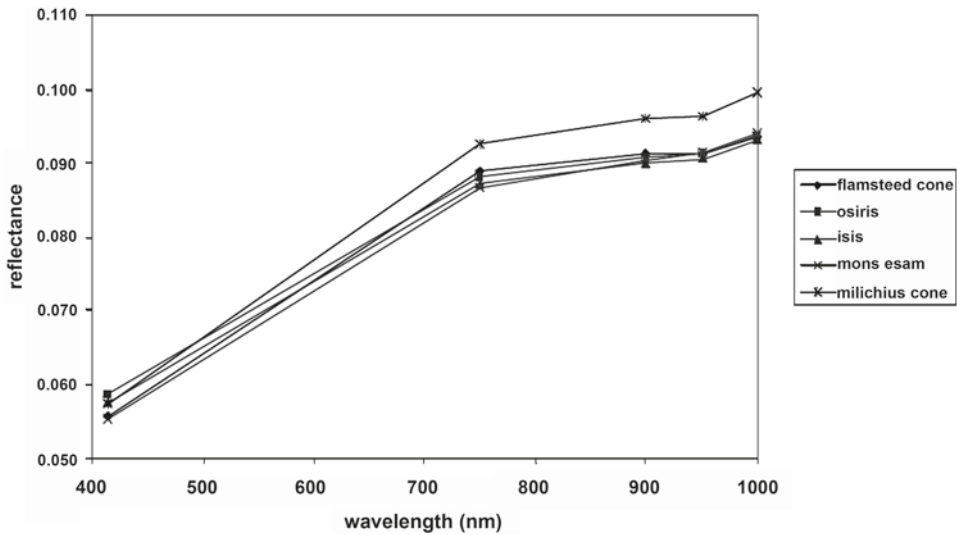


**Fig. 3.1** Clementine UV/VIS spectra of some of the lunar cones, including the cones near Milichius, discussed in Sect. 1.4 (Fig. 1.3 and Figs. 3.6, 3.7)

on  $\text{TiO}_2$  abundance data obtained with the Lunar Prospector neutron spectrometer, indicates that other effects such as ilmenite grain size or FeO content may also contribute to the UV/VIS ratio. According to these analyses,  $\text{TiO}_2$  content is monotonously increasing with  $R_{415}/R_{750}$  ratio, but the correlation is only moderate and the data display a strong scatter. Gillis-Davis et al. (2006) establish a trend with a higher slope, valid for  $R_{415}/R_{750}$  ratios of larger than about 0.62 and a  $\text{TiO}_2$  content of more than 2 wt%, represented e.g. by the Mare Tranquillitatis soils, and a distinct second trend with a lower slope, valid for smaller  $R_{415}/R_{750}$  ratios and represented e.g. by several types of soils in Oceanus Procellarum. The  $R_{950}/R_{750}$  spectral ratio is related to the strength of the ferrous absorption trough around 1,000 nm, which depends on both the FeO content of the soil and its optical maturity (Lucey et al. 2000).

More recently, Clementine spectra have been calibrated for wavelengths between 415 nm and 2,000 nm. They can be downloaded from the USGS Map-a-Planet website.<sup>1</sup> Utilising the described albedo and spectral ratio values has become a common approach to the spectrophotometric analysis of Clementine UVVIS data, as it allows for the mutual distinction between different types of basaltic mare soils and highland soils (Figs. 3.1–3.3).

Most lunar domes and cones are spectrally not distinguishable from the mare soil into which they merge, while several domes have a spectrum that is intermediate in reflectance between the dark and smooth mare units and that of the highland terrains. This characteristic is attributable to lateral mixing due to random impacts of small bodies (Chap. 1.6.3), as suggested by Li et al. (1997) and modelled in more detail by Li and Mustard (2000). This mechanism suggests the occurrence of impact induced intermixing between mare and highland soils, resulting in intermediate, “mixed” spectra of the corresponding surface regions.

<sup>1</sup> <http://www.mapaplanet.org/explorer/moon.html>.

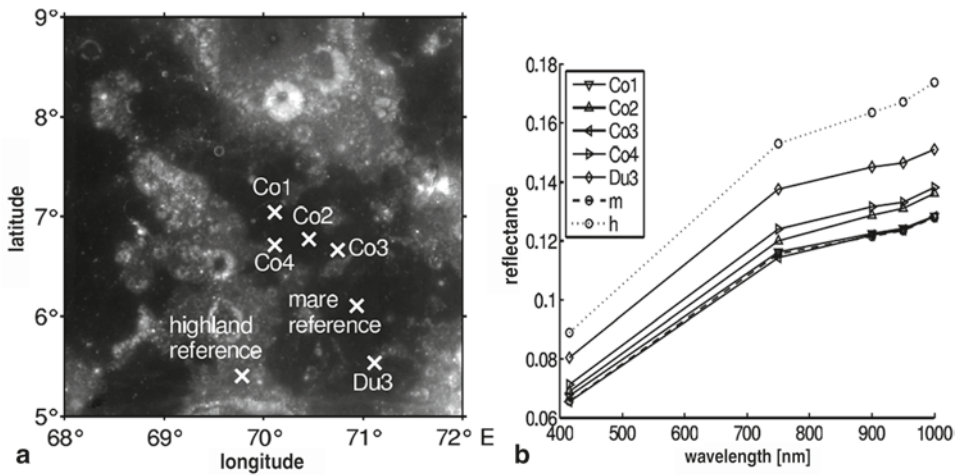


**Fig. 3.2** **a** Clementine 750 nm albedo image of eastern Mare Undarum including a group of five domes termed Condorcet 1–4 (Co 1–4) and Dubiago 3 (Du 3) (USGS, <http://www.mapaplanet.org>). The locations of these domes (Fig. 1.6c for their identification), the mare and highland reference sites are marked by *white crosses*. **b** Clementine UVVIS spectra of the indicated locations. The mare reference site is denoted by “m”, the highland reference site by “h”. The reflectance spectrum of the domes Co2, Co4 and Du3 is intermediate between the dark and smooth mare unit and that of the highland, which is of higher reflectance. An explanation for this observation is that mixing of basaltic mare lava and highland material excavated by impacts of nearby craters

A standard approach to the representation of Clementine imagery are the so-called spectral ratio images, where the red channel corresponds to the reflectance ratio  $R_{750}/R_{415}$ , the green channel to  $R_{750}/R_{950}$ , and the blue channel to  $R_{415}/R_{750}$  (Rajmon and Spudis 2001). In these images, regions which are bright in the red channel correspond to mature basalts of low  $\text{TiO}_2$  content while mature high- $\text{TiO}_2$  basalts appear bright in the blue channel. Immature basalts appear bright in the green channel. Red regions correspond to mature and blue regions to immature highland soils (Rajmon and Spudis 2001). For example, according to Staid et al. (1996) and apparent from Fig. 3.4, spectrally blue basalts make up the major part of the area of Mare Tranquillitatis. These basalts cover spectrally red basalts, which appear on the surface only at several locations where they were excavated by crater-forming impacts. Rajmon and Spudis (2001) show that the  $\text{TiO}_2$  content of the lavas erupting in the Mare Tranquillitatis region increased over time.

### 3.2 Diagnostic Spectral Parameters

Using the Clementine NIR channels at 1,100, 1,250, 1,500, and 2,000 nm in addition to the UVVIS channels allows to extract diagnostic spectral parameters which provide more detailed information about the composition of the lunar surface, such as the wavelengths and depths of characteristic absorptions.

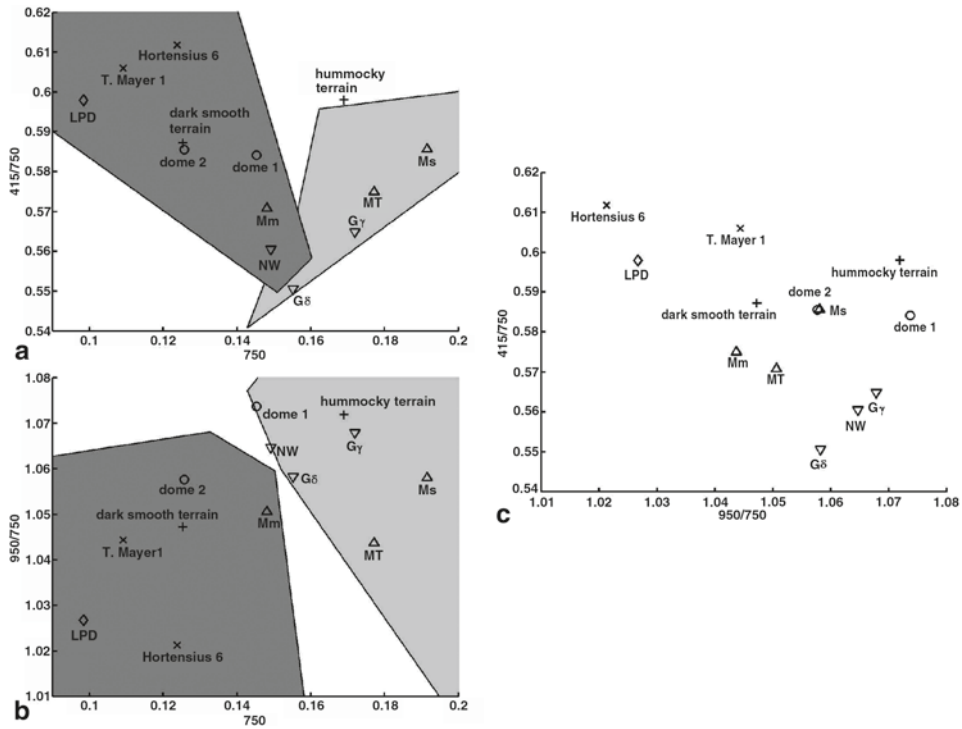


**Fig. 3.3** Spectral diagrams of the highland domes Gruithuisen  $\gamma$ ,  $\delta$  (Fig. 1.9a), and NW, the highland domes Mairan T, “middle”, and “south”, two mare domes in Doppelmayer region, a LPD and two lunar mare domes termed Tobias Mayer 1 and Hortensius 6 (Lena et al. 2007). (a)  $R_{750}$  vs.  $R_{415}/R_{750}$ ; (b)  $R_{750}$  vs.  $R_{950}/R_{750}$ ; (c)  $R_{950}/R_{750}$  vs.  $R_{415}/R_{750}$ . In (a) and (b), mare soils are represented by the *dark-grey* regions and highland soils by the *lightgrey* regions, according to Gaddis et al. (2003). Highland domes show higher  $R_{750}$  and  $R_{950}/R_{750}$  than mare references and lunar mare domes. The diagram also shows a highland component for the dome Doppelmayer 1 (“dome 1”) as a result of lateral mixing due to nearby impacts

Smrekar and Pieters (1985) point out that the minimum wavelength of the absorption trough around 1,000 nm of the mineral pyroxene is located at 900–930 nm when the calcium (Ca) content is low and at 970–1,000 nm when the Ca content is high. This property is also shown by Matsunaga et al. (2008) based on laboratory spectra. The spectral signature of plagioclase is characterized by a broad absorption band at about 1,300 nm (Matsunaga et al. 2008). Another abundant mineral on the lunar surface is olivine, which occurs as a mixture of the endmembers forsterite ( $\text{Mg}_2\text{SiO}_4$ ) and fayalite ( $\text{Fe}_2\text{SiO}_4$ ) (King and Ridley 1987). Olivine has a broad absorption band centred beyond 1,000 nm (King and Ridley 1987; Matsunaga et al. 2008). While pyroxene displays a second absorption band around 2,000 nm, olivine does not absorb at 2,000 nm, such that olivine may be identified based on a high  $R_{2000}/R_{1500}$  spectral ratio (LeMouelic et al. 1999).

The line connecting the reflectance values at 750 nm and 1,500 nm is regarded as the spectral continuum, by which the reflectance spectrum is divided in order to obtain the

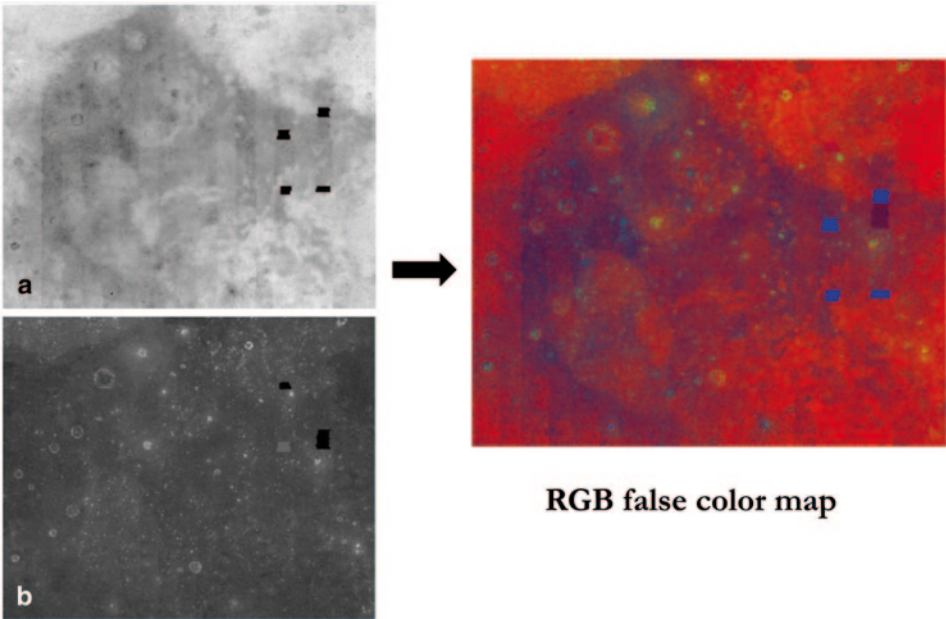
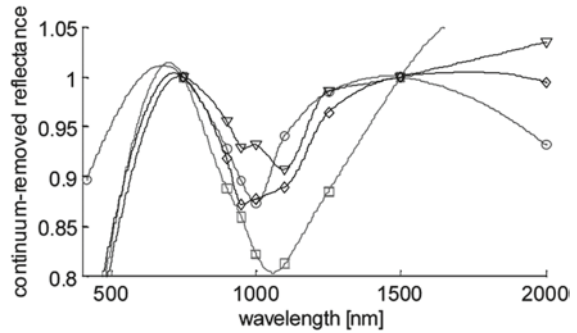


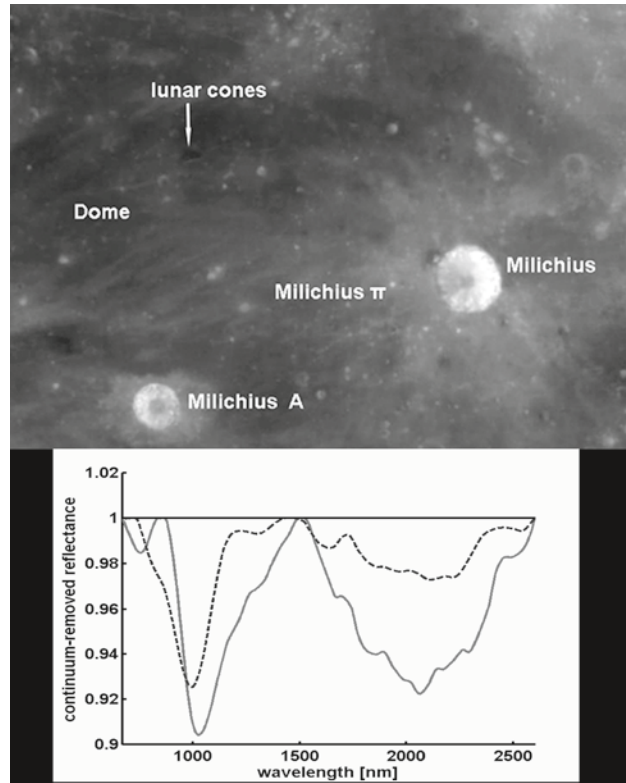
**Fig. 3.4** Clementine false color map of Mare Tranquillitatis (USGS, <http://www.mapaplanet.org>). **a** Red channel ( $R_{750}/R_{415}$ ). **b** Green channel ( $R_{750}/R_{950}$ ). Blue channel in the RGB map is inverse of the red channel

**Fig. 3.5** Example continuum-removed Clementine spectra of the Aristarchus region. *Circles* pyroxene absorption trough; *triangles* double trough (pyroxene and olivine); *diamonds* single trough with inflection feature (minor admixed olivine component); *squares* olivine trough



continuum-removed spectrum (LeMouelic et al. 2000). After interpolation using the method by Akima (1970), the absorption wavelength and the depth of the absorption trough near 1,000 nm, the corresponding values of secondary absorptions sometimes occurring at higher wavelengths, as well as the full width at half maximum (FWHM) of the absorption trough are extracted from the continuum-removed spectrum (Wöhler et al. 2011; Wöhler and Grumpe 2013). An additional spectral parameter regarded e.g. by Besse et al. (2010) is the integrated band depth (IBD), which denotes the area of an absorption trough in the continuum-removed spectrum (Fig. 3.5).

**Fig. 3.6** (*top*) Clementine 750 nm image (USGS, <http://www.mapaplanet.org>) of the Milichius region and the two lunar cones (Fig. 1.3a); (*bottom*) Continuum-removed  $M^3$  spectrum of the cone (*solid curve*) and the surrounding mare surface (*dashed curve*). The spectrum of the cone displays a broad trough around 1,000 nm with a minimum wavelength beyond 1,000 nm and the presence of an absorption trough around 2,000 nm, indicating a mixture of olivine and pyroxene. The spectrum of the surrounding surface displays a narrow trough around 1,000 nm with a minimum wavelength below 1,000 nm and an absorption around 2,000 nm, corresponding to a typical pyroxene signature



### 3.3 Petrographic Maps

Davis and Spudis (1985) show that only a small number of elementary constituents are required to explain the variations of soil composition observed across the lunar surface. Berezhnoy et al. (2005) propose a lunar rock model based on the three endmembers mare basalt (especially pyroxene), Mg-rich rock (e.g. olivine), and ferroan anorthosite (FAN). They construct a so-called “petrographic map” based on abundance measurements of the elements iron (Fe), magnesium (Mg), and aluminium (Al) obtained by the Lunar Prospector Gamma Ray Spectrometer (LP GRS), which indicates the relative fractions of the three endmembers across the lunar surface. However, as the LP GRS data are of low spatial resolution, one pixel of their petrographic map corresponds to  $5^\circ \times 5^\circ$ , i.e. about  $150 \times 150$  km at the lunar equator.

A regression method to exploit the correlations between the spectral parameters extracted from interpolated Clementine UVVIS+NIR spectra (cf. Section 3.2) and the LP GRS elemental abundance measurements is proposed by Wöhler et al. (2011). The IBD is not used in that approach because it displays a strong correlation with the product of the depth and the width of the absorption trough and therefore does not provide new, independent information. The extracted spectral parameters allow to estimate the abundances of the elements Ca, Al, Fe, Mg, Ti, and O at the resolution of the Clementine UVVIS+NIR



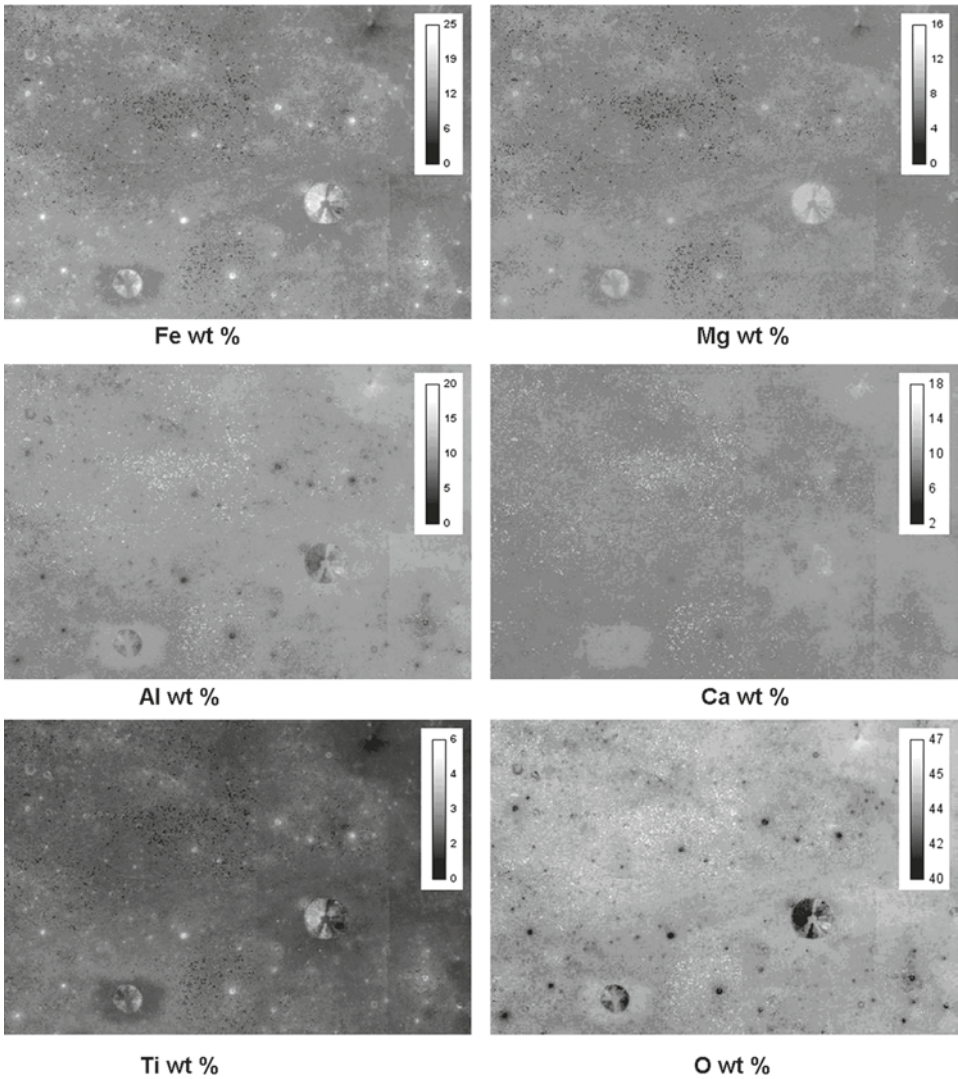
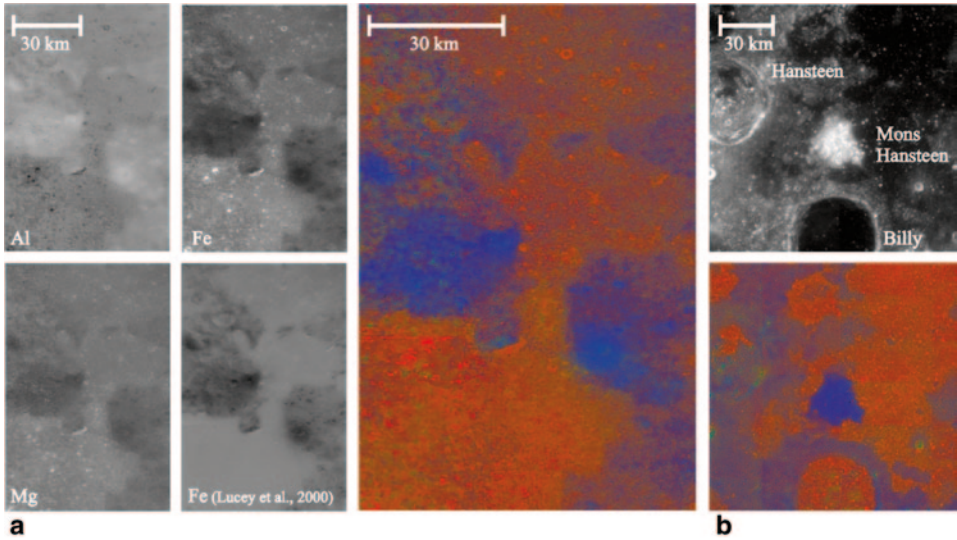


**Fig. 3.7** Milichius region (cf. also Fig. 3.6); inferred elemental abundances of Fe (0–25 wt%), Mg (0–16 wt%), Al (0–20 wt%), Ca (2–18 wt%), Ti (0–6 wt%) and O (40–47 wt%)

images of up to about 100 m per pixel. Based on the inferred Fe, Mg, and Al abundances in combination with the three-endmember model (Berezhnoy et al. 2005) using slightly adapted endmember compositions,<sup>2</sup> the regression method then allows to construct petrographic maps of the lunar surface which also have the same resolution as the Clementine UVVIS + NIR images (Figs. 3.6 and 3.7).

<sup>2</sup> The compositions of the endmembers used to construct the petrographic maps in Fig. 3.8 are 18.0 wt% Fe, 6.5 wt% Mg, 6.9 wt% Al for mare basalt; 4.0 wt% Fe, 13.0 wt% Mg, 11.0 wt% Al for Mg-rich rock; and 0.5 wt% Fe, 1.0 wt% Mg, 17.0 wt% Al for FAN.





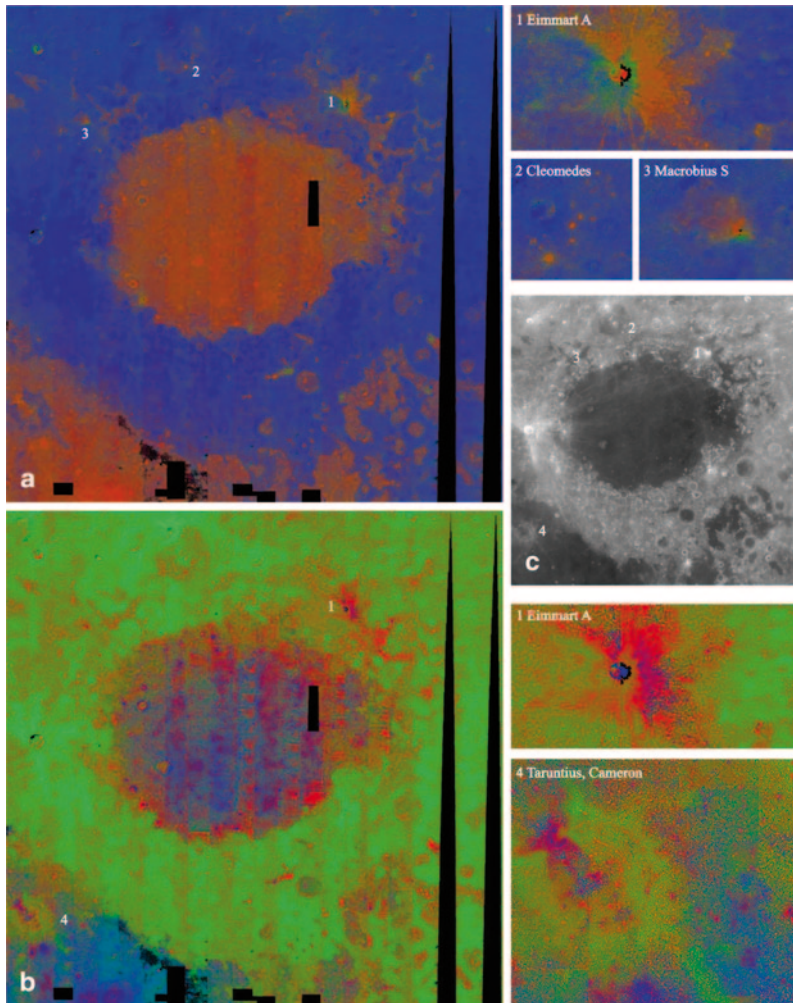
**Fig. 3.8** Gruithuisen domes and Mons Hansteen. The relative content of mare basalt, Mg-rich rock, and FAN is denoted by the red, green and blue channel of the petrographic maps. **a** Spectral analysis of the Gruithuisen domes. Abundance maps of Al (0–20 wt%), Fe (0–25 wt%), regression method vs. method by Lucey et al. (2000)), Mg (0–16 wt%), and petrographic map. **b** Spectral analysis of the region around Mons Hansteen. Clementine 750 nm image (*top*) (USGS, <http://www.mapaplanet.org>) and petrographic map (*bottom*)

Figure 3.8 shows the petrographic maps of the Gruithuisen domes and Mons Hansteen (Fig. 1.9), where the relative content of mare basalt, Mg-rich rock, and FAN is denoted by the red, green, and blue channel, respectively. The highland domes stand out clearly as anorthositic highland material (blue). Basaltic mare plains and lava-filled craters such as Billy appear reddish, while some regions at the eastern rim of Hansteen crater have a green shade, indicating an Mg-rich rock, e.g. olivine, component. In Fig. 3.8a, the Fe abundance map obtained based on the regression method is compared to the classical approach by Lucey et al. (2000), which is based on Clementine UVVIS spectral ratios.

An application of the petrographic mapping technique to Mare Crisium is shown in Fig. 3.9. A petrographic map obtained in terms of the three endmembers introduced by Berezhnoy (2005) is shown in Fig. 3.9a. In Fig. 3.9b, a petrographic map constructed in terms of three different mare basalt endmembers is shown.<sup>3</sup>

The centre and southern part of Mare Crisium are covered by high-Ti basalt, while the Ti content of the basalts occurring in the northeastern part and the rim zone is lower. The

<sup>3</sup> The compositions of the basaltic endmembers used in Fig. 3.9b are 6.3 wt% Al and 3.6 wt% Ti for high-Ti basalt, 9.25 wt% Al and 1.6 wt% Ti for low-Ti basalt, and 14 wt% Al and 0.5 wt% Ti for high-Al basalt. High-Al basalts are described e.g. by Kramer et al. (2009).



**Fig. 3.9** Analysis of Mare Crisium and surrounding conspicuous structures. (a) Red channel: mare basalt; green channel: Mg-rich rock; blue channel: ferroan anorthosite. (b) Red channel: low-Ti basalt; green channel: highland material; blue channel: high-Ti basalt. (c) Clementine 750 nm image (USGS, <http://www.mapplanet.org>). Numbers identify enlarged regions. 1: Mg-rich and basaltic ejecta of the crater Eimmart A. 2: Small craters with basaltic ejecta on the floor of the crater Cleomedes. 3: Mg-rich ejecta of the crater Macrobius S. 4: Mixture of basaltic ejecta from the small crater Cameron on the floor of the large crater Taruntius.

composition of the ejecta blanket of the crater Eimmart A (enlargement 1 in Fig. 3.9) is not homogeneous but is made up of distinct areas dominated by high-Ti (blue in Fig. 3.9b) and low-Ti (red in Fig. 3.9b) basalts, respectively, as well as mixtures thereof. Regions appearing bright in Fig. 3.9b are presumably not aluminous mare basalts but either highland material or mare basalt contaminated with highland material by lateral mixing effects according to

the mechanism suggested by Li and Mustard (2000). Enlargement 2 shows small craters with basaltic ejecta on the floor of the large crater Cleomedes (red in Fig. 3.9a). Enlargement 3 focuses on the small crater Macrobius S which reveals a small region of Mg-rich rock ejecta (green in Fig. 3.9a). The mainly high-Ti basaltic ejecta from the small crater Cameron on the floor of the large crater Taruntius become apparent in enlargement 4 (Fig. 3.9b).

---

## Abstract

This chapter describes how the dimensions of the dikes through which the dome-forming magma ascended to the surface can be modelled. Furthermore, a modelling approach to encompass the physical conditions under which putative intrusive lunar domes were formed is outlined.

Knowledge about the morphometric properties of lunar domes (diameter, height, volume) allows to estimate the rheologic properties of the magma which formed the effusive domes (Sect. 2.5), i.e. its viscosity  $\eta$  and eruption rate  $E$  as well as the duration of the effusion process  $T_e$  (Wilson and Head 2003). The lavas that constitute the mare material originate from the lunar mantle or the base of the crust (Wilson and Head 1996). In this scenario, the pressure of the magma leads to the formation of long and narrow fractures in the lunar crust, the so-called dikes, which allow its ascent towards the surface (Wilson and Head 2003; cf. also Sect. 1.1 and Fig. 1.1).

---

## 4.1 Modelling of Feeder Dike Dimensions

The rheologic parameters of lunar effusive domes allow to estimate the magma rise speed  $U$  as well as the width  $W$  and length  $L$  of the feeder dike of a dome (Wilson and Head 2003), where as a general rule the vertical extension of a dike into the crust approximately corresponds to its length (Jackson et al. 1997). We only give a short outline of this model since it has been described in detail by Wilson and Head (2003). The three parameters  $U$ ,  $W$ , and  $L$  are related to the effusion rate  $E$  by

$$E = U \cdot W \cdot L. \quad (4.1)$$

According to Wilson and Head (2003), the vertical gradient  $dp/dz$  of the magma pressure  $p$  which propagates the magma upwards through the dike is assumed to be identical to the fric-

tion occurring between the magma and the wall of the dike. As the magma is modelled as a Bingham plastic, vertical motion only occurs if the effective force on the magma exceeds the yield strength  $\tau$  of the magma. These considerations yield the magma rise speed  $U$  according to

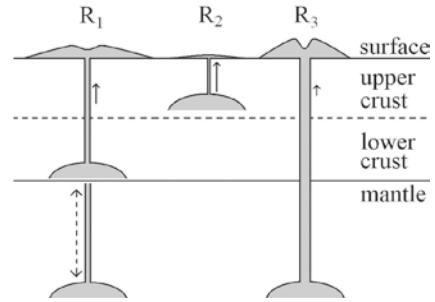
$$U = \frac{W^2}{12\eta} \left[ \frac{dp}{dz} - \frac{2\tau}{W} \right]. \quad (4.2)$$

Rubin (1993a) models pressurised magma in a dike, where the surrounding material is assumed to behave in a viscoelastic manner, i.e. not only the magma but also the surrounding rock (“host rock”) is assigned a viscosity value. He shows that the values of  $W$  and  $L$  are not independent of each other but that their ratio  $L/W$  depends on the lava viscosity  $\eta$ . An important model parameter is the ratio  $p_0/G$ , where  $p_0$  denotes the magma pressure diminished by the minimum value of the direction-dependent compressive stress of the crust, and  $G$  is the elasticity of the host rock surrounding the dike. The value of  $p_0/G$  lies in the range between  $10^{-4}$  and  $10^{-3}$  (Rubin 1993a) and typically amounts to  $10^{-3.5}$ . If the ratio between the viscosity of the host rock and that of the magma exceeds 12–14 orders of magnitude, where the viscosity of the host rock is assumed as  $10^{18}$  Pa s, the ratio  $L/W$  is approximately antiproportional to  $p_0/G$ , denoting an elastic behaviour (Rubin 1993a). For highly viscous magmas, Rubin (1993a) models the interaction between two viscous materials, where the value of  $L/W$  decreases strongly with increasing magma viscosity. By combining the results of the viscoelastic model by Rubin (1993a) with Eqs. (4.1) and (4.2), Wilson and Head (2003) arrive at a relation for the dike width  $W$  which needs to be solved numerically. Notably, both the dike length  $L$  and width  $W$  are approximately inversely proportional to the magma pressure gradient  $dp/dz$ .

An important parameter for modelling the geometry of lunar feeder dikes is the vertical pressure gradient  $dp/dz$ . Basaltic magmas on the Moon arise from the mantle (Wilson and Head 1996). A classical model of the ascent of lunar magma through the crust is developed by Head and Wilson (1992) and Wilson and Head (1996), who state that the density values of basaltic magma are between those of the mantle and the crust. If it does not exhibit an excess pressure, the basaltic magma will ascend through the mantle due to its lower density and the resulting buoyant force (Head and Wilson 1992; Wilson and Head 1996) but come to a stop at the so-called “neutral buoyancy zone” (Head and Wilson 1992), which is found to be situated near the bottom of the lunar crust (Head and Wilson 1992; Wilson and Head 1996). According to Wilson and Head (1996), an excess pressure of about 21 MPa is necessary to force magma up to the surface level and induce an eruption if a typical thickness of the lunar crust of 64 km is assumed. This corresponds to a pressure gradient of  $dp/dz = 328 \text{ Pa m}^{-1}$ .

An analysis of the structure of the lunar interior and the thickness of the crust has been performed based on Clementine data by Zuber et al. (1994). A model implying a structure of the lunar crust made up by two layers is inferred by Wiczorek and Phillips (1998) using gravity data, based on which Wiczorek et al. (2001) develop a basaltic magma ascent model. Wiczorek et al. (2001) point out the possibility that basaltic magma may display a lower density than the material of the lower crust, such that basaltic magma may be able to ascend buoyantly to the surface without requiring an excess pressure if the upper crust, which consists of anorthosite of relatively low density, is absent as the consequence of an impact event. Indeed, gravity anomalies detected by Wiczorek et al. (2006) indicate a pref-

**Fig. 4.1** Illustration of rheologic groups  $R_1$ – $R_3$ . The indicated dome diameters and heights, magma source depths, and dike widths are not to scale but illustrate relative properties. *Solid arrows indicate magma rise speed*



erential presence of mare basalts in regions where no upper crust is present. In the model by Wiczorek et al. (2001), the driving pressure gradient is given by  $dp/dz = g\Delta\rho$ , with  $\Delta\rho$  as the density difference between the ascending basaltic magma and the crustal material. At this point, however, we do not need to determine which model is “correct”.

For basaltic magmas of low  $\text{TiO}_2$  content (as found e.g. in the Mare Undarum region, Fig. 1.6c) at the temperature at which they are just about to melt (the so-called “liquidus temperature”), Wiczorek et al. (2001) derive a density difference of  $\Delta\rho \approx 200 \text{ kg m}^{-3}$ , implying a vertical pressure gradient of  $dp/dz \approx 320 \text{ Pa m}^{-1}$ . This value is nearly identical to the one suggested by Wilson and Head (1996). Hence, we have assumed the value of  $dp/dz = 328 \text{ Pa m}^{-1}$  to determine the magma rise speeds and dike geometries for lunar mare domes (Fig. 4.1).

Equations 4.1 and 4.2 show that the magma rise speed  $U$  decreases with increasing magma viscosity  $\eta$ , in turn leading to a lower effusion rate  $E$ , thus implying a larger width and length of the feeder dike of a dome (Wilson and Head 2003).

The modelling results show that dome morphology is directly related to magma rise speed and feeder dike dimensions, leading to three rheologic groups (Fig. 4.2) of lunar

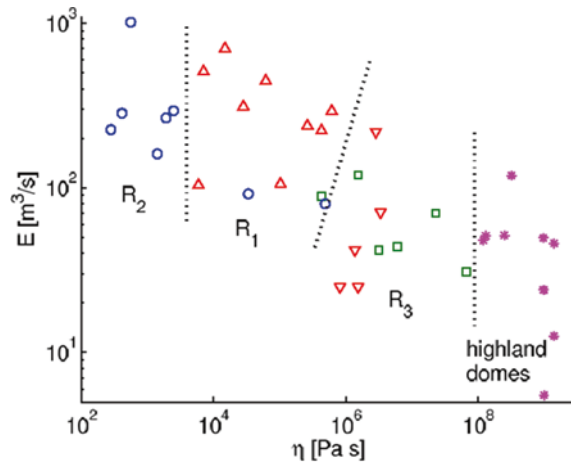


**Fig. 4.2** Rheologic properties (lava viscosity  $\eta$  vs. Effusion rate  $E$ ) of mare domes situated in the Milichius/T. Mayer region (red up-triangles: with elongated vent, red down-triangles: without elongated vent), the Hortensius region (green squares) and in Mare Tranquillitatis (blue circles) as well as the Gruithuisen and Mairan highland domes (purple stars). The highland dome data were adopted from Wilson and Head (2003). The rheologic groups  $R_1$ – $R_3$  are indicated. Cf. also Chap. 7



domes. Domes of rheologic group  $R_1$  are characterised by high effusion rates of about  $10^2 \text{ m}^3 \text{ s}^{-1}$ , moderate to large erupted lava volumes, low to moderate lava viscosities of  $10^4$ – $10^6 \text{ Pa s}$ , moderate magma rise speeds of  $10^{-4}$ – $10^{-2} \text{ m s}^{-1}$ , dike widths around 10 m, and dike lengths of 20–150 km. It comprises the domes with elongated vents in the Milichius/T. Mayer region (such as the domes M3–M7, Fig. 1.5a) and two similar domes in northern Mare Tranquillitatis near Cauchy (the domes termed C2 and C3 in Fig. 1.5f).

Domes of rheologic group  $R_2$  display similarly high effusion rates but much lower edifice volumes and thus shorter durations of the effusion process. The lavas of low viscosity between  $10^2$  and  $10^4 \text{ Pa s}$  created feeder dikes around 3 m wide and 7–16 km long. The small dikes and high effusion rates imply high magma rise speeds around  $10^{-2} \text{ m s}^{-1}$ . Class  $R_2$  comprises the very low aligned domes in northern Mare Tranquillitatis, such as NTA1–NTA6 (Fig. 1.5g), and three low dome near Arago, termed A4–A6 (Fig. 1.5e).

Domes of group  $R_3$  are characterised by relatively low lava effusion rates of some tens of  $\text{m}^3 \text{ s}^{-1}$  but large erupted lava volumes, implying long durations of the effusion process which typically amount to several years or even decades. During effusion, the lava displayed high viscosities of  $10^6$ – $10^8 \text{ Pa s}$ , ascending at low speeds of about  $10^{-5} \text{ m s}^{-1}$  through feeder dikes of about 100 m width and 130–190 km length. This group contains the relatively steep domes near Hortensius (termed H1–H6 in Fig. 1.5g) and in the T. Mayer region, such as the domes termed M8, M9 and M11, M12 (Fig. 1.5e).

In conclusion, based on their morphometric properties, i.e. diameter, height, and edifice volume, obtained by photoclinometric and shape from shading analysis of telescopic CCD images, important rheologic quantities, i.e. the lava viscosity during eruption, effusion rate, duration of the effusion process, magma rise speed, and the dimensions of the feeder dikes, may be derived and related directly to the lunar dome classes, which we will introduce in Chap. 5.

## 4.2 Time Scales Relevant During Dome Formation

To estimate the relevance of magma cooling during its ascent to the surface it is useful to introduce two time scales. Assuming that the vertical extension of a dike is similar to its length  $L$  (Head and Wilson 1992; Jackson et al. 1997), the period of time  $\tau_r$  during which the magma rises from the dike source to the surface corresponds to

$$\tau_r = L/U. \quad (4.3)$$

The second time scale, denoted by  $\tau_c$ , describes cooling of stationary magma in a dike, which is governed by conduction of heat from the hot magma into the cool surrounding host rock (Carrigan et al. 1992). It follows from the considerations by Fedotov (1976) and Carrigan et al. (1992) based on the equation of heat diffusion that the cooling time scale  $\tau_c$  of stationary magma in a dike of width  $W$  is proportional to  $W^2$  according to

$$\tau_c = 10^6 \text{ s} \cdot \left( \frac{W}{3\text{m}} \right)^2. \quad (4.4)$$

(cf. Fedotov 1976, Fig. 2 therein).

Both time scales  $\tau_r$  and  $\tau_c$  increase with increasing lava viscosity  $\eta$ . For a representative subset of lunar mare domes, the viscosity dependence of their ratio is given by  $\tau_r/\tau_c = 0.110 \eta^{0.419}$ , where  $\eta < 10^8$  Pa s, and decreases again for still higher lava viscosities (Wöhler et al. 2007).

Carrigan et al. (1992) show that if the magma rises so quickly through the dike that it reaches the surface long before it has lost a significant amount of its heat to the host rock by conduction, the temperature distribution in the dike is largely uniform and the magma temperatures at the surface and at the dike source are nearly identical. A slightly lower temperature is only observed in the immediate vicinity of the dike walls. This situation corresponds to  $\tau_r \ll \tau_c$  or  $\tau_r \approx \tau_c$ . In contrast, for  $\tau_r \gg \tau_c$  a strong temperature decrease will occur before the magma reaches the surface. This assumption of quasi-stationarity may be a good approximation for the domes of rheologic group  $R_3$ , characterised by extremely low magma rise speeds. In the general case, the thermal behaviour of the magma is complex and is governed by the relative importance of factors such as cooling due to heat conduction into the host rock, transport of heat by magma that flows horizontally, and increase of magma temperature by viscous dissipation, i.e. transformation of the kinetic energy of the flowing magma into heat (Carrigan 2000).

For mare domes of rheologic group  $R_1$ ,  $\tau_r/\tau_c$  is larger than but close to 1 for lava viscosities around  $10^4$  Pa s, such that the magma temperature could not strongly decrease during ascent. However, for higher viscosities around  $10^6$  Pa s,  $\tau_r/\tau_c$  obtains values larger than 10, which indicates that magma cooling and crystal formation should have occurred during ascent, thus resulting in the inferred higher lava viscosity. For mare domes of group  $R_2$ ,  $\tau_r$  is roughly equal to or slightly larger than  $\tau_c$ , such that the bulk temperature of the basaltic magma did not significantly decrease during its ascent to the surface. The lava viscosities of less than  $10^4$  Pa s are plausible when near-liquidus magma temperatures at the dike source are assumed. For most mare domes of group  $R_3$ , the ratio  $\tau_r/\tau_c$  obtains values around 50. Hence, magma evolution and especially crystal formation during ascent were important factors governing the properties of the effusion process of the domes of group  $R_3$ . Additionally, the formation of crystals was favoured by the long time the magma spent in the dike, indicated by the high values of  $\tau_r$  of typically  $10^3$  years, which is much longer than the duration  $T_e$  of the effusion process.

In contrast, the ratios  $\tau_r/\tau_c$  are close to 1 for the highland domes such as Gruithuisen  $\gamma$  and  $\delta$  (Fig. 1.9), such that the magma eruption temperature cannot have been much lower than the temperature at the dike source. If we assume a magma temperature above the liquidus point at the dike source, crystallisation and evolution due to cooling during ascent are not supposed to have played a more important role than e.g. for the mare domes of group  $R_1$ . Hence, it is plausible to assume for the magmas that formed the highland domes a substantially higher silica content than typical of basaltic magma, supporting the assumption of a specific phase of non-mare volcanism characterised by the effusion of highly viscous lavas according to Chevrel et al. (1999). A recent study of the Gruithuisen highland domes by Kusuma et al. (2012) relying on an analysis of LRO DIVINER spectral

data acquired at mid-infrared wavelengths also indicates a high silica content of the dome material.

---

### 4.3 Laccolith Modelling of Putative Intrusive Domes

As described in Sect. 1.6.8, some lunar domes have smooth surfaces and very low cross-sectional profiles merging smoothly into the surrounding mare lava plains, suggesting a formation by laccolithic intrusion, where the laccolith formation proceeded until the flexure of the overburden stage. Some domes show fractures on their surfaces, probably formed by the tensional stress caused by flexure of the laccolith overburden.

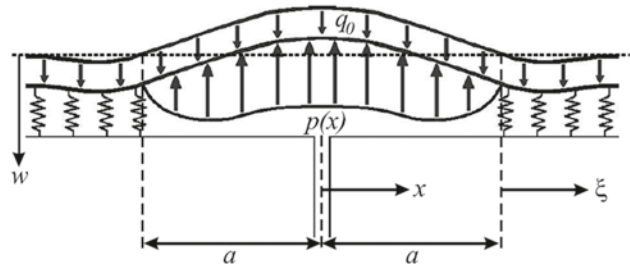
Moreover, the large and flat domes V1 and Ar1 (Fig. 1.15b and 1.15c) also display faults on their surfaces. While there is a smooth transition from the western flank of V1 into the surrounding mare surface, the eastern rim of the dome is made up by a fault about 60 m high.

#### 4.3.1 Arguments Against and In Favour of an Intrusive Origin

As an alternative mode of formation for the candidate lunar intrusive domes, introduced in Sect. 1.6.8, one might think of effusive volcanism, as the morphometric properties of several candidate intrusive domes overlap with those of some classes of effusive domes. However, in contrast to effusive lunar domes, which are largely circular and characterised by relatively sharp and circular boundaries, the candidate intrusive domes are of elongated shape. The surface of some domes merges smoothly into the surrounding mare surface, while in other cases the dome outline is limited by faults and the dome surface is crossed by fractures. The large candidate intrusive domes have much larger diameters and much lower flank slopes than all lunar effusive domes examined so far. One might also consider the candidate intrusive domes as kipukas, i.e. surface parts surrounded by the flooding mare lavas. Kipukas usually consist of a different material than the surrounding mare, such that a spectral contrast would have to be observed. A typical example of a lunar kipuka is the formation Darney  $\chi$  located in western Mare Cognitum, an elevated section of high-land terrain embayed by mare lava (Nichols et al. 1974).

The absence of a spectral contrast indicates that some candidate intrusive domes consist of the same material as the surrounding surface and suggests that they are most likely no kipukas. Due to the fact that many candidate intrusive domes are located near the borders of mare basins, another possible alternative mode of origin is their formation as structural features as a result of basin subsidence, corresponding to class four defined by Head and Gifford (1980), or as effusive features modified by a deformation of the lunar crust. However, the domes of class four do not display fractures on their summit, as it is the case for many candidate intrusive domes. A formation by intrusive processes is supported by the linear or curvilinear rilles associated with many of the candidate intrusive domes, as such

**Fig. 4.3** Sketch of a laccolith (modified from Kerr and Pollard 1998). The arrows indicate the pressure exerted by the weight of the overburden (downward arrows) and by the pressurised magma (upward arrows)



features are commonly interpreted as fractural features (Nichols et al. 1974; Wichman and Schultz 1996) that may occur as a result of the flexural uplift of a laccolith. However, alternative modes of formation cannot be ruled out definitely.

### 4.3.2 Laccolith Modelling

Kerr and Pollard (1998) introduce a laccolith model in which they treat the overburden of the pressurised magma as an elastic plate (Fig. 4.3). The force resulting from the deflection of the plate is equilibrated by the pressure of the magma and the weight of the overburden layer. The magma pressure decreases from the laccolith centre towards its border.

In the following, the overburden thickness of the putative lunar laccoliths is denoted by  $d$ . Due to the fact that all candidate lunar intrusive domes detected so far are situated in mare regions, we assume that the overburden is composed of an upper basaltic layer and a lower layer consisting of crustal material. These two layers are characterized by different elasticity coefficients. The relative extension of the uppermost surface material, which increases with decreasing curvature radius, allows for an estimation of a lower limit  $h_1$  to the thickness of the upper basaltic layer. Based on the material-specific critical tensional stress  $\sigma_{\text{crit}}$  and the coefficient of elasticity  $E_{\text{basalt}}$  of basalt, a lower limit to the thickness of the upper basaltic layer is given by  $h_1 = 2 r \sigma_{\text{crit}} / E_{\text{basalt}}$ , where the curvature radius  $r$  is inferred from the DEM of the dome. If the material undergoes a stress that exceeds  $\sigma_{\text{crit}}$ , it will tear and a fracture will form.

Kerr and Pollard (1998) show that treating the pressurised magma as a classical Newtonian fluid results in a maximum value  $p_0$  of the magma pressure  $p(x)$  at the centre of the laccolith and a decrease to zero at its borders. Here, the  $x$  coordinate denotes the horizontal distance from the laccolith centre. According to Kerr and Pollard (1998), the cross-sectional profile of the overburden is given by the deflection  $w(x)$ , which corresponds to the solution of the fourth-order differential equation

$$F \cdot w''''(x) = q_0 \cdot p(x). \quad (4.5)$$

In Eq. 4.5, the parameter  $F$  denotes the flexural rigidity of the overburden,  $w''''(x)$  is the fourth derivative of  $w(x)$ , and  $q_0$  corresponds to the weight of the overburden normalised to unit area, i.e. the pressure exerted by the overburden on the underlying layers. The value

of  $q_0$  is given by  $q_0 = \rho g d$ , where the density  $\rho$  of the overburden material corresponds to  $\rho \approx 2,900 \text{ kg m}^{-3}$  and the lunar gravitational acceleration to  $g = 1.6 \text{ m s}^{-2}$ . This basic model is extended by Kerr and Pollard (1998) by taking into account that the overburden and the rock layers below the laccolith are not infinitely rigid but behave in an elastic manner. The quantitative effect of this correction, however, turns out to be virtually negligible.

The diameter  $D$ , height  $h$ , volume  $V$ , and curvature radius  $r$  can be inferred from the constructed DEM of a candidate intrusive dome. Based on these morphometric parameters, the model by Kerr and Pollard (1998) yields values for the overburden thickness  $d$ , which corresponds to the intrusion depth, and the magma pressure  $p_0$  at the laccolith center (cf. implementation by Wöhler and Lena 2009). The modeling results show that the largest candidate intrusive domes are characterised by intrusion depths of 2–12 km and magma pressures in between 18 and 100 MPa. For several smaller and steeper candidate intrusive domes without rilles crossing their surface, the modeled intrusion depths correspond to 0.4–1.0 km. On the basis of the laccolith modeling results we divide the putative intrusive domes into three classes, as described in Chap. 5.

### 4.3.3 Comparison with Terrestrial Laccoliths

A group of 12 terrestrial laccoliths in the Ortiz porphyry belt in New Mexico is discussed by Maynard (2005), who finds intrusion depths of 1.0–3.2 km and areal extents in between 1.2 and 52 km<sup>2</sup> (corresponding to average diameters between 1.2 and 8.1 km).

Hacker et al. (2007) describe five laccoliths in southwestern Utah with intrusion depths in between 0.2–2.3 km. According to the geologic maps provided by Hacker et al. (2007), nearly all these laccoliths have elongated shapes with major axes between 1 and 8 km, where the circularities (ratio between minor and major axis) correspond to about 0.5–0.7. The exceptionally large Pine Valley laccolith of 45 by 20 km size was formed by a shallow intrusion at only about 200 m depth (Hacker et al. 2007).

Rocchi et al. (2008) examine magmatic intrusions on the Italian island of Elba which form three so-called “Christmas tree” laccoliths, where the diameters of the intrusions range from 1.6 to 10 km, their depths from 1.9 to 3.7 km, and their thicknesses from 0.05 to 0.7 km.

Gómez-Izquierdo et al. (2008) describe a laccolithic intrusion in Orciatico, Italy, with a diameter of about 1 km and a thickness of 0.125 km. Assuming a typical rate of erosion of the surface, they infer an intrusion depth of 0.4 km.

Relying on geochemical considerations, gravity data, and geological field measurements, Carlino et al. (2006) attribute the formation of Monte Epomeo on the Italian island of Ischia to a laccolithic intrusion of a diameter of 10 km at 1 km depth below the surface. They point out that the central block of Monte Epomeo is surrounded by faults, which indicates the occurrence of a piston-like laccolith uplift phase (cf. Wichman and Schultz 1996). Such faults are also observed for some of the putative lunar intrusive domes (Fig. 1.15b and 1.15c).

The Vigneux leucogranite in western France is examined by Martelet et al. (2004) based on an analysis of seismic data and numerical three-dimensional gravity modelling. Their model indicates the presence of a laccolith of about 30 km diameter (cf. Fig. 6 by Martelet et al. 2004) located at a depth of 10–15 km.

Terrestrial laccoliths and lunar candidate intrusive domes have in common that they are characterised by elongated outlines. Numerical modelling results by Michaut (2011) of the dynamical processes governing the development of laccoliths over time under terrestrial and lunar conditions support the hypothesis that the large and low lunar domes are of intrusive origin. Michaut (2010) takes into account the low lunar gravitational acceleration and assumes for the dry lunar crust that the Young modulus  $E$  denoting the crustal elasticity is 2.5 times higher than that of the “wet” crust of the Earth, leading to characteristic diameters of lunar laccoliths of 12–32 km. For most of the candidate lunar intrusive domes, the modelled sizes are found by Michaut (2010, 2011) to be consistent with morphometric properties described in Chap. 5. Furthermore, lower thicknesses are predicted by Michaut (2011) for lunar laccoliths than for terrestrial laccoliths, which is again in correspondence with available morphometric data.



---

## Abstract

This chapter describes a classification scheme for lunar domes which relies on the spectral and morphometric parameters by which they are characterised, the rheologic parameters describing the dome-forming magma, and the physical conditions under which dome formation occurred.

The classification schemes described in Chap. 2.7 are mainly based on a qualitative description of the shape of a dome and its geologic setting rather than morphometric quantities. In fact, however, effusive domes may be characterised by their specific range of values for lava viscosity, effusion rate, and duration of the effusion process. We have thus introduced a novel classification scheme for lunar domes based on a quantitative analysis according to their spectral (Chap. 3) and morphometric (Chap. 2) properties, yielding seven different classes (termed A–E, and G–H). A grouping of the domes based on a principal component analysis (PCA) in the space made up by eight spectral and morphometric features yields several clusters. Domes belonging to the same cluster share certain characteristic spectral and morphometric properties (a similar scheme is used by Pike (1978) for grouping terrestrial volcanoes). Specifically, these features are the reflectance at 750 nm wavelength, the reflectance ratios  $R_{415}/R_{750}$  and  $R_{950}/R_{750}$ , the flank slope, diameter, height, edifice volume, and form factor. Similar to Pike (1978), the logarithms of  $\zeta$ ,  $D$ ,  $h$ , and  $V$  were used as input to the PCA (Wöhler et al. 2006). This classification scheme is described in Sect. 5.1 for monogenetic domes and in Sect. 5.2 for non-monogenetic domes. A classification scheme for lunar domes of presumably intrusive origin based on their shape and morphometric properties is described in Sect. 5.3. While this chapter only outlines the general properties of different classes of lunar domes based on some selected examples, respectively, more detailed descriptions of individual domes can be found in the following chapters.

**Fig. 5.1** Diameter versus flank slope diagram for the lunar mare dome fields near Cauchy, Arago, Hortensius, and Milichius

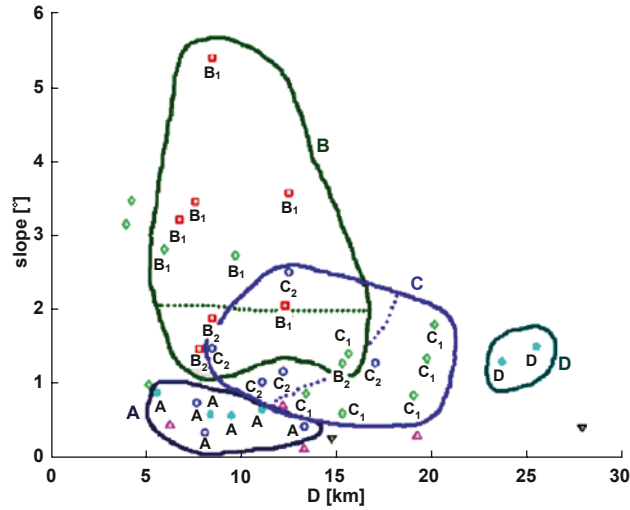
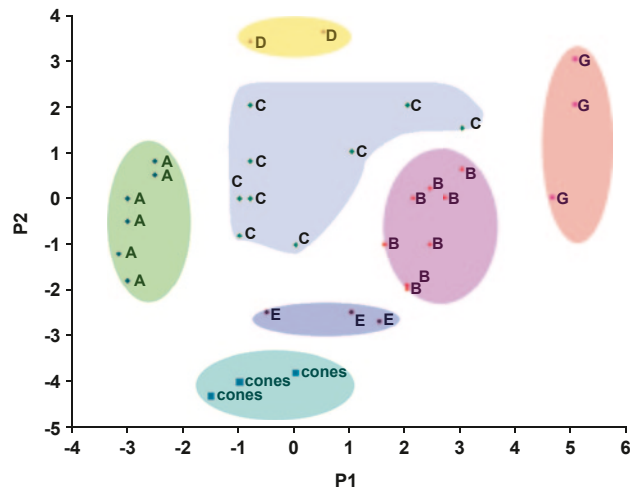


**Fig. 5.2** Classification of lunar mare domes. Scores  $P_1$  and  $P_2$  of the feature vectors describing the domes in the four examined dome fields on the first two principal components of the data distribution. The dome classes A–E and G are indicated, example domes are indicated as dots



### 5.1 Classification Based on Principal Component Analysis

An approximate dome classification can already be preliminarily inferred from the diameter vs. flank slope diagram shown in Fig. 5.1. In this diagram, however, an unambiguous class assignment cannot be obtained for all domes due to the overlap between classes B and C. To determine the class of a dome, the eight features are projected into a subspace of  $M$  dimensions by means of a principal component analysis (PCA). Setting the dimension of the subspace to three retains 87 % of the information contained in the original parameter space. In this subspace, the examined domes form several clusters which can be identified based on the correspondingly transformed dome coordinates ( $P_1, P_2, P_3$ ), where the main groups already appear in the coordinate system spanned by the first two principal components ( $P_1, P_2$ ) as shown in Fig. 5.2.

**Table 5.1** Spectral, morphometric and rheologic properties characterising the classes of effusive lunar domes. Rheologic values of class G are adopted from Wilson and Head (2003)

Class	$R_{415}/R_{750}$	Slope ( $^{\circ}$ )	D (km)	V ( $\text{km}^3$ )	Effusion rate ( $\text{m}^3 \text{s}^{-1}$ )	Effusion time (years)	Viscosity (Pa s)
A	>0.64	0.3–1.0	5–13	<3	100–620	0.05–0.3	$10^2$ – $10^3$
B <sub>1</sub>	0.55–0.64	2.0–5.4	6–15	5–32	30–200	3.0–18	$10^6$ – $10^7$
B <sub>2</sub>	0.55–0.64	1.3–1.9	8–15	2–21	80–170	0.7–1.2	$10^4$ – $10^5$
C <sub>1</sub>	0.55–0.60	0.6–1.8	13–28	7–50	200–2000	0.06–7	$10^4$ – $10^5$
C <sub>2</sub>	0.60–0.64	1.0–2.5	8–17	4–17	100–300	0.5–7	$10^4$ – $10^5$
D	>0.64	1.3–1.5	$\approx 25$	40–67			
E <sub>1</sub>	0.58–0.62	2.0–4.0	<6	0.5–0.8	$\approx 25$	1.0–1.7	$10^5$ – $10^6$
E <sub>2</sub>	0.58–0.62	<2.0	<6	0.5–0.8	100–300	0.05–0.3	$10^3$
G	0.55–0.60	>6.0	7–30	20–400	48–120	12.8–42	$10^8$ – $10^9$
H <sub>1</sub>	0.62–0.68	<5.0	<5	<2	10–100	$\approx 2$	$\approx 10^6$
H <sub>2</sub>	0.62–0.68	2.0–5.0	5–15	1–43	10–100	$\approx 4$	$\approx 10^6$
H <sub>3</sub>	0.62–0.68	5.0–9.0	5–13	7–37	10–100	$\approx 10$	$\approx 10^7$

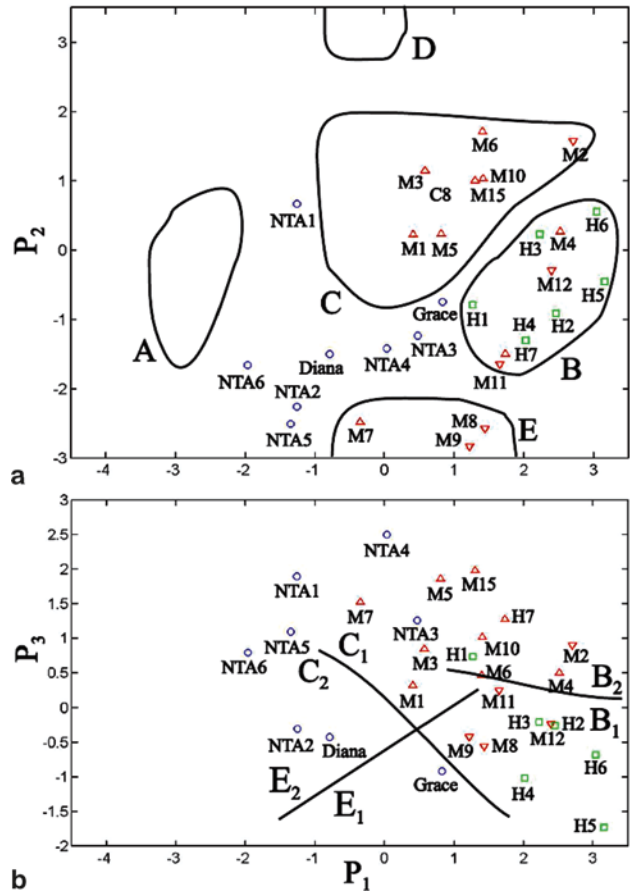
Domes with low flank slopes consisting of spectrally blue (high  $R_{415}/R_{750}$  ratio) lava are assigned to class A. Domes of class B (e.g. M11, H1 and H7) with lower slopes and volumes are assigned to subclass B<sub>2</sub>, while domes with steeper slopes and moderate to high volumes (e.g. H2–H6) belong to subclass B<sub>1</sub>. The domes in the Milichius dome field have large diameters and low to moderate slopes, resulting in high volumes. They are morphometrically similar to but spectrally different from the domes near Cauchy and in northern Mare Tranquillitatis, such that we assigned them to subclass C<sub>1</sub>, while domes with gentle flank slopes, moderate volumes and with higher  $R_{415}/R_{750}$  ratio than C<sub>1</sub> domes belong to subclass C<sub>2</sub> (Table 5.1 and Figs. 5.2 and 5.3). The class E domes represent the smallest volcanic edifices formed by effusive mechanisms observed to date. Lunar cones, which are assumed to have formed essentially from explosive eruptions (Wood 1979), have diameters still smaller by a factor of at least 2–3 and volumes lower by nearly an order of magnitude, compared to the class E domes (Fig. 5.2) (Wood 1979). In analogy to class B, we further subdivide class E into subclasses E<sub>1</sub> and E<sub>2</sub>, denoting the steep-sided flank slope larger than 2° and the shallow edifices of this class, respectively (Fig. 5.3).

The values for the lava viscosities found in our data set span a range of six orders of magnitude, approximately from  $10^2$ – $10^8$  Pa s.

In comparison, the lava that formed the Gruithuisen highland domes (class G) had viscosities around  $10^9$  Pa s (Wilson and Head 2003), which is not far beyond the range we determined for lunar mare domes. Hence, unusual lava viscosity is probably not the primary reason for the peculiar shapes of the Gruithuisen domes; they might rather be due to the low effusion rate, favouring steep slopes, the very long duration of the effusion process, yielding a high edifice volume (Table 5.1), and the fact that lava effusion occurred over at least two distinct subsequent phases (non-monogenetic domes) with durations of the effusion process of up to several decades (Wilson and Head 2003).

Consequently, the Gruithuisen highland domes on the one hand and the small and shallow class A mare domes in Mare Tranquillitatis on the other hand appear to represent

**Fig. 5.3** Classification of lunar mare domes. The scores  $P_1$ ,  $P_2$ , and  $P_3$  describe the dome properties. The subdivision of classes B, C and E into subclasses  $B_1$  and  $B_2$ ;  $C_1$  and  $C_2$  and  $E_1$  and  $E_2$  is indicated



endmembers of the dome formation process, spanning a broad continuous range of associated rheologic parameters: lava viscosities between  $10^2$  and  $10^9$  Pa s and durations of the effusion process between a few weeks and about 40 years (Table 5.1).

The dome classes A, B, C, and E refine the classes 1–3 by Head and Gifford (1980) and denote morphologically simple and likely monogenetic edifices which presumably formed during a single eruption event and thus do not show individual lava flows or other traces of several subsequent eruption events. Such domes are abundant in Mare Tranquillitatis, Mare Insularum, and Oceanus Procellarum. Class A domes display small to moderate diameters between 5 and 13 km with very low flank slopes and volumes and were formed by spectrally strongly blue lavas of high  $R_{415}/R_{750}$  spectral ratio. Class B domes have small to moderate diameters between 6 and 15 km and were formed from lavas of low to moderate  $R_{415}/R_{750}$  spectral ratio. Steep and voluminous class B domes with flank slopes larger than  $2^\circ$  are assigned to subclass  $B_1$ , while the lower edifices with flank slopes below  $2^\circ$  make up subclass  $B_2$ . Class  $B_2$  domes formed during shorter periods of time than those of class  $B_1$  (Table 5.1) resulting in shallower flanks with lower volumes. Class C domes are larger (diameter between 8 and 28 km) with flank slopes typically below  $2^\circ$ . Domes formed from spectrally

red lavas of low to moderate  $R_{415}/R_{750}$  ratio, having large diameters between 13 and 28 km and large edifice volumes of several tens of  $\text{km}^3$  are assigned to subclass  $C_1$ , while spectrally bluer domes of moderate to high  $R_{415}/R_{750}$  ratio, smaller diameters between 8 and 17 km, and lower edifice volumes of less than  $17 \text{ km}^3$  are assigned to subclass  $C_2$ .

The conditions under which domes of classes  $B_2$  and  $C_1$  formed were very similar, except that in the case of the  $C_1$  domes the effusion rates were much higher. In this scenario, the influence of the impact-induced stress fields was such that the magma flow through the crust likely experienced less resistance for the class  $C_1$  domes, while the magma properties themselves were not perceivably different. Class E, made up by domes with exceptionally small diameters below 6 km and very low edifice volumes below  $1.2 \text{ km}^3$ , represents intermediate objects between lunar domes and lunar cones, small volcanic edifices formed by explosive volcanic eruptions. Between classes  $B_1$  and  $E_1$ , the principal difference is the effusion time but not the flank slope, since the duration of the effusion process was longer for class  $B_1$  domes. Between class A and  $E_2$ , the discriminative parameter is the spectral appearance (higher  $R_{415}/R_{750}$  ratio and thus higher  $\text{TiO}_2$  content for class A) and not primarily the morphometric and rheologic properties.

---

## 5.2 Non-monogenetic Lunar Effusive Domes

Edifices of more complex morphology, displaying large diameters above 20 km, low flank slopes, and very high edifice volumes, are represented by class D. Examples are Arago  $\alpha$  and  $\beta$  in western Mare Tranquillitatis. The Gruithuisen and Mairan highland domes, which have more highland-like spectral signatures and high flank slopes of  $5\text{--}15^\circ$ , are comprised by class G.

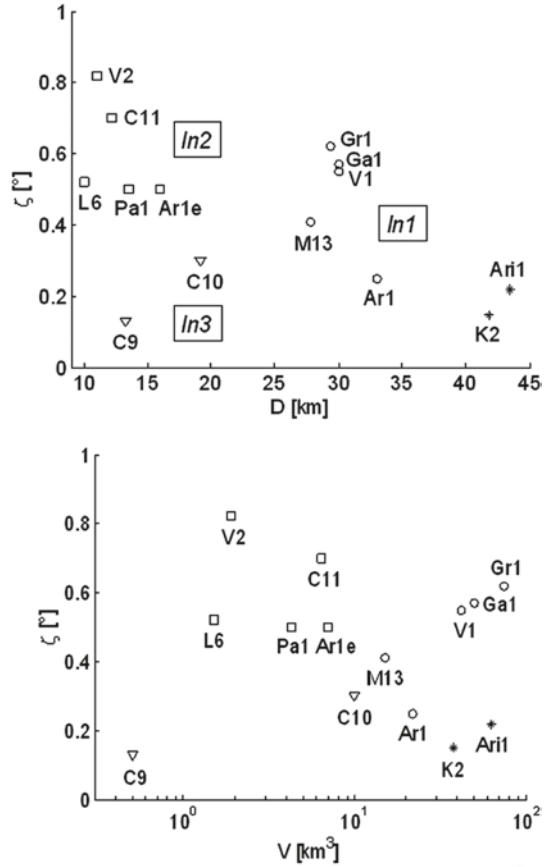
In the Marius Hills region, low domes can be found as well as edifices with steep flanks and surfaces of high roughness. Commonly, these features are the result of a superposition of cones on lava flows or of steep domes on low domes (Whitford-Stark and Head 1977) and are classified as class 7 domes by Head and Gifford (1980). We assign the non-monogenetic Marius domes to class H. Small domes of less than 5 km diameter belong to subclass  $H_1$ . The irregular shapes of domes of subclass  $H_2$  with more than 5 km diameter and flank slopes below  $5^\circ$  indicate a formation during several effusive episodes. Domes of subclass  $H_3$  have diameters comparable to those of monogenetic class  $B_1$  domes, but their flank slopes are all steeper than  $5^\circ$  and reach values of up to  $9^\circ$ . Such extraordinarily steep flank slopes have not been observed for monogenetic mare domes located in other dome fields.

---

## 5.3 Classes of Lunar Intrusive Domes

A subset of lunar domes with very low flank slopes differs considerably in several respects from the more typical lunar effusive domes (Wöhler and Lena 2009). Some of these domes are exceptionally large, and many of them are associated with faults or linear rilles of presumably tensional origin, while they do not show summit pits. They were formed in differ-

**Fig. 5.4** Diameter  $D$  vs. flank slope  $\zeta$  diagram (*top*, also indicating the dome classes In1–In3) and volume  $V$  vs. flank slope  $\zeta$  (*bottom*) diagrams of the examined candidate intrusive domes



ent dome fields, are associated with a large variety of lava types, and are characterised by very low flank slopes in the range  $0.1\text{--}0.9^\circ$  and by elongated outlines. The morphometric properties represented by the intrusive dome classes In1–In3 (Fig. 5.4) overlap with the values characterising several classes of effusive domes. A reliable discriminative criterion, however, is the circularity  $c$  of the dome outline as defined in Chap. 2. The intrusive domes regarded in our studies (Fig. 1.15) have circularity values below 0.8, while we found that the circularity is always higher than 0.9 for the effusive domes having flank slopes below  $0.9^\circ$  and displaying effusive vents.

We divide the candidate intrusive lunar domes into three classes based on the diagram shown in Fig. 5.4. Class In1 comprises large domes with diameters above 25 km and flank slopes of  $0.2\text{--}0.6^\circ$ , class In2 is made up by smaller and slightly steeper domes with diameters of 10–15 km and flank slopes between  $0.4^\circ$  and  $0.9^\circ$ , and domes of class In3 have diameters of 13–20 km and flank slopes below  $0.3^\circ$  (Table 5.2). Based on the laccolith modelling described in Sect. 4.3.2, intrusive domes of class In1 are characterised by upper-



**Table 5.2** Morphometric properties of the putative intrusive domes, modelling results for the minimum basaltic layer thickness  $h_1$ , intrusion depth  $d$ , and maximum magma pressure  $p_0$

Class	D (km)	Slope (°)	$h_1$ (km)	$d$ (km)	$p_0$ (MPa)
In1	>25	0.2–0.6	0.2–1.2	2.3–12	18–100
In2	10–15	0.4–0.9	<0.3	0.4–1.0	3–8
In3	13–20	<0.3	0.6–1.0	1.9–2.5	15–22

most basaltic layer thicknesses of 0.2–1.2 km, intrusion depths of 2.3–12 km and magma pressures of 18–100 MPa.

For the smaller and steeper domes of class In2, the uppermost basaltic layer has a thickness of typically only 0.1–0.2 km, the magma intruded to shallow depths between 0.4 and 1.0 km while the inferred magma pressures range from 3 to 8 MPa. Class In3 domes are similar to those of class In1 with similar thicknesses of the uppermost basaltic layer ranging from 0.6 to 1.0 km, intrusion depths of 1.9–2.5 km, and magma pressures of 15–22 MPa.

## 5.4 Conclusion

We have presented an analysis of monogenetic effusive and putative intrusive mare domes, of more complex volcanic edifices like those encountered in the Marius Hills region, and of lunar domes situated inside or near large impact craters. Lunar cones and highland domes make up distinct classes of their own in our scheme. Lunar mare domes in various regions fit well into the established classification scheme, supporting its general validity.

---

## Part II

# Guide to Observing Lunar Domes on the Moon

---

## Abstract

This chapter provides an overview of effusive lunar domes bisected by linear rilles. A description of the formation conditions is provided according to the modelling approaches described in the previous chapters.

The surface appearance of dike emplacement in the crust is depending on the depth below the surface to which the dike penetrates, as discussed by Wilson and Head (1996, 2002). As described in Sect. 1.6.4, if a dike ascends to shallow depth and reaches the surface at some points, lava may effuse, and the dike may form a rille at the surface at which a dome may form (Head and Wilson 1996).

In this chapter we describe the morphometric and rheologic properties for some bisected domes: Birt 1 and 2, Menelaus 1 and 2, and Gassendi 1 (Fig. 6.1 for their identification).

---

## 6.1 The Birt Domes

The two domes near the crater Birt in Mare Nubium are situated at the northern end of Rima Birt. Rose and Spudis (2000) distinguish between five different mare units, for which they infer durations of the effusion process of only several weeks or months with long interruptions.

The well-known fault Rupes Recta (also known as the “Straight Wall”) is situated in western Mare Nubium. The formation of Rupes Recta is commonly regarded as a result of the stress field in the lunar crust generated by the impact which formed the Imbrium basin (Wilhelms 1987). The length of the nearby rille Rima Birt amounts to more than 50 km. Two domes are situated at the northern end of Rima Birt, supporting a volcanic origin of the rille (Fig. 1.10). An elongated vent at the northern end of Rima Birt bisects the dome Birt 1 located at 9.66°W and 20.73°S. A second rille, which is straight and much shorter than Rima Birt, transects the western edge of Birt 1 and bisects the neighbouring dome Birt

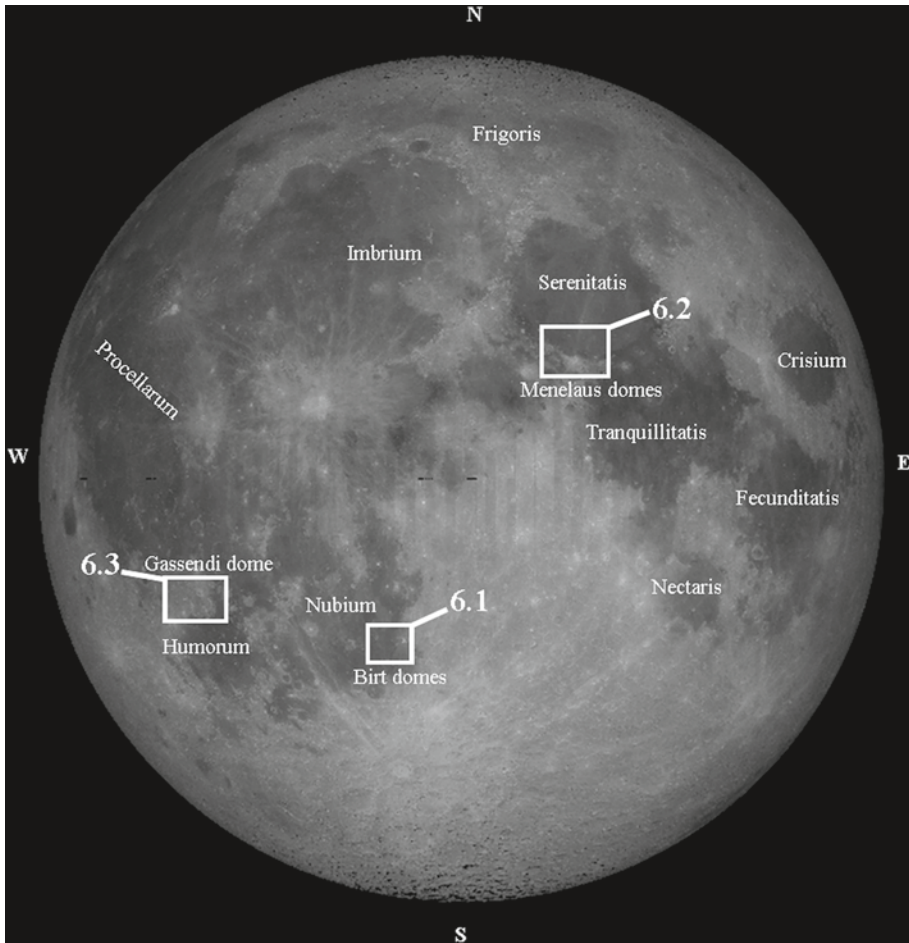


**Fig. 6.1** Lunar map of the bisected effusive domes described in the text. Basemap: Clementine (NASA, <http://photojournal.jpl.nasa.gov/catalog/PIA00302>)

2 situated at  $9.98^{\circ}\text{W}$  and  $20.39^{\circ}\text{S}$ . These two segments may be attributed to two different dikes oriented in parallel (Fig. 6.2).

Moreover, the dome-forming effusive volcanism in this region was presumably associated with pyroclastic activity, since the Birt domes are located in a dark region interpreted as pyroclastic material by Holt (1974). The short linear rille bisecting the dome Birt 2 also cuts through the surface of Birt 1, which indicates that the formation of the domes did not occur simultaneously but that Birt 2 and the associated linear rille bisecting its surface formed after Birt 1.

The diameters of the domes Birt 1 and 2 were determined to  $16.0 \pm 0.5$  km and  $7.8 \pm 0.5$  km. Their heights amount to  $170 \pm 20$  m and  $70 \pm 10$  m, resulting in flank slopes of  $1.22 \pm 0.10^{\circ}$  and  $1.03 \pm 0.15^{\circ}$  (Fig. 6.3). The edifice volumes correspond to  $17.3$  and  $1.3$  km<sup>3</sup>. The Clementine UVVIS spectral data of the dome Birt 1 reveal a 750 nm reflectance of

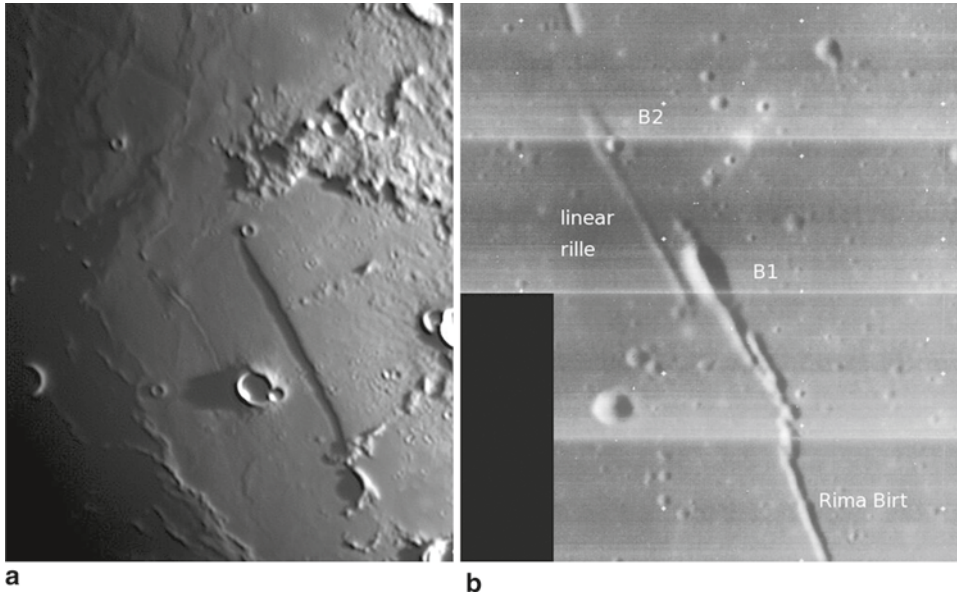
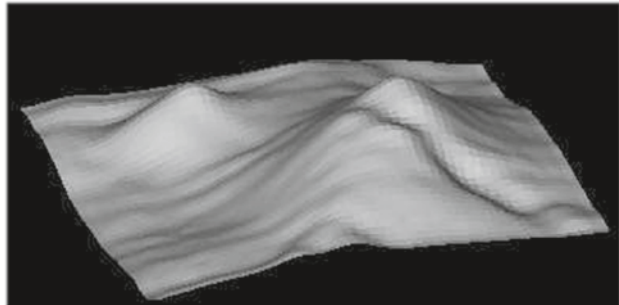


**Fig. 6.2** a Telescopic image of the two bisected domes at the northern end of Rima Birt. (Image by J. Phillips). b Mosaic of Lunar Orbiter images IV-113-H1 and IV-113-H2 (NASA/USGS), showing the two rilles

**Fig. 6.3** DEM of the region around Birt 1 and 2



$R_{750}=0.0985$ , a low value for the UV/VIS colour ratio of  $R_{415}/R_{750}=0.5935$ , and a weak mafic absorption with  $R_{950}/R_{750}=1.0216$ . The spectral data for the northern dome Birt 2 indicate a 750 nm reflectance of  $R_{750}=0.0978$ , a low UV/VIS colour ratio of  $R_{415}/R_{750}=0.5961$ , and a weak mafic absorption with  $R_{950}/R_{750}=1.0398$  suggesting a high soil maturity.

The dome Birt 1 belongs to class  $C_1$ , while Birt 2 belongs to class  $C_1$  with a tendency towards class  $C_2$  due to its smaller diameter and lower edifice volume. Based on rheologic modelling (Sect. 2.5) we obtain effusion rates of  $623$  and  $228 \text{ m}^3 \text{ s}^{-1}$ , magma viscosities of  $5.7 \times 10^5$  and  $4.5 \times 10^4 \text{ Pa s}$ , and durations of the effusion process of  $0.88$  and  $0.18$  years, respectively. For these calculations we assumed a magma density of  $\rho=2,900 \text{ kg m}^{-3}$  (Wieczorek et al. 2001). With their high effusion rates, moderate to large erupted lava volumes, and low to moderate lava viscosities, the domes Birt 1 and 2 belong to rheologic

group  $R_1$ . Hence, they are similar to many of the domes in the region around Milichius and Tobias Mayer. Furthermore, Rima Birt, the major axes of the vents of the domes, the outflow channel of Birt 1, and the linear rille associated with Birt 2 are oriented in parallel, approximately in the same direction as Rupes Recta and thus radial to the Imbrium basin. Similar alignments have been observed in the dome field around Milichius and Tobias Mayer and for the chain of domes situated in northern Mare Tranquillitatis. Another alignment has been observed for domes in Mare Undarum, radial to Crisium basin (Chap. 7). In the line of thought of the model by Rubin (1993b), these alignments indicate that the Birt domes were formed by dikes whose ascent was guided by the crustal fractures and the stress field, i.e. the direction of the lowest compressional crustal stress (Rubin 1993b), of the Imbrium impact basin (Sect. 1.6.7, cf. also Sects. 7.1.1 and 7.1.11).

An important parameter for modelling the geometry of lunar feeder dikes is the vertical pressure gradient  $dp/dz$ , described in Sect. 4.1, where to compute the dike width  $W$  and length  $L$ , a default value of  $dp/dz=328 \text{ Pa m}^{-1}$  is used. In contrast, for the bisected Birt domes the visible expression of the dike of the dome Birt 2, i.e. the linear rille of 18.2 km length that bisects the dome surface, may be used in order to estimate the pressure gradient  $dp/dz$  that occurred during dome formation.

Thus, based on the dike model by Wilson and Head (2003) described in Sect. 4.1 with  $p_0/G=10^{-3.5}$ , a pressure gradient of  $dp/dz=1,043 \text{ Pa m}^{-1}$  is required for a dike length of  $L=18.2 \text{ km}$  that equals the length of the linear rille associated with Birt 2. The corresponding dike width amounts to  $W=4.1 \text{ m}$  and the magma rise speed to  $U=3.1 \times 10^{-3} \text{ m s}^{-1}$ . For the “default value” of  $dp/dz=328 \text{ Pa m}^{-1}$ , the dike model yields  $U=3.7 \times 10^{-4} \text{ m s}^{-1}$ ,  $W=11.7 \text{ m}$ , and  $L=52.5 \text{ km}$ . For the larger dome Birt 1, assuming the same pressure gradient of  $dp/dz=1,043 \text{ Pa m}^{-1}$  implies  $U=1.1 \times 10^{-3} \text{ m s}^{-1}$ ,  $W=11.2 \text{ m}$ , and  $L=50 \text{ km}$ . These pressure gradients are difficult to explain solely by a positive magma buoyancy due to the density difference between the material of the crust and the ascending magma, demonstrating that an excess pressure in the magma reservoir as proposed by Head and Wilson (1992) and Wilson and Head (1996, 2002) appears to be inevitable to allow the ascent of magma to the surface. However, the dike may also be partially covered such that its true length may exceed the extension of its visible part (Head and Wilson 1992), resulting in a lower modeled value of the pressure gradient.

## 6.2 The Domes near the Crater Menelaus

The Menelaus region is situated at the southern rim of Mare Serenitatis and is dominated by the Menelaus rilles (Fig. 6.4). Howard et al. (1973) distinguish between two different lava flows, where the more recent lava flow covers the rilles transecting the older flow (Fig. 6.5).

The Menelaus rilles intersect two domical structures situated at  $17.80^\circ\text{N}$  and  $15.75^\circ\text{E}$  (Menelaus 1) and at  $17.57^\circ\text{N}$  and  $16.45^\circ\text{E}$  (Menelaus 2), respectively. The western dome is also termed Menelaus  $\sigma$  (Howard et al. 1973). The diameters of the domes Menelaus 1 and 2 are determined to  $10 \times 16 \pm 0.5 \text{ km}$  and  $13 \times 16 \pm 0.5 \text{ km}$ , respectively. The heights of the domes amount to  $180 \pm 20 \text{ m}$  and  $110 \pm 10 \text{ m}$ , resulting in flank slopes of  $1.60 \pm 0.20^\circ$





**Fig. 6.4** Telescopic image by J. Phillips (*upper left*). Image simulated based on the LOLA DEM using LTVT, assuming the same illumination conditions as in the telescopic image (*top right*). Dome Menelaus 1 (Kaguya image at 1,000 nm, *bottom left*). Dome Menelaus 2 (Kaguya image at 1,049 nm, *bottom right*). Menelaus 1 is the western and Menelaus 2 the eastern dome. Kaguya images are courtesy of JAXA. (The Kaguya image archive is accessible at <https://www.soac.selene.isas.jaxa.jp/archive/>. We thank the Kaguya (SELENE) TC team and the SELENE Data Archive for providing the Kaguya (SELENE) data. SELENE is a Japanese mission developed and operated by JAXA)

and  $0.9 \pm 0.10^\circ$ , respectively (Fig. 6.6). The edifice volumes correspond to 11.2 and 8.9 km<sup>3</sup>. For both domes, Clementine UVVIS spectral data indicate a moderate  $R_{415}/R_{750}$  ratio of about 0.60 and furthermore reveal a 750 nm reflectance of  $R_{750}=0.09$  and a weak mafic absorption with  $R_{950}/R_{750}=1.06$ , suggesting a high soil maturity. If an effusive volcanic origin is assumed for the two domes, the rheologic model (Sect. 2.5) yields high effusion rates of 225 and 481 m<sup>3</sup> s<sup>-1</sup> for Menelaus 1 and 2. They were formed from lava of viscosities of  $1.3 \times 10^6$  and  $9.1 \times 10^4$  Pa s over a period of time of 1.6 and 0.6 years, respectively.

The inferred rheologic properties are comparable to those of the class C<sub>2</sub> domes in the Cauchy region in Mare Tranquillitatis such as Cauchy ω and τ. According to the dike model

**Fig. 6.5** Clementine 750 nm image of the Menelaus region (USGS, <http://www.mapaplanet.org>)

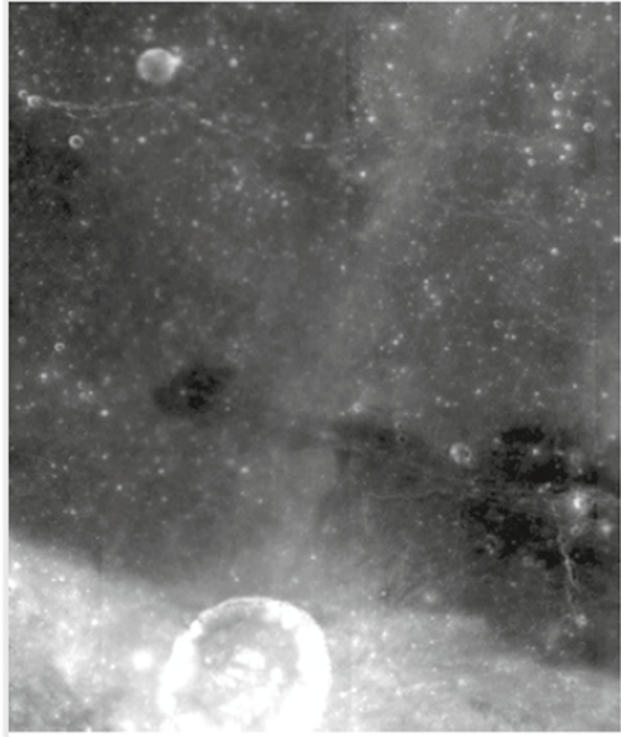
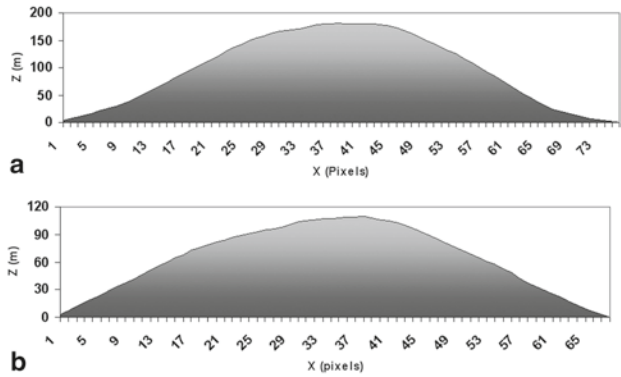
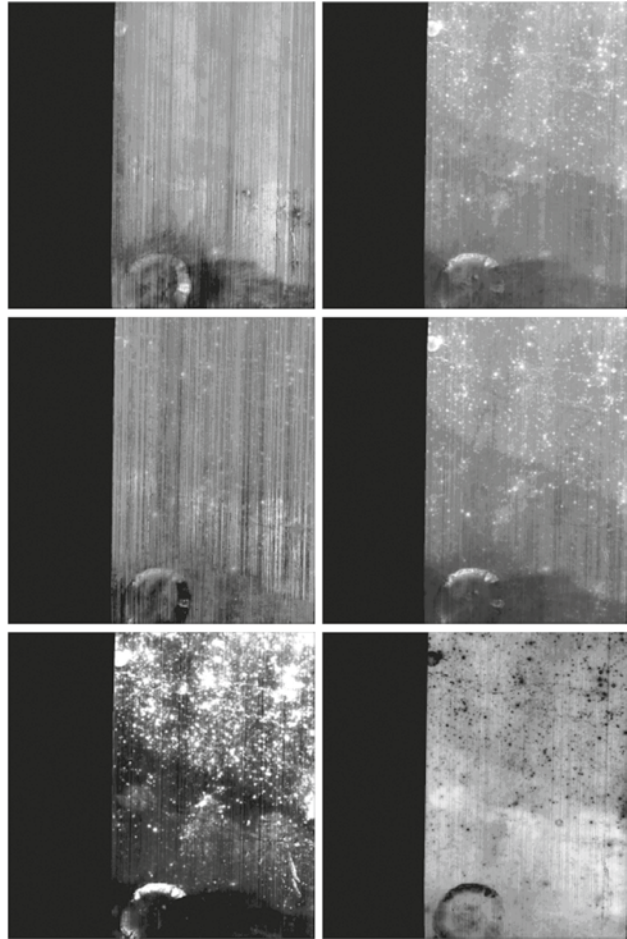


**Fig. 6.6** **a** Cross-sectional profile of Menelaus 1 in east-west direction. **b** Cross-sectional profile of Menelaus 2 in east-west direction



(Sect. 4.1) we estimate for the dome Menelaus 1 a magma rise speed of  $U=2.5 \times 10^{-5} \text{ m s}^{-1}$ , a dike width of 47 m, and a dike length of 188 km. For the dome Menelaus 2, the estimated magma rise speed amounts to  $U=4.4 \times 10^{-4} \text{ m s}^{-1}$  and the dike width and length to 16 m and 70 km, respectively. These modelling results were obtained assuming a vertical magma pressure gradient of  $328 \text{ Pa m}^{-1}$ , the value inferred as the minimum value required according to Wilson and Head (1996) for magma to ascend from the bottom of the lunar crust and erupt onto the surface (Sect. 4.1). The dike lengths resulting from the model are

**Fig. 6.7** Spectral parameter maps inferred from Chandrayaan-1 M<sup>3</sup> multispectral data (longitude range from 14 to 18°E, latitude range from 16 to 20°N). After applying a thermal correction to the radiance spectra, a division by the wavelength-specific solar irradiance was performed and the resulting reflectance spectrum was smoothed by a spline. Row-wise from *top left* to *bottom right*: Absorption wavelength (grey value interval 900–1,000 nm), relative band depth of 1,000 nm absorption after continuum removal (0–0.25), FWHM of 1,000 nm absorption (150–350 nm), integrated band depth (IBD) of the 1,000 nm absorption after continuum removal (grey value interval 0–70), IBD of the pyroxene absorption at ~2,000 nm after continuum removal (grey value interval 0–10), spectral ratio  $R_{2018}/R_{1509}$  (grey value interval 1.15–1.45)



thus comparable to the extension of the linear rilles associated with the two domes, which corresponds to about 100–150 km, suggesting that the Menelaus rilles may represent the surface expressions of dome-forming dikes (cf. Head and Wilson 1996).

The continuum-removed spectra from Kaguya VIS+NIR imagery of the bisected domes show a strong absorption trough at about 1,000 nm with an inflection at 1,049 nm due to the presence of an olivine component. These findings are supported by the spectral parameters inferred from 85-band Chandrayaan-1 M3 hyperspectral data (Fig. 6.7).

An increased absorption wavelength, a broadened absorption trough near 1,000 nm, and an increased  $R_{2018}/R_{1509}$  spectral ratio indicate the presence of olivine-bearing mare basalt (Smrekar and Pieters 1985; LeMouélic et al. 2000). This is observed for the domes and the mare surface along the Menelaus rilles, as also visible in the corresponding petrographic map of Fig. 6.8.



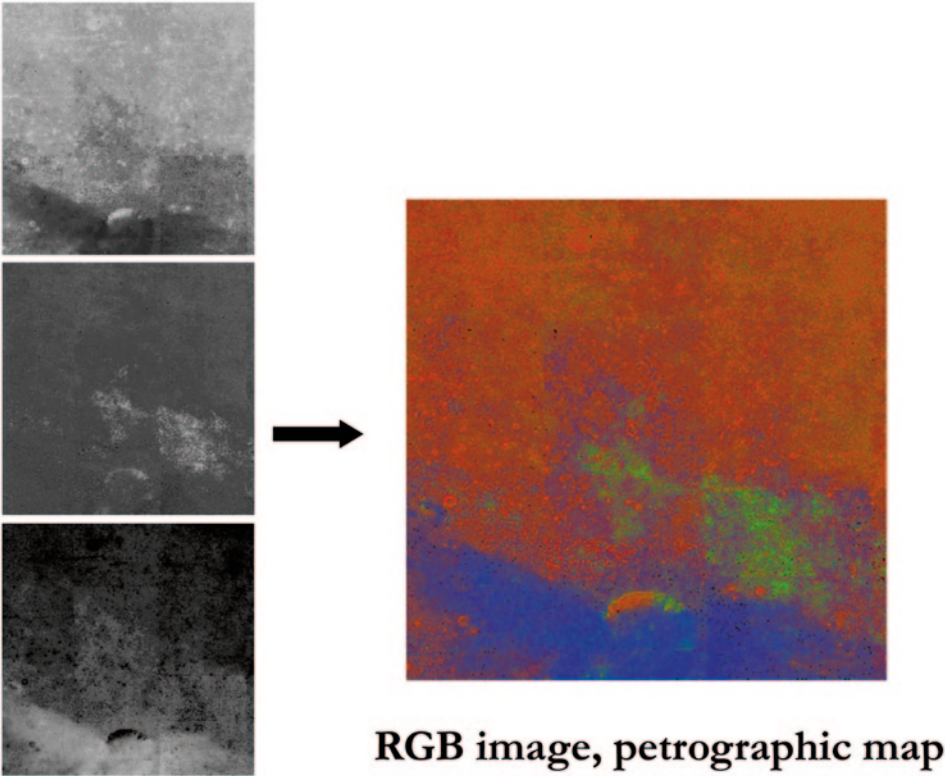


**Fig. 6.8** Petrographic map which indicates the relative fractions of the three end-members mare basalt (*top*), Mg-rich rock (*middle*), and ferroan anorthosite (FAN, *bottom*), obtained based on Clementine data. The region along the Menelaus rilles displays a high content of Mg-rich rock

**Fig. 6.9** Section of LROC WAC image M116622722ME (NASA/GSFC/Arizona State University) with the bisected dome near Gassendi (marked by an arrow)

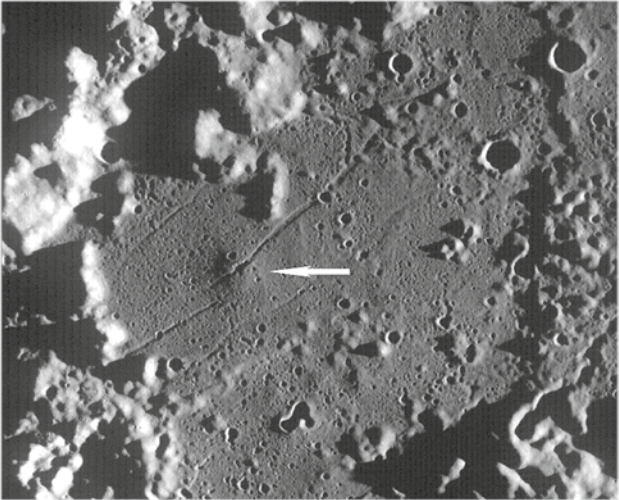


**Fig. 6.10** Telescopic image of the bisected dome (*top*). (Image by J. Phillips). Cross-sectional profile of the dome in east-west direction (*bottom*)

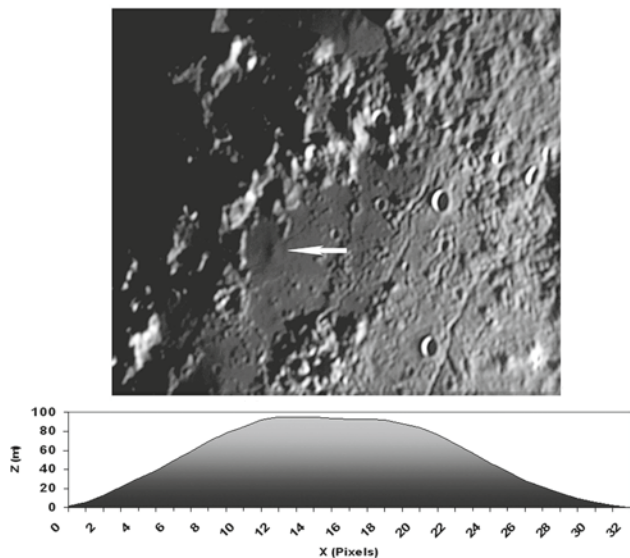
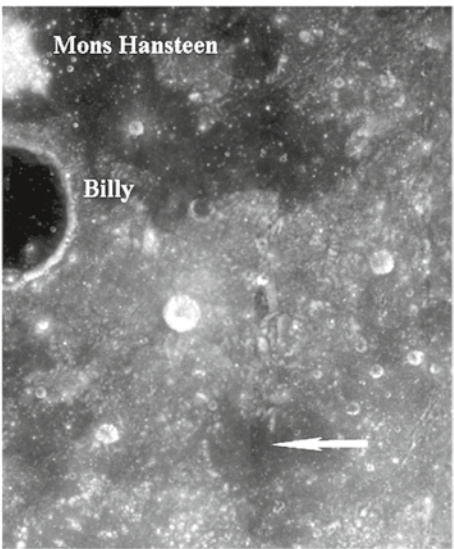


**Fig. 6.11** Section of the Clementine 750 nm image (USGS, <http://www.mapaplanet.org>) of the region around the dome Gassendi 1, which is marked by an *arrow*



### 6.3 The Bisected Dome near Gassendi

A linear rille bisects a small dome west of Gassendi and south of Billy (Wood 2006). The dome coordinates are  $47.48^{\circ}\text{W}$  and  $16.18^{\circ}\text{S}$ . The length of the bisecting rille corresponds to 56 km (Figs. 6.9–6.11). The diameter of this dome amounts to  $7.8 \pm 0.5$  km and its height was determined to  $95 \pm 10$  m, resulting in flank slope of  $1.40 \pm 0.10^{\circ}$ . The edifice volume

corresponds to  $2.3 \text{ km}^3$ . The Clementine UV/VIS spectral data of the dome reveal a 750 nm reflectance of  $R_{750}=0.1111$ , a low value for the UV/VIS colour ratio of  $R_{415}/R_{750}=0.5893$ , and a weak mafic absorption of  $R_{950}/R_{750}=1.0571$ .

The dome belongs to class  $C_2$ . Based on rheologic modelling (Sect. 2.5) we obtain an effusion rate of  $190 \text{ m}^3 \text{ s}^{-1}$ , a magma viscosity of  $8.1 \times 10^4 \text{ Pa s}$ , and a duration of the effusion process of 0.38 years. For the “default value” of  $dp/dz=328 \text{ Pa m}^{-1}$ , the dike model (Sect. 4.1) yields a magma rise speed of  $U=9.1 \times 10^{-5} \text{ m s}^{-1}$  and dimensions of the feeder dike of  $W=21.6 \text{ m}$ , and  $L=97 \text{ km}$ .

Using the same approach as for the Birt domes with  $p_0/G=10^{-3.5}$ , a pressure gradient of  $dp/dz=574 \text{ Pa m}^{-1}$  is required to obtain a dike length of  $L=56 \text{ km}$  that equals the length of the linear rille associated with Gassendi 1 (however, the true dike length may exceed that of its visible part (Head and Wilson 1992)). The corresponding dike width amounts to  $W=12.4 \text{ m}$  and the magma rise speed amounts to  $U=2.7 \times 10^{-4} \text{ m s}^{-1}$ . As for Birt 1 and Menelaus 2, the inferred rheologic properties for Gassendi 1 suggest rapid effusive eruptions lasting only a few months.



---

**Abstract**

This chapter provides a detailed description of a large number of lunar domes in a variety of regions according to their determined spectral and morphometric properties as well as the inferred rheologic properties of the dome-forming magma and the corresponding feeder dike dimensions.

In this chapter we describe the morphometric and rheologic properties of the examined effusive domes, including several lunar regions and dome fields (Fig. 7.1).

---

## **7.1 Effusive Lunar Domes Located from Selenographic Longitude 0° to 90° East**

### **7.1.1 Mare Tranquillitatis**

The Cauchy region and northern Mare Tranquillitatis exhibits a large number of lunar mare domes (Fig. 1.5d–g). The strongly different shapes of these domes indicate that they were formed by lavas with a broad range of viscosities erupting at different effusion rates (Whitford-Stark and Head 1977). As described in Chap. 3, the older lavas in Mare Tranquillitatis are spectrally red (high  $R_{750}/R_{415}$  colour ratio) and are thus characterised by a lower titanium content than the more recent lavas, which appear spectrally blue (Rajmon and Spudis 2001).

**Domes in the Arago and Carrel region** The crater Arago is situated in western Mare Tranquillitatis, northwest of the lava-flooded slightly oval structure Lamont (Rükl 1999). According to Dvorak and Phillips (1979), the structure Lamont is a mass concentration (“mascon”) inducing a gravity anomaly, and the associated system of wrinkle ridges was formed as the result of compressional stress in the lunar crust. North and west of the crater Arago, the lunar domes Arago  $\alpha$  (termed A2, Figs. 1.5d and 7.2) and Arago  $\beta$  (termed A3,

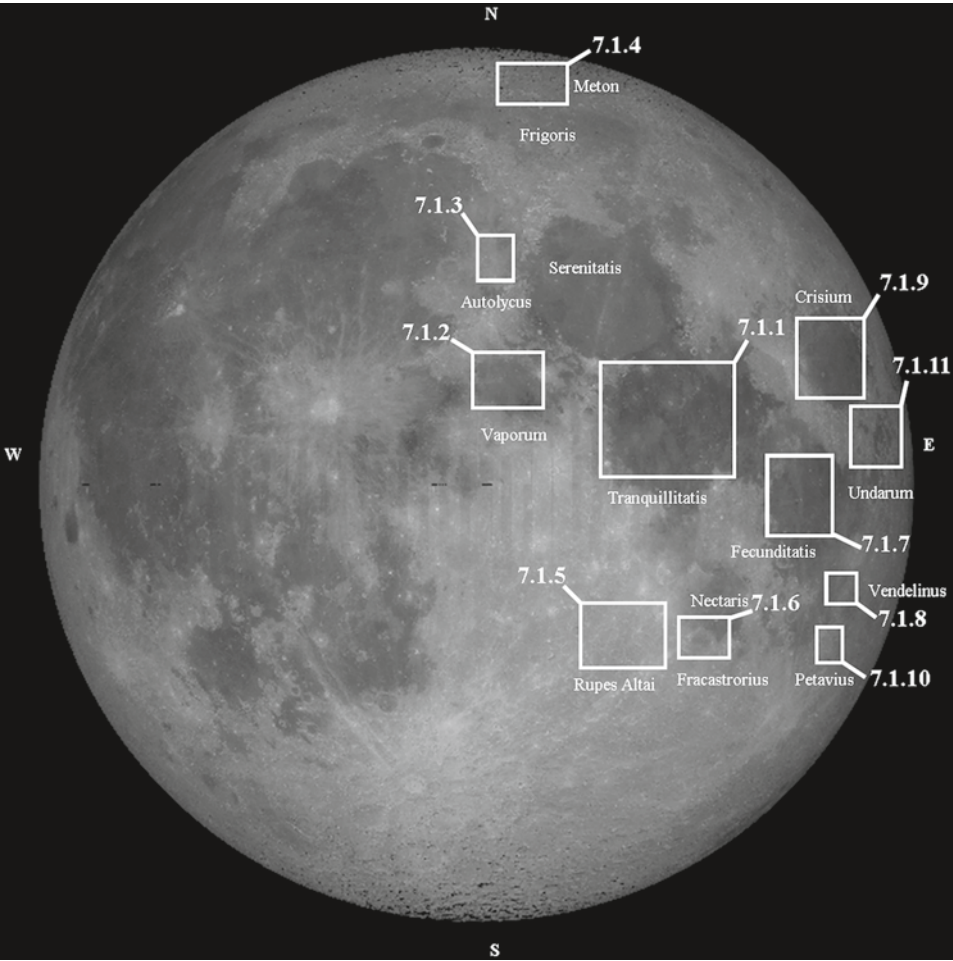


**Fig. 7.1** Lunar map of the effusive domes, located from selenographic longitude 0° to 90° East, described in the text. Basemap: Clementine (NASA, <http://photojournal.nasa.gov/catalog/PIA00302>)

**Fig. 7.2** Telescopic image of the domes A1–A3.  
(Image by Z. Pujic)

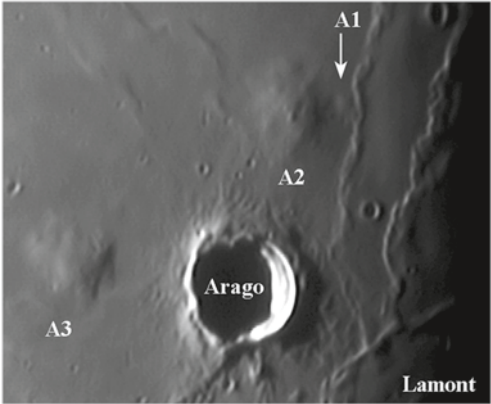
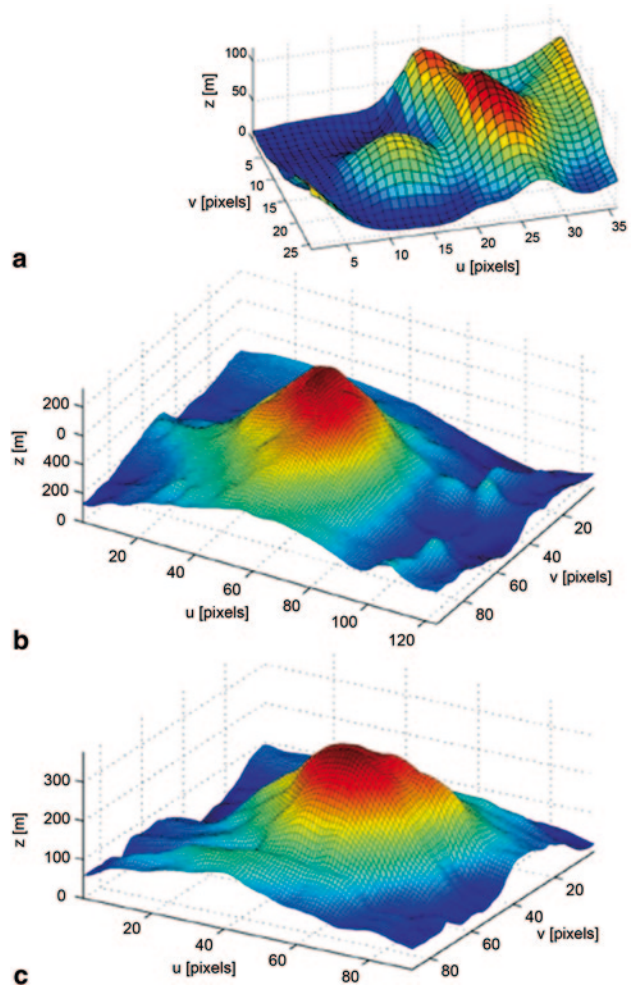


**Fig. 7.3** DEMs constructed for the domes A1–A3 based on telescopic CCD image data. (a) Arago 1 (A1), (b) Arago alpha (A2), (c) Arago beta (A3)



Figs. 1.5d and 7.2) are situated. The surfaces of these domes are relatively rough and show protrusions. Three aligned domes termed A4–A6 with diameters in between 8 and 11 km are situated between Arago  $\alpha$  and the crater Maclear (Fig. 1.5e).

Another low dome, A1 (Fig. 7.2), is located near a ridge to the east of A2 at  $21.96^\circ$  E and  $7.66^\circ$  N. Its diameter was determined to  $5.6 \pm 0.3$  km and its height amounts to  $45 \pm 10$  m, resulting in a flank slope of  $0.88 \pm 0.30^\circ$ . The diameters of the large domes Arago  $\alpha$  (A2, located at  $21.70^\circ$  E and  $7.56^\circ$  N) and Arago  $\beta$  (A3, located at  $20.07^\circ$  E and  $6.24^\circ$  N) correspond to  $25.4 \pm 0.3$  km and  $23.6 \pm 0.3$  km, respectively. Their heights amount to  $330 \pm 30$  m and  $270 \pm 30$  m, resulting in flank slopes of  $1.50 \pm 0.30^\circ$  and  $1.30 \pm 0.30^\circ$ , respectively (Fig. 7.3). These domes belong to class A (cf. Chap. 5) and were formed of basalts of relatively high  $\text{TiO}_2$  content, as they appear strongly blue in the Clementine UV/VIS colour ratio image (Fig. 7.4).

The edifice volumes for the domes A1–A3 correspond to 0.3, 67.0 and 39.9  $\text{km}^3$ , respectively. For both domes, Clementine UVVIS spectral data indicate a  $R_{415}/R_{750}$  ratio of about

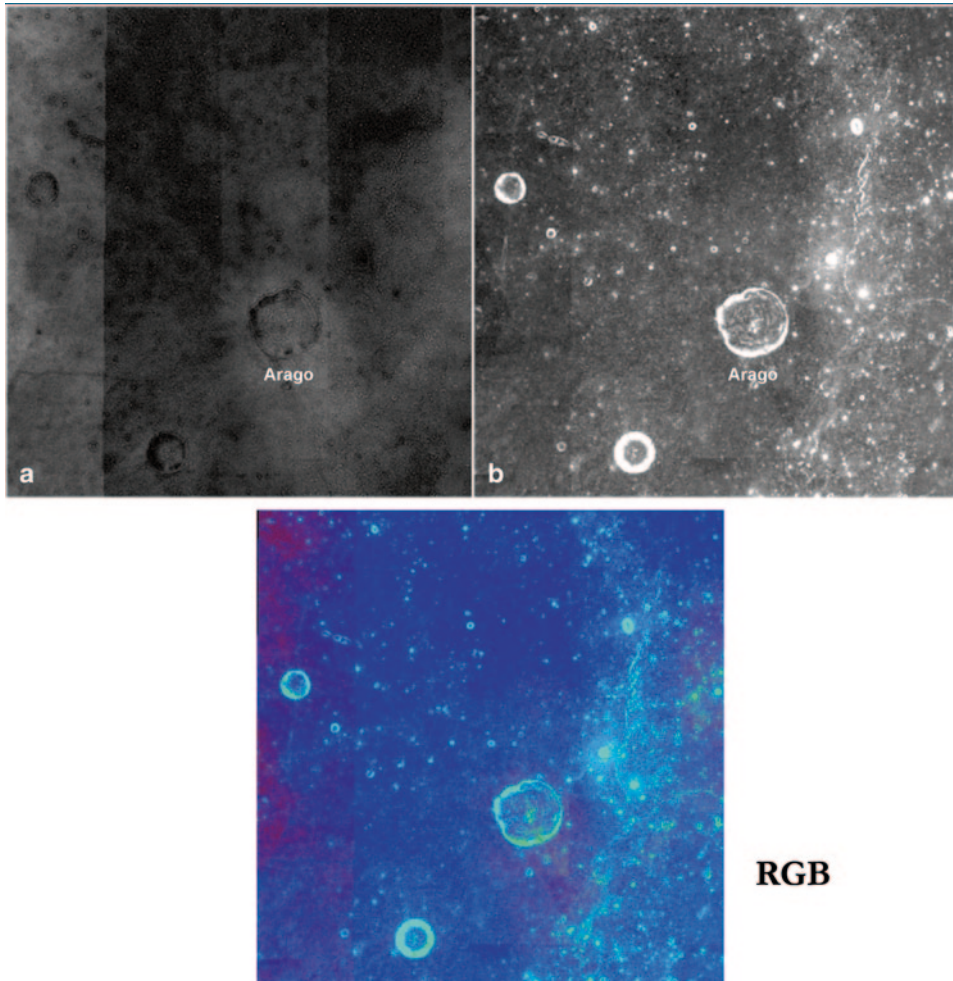


**Fig. 7.4** Clementine false color map of the region including Arago crater (USGS, <http://www.mapaplanet.org>). **a** Red channel ( $R_{750}/R_{415}$ ). **b** Green channel ( $R_{750}/R_{950}$ ). Blue channel in the RGB map is inverse of the red channel

0.67 and furthermore reveal a 750 nm reflectance of  $R_{750}=0.09$  and a weak mafic absorption with  $R_{950}/R_{750}$  about 1.57, suggesting a high soil maturity. Based on rheologic modelling (Sect. 2.5) we obtain for the low dome A1 an effusion rate of  $121 \text{ m}^3 \text{ s}^{-1}$ , magma viscosities of  $4.9 \times 10^3 \text{ Pa s}$ , and a duration of the effusion process of 0.08 years. In contrast, the two large domes A2 and A3 belong to class D. According to their more irregular shapes, they presumably formed during several stages of effusion, representing non-monogetic domes (cf. Sect. 5.2).

The three aligned domes termed A4–A6 are located north of the dome A2 (Fig. 1.5e) have diameters of  $11.1 \pm 0.3 \text{ km}$ ,  $8.4 \pm 0.3 \text{ km}$ , and  $9.5 \pm 0.3 \text{ km}$ , respectively. Their heights amount to  $65 \pm 10 \text{ m}$ ,  $45 \pm 5 \text{ m}$ , and  $50 \pm 5 \text{ m}$ , resulting in flank slopes of  $0.66 \pm 0.10^\circ$ ,  $0.59 \pm 0.10^\circ$ , and  $0.58 \pm 0.10^\circ$ . The edifice volumes correspond to  $3.2$ ,  $1.4$ , and  $1.8 \text{ km}^3$ . The

soil of these domes is spectrally bluish with high  $R_{415}/R_{750}$  spectral ratios of 0.67–0.68, indicating a high  $\text{TiO}_2$  content. Being typical representatives of class A, they show low flank slopes below  $1^\circ$ , implying low lava viscosities of about  $10^3$  Pa s, high effusion rates of about  $300 \text{ m}^3 \text{ s}^{-1}$ , and very short durations of the effusion process of 2–4 months.

The low lava viscosities may be partially due to the high  $\text{TiO}_2$  content but also, at least for the domes A1 and A4–A6, to a shallow depth of the magma reservoir, which prevents cooling and crystallisation of the magma during its fast ascent to the surface. Hence, these domes belong to rheologic group  $R_2$  and thus result from the eruption of hardly evolved basaltic magma. The dike model (Sect. 4.1) yields for these domes values of magma rise speed of about  $3 \times 10^{-3} \text{ m s}^{-1}$ , dike widths  $W$  of 3–5 m, and dike lengths  $L$  of 14–22 km. Wieczorek et al. (2006) determine a total crustal thickness of 32 km and an upper crustal thickness of 15 km for western Mare Tranquillitatis. Hence, the dike lengths of 14–22 km indicate that the magma that formed the domes A1 and A4–A6 originated from the border region between upper and lower crust.

Two further low domes termed Carrel 1 (Car1) and Arago 7 (A7) share similar characteristics (Table 7.1). The dome Car1 has a diameter of  $8.6 \pm 0.5$  km and is located inside the crater Carrel (also known as Jansen B). Lunar Orbiter imagery acquired under a moderate solar elevation angle does not show the dome clearly but a small positive relief on its flank is visible. It likely represents a pre-existing small peak surrounded by the dome-forming lava (Fig. 7.5b). The low dome A7 has a diameter of  $6.3 \pm 0.5$  km. According to their rheologic properties, the low domes Car1 and A7 (Fig. 7.5 and Table 7.1) belong to class A and to rheologic group  $R_2$ . They were formed by lava of viscosities between  $2 \times 10^3$  Pa s and  $4 \times 10^3$  Pa s, and the duration of the effusion process was only 0.07 years. According to the thicknesses of the total crust and the upper crust in northern Mare Tranquillitatis derived by Wieczorek et al. (2006), the magma reservoirs of A7 and Car1 are located in the upper crust.

**Domes in the Cauchy region** The region to the west and southwest of the craters Cauchy and Cauchy A in Mare Tranquillitatis is characterised by a large number of mare domes. Some of these domes show an alignment approximately parallel with respect to the graben Rima Cauchy and the fault Rupes Cauchy, which are in turn oriented approximately radially with respect to the center of the Imbrium basin (Fig. 7.6). These elongated structures may indicate a system of fractures that formed as a consequence of the Imbrium impact 3.85 Ga ago (Wilhelms 1987). A conspicuous alignment of mare domes, which also shows an orientation radial to the Imbrium basin, can be observed northwest of the crater Cauchy A (Fig. 1.5f). Rubin (1993b) points out that the orientation of a dike follows the field of crustal stress (Sect. 1.6.7), implying dike orientations in the Cauchy region radial to the Imbrium basin. According to the mechanism suggested by Head and Wilson (1996) and Petrycki and Wilson (1999), the formation of the domes may be due to the ascent of dikes to a depth below the surface which was so low that an eruption of lava could occur.

In the Cauchy region, the dome termed C11 is apparently associated with a part of a mare ridge (Fig. 7.7). Due to the gentle slope of its flank of  $0.60 \pm 0.15^\circ$ , its very elongated shape and the lack of a summit crater it is considered as a putative intrusive dome: we will describe it, together with the large and flat domes C9, C10, and C16, in the chapter about intrusive domes (Chap. 8).



**Table 7.1** Morphometric and rheologic properties of further domes described in the text, located in the region around Cauchy, in northern Mare Tranquillitatis, and in Mare Undarum near the crater Condorcet

Dome	Longi- tude (°)	Lati- tude (°)	$R_{750}$	$R_{415}/R_{750}$	$R_{950}/R_{750}$	Slope (°)	D (km)	h (m)	V (km <sup>3</sup> )	$\eta$ (Pa s)	E (m <sup>3</sup> s <sup>-1</sup> )	T (years)	U (m s <sup>-1</sup> )	W (m)	L (Km)
A7	24.12	11.28	0.0804	0.6794	1.0604	0.82	6.3	45	0.6	$3.7 \times 10^3$	317	0.07	$4.0 \times 10^{-3}$	4.2	19
Carl	27.13	10.19	0.0955	0.6402	1.0264	0.59	8.6	45	0.7	$1.8 \times 10^3$	356	0.07	$7.8 \times 10^{-3}$	3.2	14
C1	37.48	7.11	0.0863	0.6508	1.0588	0.35	8.1	25	0.7	$1.2 \times 10^2$	456	0.05	$6.7 \times 10^{-2}$	1.2	5.5
C4	36.78	8.85	0.0820	0.6621	1.0547	0.43	13.3	50	3.2	$1.0 \times 10^4$	615	0.17	$1.9 \times 10^{-2}$	2.7	12
C5	33.02	10.56	0.0902	0.6452	1.0489	1.03	11.1	100	5.4	$4.4 \times 10^4$	214	0.80	$3.5 \times 10^{-4}$	12	52
C6	31.97	10.76	0.0842	0.6558	1.0685	0.74	7.7	50	1.0	$3.8 \times 10^3$	206	0.15	$2.5 \times 10^{-3}$	4.3	19
C8	30.72	14.40	0.0975	0.6346	1.0465	2.50	12.5	270	17.0	$3.9 \times 10^6$	101	5.36	$7.6 \times 10^{-6}$	75	180
C12	37.20	12.37	0.0904	0.6165	1.0681	0.45	6.3	25	0.5	$2.2 \times 10^2$	405	0.04	$4.1 \times 10^{-2}$	1.5	6.9
C13	39.32	13.50	0.0867	0.6396	1.0686	1.00	11.0	95	5.0	$3.5 \times 10^4$	269	0.59	$5.4 \times 10^{-4}$	11	47
C14	33.92	10.62	0.0864	0.6437	1.0484	0.73	7.0	45	0.8	$2.9 \times 10^3$	278	0.14	$4.0 \times 10^{-3}$	3.8	17
C15	33.19	11.76	0.0896	0.6355	1.0542	0.48	13.0	55.0	3.6	$1.7 \times 10^3$	783	0.22	$1.6 \times 10^{-2}$	3.3	15
C17	32.44	12.49	0.0871	0.6434	1.0667	0.82	7.0	50.0	0.96	$4.8 \times 10^3$	250	0.18	$2.5 \times 10^{-3}$	4.7	21
NTA1	35.05	14.73	0.0999	0.5995	1.0520	0.34	17.1	50	3.9	$5.6 \times 10^2$	1016	0.12	$4.4 \times 10^{-2}$	2.3	10
NTA2	35.30	14.36	0.0942	0.6197	1.0488	0.70	5.7	35	0.6	$1.4 \times 10^3$	161	0.12	$4.4 \times 10^{-3}$	2.8	13
NTA3	36.13	14.01	0.1047	0.6152	0.9971	0.62	9.2	50	2.0	$2.5 \times 10^3$	294	0.21	$5.0 \times 10^{-3}$	3.6	16
NTA4	36.47	13.68	0.1052	0.6103	0.9916	0.62	8.3	45	0.8	$1.9 \times 10^3$	266	0.10	$5.6 \times 10^{-3}$	3.3	15
NTA5	36.72	13.57	0.0985	0.6046	1.0366	0.50	5.7	25	0.4	$2.8 \times 10^2$	226	0.05	$2.1 \times 10^{-2}$	1.5	6.9
NTA6	37.49	13.07	0.0942	0.6124	1.0570	0.49	7.0	30	0.6	$4.1 \times 10^2$	284	0.06	$2.9 \times 10^{-2}$	1.8	8.1
D	35.57	14.31	0.0937	0.6270	1.0482	1.31	6.1	70	1.1	$3.4 \times 10^4$	92	0.38	$1.9 \times 10^{-4}$	10	46
C7, G	35.86	14.23	0.0980	0.6161	1.0362	2.00	8.0	140	4.7	$4.9 \times 10^5$	80	1.88	$1.8 \times 10^{-5}$	32	141
Co1	70.30	7.05	0.1167	0.5746	1.0943	1.7	9.7	150	9.5	$4.3 \times 10^5$	89	3.40	$2.2 \times 10^{-5}$	30	133
Co2	70.64	6.78	0.1141	0.5709	1.0929	1.45	10.3	130	7.4	$1.9 \times 10^5$	172	1.40	$8.6 \times 10^{-5}$	21	94
Co3	70.93	6.67	0.1257	0.5783	1.0619	1.13	11.2	110	5.3	$6.8 \times 10^4$	309	0.54	$3.6 \times 10^{-4}$	14	62
Co4	70.30	6.72	0.1163	0.5697	1.0779	2.78	11.1	270	15.3	$5.2 \times 10^6$	102	4.80	$6.8 \times 10^{-6}$	84	178



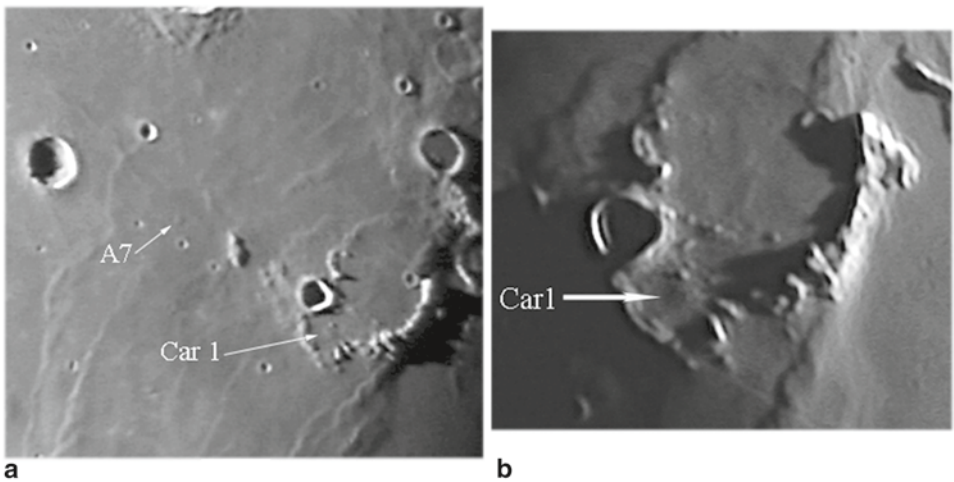


**Fig. 7.5** **a** Telescopic image of the domes A7 and Car1. (Image by KC Pau). **b** Telescopic image of Car1. (Image by G. Sbarufatti)

**Fig. 7.6** Telescopic CCD image of the Cauchy region. (Image by M. Wirths)

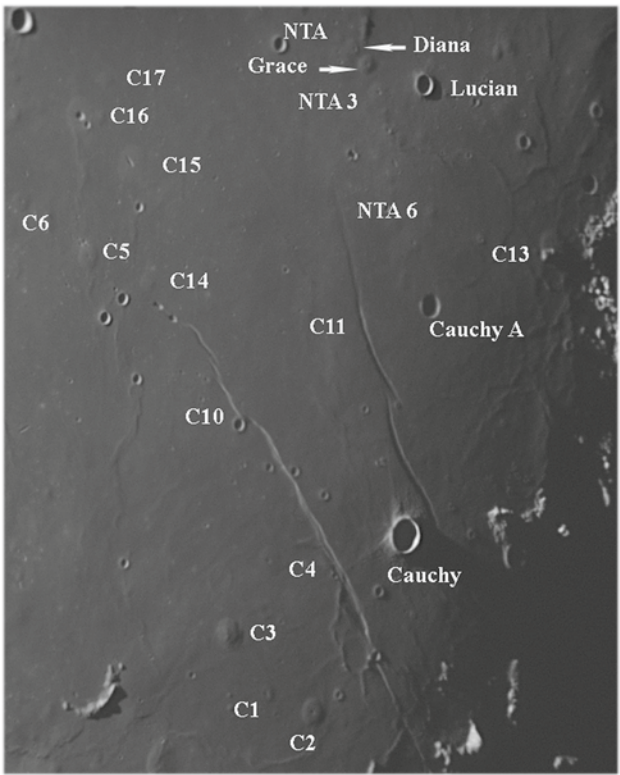


**Fig. 7.7** Telescopic images of the Cauchy region. (*Left* image by P. Lazzarotti; *right* image by C. Wöhler)

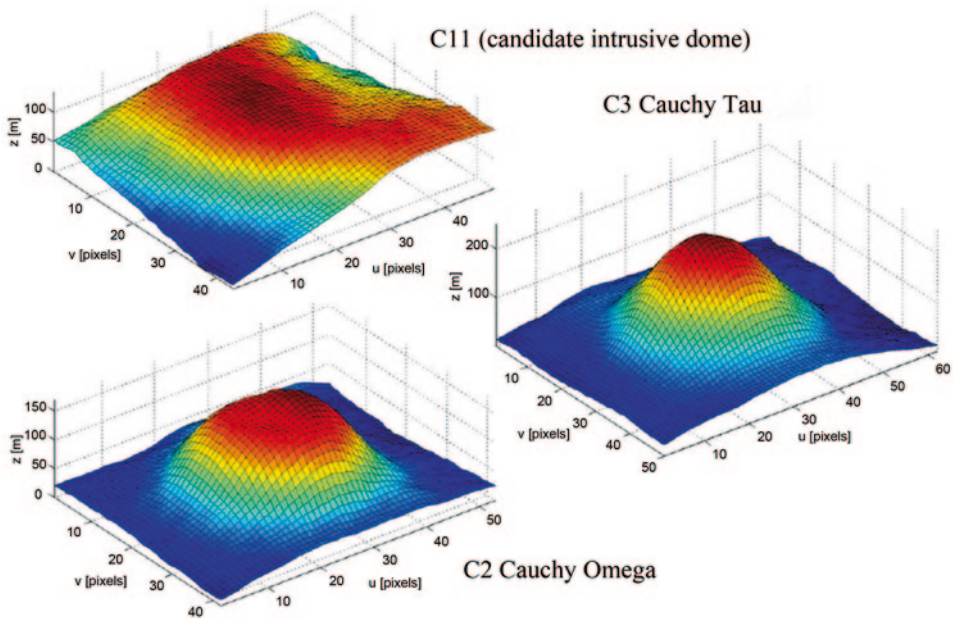
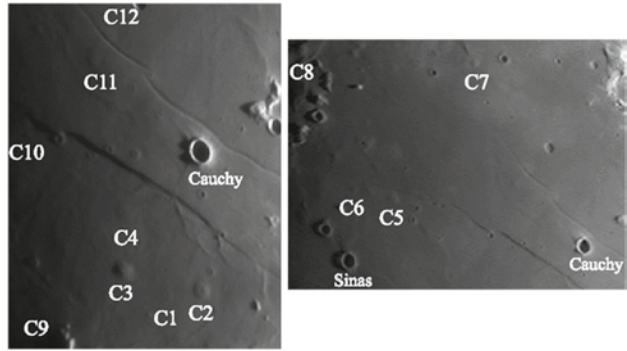


**Fig. 7.8** DEMs constructed for the domes C11, C2, and C3

Two well-known domes in this region are Cauchy  $\omega$  (C2) and  $\tau$  (C3). For the dome Cauchy  $\omega$  we determined a height of  $125 \pm 15$  m and a diameter of  $12.2 \pm 0.3$  km, corresponding to a flank slope of  $1.17 \pm 0.15^\circ$ . For the nearby dome Cauchy  $\tau$  we estimated a diameter of  $17.0 \pm 0.3$  km, a height of  $190 \pm 20$  m and a flank slope of  $1.28 \pm 0.14^\circ$  (Fig. 7.8). Another similar dome, termed C5, is located at  $38.32^\circ$  E and  $7.23^\circ$  N (Figs. 7.6, 7.9). The dome diameter amounts to  $11.1 \pm 0.5$  km and its height is determined to  $100 \pm 10$  m, resulting in flank slope of  $1.03 \pm 0.10^\circ$ . While the dome C3 does not have a summit vent (Fig. 7.10), C2 has a pronounced elongated vent. The vents of the domes C1, C4, C13 and C15 are clearly visible in the Lunar Orbiter and LROC WAC imagery. Clementine UVVIS spectral data indicate a  $R_{415}/R_{750}$  ratio of about 0.63–0.64, a 750 nm reflectance of 0.08–0.09, and a  $R_{950}/R_{750}$  ratio of about 1.05–1.06. With their inferred moderate lava viscosities of  $4.0 \times 10^4$ –

**Fig. 7.9** Telescopic image of the region north of the crater Sinas. (Image by J. Phillips)

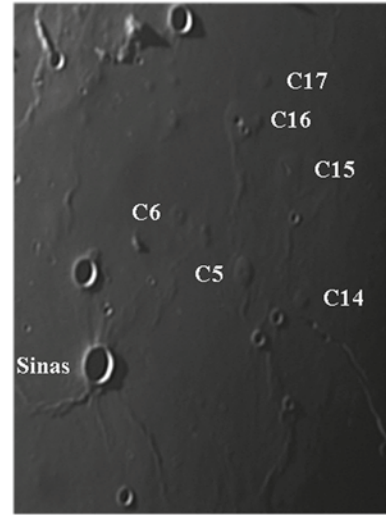
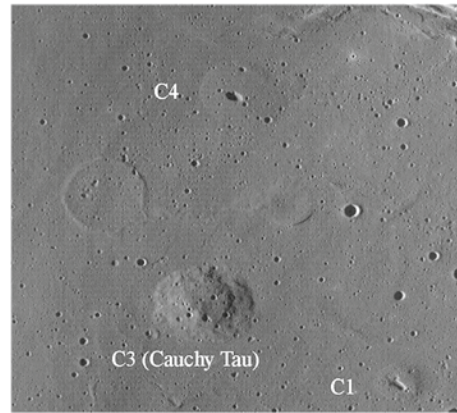


**Fig. 7.10** Section of LROC WAC image M117250291ME (NASA/GSFC/Arizona State University), showing the domes C1, C3, and C4



$3.4 \times 10^5 \text{ Pa s}$  and effusion rates of about  $260 \text{ m}^3 \text{ s}^{-1}$ , the domes C2, C3, and C5 share the properties of rheologic group  $R_1$  and belong to dome class  $C_2$  introduced in Chap. 5.

The magma rise speed obtained according to Sect. 4.1 amounts to several  $10^{-4} \text{ m s}^{-1}$ , and the feeder dikes were several tens of metres wide and between 50 and 120 km long. Other low domes situated in the Cauchy region, termed C1, C4, C6, C14, C15 and C17 (Table 7.1 and Figs. 7.6, 7.9, 7.11), show the characteristic properties of class A domes with small edifice volumes and high  $R_{415}/R_{750}$  ratios and belong to rheologic group  $R_2$ .

The inferred rheologic results indicate magma rise speed of  $10^{-2}$ – $10^{-3} \text{ m s}^{-1}$ , while the feeder dikes were only 1–5 m wide and 5–20 km long. The magma source regions are thus located in the upper crust, which is 32 km thick in this region (Wieczorek et al. 2006).

The dome C13 (Table 7.1) displays a summit vent and two protrusions which are probably pre-existing non-volcanic hills (Fig. 7.6). It is of subclass  $C_2$  with a tendency towards

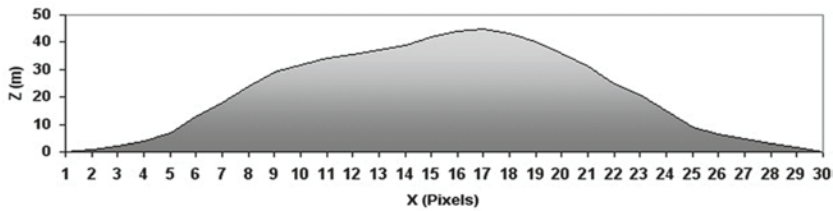


**Fig. 7.11** Cross-sectional profile of C14 in east-west direction

class A due to its somewhat larger diameter and high edifice volume and belongs to rheologic group  $R_1$ . The dome-forming magma ascended at a speed of  $5.4 \times 10^{-4} \text{ m s}^{-1}$  through a dike 11 m wide and 47 km long. Hence, for C13 the magma reservoir is located in the lower crust, regarding the thicknesses of the total and the upper crust of 55 and 32 km, respectively, in northern Mare Tranquillitatis (Wieczorek et al. 2006).

The dome C8 is another representative of class  $C_2$ . It has high a flank slope of  $2.5^\circ$ , implying a high lava viscosity of  $10^6 \text{ Pa s}$ , an effusion rate of  $100 \text{ m}^3 \text{ s}^{-1}$ , and thus a duration of the effusion process of more than 5 years. The magma that formed this relatively steep mare dome presumably originated from the lunar mantle and ascended through a dike of 180 km length.

The vents of C1, C4, C13, and C15 are all elongated in about the same direction. This direction is approximately radial to Mare Imbrium and is furthermore parallel to Rima and Rupes Cauchy and also to the direction in which the eight domes in northern Mare Tranquillitatis are aligned. This vent elongation may thus be explained by the formation along crustal fractures model (Sect. 1.6.7).

**Domes of the Northern Tranquillitatis Alignment (NTA)** North of Rima Cauchy, an alignment of lunar mare domes is situated, which we termed Northern Tranquillitatis Alignment (NTA). These aligned domes include the well-known edifices Diana (D) and Grace (C7) as well as at least six more unnamed domes (Figs. 1.5g, 7.6). This particular alignment of domes extending just at the southern end of Mons Esam is not visible in Lunar Orbiter and Clementine images but only in telescopic CCD images acquired at very low solar altitude. The domes Diana (D in Table 7.1) and Grace (C7 in Table 7.1) are described by Weitz and Head (1999) using topographic maps derived from Apollo 15–17 orbital stereo imagery. We obtained height values of  $70 \pm 10 \text{ m}$  and  $140 \pm 15 \text{ m}$  for Diana and Grace, respectively. Grace (C7) belongs to class  $C_2$ , while its neighbour Diana with its smaller diameter, lower flank slope, and very low edifice volume (Table 7.1 and Fig. 5.3) is intermediate between classes A,  $C_2$ , and  $E_2$ .

For Diana the inferred dike length (cf. Sect. 4.1) of 46 km indicates that the magma reservoir is located in the lower crust. In contrast, the magma that formed Grace originated from the mantle through a dike of 140 km length. The large but very low dome NTA1 is a typical class C representative with respect to its morphometric properties, consists of

material of intermediate  $R_{415}/R_{750}$  ratio and is situated between classes  $C_1$  and  $C_2$ . Due to their small diameters below 6 km and low flank slopes, the domes NTA2 and NTA5 are intermediate objects between classes A and  $E_2$  (Fig. 5.3). The domes NTA3 and NTA4 are smaller and have moderate diameters typical of class  $B_2$  and low flank slopes typical of class  $C_1$ , such that they are situated between these two classes (Fig. 5.3). Dome NTA6 displays morphometric properties typical of class A, but it is located near the margin of class A towards class  $E_2$  due to its spectrally atypically red surface. Another exemplar of class  $E_2$  is represented by the low dome C12, characterized by a circular shape with a base diameter of 6.3 km, a flank slope of only  $0.45^\circ$  and a small edifice volume of  $0.5 \text{ km}^3$  (Table 7.1 and Fig. 7.7). The domes NTA1–NTA6 and C12 are characterized by low lava viscosities between  $10^2$  and  $10^3 \text{ Pa s}$ , high effusion rates that may still exceed those inferred for rheologic group  $R_1$  (up to  $1,000 \text{ m}^3 \text{ s}^{-1}$ ), and very short durations of the effusion process between 2 and 10 weeks (cf. Sect. 2.5).

To date, mare domes like those examined in our studies, which were formed by lavas of high  $\text{TiO}_2$  content and low viscosity ascending at high speeds through narrow dikes, have only been found in Mare Tranquillitatis and in Mare Vaporum near Hyginus.

### 7.1.2 Mare Vaporum and Hyginus

The surface of Mare Vaporum is to some extent superposed by Imbrium ejecta. In the southeastern part of Mare Vaporum, pyroclastic deposits can be observed (Gaddis et al. 2003). The prominent Hyginus rille in Mare Vaporum is interpreted by Head and Wilson (1996) as a graben that was formed by a dike which ascended to a depth of 1.5–2 km below the surface. An inconspicuous linear rille of 80 km length is apparent just south of the crater Manilius (Fig. 7.12a, b). Its orientation is approximately parallel to the much more impressive nearby Ariadaeus rille and radial with respect to the Imbrium basin.

A low dome termed Hyginus 1 (Hy1) located at  $08.26^\circ \text{ E}$  and  $10.52^\circ \text{ N}$  is situated in a complex volcanic region characterised by pyroclastic material and hummocky terrain. It is  $9.3 \pm 0.5 \text{ km}$  in diameter and has a summit crater. Its height amounts to  $70 \pm 10 \text{ m}$ , corresponding to an average flank slope of  $0.86 \pm 0.20^\circ$ . The dome edifice volume is  $2.2 \text{ km}^3$ . The low slope and edifice volume of the dome Hy1 yield a high effusion rate of  $218 \text{ m}^3 \text{ s}^{-1}$ , a low lava viscosity of  $1.2 \times 10^4 \text{ Pa s}$ , and a short duration of the effusion process of only 0.32 years or less than 4 months (cf. Sect. 2.5). The Clementine UVVIS data reveal that the dome appears spectrally blue with  $R_{415}/R_{750} = 0.62$ , indicating a moderate  $\text{TiO}_2$  content. Hence, Hy1 belongs to class A. The reflectance spectrum of the dome is intermediate between the dark and smooth mare unit to the west and that of the hummocky terrain, which is of higher reflectance. A possible explanation for this observation is that lateral mixing of basaltic mare lava and highland material excavated by impacts of nearby craters (Li and Mustard 2000) occurred, leading to an intermediate spectrum.



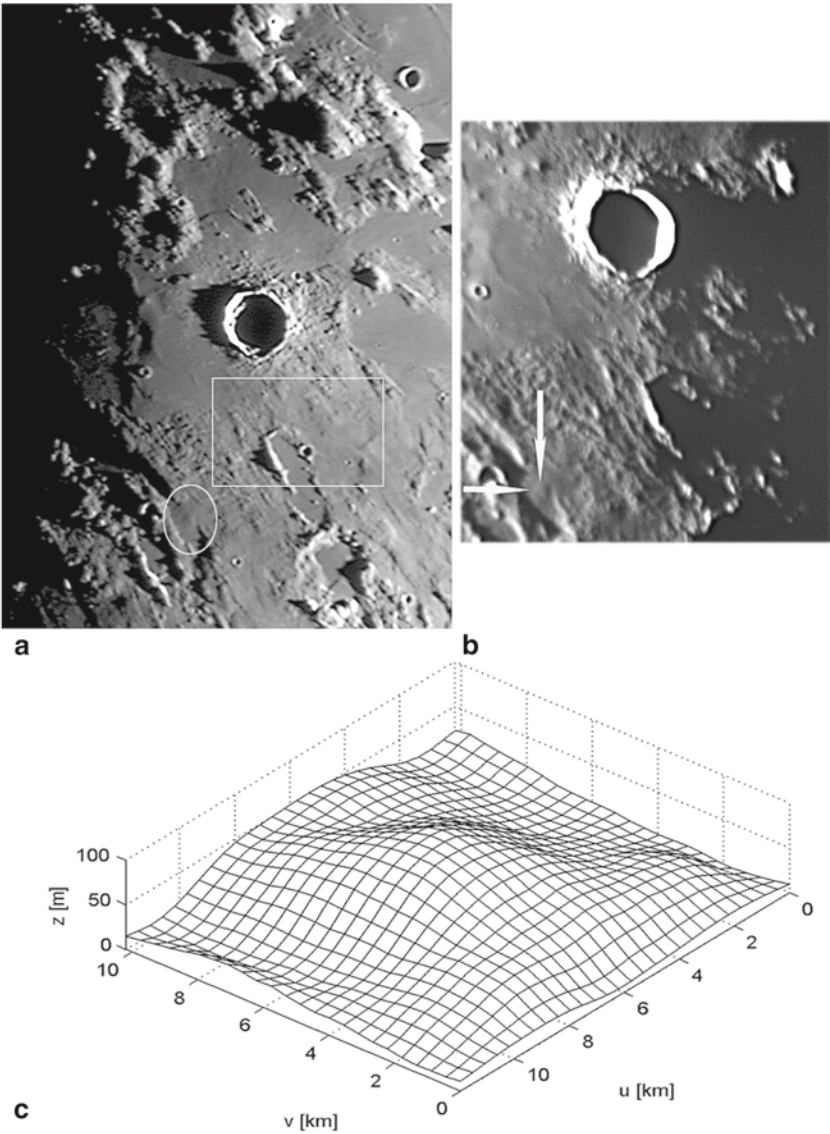


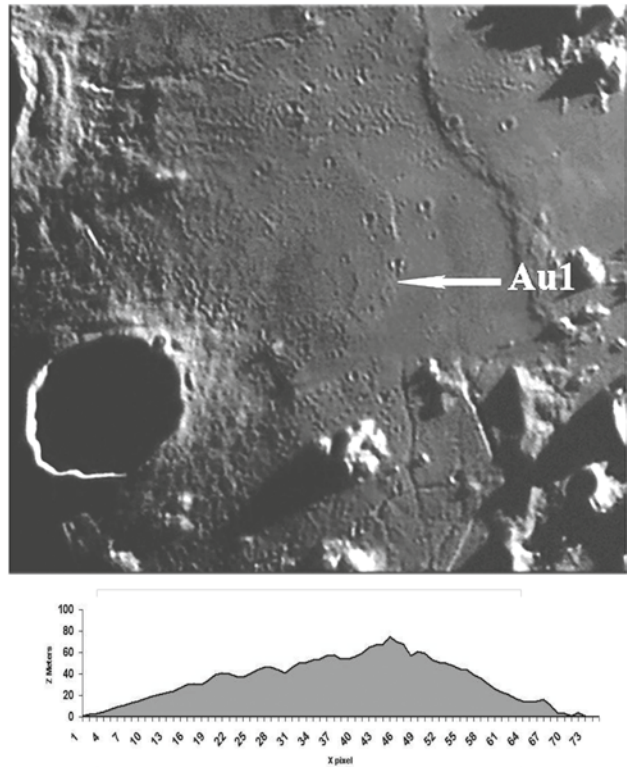
**Fig. 7.12** **a** Telescopic image of Hy1 and the rille south of the crater Manilius. (Image by K. C. Pau). **b** Telescopic image of Hy1. (Image by K. C. Pau). **c** DEM of the dome Hy1

### 7.1.3 Autolycus

Another large and low dome is situated at  $3.82^{\circ}$  E and  $30.50^{\circ}$  N in Mare Imbrium, east of the crater Autolycus. This dome, termed Autolycus 1 (Au1), is detectable only in telescopic CCD images acquired at low solar elevation (Fig. 7.13). The elevation difference between



**Fig. 7.13** Telescopic image of Au1 (*top*). (Image by P. Lazzarotti). Cross-sectional profile of the dome Au1 (*bottom*)



the dome centre and its western border inferred from the LOLA DEM corresponds to about 70 m and may be regarded as an approximate value of the dome height.

We have also generated a cross-sectional profile of the dome based on a telescopic CCD image. The base diameter amounts to  $28.0 \pm 0.3$  km and its height is determined to  $75 \pm 10$  m, resulting in a flank slope of  $0.31 \pm 0.03^\circ$ . The edifice volume corresponds to  $23 \text{ km}^3$ . The Clementine UVVIS spectral data of the dome reveal a moderate value of the UV/VIS colour ratio of  $R_{415}/R_{750} = 0.6012$ . According to the parameters described in Chap. 5, the circularity of the dome of 0.99 should be attributed to an effusive construct. Regarding Au1 as an effusive dome would imply to assign it to the effusive class  $C_1$ . Based on rheologic modelling (Sect. 2.5) we obtain a high effusion rate of about  $2,700 \text{ m}^3 \text{ s}^{-1}$ , a low magma viscosity of  $1.2 \times 10^3 \text{ Pa s}$ , and a duration of the effusion process of 0.24 years. For the “default” vertical pressure gradient of  $dp/dz = 328 \text{ Pa m}^{-1}$ , the dike model (Sect. 4.1) yields a high magma rise speed of  $5.5 \times 10^{-2} \text{ m s}^{-1}$ , a dike width of 5.5 m, and a length of 15 km.

#### 7.1.4 Meton

North of Mare Frigoris, the so-called “highland plains” or “light plains” are located, which are described by Lucchitta (1978) and reported in USGS map I-1062 as smooth surface. Koehler et al. (1999, 2000) spectrally distinguish two units characterized by highland-

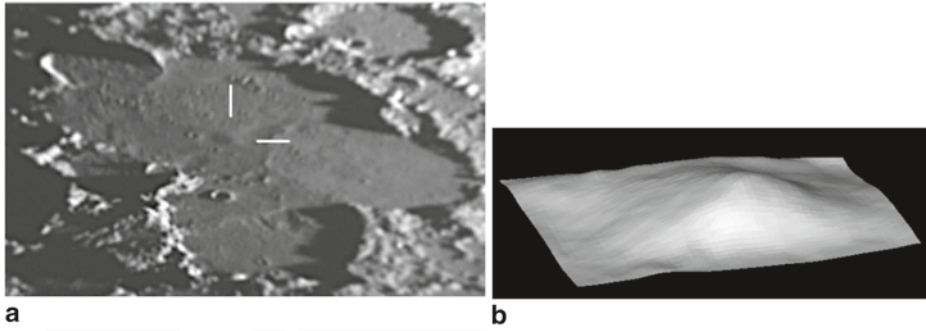
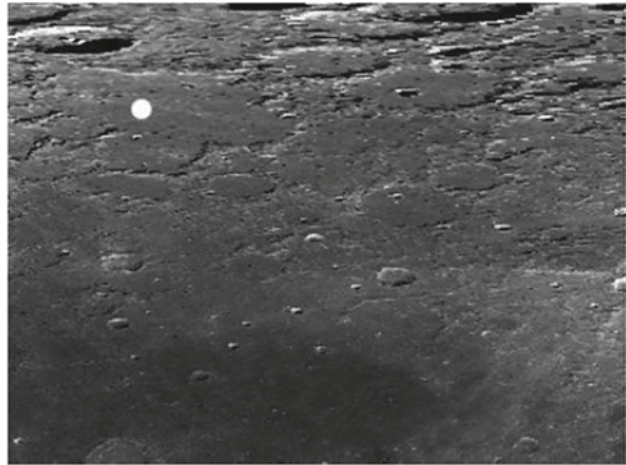


**Fig. 7.14** **a** Telescopic image of Met1. (Image by J. Phillips). **b** 3D reconstruction result for the dome Met1

**Fig. 7.15** Clementine 750 nm image of the crater Meton and the region north of Mare Frigoris (USGS, <http://www.mapaplanet.org>). The dome Meton 1 is marked by a *white dot*



like and mare-like properties, respectively. The mare-like component is associated with the basaltic plains of Mare Frigoris. Koehler et al. (2000) conclude that older basalts (cryptomaria) may be covered by the light plains. However, they point out that this would imply the presence of dark-haloed impact craters which have not been detected in this region. Kramer et al. (2009) show that the basaltic plains of Mare Frigoris are characterized by an exceptionally low Fe and high Al content and therefore presumably consist of high-alumina mare basalts.

On the floor of the crater Meton located in the northern light plains region, an elusive domical structure can be observed. The selenographic position of this dome, termed Meton 1 (Met1), is  $19.73^\circ$  E and  $73.02^\circ$  N (Figs. 7.14, 7.15). The dome diameter corresponds to  $14.5 \pm 0.5$  km and its height to  $90 \pm 10$  m, resulting in an average flank slope of  $0.71 \pm 0.10^\circ$ . The dome volume amounts to  $4.5 \text{ km}^3$ . Accordingly, the rheologic model yields a magma viscosity of  $1.4 \times 10^4 \text{ Pa s}$ , an effusion rate of  $1,900 \text{ m}^3 \text{ s}^{-1}$ , and a short duration of the effusion process of 0.07 years, i.e. about a month. Based on the dike model

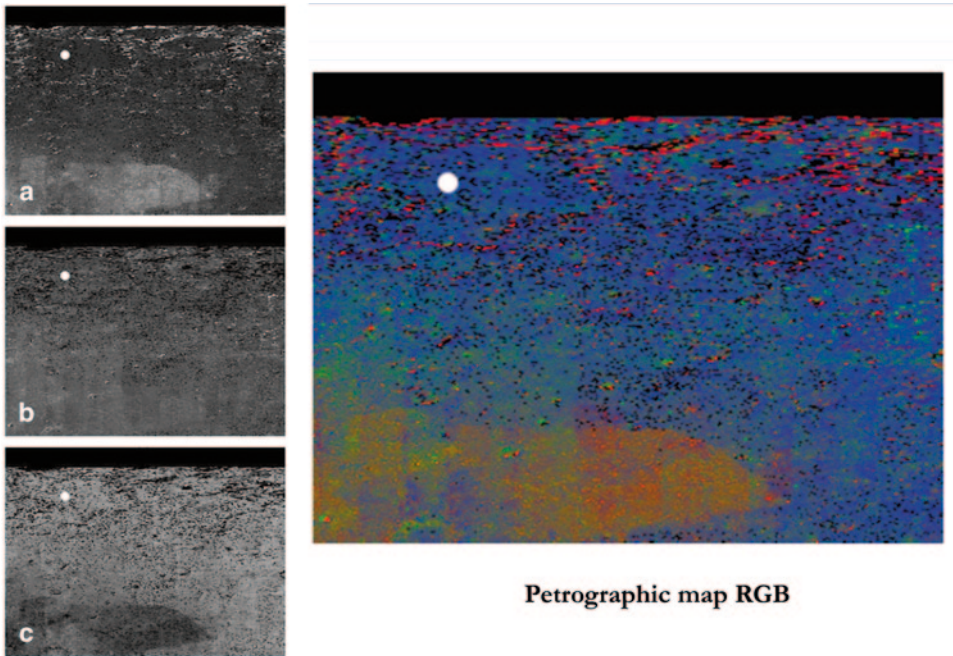


**Fig. 7.16** Petrographic map. The dome Meton 1 is marked by a *white dot*. Relative content of **a** mare basalt, **b** Mg-rich rock (*green channel*), **c** ferroan anorthosite (FAN, *blue channel*) and the corresponding RGB image

outlined in Sect. 4.1, a magma rise speed of  $7.3 \times 10^{-3} \text{ m s}^{-1}$ , a width of the feeder dike of 7.7 m and a length of 34 km can be inferred. When assuming a vertical extension of the dome-forming dike comparable to its inferred length (Jackson et al. 1997), the origin of the dome material is in the lower lunar crust. According to its morphometric properties, the viscosity of the dome-forming magma, and the dike geometry, Meton 1 belongs to class B<sub>2</sub>, like some domes observed in western Mare Crisium and Mare Undarum described in Sects. 7.1.9, 7.1.11.

The continuum-removed spectrum of the dome Meton 1 shows a shallow and narrow absorption trough with a minimum at 940 nm and a FWHM of 170 nm, which is presumably due to pyroxene of moderate Ca content. The overall shape of the spectrum is highland-like, but the Clementine reflectance at 750 nm is lower than the values of nearby highland terrain on the rim of Meton (0.20 vs. 0.31).

The petrographic map reveals a high content of Mg-rich rock (Fig. 7.16b). The Al abundance map in Fig. 7.17 shows that the basalts of eastern mare Frigoris have an extraordinarily high Al content, as the contrast between them and the adjacent highland terrain to the east is unusually low. This supports the conclusion by Kramer et al. (2009) that Mare Frigoris is characterized by compositionally exceptional high-alumina basalts.

According to Fig. 7.17, the inferred Al and Mg abundances of the dome Meton 1 are fairly similar to those of the Frigoris basalts (14.6 and 5.0 wt% vs. 11.5 and 6.7 wt%), while



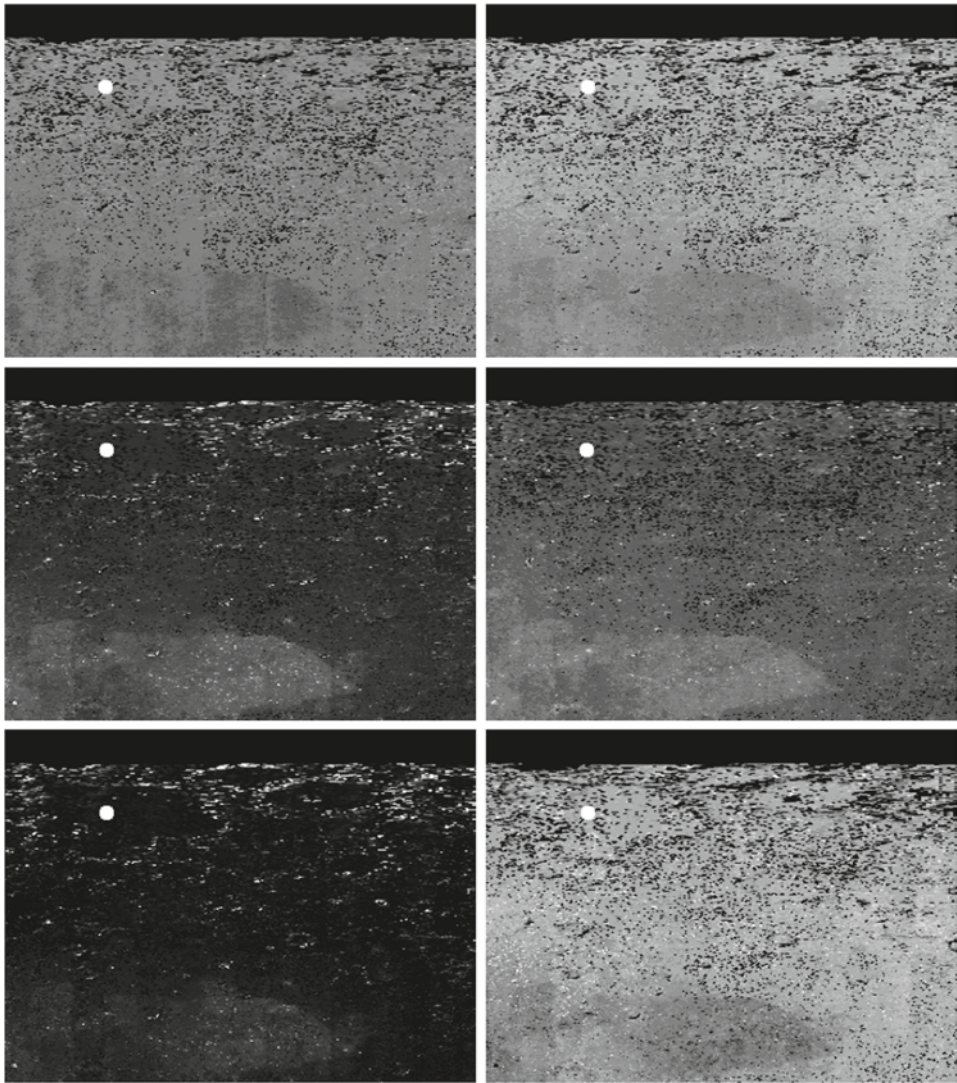


**Fig. 7.17** Elemental abundance maps of (per row, *top left to bottom right*) Ca (grey value range 2–18 wt%), Al (0–20 wt %), Fe (0–25 wt%), Mg (0–16 wt%), Ti (0–6 wt%), and O (40–47 wt%). Spatial resolution is  $0.1^\circ$  ( $\sim 3$  km). In each map the dome Meton 1 is marked by a *white dot*

its Fe and Ti abundances are much lower (3.8 and 0.2 wt% vs. 8.1 and 0.8 wt%). Hence, the composition of the dome-forming material is not typical of mare basalt due to its high Al and low Fe and Ti content. Hence, our results suggest the occurrence of a possibly non-mare volcanic episode in the region north of Mare Frigoris. The petrographic map reveals that the Mg-rich rock fractions are similar for the dome Meton 1 and the Frigoris basalts, while the mare basalt fraction of the dome is lower and its ferroan anorthosite fraction is higher.

**Fig. 7.18** Telescopic image of the dome Piccolomini 1 (Pi1). (Image by P. Lazarotti)

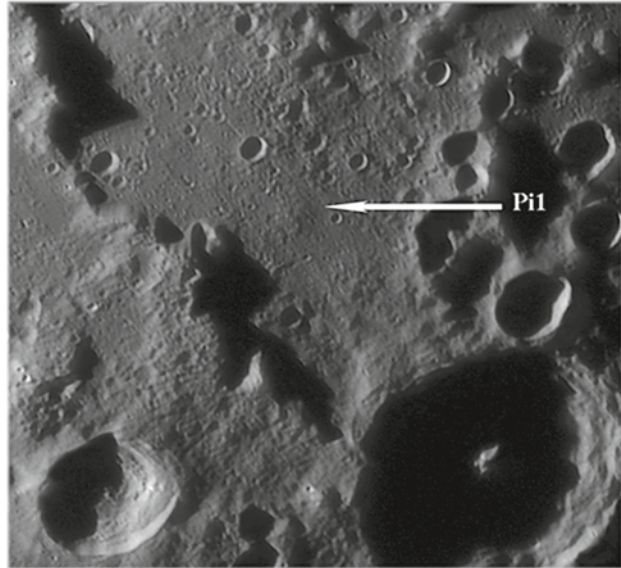
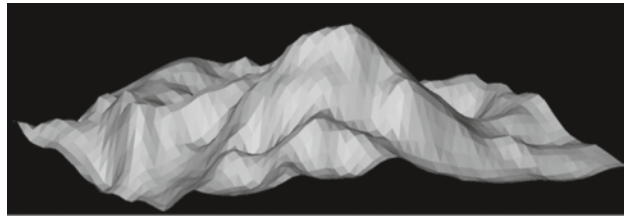


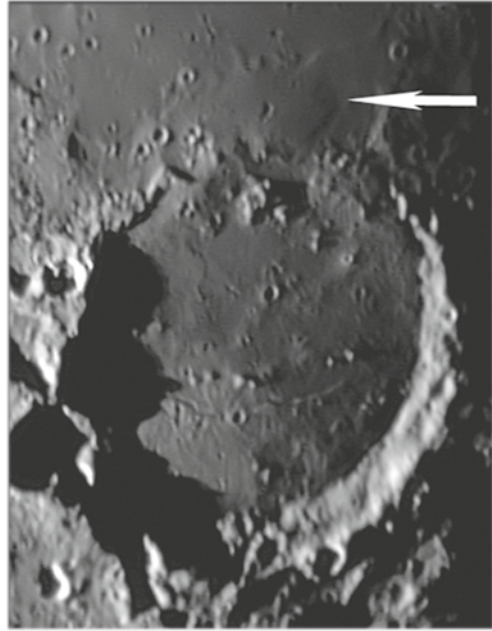
**Fig. 7.19** DEM of the dome Pi1 view from southwestern direction. The vertical axis is 15 times exaggerated



### 7.1.5 Rupes Altai and Piccolomini

Another prominent dome is located northwest of the crater Piccolomini at longitude  $28.56^\circ$  E and latitude  $27.46^\circ$  S (Fig. 7.18), in the Nectaris basin on the lower side of Rupes Altai. The dome, termed Piccolomini 1 (Pi1), has a diameter of  $14.0 \pm 0.3$  km and its summit appears to be degraded. The height of Pi1 amounts to  $350 \pm 50$  m, resulting in a flank slope of  $2.90 \pm 0.30^\circ$  (Fig. 7.19). The edifice volume has been determined to  $17.9 \text{ km}^3$ . For the surface around the dome Pi1, Clementine UVVIS imagery reveals a spectrally red appearance with  $R_{415}/R_{750} = 0.5920$ , indicating a low  $\text{TiO}_2$  content, and a high  $R_{950}/R_{750}$  ratio of 1.0866, similar to the nearby highland area. The dome Pi1 belongs to class  $B_1$  and to rheologic group  $R_3$  due to its high lava viscosity of  $1.0 \times 10^7 \text{ Pa s}$ , effusion rate of  $208 \text{ m}^3 \text{ s}^{-1}$ , and long duration of the effusion process of 2.7 years (cf. Sect. 2.5). The magma ascended at a speed of  $7.9 \times 10^{-6} \text{ m s}^{-1}$  through a dike of 163 m width and 159 km length (cf. Sect. 4.1). Hence, the dome was formed by magma of high viscosity, ascending at low speed from a magma reservoir located deeply below the lunar crust.

**Fig. 7.20** Telescopic CCD image of the dome Fracastorius 1 (Fr1) (*arrow*). (Image by M. Whirts)



### 7.1.6 Fracastorius

Fracastorius is a crater of 124 km diameter whose nearly invisible northern rim overlaps with the plains of Mare Nectaris (Rükl 1999). Immediately north of the relicts of the northern crater wall lies a large and elongated lunar dome termed Fracastorius 1 (Fr1, located at  $33.02^\circ$  E and  $18.94^\circ$  S; Fig. 7.20). The diameter has been determined to  $37.0 \times 27.0 \pm 1$  km. A summit vent is well detectable, for which we estimated a diameter of  $3.6 \pm 0.4$  km.

Our estimation of the dome height derived by photoclinometry indicates a height of  $340 \pm 50$  m near the vent and  $440 \pm 50$  m at the highest point, south of the vent. This dome is very large and has a flat surface with a relatively steep margin. The average flank slope amounts to about  $1^\circ$  near the vent, but parts of the eastern flank are steeper than  $2.7^\circ$ . Shadow length measurements carried out on the northern and southern part of the eastern flank yield height differences of  $300 \pm 50$  m and  $190 \pm 50$  m, respectively. In the LOLA DEM, the elevation difference between the dome centre and its eastern border corresponds to about 290 m and may be regarded as an approximate value of the dome height. In fact, with the LOLA DEM it is not always possible to measure dome heights unambiguously, due to the unclear definition of the surrounding surface relative to which the height is measured. Clearly these data can be improved by new future observations and measurements.

Clementine UVVIS spectral data of Fr1 indicate a  $R_{415}/R_{750}$  ratio of 0.6010, a 750 nm reflectance of 0.1273, and a  $R_{950}/R_{750}$  ratio of 1.0647. The dome belongs to class D and

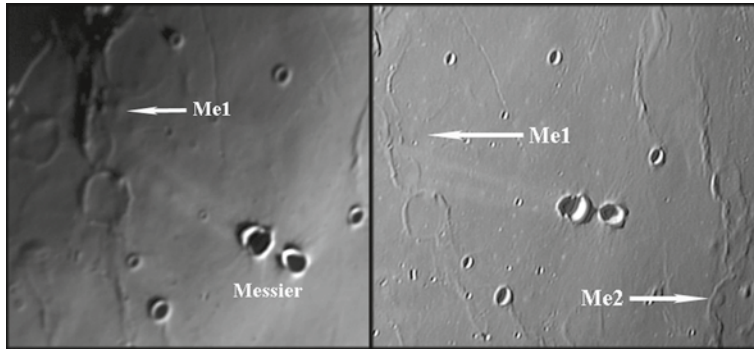


**Fig. 7.21** Telescopic image of Me1 (*left*). (Image by J. Phillips). Telescopic image of two domes Me1 and Me2 (*right*). (Image by G. Sbarufatti)

probably represents a non-monogetic dome likely formed during several stages of effusion, similar to the domes A2 and A3 near Arago described in Sect. 5.2.

### 7.1.7 Mare Fecunditatis

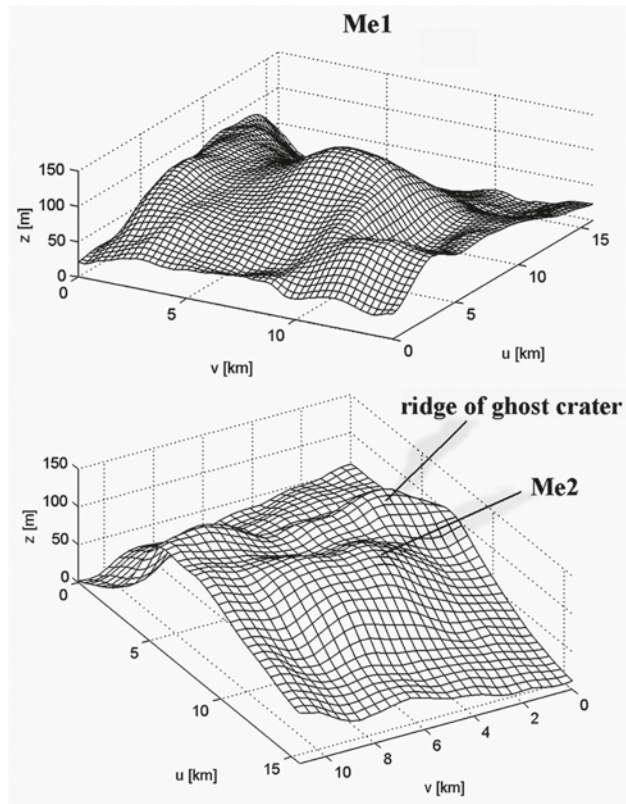
The stratigraphy of Mare Fecunditatis is described by Rajmon and Spudis (2000), who state that it is older than the Nectaris basin. Based on Clementine UVVIS imagery, they find that the mare material is relatively thin and most of it consists of low-titanium basalt while several smaller regions have a high Ti content. According to Whitford-Stark (1986), the Luna 16 sample-return mission has shown that the basalts of Mare Fecunditatis are of variable composition, as both Al-rich and Fe-rich basalts were found.

Based on telescopic CCD images of Mare Frigoris, two domes have been identified (Fig. 7.21), termed Messier 1 (Me1), located at longitude 43.47° E and latitude 1.95° S with a diameter of  $7.7 \pm 0.5$  km, and Messier 2 (Me2), situated at the inner rim of an unnamed ghost crater. Me2 is located at longitude 50.42° E and latitude 2.5° S with a base diameter of  $8.7 \times 6.4 \pm 0.5$  km and a central pit.

The constructed DEMs indicate heights of  $85 \pm 10$  m and  $80 \pm 10$  m, resulting in average flank slopes of  $1.26 \pm 0.10^\circ$  and  $1.12 \pm 0.10^\circ$  for Me1 and Me2, respectively (Fig. 7.22). The edifice volumes are determined to 4.1 and 2.8 km<sup>3</sup>. The Clementine UVVIS data indicate for Me1 a 750 nm reflectance of  $R_{750} = 0.1047$ , a moderate value for the UV/VIS colour ratio of  $R_{415}/R_{750} = 0.6007$ , indicating a moderate TiO<sub>2</sub> content, and a weak mafic absorption with  $R_{950}/R_{750} = 1.0458$ . The spectral data reveal similar spectral properties for the dome Me2 with a 750 nm reflectance of  $R_{750} = 0.1004$ , a moderate value of the UV/VIS colour ratio of  $R_{415}/R_{750} = 0.6138$ , and a weak mafic absorption with  $R_{950}/R_{750} = 1.0404$ . For both domes, rheologic modelling (Sect. 2.5) yields effusion rates of 122 m<sup>3</sup> s<sup>-1</sup> (Me1) and 148 m<sup>3</sup> s<sup>-1</sup> (Me2), respectively. They were formed from lava of moderate viscosities of  $4.9 \times 10^4$  Pa s and  $3.1 \times 10^4$  Pa s over periods of time of 0.55 and 0.60 years, i.e. about 7 months.



**Fig. 7.22** DEMs of the domes Me1 and Me2



Both domes, which are similar to each other with respect to their morphometric, rheologic, and spectral properties, belong to class  $C_2$  with a tendency towards class  $C_1$  due to their moderate  $R_{415}/R_{750}$  value. With their inferred moderate lava viscosities these domes share the properties of rheologic group  $R_1$ . Accordingly, the inferred magma rise speed amounts to several  $10^{-4} \text{ m s}^{-1}$  and their feeder dikes were 10–12 m wide and 45–54 km long.

### 7.1.8 Vendelinus

The degraded crater Vendelinus is situated adjacent to Mare Fecunditatis to the east. The crater Lohse (indicated in Fig. 7.23) is located just north-northwest of Vendelinus (Rükl 1999).

We have identified two domes (Fig. 7.23), termed Vendelinus 1 (Ve1), located at longitude  $57.83^\circ \text{ E}$  and latitude  $15.74^\circ \text{ S}$  with a diameter of  $16.8 \pm 0.6 \text{ km}$ , and Vendelinus 2 (Ve2), located at  $59.00^\circ \text{ E}$  and  $17.75^\circ \text{ S}$  with a diameter of  $13.5 \pm 0.6 \text{ km}$ . The constructed DEMs indicate heights of  $80 \pm 10 \text{ m}$  and  $30 \pm 10 \text{ m}$ , resulting in average flank slopes of  $0.55 \pm 0.07^\circ$  and  $0.25 \pm 0.10^\circ$  for Ve1 and Ve2, respectively (Fig. 7.24a–b). Despite their very

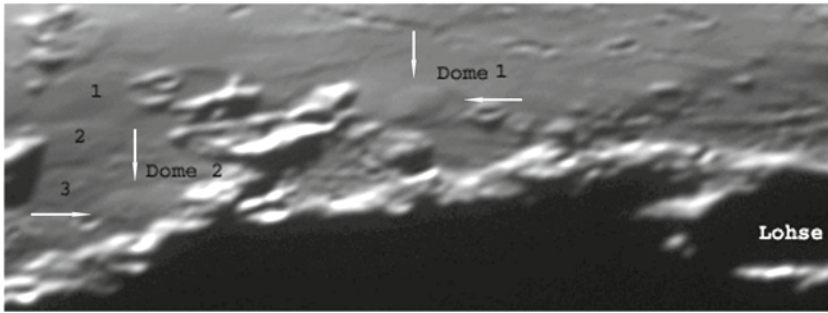


**Fig. 7.23** Telescopic image of the region west of Vendelinus. North is to the right. (Image by J. Phillips)

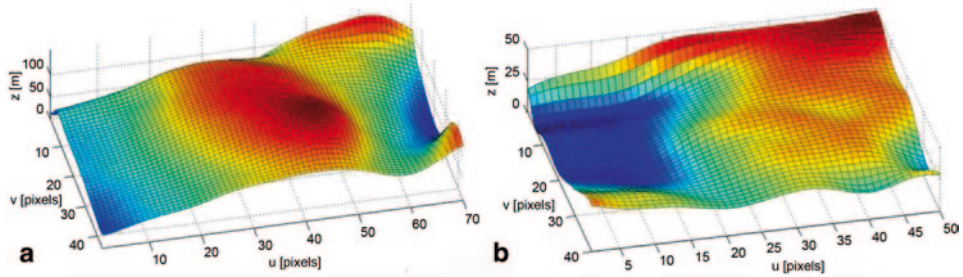


**Fig. 7.24** a DEM of the dome Ve1. b DEM of the dome Ve2

low flank slopes, the domes Ve1 and Ve2 are presumably no intrusive structures as their circularity exceeds 0.9. The edifice volumes are determined to 7.2 and 2.1 km<sup>3</sup>. The Clementine UVVIS spectral data reveal for Ve1 a 750 nm reflectance of  $R_{750}=0.1410$ , a moderate value for the UV/VIS colour ratio of  $R_{415}/R_{750}=0.5913$ , and a weak mafic absorption with  $R_{950}/R_{750}=1.0628$ . The spectral data show similar spectral properties for the dome Ve2 with a 750 nm reflectance of  $R_{750}=0.1589$ , a moderate value for the UV/VIS colour ratio of  $R_{415}/R_{750}=0.6038$ , and a weak mafic absorption with  $R_{950}/R_{750}=1.0567$ . Moreover, several other dome-like features are located to the southwest of crater Vendelinus (Fig. 7.23, structures labelled as 1–3), which might be very low intrusive swells. The rheologic model (Sect. 2.5) yields for Ve1 an effusion rate of 613 m<sup>3</sup> s<sup>-1</sup>, while for Ve2 the effusion rate amounts to 1,056 m<sup>3</sup> s<sup>-1</sup>. They were formed from lava of low viscosities of  $5.6 \times 10^3$  Pa s and  $8.6 \times 10^1$  Pa s over periods of time of 0.37 and 0.06 years, respectively. Both domes, which are similar to each other with respect to their morphometric, rheologic, and spectral properties, belong to class C<sub>1</sub>. According to the model described in Sect. 4.1, for the dome Ve1 the magma ascended at a speed of  $5.3 \times 10^{-3}$  m s<sup>-1</sup> through a dike 5 m wide and 23 km long. For the low dome Ve2, a high magma rise speed of  $1.5 \times 10^{-1}$  m s<sup>-1</sup>, a width of the feeder dike of only 1 m and a length of only 6 km can be inferred.

**Fig. 7.25** **a** Telescopic image of the dome Ye1. (Image by KC Pau). **b** Contrast-enhanced excerpt from the global LROC WAC mosaic (NASA/GSFC/Arizona State University) showing the dome Ye1



### 7.1.9 Mare Crisium and Yerkes

Mare Crisium is characterized by several concentric rings (Spudis 1993). The interpretation of the multi-ring pattern by Spudis (1993) comprises one ring of 360 km diameter inside the mare, which is indicated by ridges forming a circular structure, and a ring of 540 km diameter delimiting the mare surface. A further ring of 740 km diameter is identified by Spudis (1993) as the main ring of the Crisium basin, while two larger rings with diameters of 1,080 and 1,600 km are less pronounced.

In the western part of Mare Crisium the lava-filled crater Yerkes is situated, to the west of which a classical effusive dome is detectable, termed Yerkes 1 (Ye1). It is located at  $49.96^\circ$  E and  $14.82^\circ$  N and has a diameter of  $9.6 \pm 0.5$  km (Fig. 7.25a). The dome surface is crossed by rilles (Fig. 7.25b). The Clementine UVVIS spectral data reveal for Ye1 a 750 nm reflectance of  $R_{750} = 0.1588$ , a moderate value of the UV/VIS colour ratio of  $R_{415}/R_{750} = 0.5912$ , indicating a moderate  $\text{TiO}_2$  content, and a weak mafic absorption with  $R_{950}/R_{750} = 1.0654$ .

Based on photoclinometry and shape from shading applied to telescopic CCD images of the dome (Fig. 7.26), we determined a height of  $110 \pm 20$  m, a flank slope of  $1.36 \pm 0.30^\circ$ , and a volume of  $4.8 \text{ km}^3$ . Based on rheologic modelling (Sect. 2.5) we obtain a magma viscosity of  $1.0 \times 10^5 \text{ Pa s}$ , an effusion rate of  $146 \text{ m}^3 \text{ s}^{-1}$ , a duration of the effusion process of 1 year, a magma rise speed of  $1.2 \times 10^{-4} \text{ m s}^{-1}$ , a width of the feeder dike of 16 m and a length of 73 km.

With its low flank slope and rather low edifice volume, Ye1 belongs to class  $B_2$  as introduced in Chap. 5. If the effusion of lava continues over a long period of time, a steep flank slope and high edifice volume may occur as in the case of class  $B_1$  domes (as for the dome Piccolomini 1), while short durations of the effusion process result in lower and less voluminous edifices, as it is the case for domes of class  $B_2$  such as Ye1. Assuming a vertical dike extension comparable to the dike length (Jackson et al. 1997), it follows that for Ye1 the

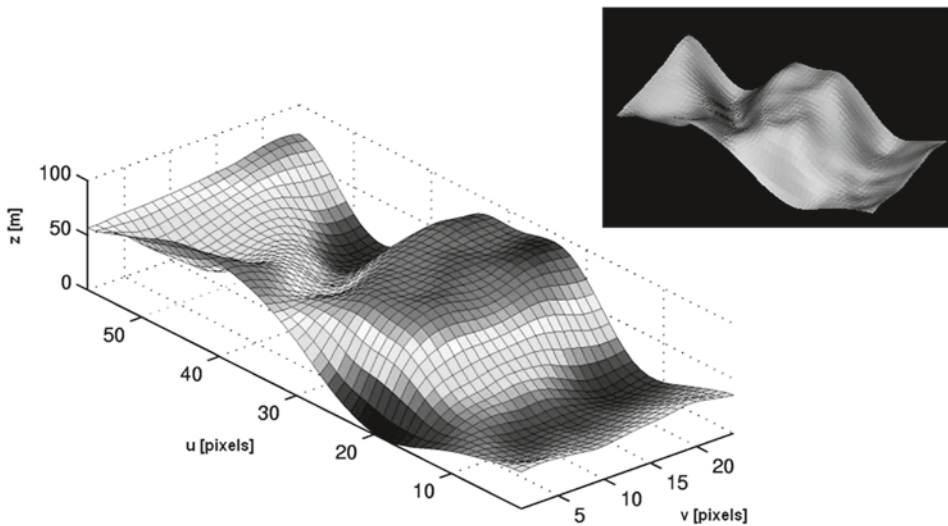


**Fig. 7.26** DEM of the northern part of the dome Ye1, viewed from northwestern direction

dome-forming magma originated in the upper lunar mantle, given the crustal thickness of 25–30 km in the western Crisium region according to Wieczorek et al. (2006).

### 7.1.10 Petavius

The crater Petavius is approximately centred at the selenographic coordinates 60.60° E and 25.50° S (Rükl 1999). It is a so-called “floor-fractured crater”, where pressurized magma led to uplift and fracturing of the crater floor (Wilhelms 1987; cf. also Wichman and Schultz 1996). Several linear and sinuous rilles are apparent on the floor of Petavius (Figs. 1.7b, 7.27). Under steep illumination, two dark regions are apparent on the crater floor, which are interpreted as pyroclastic deposits (LPDs) by Gaddis et al. (2003). A large LPD with an area of 1,645 km<sup>2</sup> lies in the northern part of the floor of Petavius (Gaddis et al. 2003). In the southernmost part of Petavius another, smaller LPD is situated (Gaddis et al. 2001).

A domical structure associated with a shallow, rimless vent of  $3.0 \pm 0.6$  km diameter is found on the edge of the southern LPD, centred at 60.70° E and 26.90° S. According to the DEM, the vent has a depth of  $80 \pm 10$  m. The depth value is significantly lower than  $D/5$ , the latter value being typical of small fresh impact craters of similar diameter (Wood and Andersson 1978). The location of the vent on the dome relief (Fig. 7.28) and its association with the LPD is suggestive of a volcanic origin, but it may also be a strongly degraded small impact crater.

The dome has a diameter of  $19.8 \pm 0.6$  km and an effective height of  $240 \pm 20$  m, resulting in an average flank slope of  $1.4 \pm 0.2^\circ$ . The edifice volume amounts to 18.8 km<sup>3</sup>. The

**Fig. 7.27** Telescopic image of the dome Petavius 1 (Pe1). (Image by S. Lammel)

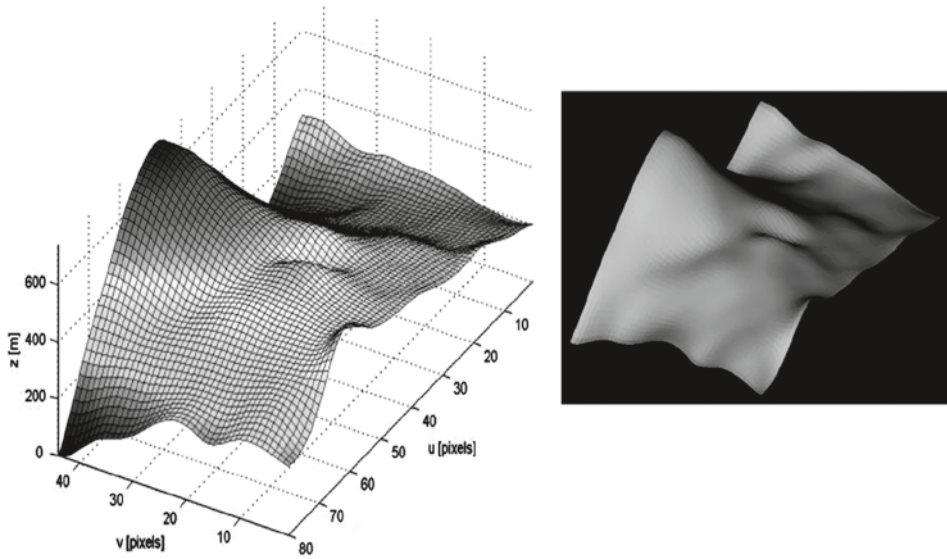
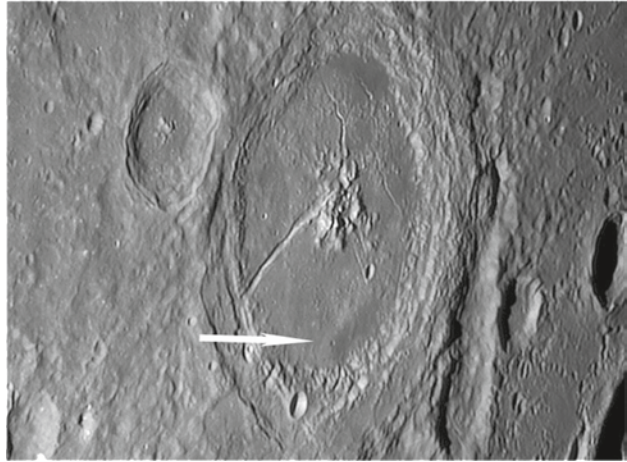


**Fig. 7.28** DEM of the dome Pe1

most elevated part of the surface section covered by the DEM has a height of  $530 \pm 30$  m, resulting in an average slope of  $3.1 \pm 0.3^\circ$ . The higher elevation south of the vent, however, is probably too high and too steep to be of volcanic origin. Hence, the dome appears to be placed adjacent to a hummocky deposit, which is supported by the close proximity of this region to the rugged inner crater rim of Petavius.



Clementine UVVIS spectral data reveal for Pe1 a 750 nm reflectance of  $R_{750}=0.1826$ , a moderate value for the UV/VIS colour ratio of  $R_{415}/R_{750}=0.6059$ , indicating a moderate  $\text{TiO}_2$  content, and a weak mafic absorption with  $R_{950}/R_{750}=1.0534$ . Hence, the dome Pe1 belongs to class  $C_1$ .

The rheologic model (Sect. 2.5) yields a magma viscosity of  $7.4 \times 10^5$  Pa s, an effusion rate of  $417 \text{ m}^3 \text{ s}^{-1}$ , and a duration of the effusion process of 1.4 years. Based on the visco-elastic dike model (Sect. 4.1), a magma rise speed of  $6.6 \times 10^{-5} \text{ m s}^{-1}$ , a width of the feeder dike of 37 m and a length of 168 km can be inferred. When assuming a vertical extension of the dome-forming dike comparable to its inferred length (Jackson et al. 1997), the origin of the dome material is in the mantle. Our interpretation of the spectrophotometric and morphometric results we obtained for this rather peculiar volcanic region is that the LPD is accompanied by a vent and an effusive lunar dome which is situated adjacent to a hummocky deposit. Possibly this region has undergone an effusive and a subsequent explosive phase of volcanism.

### 7.1.11 Mare Undarum

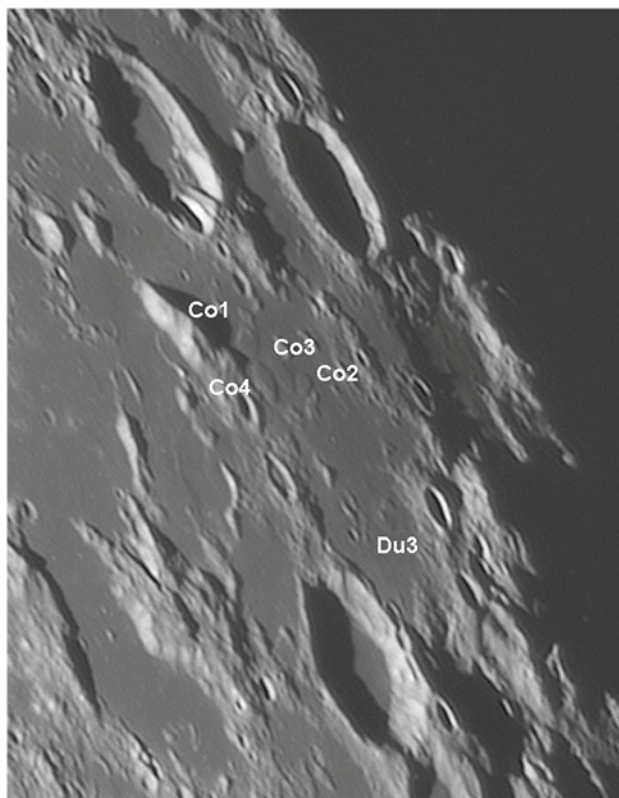
The area of Mare Undarum is mapped in the USGS lunar geologic map I-837 (Olson and Wilhelms 1974) as two different basalt units. The darker unit is described as having a lower age than the brighter unit by Olson and Wilhelms (1974). The region is located between rings of the Crisium basin (Spudis 1993).

Four domes termed Condorcet 1–4 (Co1–4) are situated between the craters Condorcet P and Dubiago, immediately east of Dubiago V and W (Figs. 1.6c, 7.29, 7.30). The fifth dome, termed Dubiago 3, is located about 35 km further south and appears to be elongated in shape with a low flank slope. We will describe it in more detail in Chap. 8 about putative lunar intrusive domes. The domes Condorcet 1–3 are aligned radially with respect to the Crisium basin. These domes have moderate diameters between 10 and 12 km (Table 7.1). Condorcet 1–3 are typical effusive mare domes, given their low flank slopes. The edifice volume is moderate ( $5\text{--}10 \text{ km}^3$ ) for Condorcet 1–3 and amounts to a large value of  $15.3 \text{ km}^3$  for Condorcet 4. Based on the spectral and morphometric data (Table 7.1), the steeper dome Condorcet 4 clearly belongs to class  $B_1$ , while its neighbour Condorcet 2 with its low flank slope of  $1.45^\circ$  and rather low edifice volume belongs to class  $B_2$ . The dome Condorcet 1 is of class  $B_2$  with some tendency towards class  $C_1$ , while the low dome Condorcet 3 with its still lower flank slope of  $1.13^\circ$ , lower edifice volume, and shorter duration of the effusion process is a typical class  $C_1$  representative with respect to its morphometric properties.

According to the rheologic model (Sect. 2.5), the domes Co1–Co3 formed from lavas with viscosities around  $10^5$  Pa s which erupted at high effusion rates between 100 and  $300 \text{ m}^3 \text{ s}^{-1}$  over comparably short periods of time between 0.5 and 3.4 years. Condorcet 1–3 resemble the dome Yerkes 1 at the western border of Mare Crisium, indicating similar interior conditions during dome formation on regional scales. Condorcet 4 originates from high-viscosity lavas of  $5.2 \times 10^6$  Pa s, erupting at an effusion rate of  $102 \text{ m}^3 \text{ s}^{-1}$  over a



**Fig. 7.29** Telescopic image of the domes Condorcet 1–4 and Dubiago 3. (Image by S. Lammel)



relatively long period of time of 4.8 years. According to its different character (large volume and steep flank slope of  $2.8^\circ$ ), the magma rise speed was 1–2 orders of magnitude lower than for Co1–Co3, probably due to a lower lava temperature and thus an increased degree of crystallisation during magma ascent. Compared to Co1–3, Condorcet 4 was formed by a considerably wider feeder dike of 84 m with a length of 178 km, according to the dike model (Sect. 4.1). Assuming a vertical dike extension comparable to the dike length, it follows that for Co1–Co3 the dome-forming magma originated in the upper lunar mantle, given the crustal thickness of 55 km in the Mare Undarum region according to Wiczorek et al. (2006).

Condorcet 1 and 3 are spectrally not distinguishable from the mare-like surface into which they merge, while Dubiago 3 and to a lesser extent also Condorcet 2 and 4 have spectra which are intermediate in reflectance between the dark and smooth mare unit and that of the nearby hummocky terrain, which is of higher reflectance and shows a typical highland signature (Fig. 3.2). The observed intermediate spectral signatures may be due to lateral mixing between mare and highland soils (Li and Mustard 2000, 2005), as Mare Undarum is characterised by small basaltic areas rather than extended plains.

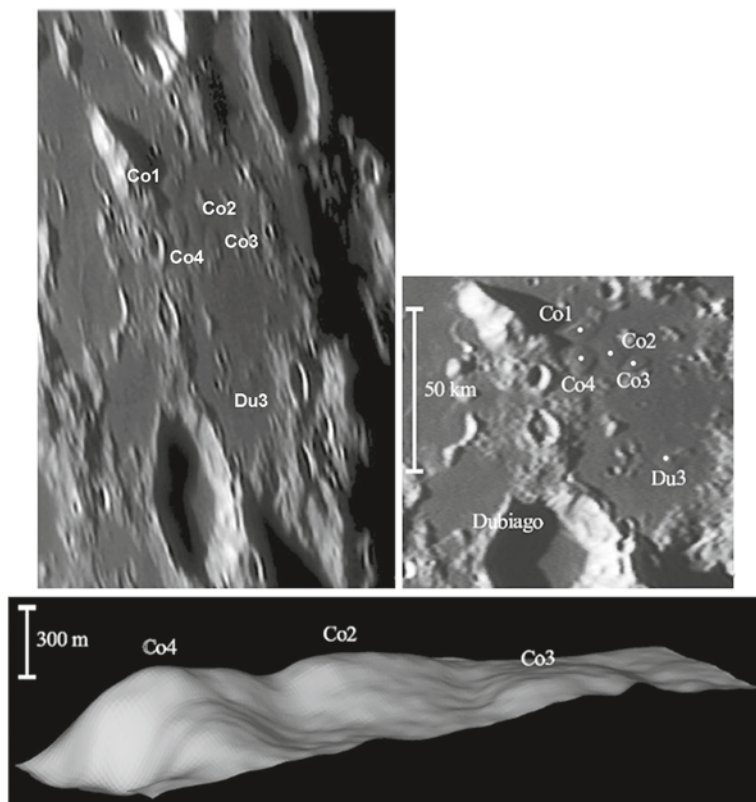


**Fig. 7.30** Telescopic image of the domes Condorcet 1–4 and Dubiago3 (*top left*). (Image by P. Lazarotti). Image of Fig. 7.29 rectified to perpendicular view (*top right*). DEM of the domes Condorcet 4, 2, and 3, viewed from southwestern direction (*bottom*). The vertical axis is ten times exaggerated

The alignment of the domes Condorcet 1–3 radial to the Crisium basin supports the hypothesis that the impact-induced stress fields caused by large impact events facilitated the ascent of dome-forming dikes from the lunar mantle through the crust (Sect. 1.6.7).

## 7.2 Effusive Lunar Domes Located from Selenographic Longitude 0° to 90° West (Fig. 7.31)

### 7.2.1 Palus Putredinis

The mare region southeast of the crater Archimedes in Mare Imbrium is termed Palus Putredinis (Fig. 7.32) (Rükl 1999). It is situated close to the so-called “Apennine Bench Formation” with its rough and relatively bright surface (Wilhelms 1987).

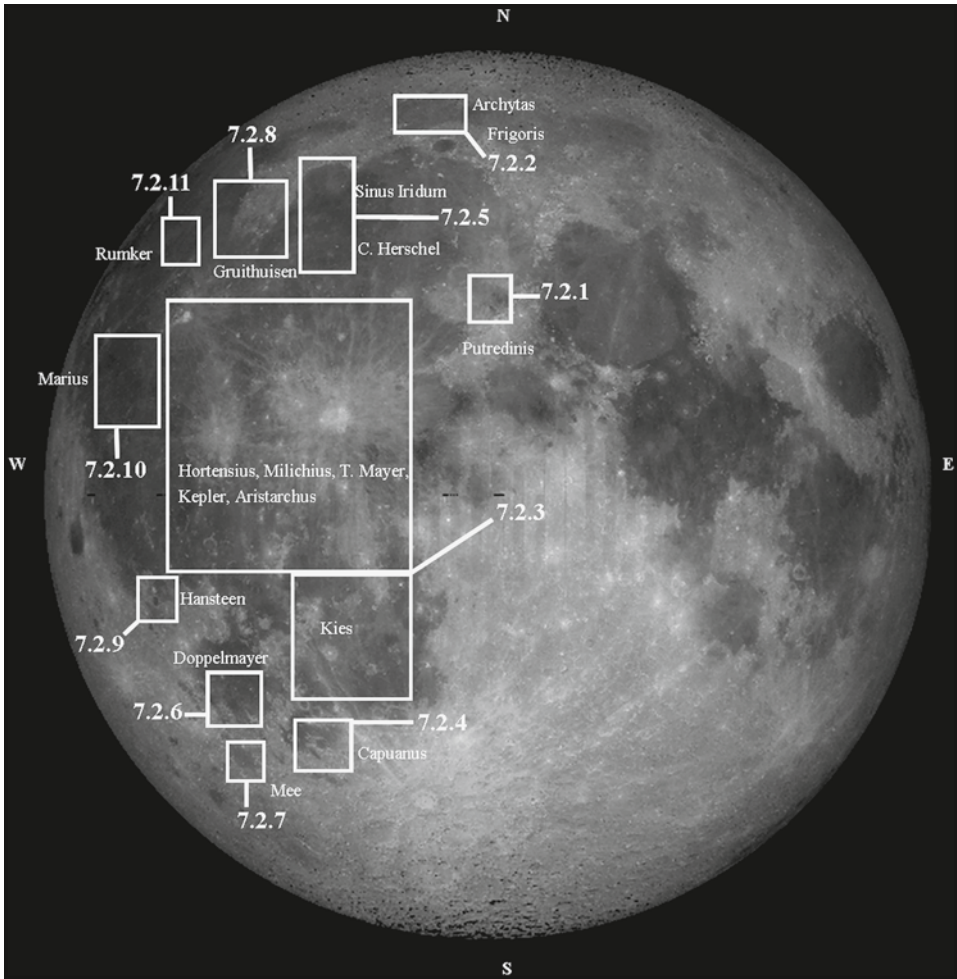


**Fig. 7.31** Lunar map of the effusive domes, located from selenographic longitude  $0^{\circ}$  to  $90^{\circ}$  West, described in the text. Basemap: Clementine (NASA, <http://photojournal.jpl.nasa.gov/catalog/PIA00302>)

Several domes are located in this region. We have examined one dome, termed Putredinis 1 (Pu1), located at  $01.44^{\circ}$  W and  $26.30^{\circ}$  N. Its diameter corresponds to  $7.0 \pm 0.5$  km and its height to  $90 \pm 10$  m, resulting in a flank slope of  $1.47 \pm 0.10^{\circ}$ . The edifice volume has been determined to  $1.78 \text{ km}^3$ .

The Clementine UVVIS spectral data reveal a 750 nm reflectance of  $R_{750} = 0.0781$ , a low value of the UV/VIS colour ratio of  $R_{415}/R_{750} = 0.5634$ , indicating a low  $\text{TiO}_2$  content, and a weak mafic absorption with  $R_{950}/R_{750} = 1.0786$ . The dome belongs to class  $C_2$ . The rheologic model (Sect. 2.5) indicates that the lava viscosity amounts to  $8.1 \times 10^4 \text{ Pa s}$ , effusion occurred at a rate of  $107 \text{ m}^3 \text{ s}^{-1}$  over a period of time of 0.53 years (about 28 weeks). Based on the estimated lava viscosity and effusion rate, the dike model (Sect. 4.1) yields a magma

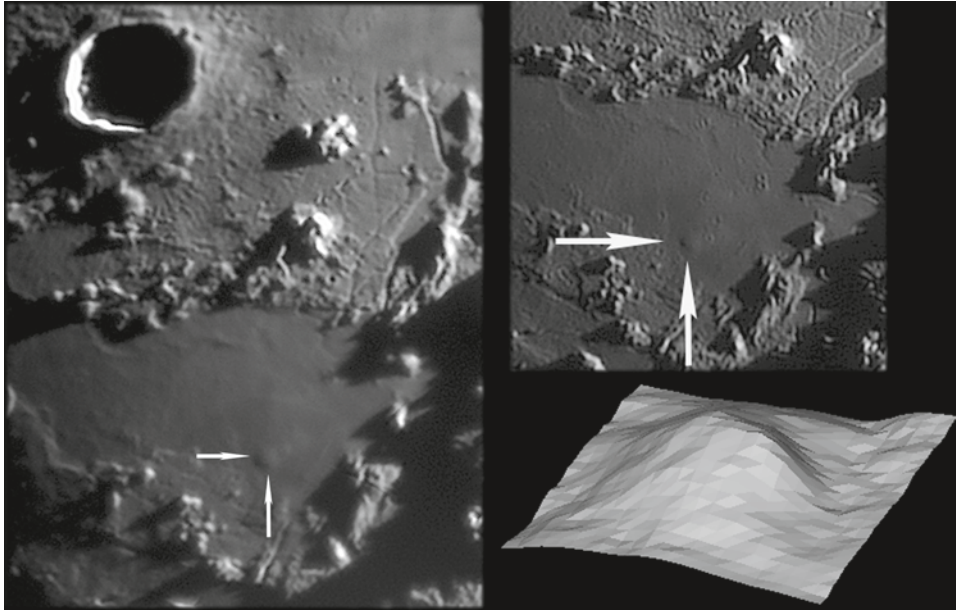


**Fig. 7.32** Telescopic image of the dome Pu1 (*left*). (Image by G. Tarsoudis). Telescopic image of Pu1 (*top right*). (Image by R. Lena). DEM of the dome (*bottom right*)

rise speed of  $1.1 \times 10^{-4} \text{ m s}^{-1}$ , a dike width of 15 m and a length of 67 km. According to the rheologic properties inferred for the dome Putredinis 1, it clearly belongs to rheologic group  $R_1$ , like e.g. several domes in the Milichius/T. Mayer region and the domes Cauchy  $\omega$  and  $\tau$  (C2 and C3) in Mare Tranquillitatis.

### 7.2.2 Mare Frigoris and Region Around Archytas

The elongated lava plain of Mare Frigoris may be part of a ring structure of the Imbrium basin (Spudis 1993). Alternatively, according to Whitford-Stark (1990) the structure may belong to the putative Procellarum or Gargantuan basin postulated by Cadogan (1974), the existence of which, however, is still disputed. According to the geologic map of the Mare Frigoris basalt units by Whitford-Stark (1990), a variety of  $\text{TiO}_2$  contents can be observed. It is found by Kramer et al. (2009) that the Mare Frigoris basalts are dominated by “high-alumina mare basalts” of unusually low Fe and high Al content (cf. Sect. 7.1.4).

In this region, two domes termed Archytas 1 (Ar1) and Archytas 2 (Ar2) displaying different morphometric properties are detectable. Archytas 1 (Fig. 7.33) with its large diameter and low slope of only  $0.25^\circ$  is considered a putative intrusive dome. Further west the prominent dome Archytas 2 is located at  $2.71^\circ \text{ W}$  and  $56.52^\circ \text{ N}$ . Small hills can be observed on its surface, which are well visible in the LRO WAC image (Fig. 7.33). They likely represent pre-existing small peaks surrounded by the dome. The diameter of Ar2 amounts to  $11 \pm 0.4 \text{ km}$



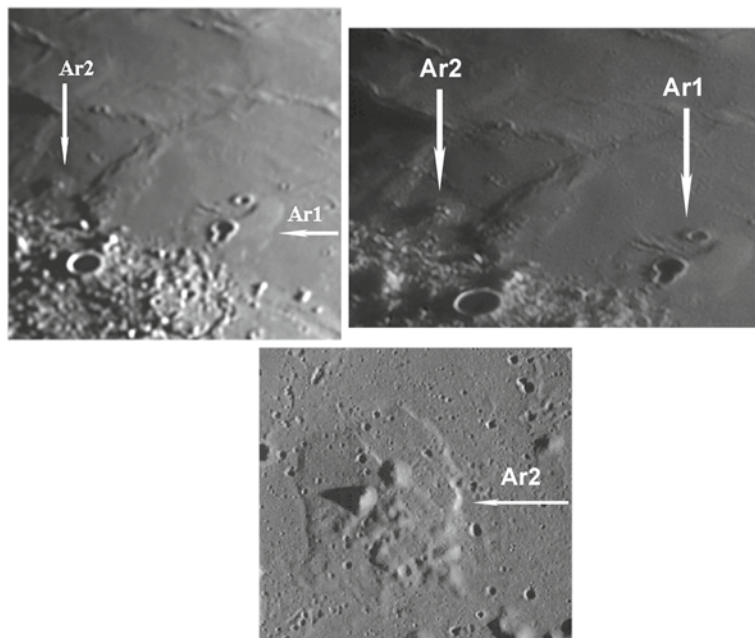


**Fig. 7.33** Telescopic image of the domes near Archytas (*left*). (Image by J. Phillips). Telescopic image of the domes near Archytas (*right*). (Image by C. Zannelli). LROC WAC image M117515873ME of the dome Ar2 (*bottom*). (NASA/GSFC/Arizona State University)

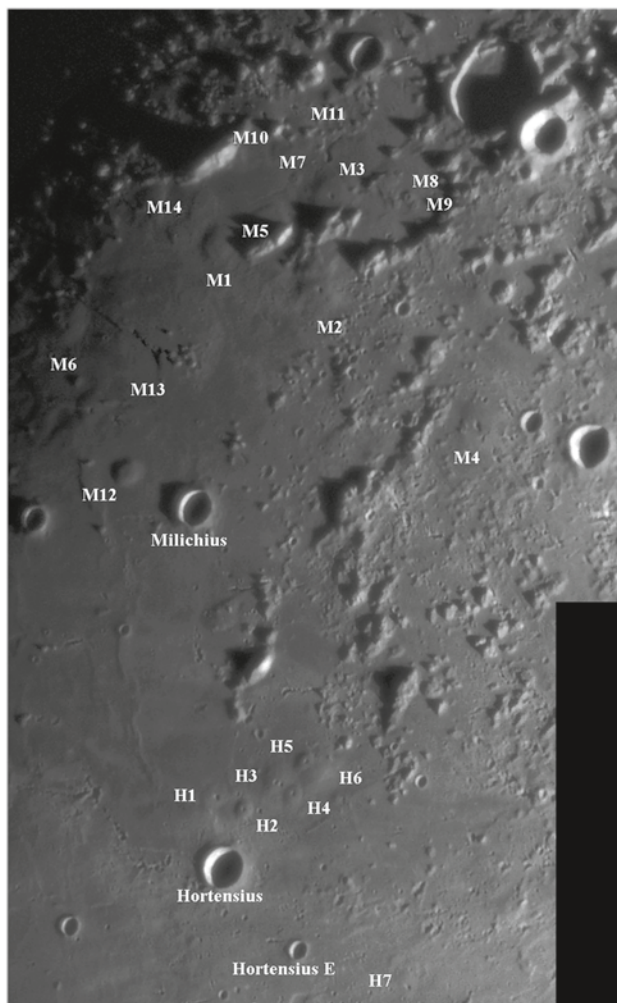
and the height to  $265 \pm 30$  m, resulting in an average slope of  $2.7 \pm 0.10^\circ$ . The dome volume is estimated to  $12.6 \text{ km}^3$ . The Clementine UVVIS spectral data of Ar2 reveal a 750 nm reflectance of  $R_{750} = 0.1423$ , an extraordinarily low value for the UV/VIS colour ratio of  $R_{415}/R_{750} = 0.5394$ , indicating a low  $\text{TiO}_2$  content, and a moderate mafic absorption with  $R_{950}/R_{750} = 1.0140$ , likely due to fresh material excavated by the impacts of nearby craters.

The rheologic model (Sect. 2.5) yields an effusion rate of  $119 \text{ m}^3 \text{ s}^{-1}$ . It was formed from lava of viscosity of  $4.4 \times 10^6 \text{ Pa s}$ , over a period of time of 3.4 years. Clearly Ar2 belongs to class B<sub>1</sub>. The dike model (Sect. 4.1) yields a magma rise speed of  $4.4 \times 10^{-6} \text{ m s}^{-1}$ , a dike width of 114 m and a length of 170 km, indicating an origin of the dome-forming magma well below the lunar crust.

### 7.2.3 Dome Suite near Hortensius and Domes and Swells Between Milichius and Tobias Mayer, Mare Nubium and Aristarchus

Two dome fields are situated in eastern Oceanus Procellarum near the craters Hortensius, Milichius, and Tobias Mayer, in a region located south of the outer rim of the Imbrium basin also known as Mare Insularum (Figs. 1.5a–c, 7.34, 7.35). These two dome fields cover

**Fig. 7.34** Telescopic image of the cluster of domes between Hortensius, Milichius and Tobias Mayer. (Image by P. Lazzarotti)



most of the northern part of Mare Insularum. According to the Clementine UV/VIS spectral ratio map by Hiesinger et al. (2003), the  $\text{TiO}_2$  content of the lavas of Mare Insularum is low to moderate. Furthermore, they are partially covered by material ejected during the formation of nearby impact craters such as Copernicus and Eratosthenes (Hiesinger et al. 2003).

A low dome termed M15 is situated near the crater Tobias Mayer C at  $25.20^\circ$  W and  $10.10^\circ$  N (Fig. 7.36). Lunar Orbiter frame IV-133-H2 displays a fissure recognisable on the summit of M15 (Fig. 7.37), which may be interpreted as an outflow channel and thus supports the assumption of volcanic activity. M15 has a large diameter of about 21 km and a height of  $110 \pm 10$  m, yielding an average flank slope of  $0.6 \pm 0.1^\circ$ . The dome edifice volume has been determined to  $17.0 \text{ km}^3$ . The Clementine UVVIS spectral data reveal a rather high 750 nm reflectance of  $R_{750} = 0.1411$ , a moderate value of the UV/VIS colour ratio of



**Fig. 7.35** Telescopic image of the cluster of domes between Hortensius, Milichius and Tobias Mayer. (Image by J. Phillips)

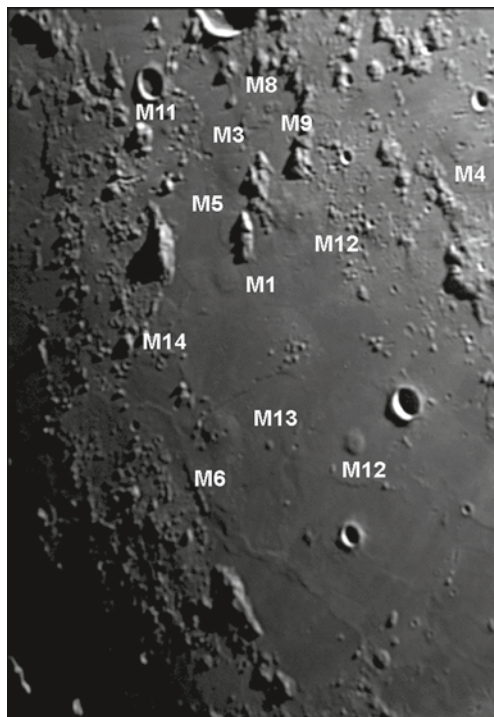
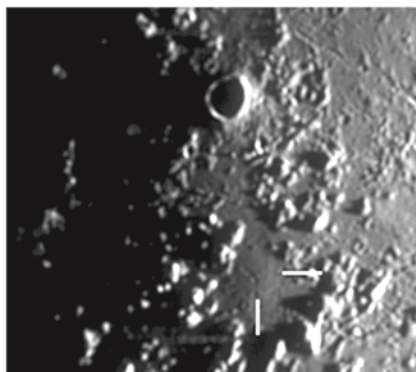
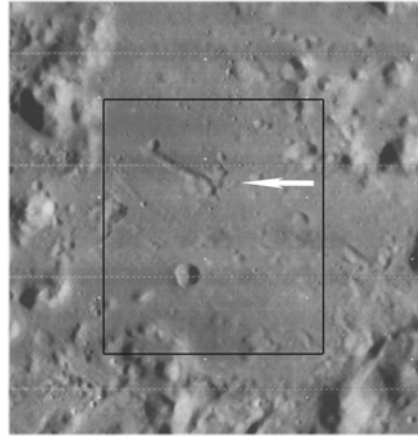


**Fig. 7.36** Telescopic image of M15. (Image by J. Phillips)



$R_{415}/R_{750}=0.5920$ , indicating a moderate  $\text{TiO}_2$  content, and a weak mafic absorption with  $R_{950}/R_{750}=1.0389$ , indicating a high soil maturity. The rheologic model (Sect. 2.5) yields an effusion rate of  $704 \text{ m}^3 \text{ s}^{-1}$ , a lava viscosity of  $1.5 \times 10^4 \text{ Pa s}$ . It formed over a period of time of 0.9 years. According to our classification scheme, M15 belongs to class  $C_1$ , as it is the case for M1, M3, and M5 with volumes smaller than  $12 \text{ km}^3$  and M2, M6, and M10 with volumes larger than  $20 \text{ km}^3$  (Table 7.2). The low flank slopes of these domes suggest high effusion rates of the erupted lavas in between  $200$  and  $500 \text{ m}^3 \text{ s}^{-1}$ , where the lower volumes

**Fig. 7.37** Lunar Orbiter frame IV-133-H2 (NASA/USGS), showing the vent of M15



of the smaller domes are attributed to a shorter duration of the effusion process (5 months for M5 compared to more than 7 years for M2). The lava viscosity amounts to between  $6 \times 10^3$ – $3 \times 10^6$  Pa s (Table 7.2 and Figs. 7.34, 7.35).

The dome termed Tobias Mayer 1 (M1), located at  $31.58^\circ$  W and  $12.76^\circ$  N (Fig. 7.35), has a diameter of  $13.4 \pm 0.33$  km, a flank slope of  $0.9 \pm 0.1^\circ$ , and an edifice volume of  $8.2 \text{ km}^3$ . Several domes in this region (M1, M2, M3, M5, M6, M7, M10) have large diameters and low to moderate flank slopes (Table 7.2). They are part of a basaltic unit of low to moderate  $\text{TiO}_2$  content. With their smaller diameters and steeper slopes, the domes M4, M11, and M12 (Fig. 7.34) belong to class  $B_1$ . M11 consists of spectrally very red low- $\text{TiO}_2$  material.

The dome M7 is morphometrically similar to the small, low, low-volume class A domes of the Cauchy and Arago dome fields but consists of spectrally red material, belonging to class  $E_2$  (Fig. 5.3). M8 and M9 are also small and spectrally red but steeper than M7. Their slopes correspond to  $3.2$ – $3.5^\circ$  and belong to class  $E_1$ . M13, with its large diameter and low slope of only  $0.41^\circ$ , is considered a putative intrusive dome. It is described in Chap. 8.

For the domes with elongated vents in the Milichius/T. Mayer region, the dike model (Sect. 4.1) yields rise speeds between  $10^{-6}$  and  $10^{-2} \text{ m s}^{-1}$ , dike widths between 5 and 30 m, and dike lengths between 20 and 150 km. For these domes, all elongated vents except that of M1 are oriented radially with respect to the Insularum basin described by Spudis (1993) and the East Procellarum basin postulated by de Hon (1979) (cf. also Spudis 1993). Furthermore, the domes M3, M4, M10, and M15 are forming a chain of 210 km length which is aligned in the same direction. The shallow vent of M1 is oriented radially with respect to the Imbrium basin.

In the Hortensius region, domes of moderate to steep slope covering a wide range of volumes can be found (Figs. 1.5c, 7.38, 7.39). They are all part of a moderate- $\text{TiO}_2$  basaltic unit. The dome Hortensius 7 (H7) is located at  $25.17^\circ$  W and  $6.07^\circ$  N near the crater Hortensius E and has a diameter of  $7.8 \pm 0.35$  km (Fig. 7.39). Furthermore, a summit pit of about  $3.10 \pm 0.35 \text{ km} \times 1.60 \pm 0.35 \text{ km}$  is apparent (Fig. 7.40). It is probably the remnant of the vent from which the dome-forming lava erupted. For H7 we determined a height of  $100 \pm 15 \text{ m}$ , corresponding to a flank slope of  $1.47 \pm 0.15^\circ$  (Fig. 7.41). The edifice volume

**Table 7.2** Morphometric and rheologic properties of further domes described in the text, located in the region of Hortensius, Milichius-Tobias Mayer, Mare Nubium and Aristarchus

Dome	Longitude (°)	Latitude (°)	$R_{750}$	$R_{415}/R_{750}$	$R_{950}/R_{750}$	Slope (°)	D (km)	h (m)	V (km <sup>3</sup> )	$\eta$ (Pa s)	E (m <sup>3</sup> s <sup>-1</sup> )	T (years)	U (m s <sup>-1</sup> )	W (m)	L (Km)
M1	-31.58	12.76	0.1090	0.6060	1.0444	0.86	13.4	100	8.2	$2.8 \times 10^4$	312	0.83	$7.4 \times 10^{-4}$	9.7	43
M2	-30.05	12.79	0.1267	0.5837	1.0284	1.80	20.1	320	50.0	$2.8 \times 10^6$	219	7.23	$1.8 \times 10^{-5}$	66	183
M3	-30.43	13.78	0.1063	0.5923	1.0538	1.40	15.6	190	12.0	$4.3 \times 10^5$	223	1.71	$5.7 \times 10^{-5}$	30	133
M4	-27.39	12.04	0.1383	0.5980	1.0246	1.27	15.3	170	21.0	$2.6 \times 10^5$	239	2.78	$9.1 \times 10^{-5}$	24	109
M5	-31.01	13.24	0.1181	0.5978	1.0184	0.60	15.3	80	6.8	$7.1 \times 10^3$	509	0.42	$3.7 \times 10^{-3}$	5.6	25
M6	-32.74	11.48	0.1024	0.6068	1.0272	1.34	19.7	230	33.0	$6.1 \times 10^5$	293	3.57	$5.4 \times 10^{-5}$	35	155
M7	-30.96	13.75	0.1168	0.6151	1.0233	0.99	5.2	45	0.4	$5.9 \times 10^3$	104	0.11	$9.2 \times 10^{-4}$	5.1	23
M8	-29.50	14.06	0.1214	0.5951	1.0428	3.46	4.3	130	1.2	$1.5 \times 10^6$	25	1.54	$2.4 \times 10^{-6}$	51	187
M9	-29.40	13.98	0.1215	0.5951	1.0427	3.15	4.0	110	0.9	$8.1 \times 10^5$	25	1.10	$3.8 \times 10^{-6}$	39	174
M10	-31.70	14.06	0.1227	0.5976	1.0329	0.84	19.0	140	21.0	$6.2 \times 10^4$	448	1.49	$5.6 \times 10^{-4}$	13	60
M11	-31.08	14.77	0.1186	0.5908	1.0297	2.80	6.0	150	2.3	$1.4 \times 10^6$	42	1.75	$4.6 \times 10^{-6}$	48	188
M12	-31.20	10.08	0.1156	0.6116	1.0117	2.72	9.7	230	11.0	$3.4 \times 10^6$	71	4.91	$5.6 \times 10^{-6}$	70	182
M14	-32.13	12.76	0.1056	0.6094	1.0374	0.27	14.8	35	1.7	$1.4 \times 10^2$	1100	0.05	$1.5 \times 10^{-1}$	1.5	6.5
M15	-25.40	10.10	0.1411	0.5920	1.0389	0.60	21.0	110	17.0	$1.5 \times 10^4$	704	0.90	$2.7 \times 10^{-3}$	7.6	34
H1	-28.41	7.18	0.1308	0.6203	1.0278	1.89	8.5	140	3.4	$4.3 \times 10^5$	89	1.21	$2.3 \times 10^{-5}$	30	133
H2	-28.01	7.12	0.1281	0.6225	1.0131	3.45	7.6	230	6.3	$6.0 \times 10^6$	44	4.54	$2.8 \times 10^{-6}$	89	176
H3	-27.78	7.59	0.1174	0.6105	1.0197	2.05	12.3	220	17.0	$1.5 \times 10^6$	120	4.51	$1.2 \times 10^{-5}$	51	187
H4	-27.51	7.47	0.1209	0.6154	1.0303	3.21	6.8	190	5.0	$3.2 \times 10^6$	42	3.77	$3.6 \times 10^{-6}$	69	182
H5	-27.54	7.87	0.1183	0.6066	1.0287	5.39	8.5	400	18.0	$6.6 \times 10^7$	31	18.27	$9.2 \times 10^{-7}$	243	145
H6	-27.34	7.82	0.1237	0.6118	1.0213	3.57	12.5	390	32.0	$2.3 \times 10^7$	70	14.57	$2.8 \times 10^{-6}$	157	160
H7	-25.17	6.07	0.1463	0.6149	1.0156	1.47	7.8	100	2.4	$1.0 \times 10^5$	106	0.72	$8.7 \times 10^{-5}$	17	74
K1	-24.18	-26.84	0.1169	0.6298	1.0464	1.35	13.6	160	13.0	$2.6 \times 10^5$	201	2.0	$7.6 \times 10^{-5}$	24	108
He1	-50.00	20.21	0.1085	0.6245	0.9753	2.50	14.4	230	21.0	$1.3 \times 10^6$	157	4.2	$1.7 \times 10^{-5}$	47	188

**Fig. 7.38** Telescopic image of the Hortensius and Milichius domes. (Image by M. Wirths)

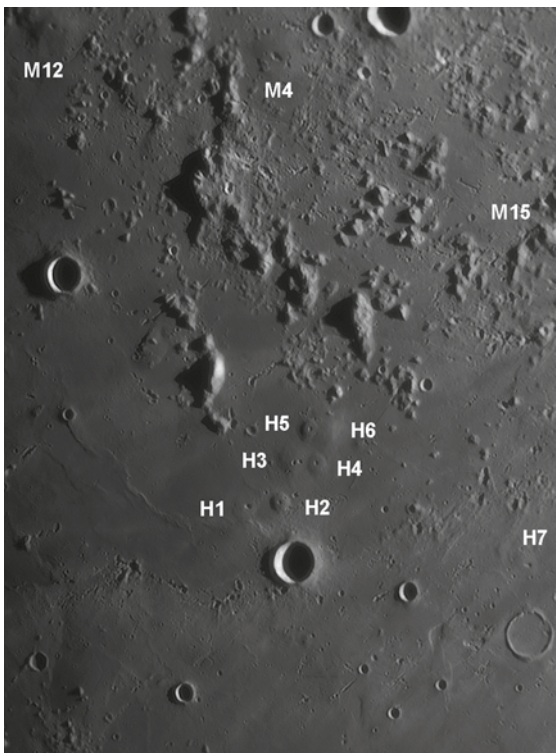
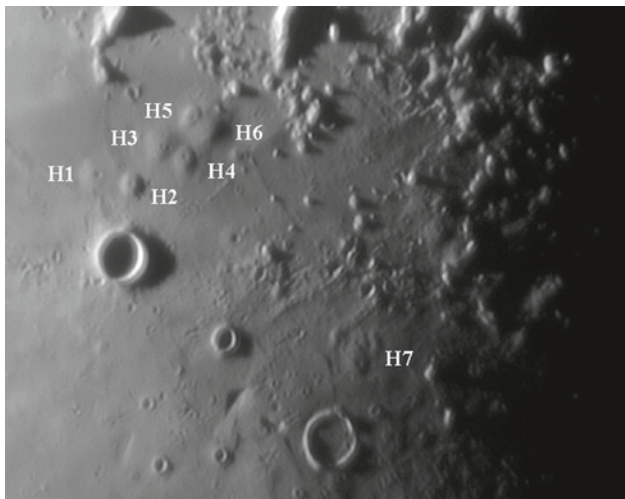


**Fig. 7.39** Telescopic image of the Hortensius domes. (Image by Z. Pujic)



amounts to 2.4 km<sup>3</sup>. The dome belongs to class B<sub>2</sub>. The low slope and edifice volume of the dome imply according to the rheologic model (Sect. 2.5) a moderately high effusion rate of 106 m<sup>3</sup> s<sup>-1</sup>, a low lava viscosity of 1.0 × 10<sup>5</sup> Pa s, and a short duration of the effusion process of only 0.72 years.

**Fig. 7.40** Lunar Orbiter frame IV-126-H1 (NASA/USGS), showing the vent of H7

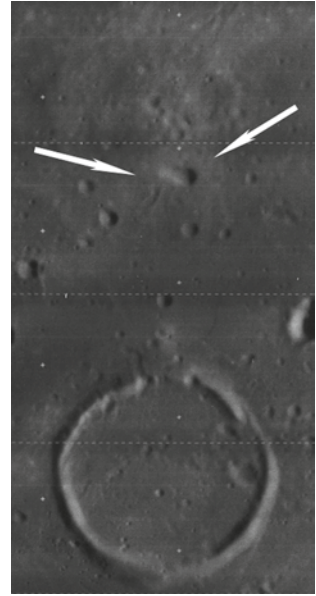
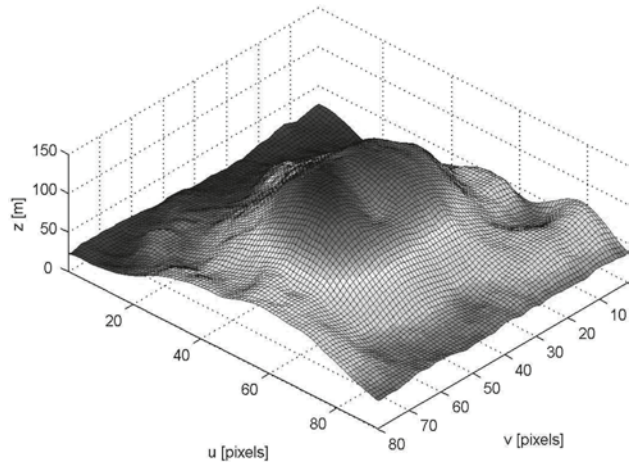


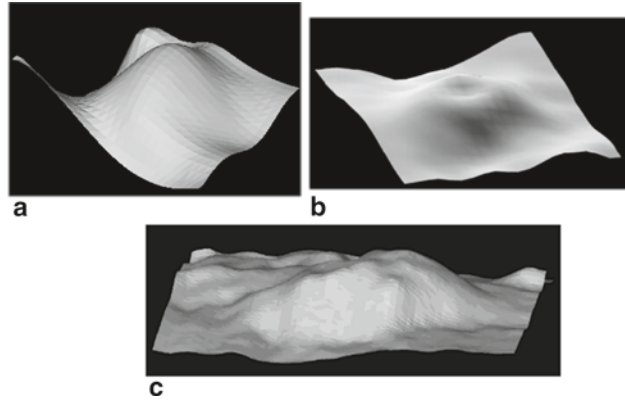
**Fig. 7.41** DEM of the dome H7, viewed from southeastern direction



The domes H2–H6 (Figs. 7.38–7.39) belong to class B<sub>1</sub> according to their steep slopes in between 2.1° and 5.4° and moderate to high volumes (5–32 km<sup>3</sup>). Like H7, the dome H1 with its lower flank slope of 1.9° and lower volume (Table 7.2) belongs to class B<sub>2</sub>. The domes H5 and H6 are the steepest mare domes examined in this lunar region, with flank slopes of up to 3.4°, and they are among those with the highest volumes. H6 has a diameter of  $12.5 \pm 0.35$  km and an edifice volume of 32 km<sup>3</sup>. Its rheologic parameters (Sect. 2.5) are  $2.3 \times 10^7$  Pa s for the lava viscosity,  $70 \text{ m}^3 \text{ s}^{-1}$  for the effusion rate, and 14.6 years for the duration of the effusion process. According to the dike model (Sect. 4.1), feeder dike of H6 has a modelled width of 157 m and a length of 160 km. For all other Hortensius domes,



**Fig. 7.42** DEMs of some domes described in the text.  
a M11. b K1. c Ke1



we estimated eruption rates between  $30$  and  $120 \text{ m}^3 \text{ s}^{-1}$ . However, the steeper and spherically shaped class  $B_1$  domes mainly formed out of lava of higher viscosities between  $10^6$  and  $10^8 \text{ Pa s}$  and over longer periods of time (around 4 years, up to 18 years for the high volume edifice H5) than the lower class  $B_2$  edifices H1 and H7, having formed from lavas of viscosity of several  $10^5 \text{ Pa s}$  over periods of time of about 1 year.

The formation conditions of M4, M11, and especially M12 (Milichius  $\pi$ ) are supposedly similar to those encountered in the Hortensius dome field, regarding the observed spectral and morphometric properties and the similarities in the estimated rheologic parameters (Table 7.2). Possibly these domes formed simultaneously with the Hortensius domes.

Two lunar domes located in western Mare Nubium and in the Aristarchus region, respectively, have similar properties. The mare dome Kies  $\pi$  (K1) situated at  $24.18^\circ \text{ W}$  and  $26.84^\circ \text{ S}$  west of the lava-flooded crater Kies in western Mare Nubium (Figs. 7.42b, 7.43a) belongs to class  $C_1$ . Its diameter corresponds to  $13.6 \pm 0.5 \text{ km}$  and its height to  $160 \pm 20 \text{ m}$ , resulting in a flank slope of  $1.35 \pm 0.10^\circ$ . The edifice volume is determined to  $13.0 \text{ km}^3$ . The

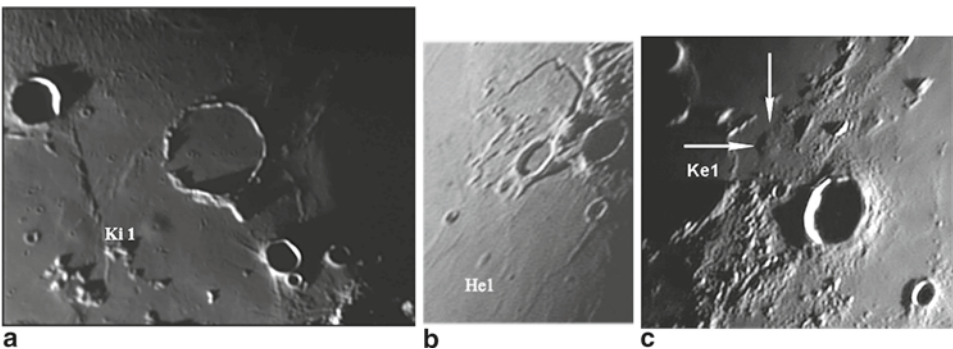


**Fig. 7.43** a Telescopic image of the dome Kies  $\pi$  (K1). (Image by J. Phillips). b Telescopic image of Herodotus  $\omega$  (He1). (Image by C. Wöhler). c Telescopic image of the dome near Kepler (Ke1). (Image by R. Lena)



Clementine UVVIS spectral data reveal a 750 nm reflectance of  $R_{750}=0.1169$ , a UV/VIS colour ratio of  $R_{415}/R_{750}=0.6298$ , indicating a moderate  $\text{TiO}_2$  content, and a weak mafic absorption with  $R_{950}/R_{750}=1.0464$ . A summit pit with an estimated size of  $3.6\pm0.5$  km is apparent.

Another typical mare dome, Herodotus  $\omega$  (He1), is situated southwest of the crater Aristarchus at  $50.00^\circ$  W and  $20.21^\circ$  N (Fig. 7.43b). With its moderate to steep slope of  $2.50\pm0.20^\circ$ , rather large diameter of  $14.4\pm0.5$  km, edifice volume of  $21\text{ km}^3$ , and moderate  $R_{415}/R_{750}$  ratio of 0.6245, it belongs to class B<sub>1</sub>, like M4, M11, M12 and H2–H6. Due to the fact that it is covered by immature ejecta from the nearby crater Aristarchus, it displays a strong mafic absorption band corresponding to a low  $R_{950}/R_{750}$  ratio of 0.9753.

The dome Kepler 1 (Ke1) is located at  $39.53^\circ$  W and  $8.88^\circ$  N (Figs. 7.42c, 7.43c) to the west of the conspicuous crater Kepler with its extended ray system. Lunar Orbiter imagery acquired under moderate solar elevation angles does not show the dome clearly but several craterlets on its summit. Ke1 has a diameter of  $13.9\pm0.5$  km and a height of  $170\pm20$  m, resulting in flank slope of  $1.4\pm0.10^\circ$ . The dome edifice volume is determined to  $12.5\text{ km}^3$ . The rheologic model (Sect. 2.5) yields estimates of the lava viscosity of  $3.3\times10^5$  Pa s, an effusion rate of  $299\text{ m}^3\text{ s}^{-1}$ , and a duration of the effusion process of 1.3 years.

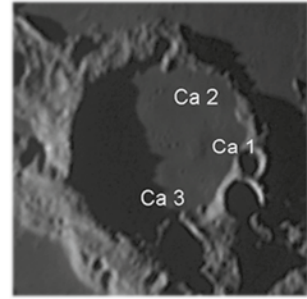
The morphometric and rheologic properties for Ke1 are comparable to those of the class C<sub>2</sub> domes in the Cauchy region in Mare Tranquillitatis, such as Cauchy  $\omega$  and  $\tau$ . The Clementine UVVIS spectral data reveal a 750 nm reflectance of  $R_{750}=0.1399$ , a UV/VIS colour ratio of  $R_{415}/R_{750}=0.6119$ , indicating a moderate  $\text{TiO}_2$  content, and a strong mafic absorption of  $R_{950}/R_{750}=0.9833$  likely due to the fresh material excavated by the impacts of nearby craters. Using the dike model (Sect. 4.1), for Ke1 we modeled a magma rise speed of  $4.4\times10^{-5}\text{ m s}^{-1}$ . The inferred dike width amounts to 39 m and the dike length to 173 km. Hence the magma reservoir feeding the dome-forming eruptions was located in the upper lunar mantle, well below the crust.

## 7.2.4 Capuanus and Palus Epidemiarum

We have examined three lunar domes on the floor of the lava-filled crater Capuanus in Palus Epidemiarum (Figs. 1.7a, 7.44) (Rükl 1999). They are termed Ca1–Ca3 and are located at  $(26.18^\circ\text{ W}, 34.20^\circ\text{ S})$ ,  $(26.72^\circ\text{ W}, 33.75^\circ\text{ S})$ , and  $(26.60^\circ\text{ W}, 34.40^\circ\text{ S})$ , respectively. For the domes Ca1 and Ca2, diameters of  $7.0\pm0.4$  km and  $9.0\pm0.4$  km, respectively, were found. Their heights correspond to  $100\pm10$  m, resulting in flank slopes of  $1.63\pm0.16^\circ$  and  $1.27\pm0.13^\circ$ , while the edifice volumes correspond to 1.9 and  $3.2\text{ km}^3$ . The dome Ca3 has a smaller diameter of  $5.5\pm0.4$  km and a lower height of  $50\pm5$  m, resulting in a flank slope of  $1.04\pm0.10^\circ$ . The edifice volume of Ca3 has been determined to  $0.59\text{ km}^3$  (Fig. 2.10). In the LOLA DEM, the elevation differences between the dome centers and the surrounding surface are in good agreement with the image-based photoclinometry and shape from shading analysis.

Rheologic modelling (Sect. 2.5) yields effusion rates of 125, 207, and  $154\text{ m}^3\text{ s}^{-1}$ , respectively. Ca1 and Ca2 were formed from lava of viscosities of  $3.3\times10^5$  and  $1.8\times10^5$  Pa s over

**Fig. 7.44** Telescopic image of the Capuanus domes. (Image by J. Phillips)



similar periods of time of about 0.5 years. The dome Ca3 was formed from lava of lower viscosity of  $2.1 \times 10^4$  Pa s over a shorter period of time of 0.12 years. The estimated dome volumes correspond to 1.90, 3.17 and  $0.59 \text{ km}^3$  for Ca1, Ca2 and Ca3, respectively. For Ca1 the magma rise speed amounts to  $3.9 \times 10^{-5} \text{ m s}^{-1}$  and the dike width and length have been inferred (Sect. 4.1) to 27 and 120 km. For Ca2 the magma rise speed was higher and amounts to  $1.1 \times 10^{-4} \text{ m s}^{-1}$ , and the dike width and length are 21 and 93 km, respectively. For Ca3 the magma rise speed amounts to  $4.7 \times 10^{-4} \text{ m s}^{-1}$  and the dike width and length to 9 m and 38 km, respectively. The domes Ca1 and Ca2 belong to class  $C_2$ , while the smaller dome Ca3 is a typical exemplar of the class  $E_2$ . The inferred rheologic properties of Ca3 are comparable to those of the dome M7 in the Milichius region and to some of the aligned domes in northern Mare Tranquillitatis. Based on the inferred rheologic properties and associated dikes geometry, Ca1 and Ca2 belong to the rheologic group  $R_1$ , while the dome Ca3 is a typical representative of rheologic group  $R_2$ . These rheologic values were inferred assuming the minimum vertical magma pressure gradient of  $dp/dz = 328 \text{ Pa m}^{-1}$  required to drive magma to the lunar surface (cf. Wilson and Head 1996). When the value of  $dp/dz$  is doubled, the modelled magma rise speeds correspond to  $1.6 \times 10^{-4} \text{ m s}^{-1}$ ,  $4.2 \times 10^{-4} \text{ m s}^{-1}$ , and  $1.8 \times 10^{-3} \text{ m s}^{-1}$ , the dike widths to 13, 11, and 4 m, and the dike lengths to 60, 47, and 20 km. For the latter value of  $dp/dz$ , the dike lengths of Ca1 and Ca2 are comparable to the diameter of the crater Capuanus of 60 km. Hence, the modeled lengths of the dome-forming dikes would become comparable to the diameter of Capuanus for a vertical magma pressure gradient of about  $650 \text{ Pa m}^{-1}$ .

The spectral analysis shows that the dome Ca3 has a relatively high 750 nm reflectance of  $R_{750} = 0.1337$  with a UV/VIS colour ratio of  $R_{415}/R_{750} = 0.6104$ , indicating a moderate  $\text{TiO}_2$  content, and  $R_{950}/R_{750} = 0.1066$ . The dome Ca2 shows the lowest  $R_{415}/R_{750}$  ratio of the three examined domes with a  $R_{415}/R_{750} = 0.6012$ , indicating a lower  $\text{TiO}_2$  content. According to the petrographic map shown in Fig. 7.45, the floor of Capuanus appears to be composed of mare material, primarily visible in the region of Ca2. Furthermore, the elemental abundance maps derived by the Clementine UVVIS+NIR imagery show that the composition of Ca2 and Ca3 corresponds to low-Ti basalt while Ca1 consists of basalt having a lower Al and a higher Ti content (Fig. 7.46). The presence of the domes and the observed variety of basalt compositions suggest a complex volcanic history of Capuanus crater.

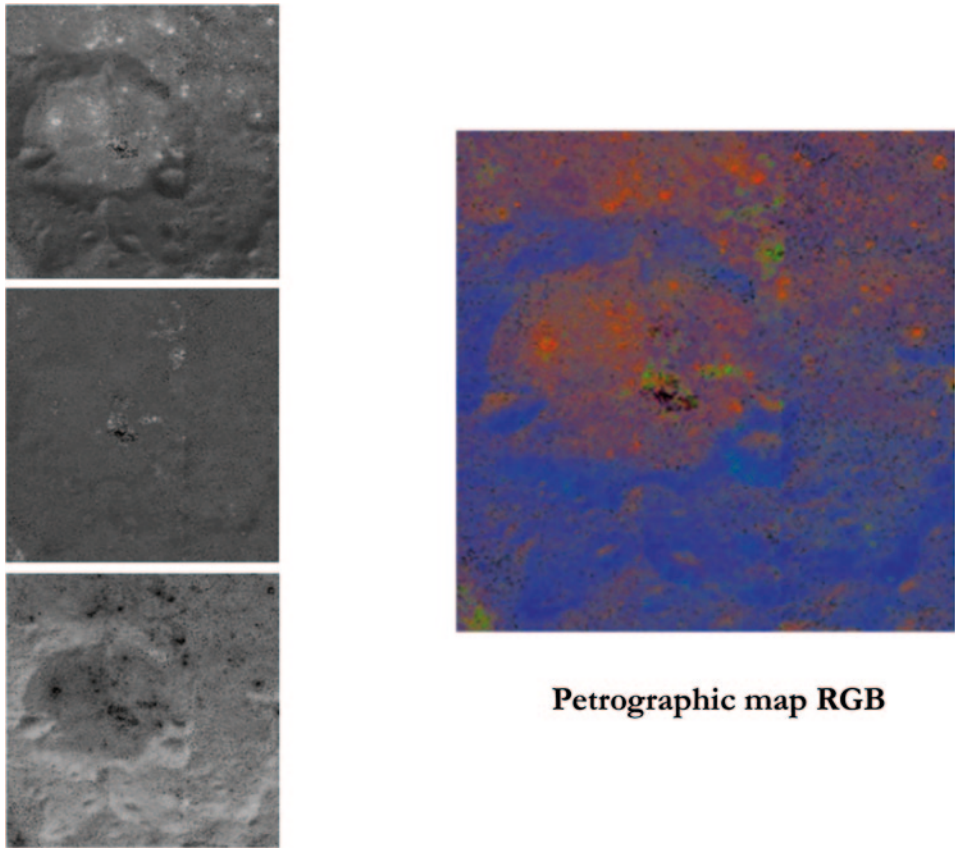


**Fig. 7.45** Petrographic map of Capuanus obtained based on Clementine UVVIS data. The relative content of mare basalt, Mg-rich rock, and FAN is denoted by the *red (top image)*, *green (middle image)*, and *blue channel (bottom image)* of the corresponding RGB image, respectively

### 7.2.5 Region Around C. Herschel in Mare Imbrium and Sinus Iridum

We have examined a dome located at  $32.57^\circ$  W and  $34.76^\circ$  N in western Mare Imbrium near the crater C. Herschel. This dome, termed C. Herschel 1 (CH1), has a diameter of  $16.8 \pm 0.4$  km, a height of  $64 \pm 10$  m, resulting in a flank slope of  $0.44^\circ$ . The estimated volume corresponds to  $7.1 \text{ km}^3$ . The Clementine UVVIS spectral data of the dome CH1 reveal a 750 nm reflectance of  $R_{750} = 0.1051$ , a moderate value of the UV/VIS colour ratio of  $R_{415}/R_{750} = 0.5957$ , and  $R_{950}/R_{750} = 1.0513$ . A small dot is visible on the summit of CH1, but it cannot be clearly identified as a vent in the LRO image (Fig. 7.47). Due to its circularity of 0.97, CH1 should be regarded as an effusive structure, which would imply to assign it to the effusive class  $C_1$ .

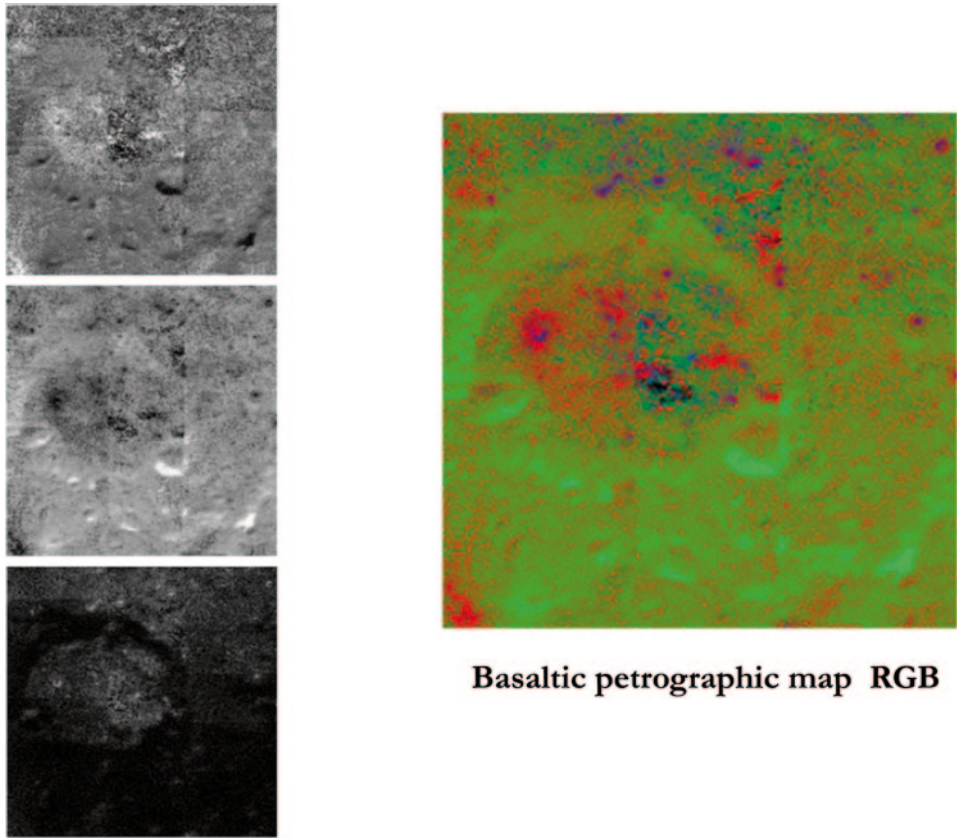
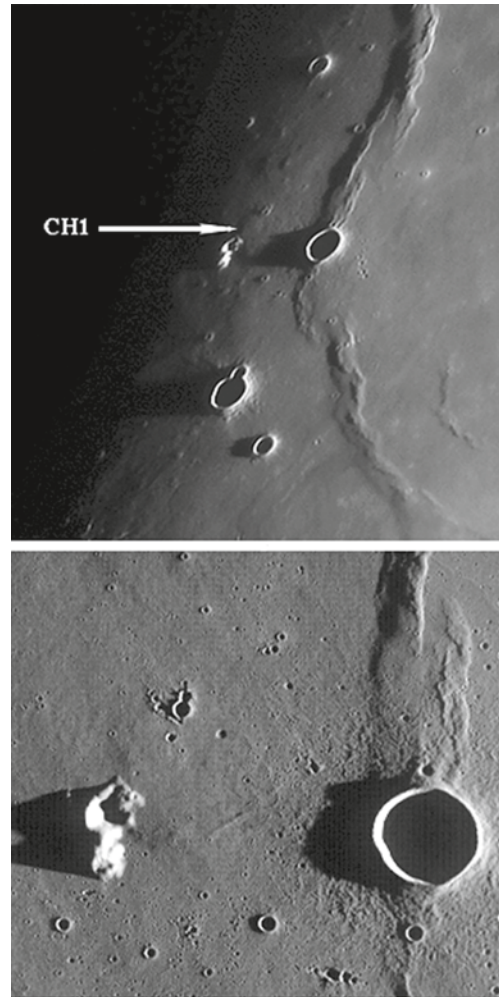


**Fig. 7.46** Basaltic petrographic map of Capuanus obtained based on Clementine UVVIS data. Low-Ti basalt (*top*), high-alumina basalt and highland material (*middle*), high-Ti basalt (*bottom*) and the corresponding RGB image

Sinus Iridum is a semi-circular mare region adjacent to Mare Imbrium at the northwest (Rükl 1999). We examined two different domes in Sinus Iridum. The first one, named Laplace 5 (L5), is located at longitude  $28.66^\circ$  W and latitude  $47.17^\circ$  N and has a diameter of  $9.0 \pm 0.5$  km (Fig. 7.48). Its height has been determined to  $125 \pm 15$  m, resulting in an average flank slope of  $1.60 \pm 0.10^\circ$ . The edifice volume has been determined to  $3.7$  km<sup>3</sup>. The Clementine UVVIS spectral data reveal a 750 nm reflectance of  $R_{750} = 0.1205$ , a low value of the UV/VIS colour ratio of  $R_{415}/R_{750} = 0.5533$ , indicating a low TiO<sub>2</sub> content, and  $R_{950}/R_{750} = 1.0290$ . The second dome, named Laplace 6 (L6), is situated at  $29.16^\circ$  W and  $47.08^\circ$  N and is considered a putative intrusive dome described further in Chap. 8. Laplace 5 belongs to class B<sub>2</sub>. Rheologic modeling (Sect. 2.5) of the effusive dome L5 indicates that it was formed by lava of moderate viscosity of  $2.4 \times 10^5$  Pa s erupting at a high effusion rate of  $111$  m<sup>3</sup> s<sup>-1</sup> over a period of time of 1.2 years. The dike model (Sect. 4.1) yields a magma rise speed of  $4.5 \times 10^{-5}$  m s<sup>-1</sup>, a dike width of 23 m, and a length of 107 km.

**Fig. 7.47** Telescopic image of CH1 dome (*top*). (Image by S. Lammel). LROC WAC image M116526790ME of CH1 (NASA/GSFC/Arizona State University) (*bottom*)



### 7.2.6 The Doppelmayer Region

The crater Doppelmayer is situated immediately south of Mare Humorum (Rükl 1999). The formation of the Humorum basin occurred about 3.9 Ga ago (Wilhelms 1987). Mare ridges and graben were formed due to faulting when the central basin part sank down as it was filled by mare lava (Wilhelms 1987).

We have examined two domes (Fig. 7.49) termed Doppelmayer 1 (Do1) and 2 (Do2). Doppelmayer 1 is situated at  $41.92^{\circ}$  W and  $30.08^{\circ}$  S, while the dome Doppelmayer 2 is located further south at  $43.42^{\circ}$  W and  $30.66^{\circ}$  S. Do1 appears to be smooth with a shallow, elongated crater on its summit. The location of this elongated crater pit on the dome relief suggests that it is the remnant of the effusion vent, but it might also be, as an alternative



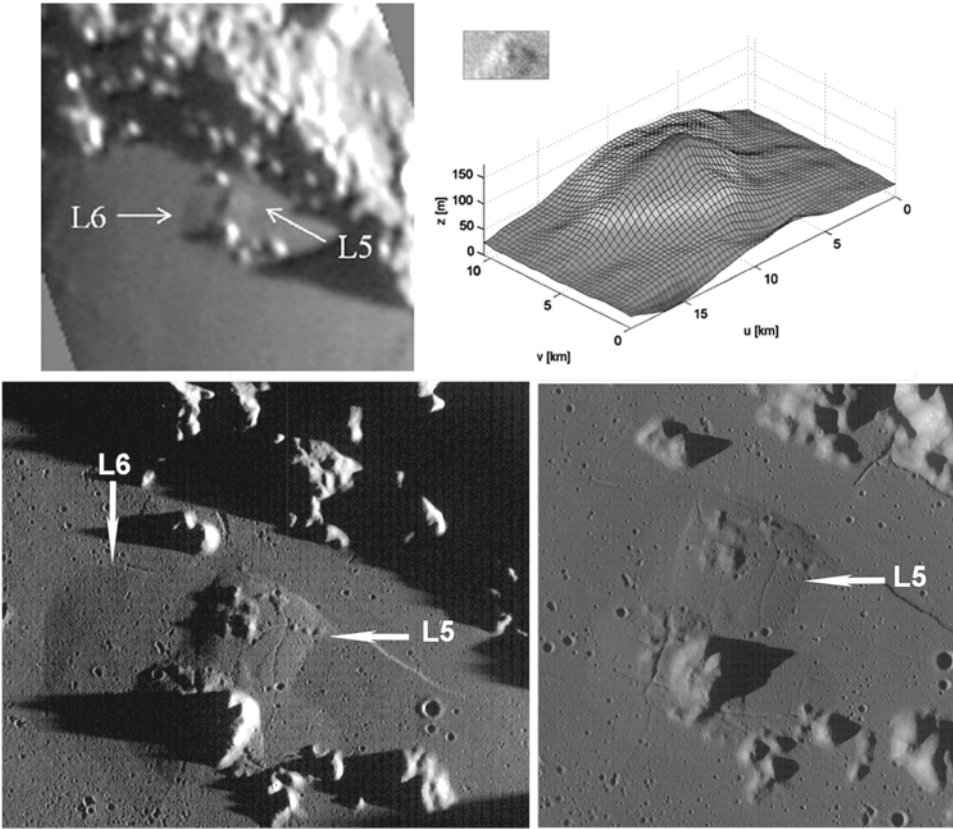
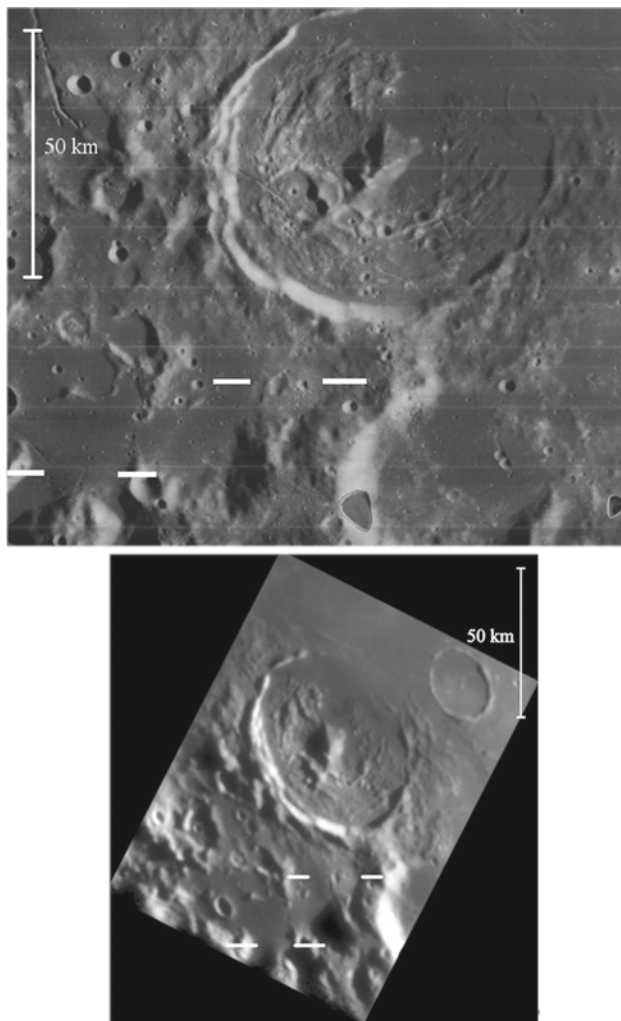


**Fig. 7.48** Telescopic image of domes Laplace 1 and 2 (*top left*). (Image by C. and A. Wöhler). DEM of the dome L5 (*top right*). LROC WAC image M116506243ME showing the domes L5 and L6 (NASA/GSFC/Arizona State University) (*bottom left*). LROC WAC image M117678537ME (NASA/GSFC/Arizona State University) (*bottom right*). Due to the high illumination angle, only the dome L5 is detectable, while the dome L6 is not clearly visible

explanation, a degraded impact or secondary crater. However, our interpretation that it is of volcanic origin is based on the observation that in the Lunar Orbiter image shown in Fig. 7.49, the summit crater is elongated and appears rimless and without a sharp outline. Hence, it looks different from nearby degraded small craters of impact origin. Furthermore, in the Lunar Orbiter image its rim does not cast a shadow at a solar elevation of  $16^\circ$ , under which the image was acquired. The dome diameter amounts to  $16.8 \pm 0.3$  km, the vent has a diameter of  $3.3 \pm 0.3$  km. Its depth was estimated based on the observed length of the shadow cast by its rim, which yields  $128 \pm 30$  m. The depth derived from the shadow length measurement must be considered as a lower limit because the shadow is not cast right into the middle of the vent but slightly off-center on its inner wall.



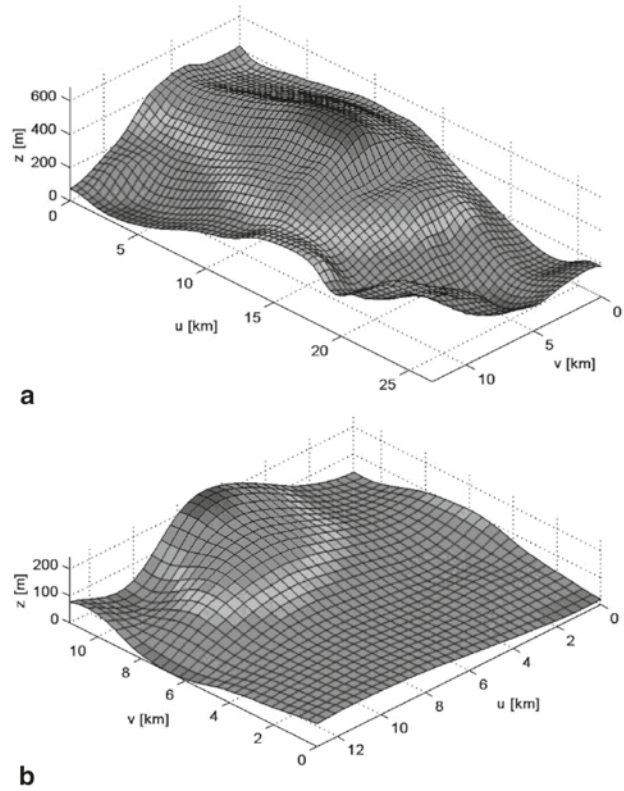
**Fig. 7.49** Lunar Orbiter high-resolution image IV-143-H1 of the region around Doppelmayer (*top*) (NASA/USGS). Telescopic image of two domes in Doppelmayer (*bottom*). (Image by J. Phillips). The two domes termed Doppel-mayer 1 and 2 are indicated by *horizontal line pairs*



Do1 has a height of  $410 \pm 40$  m, a flank slope of  $2.8 \pm 0.30^\circ$ , and an edifice volume of  $34 \text{ km}^3$ . However, the flank slope is an average value since the profile of Do1 is somewhat asymmetric, with the eastern flank being steeper than the western flank. The dome Do2 is situated adjacent to a non-volcanic mountain and has a diameter of  $12.6 \pm 0.3$  km. Do2 is lower and less voluminous than Do1, displaying a height of  $160 \pm 20$  m, a flank slope of  $1.15 \pm 0.15^\circ$ , and an edifice volume of  $2.8 \text{ km}^3$  (Fig. 7.50). Applying the rheologic model (Sect. 2.5), we obtained for the two domes comparable effusion rates of  $121 \text{ m}^3 \text{ s}^{-1}$  for Do1 and  $173 \text{ m}^3 \text{ s}^{-1}$  for Do2. They formed out of lava with viscosities of  $1.4 \times 10^7 \text{ Pa s}$  and  $3.1 \times 10^5 \text{ Pa s}$  over periods of time of 8.9 and 0.5 years, respectively.

Based on the dike model (Sect. 4.1), we obtained for Do1 a low magma rise speed of  $5.7 \times 10^{-6} \text{ m s}^{-1}$ , a dike width of 127 m, and a dike length of 167 km. The less viscous

**Fig. 7.50** **a** DEM of Do1, viewed from south-eastern direction. **b** DEM of Do2, viewed from north-eastern direction



lava of Do2 ascended at a higher speed of  $5.2 \times 10^{-5} \text{ m s}^{-1}$ , and its feeder dike is narrower ( $W=27 \text{ m}$ ) than the dike that formed Do1 but of comparable length ( $L=121 \text{ km}$ ). If we assume that the vertical extension of a dike is similar to its length (Head and Wilson 1992; Jackson et al. 1997), the magmas which formed the Doppelmayer domes originate from well below the lunar crust, for which a total thickness of 50 km is given by Wieczorek et al. (2006) for the region in which the domes are located.

The dome Do1 is spectrally red ( $R_{415}/R_{750}=0.5841$ ) and shows a very weak mafic absorption ( $R_{950}/R_{750}=1.0737$ ), implying a low  $\text{TiO}_2$  and FeO content. The overall spectral signature corresponds to that of a mixture between mare and highland soils (Fig. 3.3). The Clementine UVVIS spectral data of the dome Do2 reveal a 750 nm reflectance of  $R_{750}=0.1256$ , a UV/VIS colour ratio of  $R_{415}/R_{750}=0.5856$ , and  $R_{950}/R_{750}=1.0577$ .

Accordingly, Do1 belongs to class  $C_1$  with a tendency towards  $B_1$  due to its relatively steep flank slope. Do2 is a typical effusive mare dome, given its spectral and morphometric properties, and belongs to class  $C_1$ .

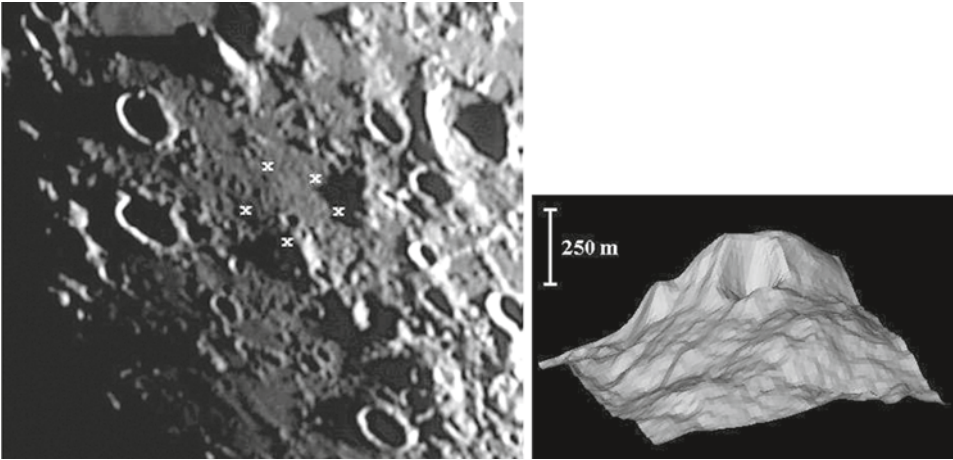


**Fig. 7.51** Telescopic image of the dome Mee 1 (*left*). (Image by J. Phillips). DEM of the dome Mee 1, viewed from northeastern direction (*right*). The vertical axis is 15 times exaggerated. The dome is apparent in the foreground, while the elevated terrain in the back ground corresponds to the northern end of the non-volcanic ridge visible in the telescopic CCD image

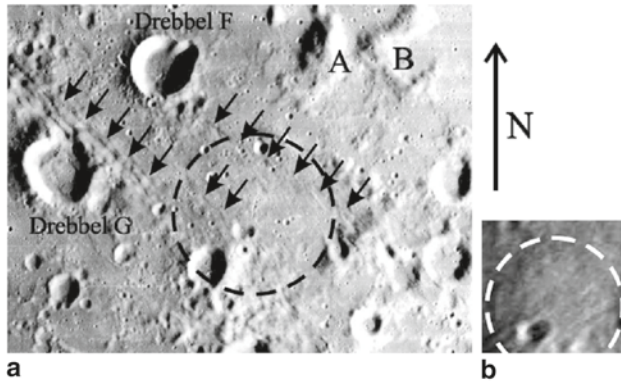


**Fig. 7.52** **a** Enlarged and contrast-enhanced section of Lunar Orbiter image IV-148-H2 (NASA/USGS). The dome Mee 1 is marked by a *circle* and lineations running radial to the Orientale basin are indicated by *arrows*. Two hills which are part of the uneven Orientale ejecta surrounding the dome are marked by *A* and *B*. **b** Telescopic CCD image of Mee 1 rectified to perpendicular view, indicating the regular circular shape of the dome outline. (Image by J. Phillips)

### 7.2.7 Region Around Mee

The lunar dome Mee 1 is situated near the craters Mee H and Drebbel F in a region exhibiting cryptomare deposits, probably the result of early mare volcanism prior to the impact that formed Mare Orientale (Hawke et al. 2007). The area around Mee 1 (Figs. 7.51, 7.52) is char-

acterised by lineations running radial to the Orientale basin and crossing the dome surface in some parts, thus indicating that the dome, located at 42.92° W and 43.50° S, was formed prior to the Orientale impact event. Mee 1 has a diameter of  $25 \pm 0.5$  km, a height of  $250 \pm 25$  m, a flank slope of  $1.15 \pm 0.10^\circ$ , and a volume of  $44 \text{ km}^3$ . Based on the models in Sects. 2.5 and 4.1, we obtained a magma viscosity of  $5.1 \times 10^5 \text{ Pa s}$ , a high effusion rate of  $869 \text{ m}^3 \text{ s}^{-1}$ , a duration of the effusion process of 1.6 years, a magma rise speed of  $1.9 \times 10^{-4} \text{ m s}^{-1}$ , a width of the feeder dike of 32 m and a length of 144 km. The Clementine UVVIS spectral data reveal a 750 nm reflectance of  $R_{750} = 0.1677$ , a UV/VIS colour ratio of  $R_{415}/R_{750} = 0.5863$ , and  $R_{950}/R_{750} = 1.0374$ . Accordingly, Mee 1 belongs to class  $C_1$  and to rheologic group  $R_1$ , the latter indicating an origin of the dome-forming magma from well below the lunar crust.

In this region, the Orientale impact event has led to mixing between mare and highland soils (Hawke et al. 2007). The observed spectral appearance of Mee 1 is therefore probably due to pronounced lateral mixing, resulting in highland material partially covering the mare surface around Mee 1. Hence, the dome Mee 1 may be called “cryptomare dome”. The material covering the cryptomare region around Mee 1 was presumably ejected during the impact event that formed the Orientale basin (Hawke et al. 1999, 2006, 2007), which was formed soon after the Imbrium basin 3.85 Ga ago (Wilhelms 1987). The dome Mee 1 was thus formed before the Orientale impact event. For comparison, the domes near Milichius, including M2 and M6, were formed during the Eratosthenian period, corresponding to 3.2–1.1 Ga ago (Wilhelms and McCauley 1971; Wenker 1999) and are thus more than 0.5 Ga younger than Mee 1. The mare surface in and around Mare Humorum, part of which is associated with the dome Doppelmayer 2, has an estimated age of about 3.2 Ga (Hiesinger et al. 2003), while the lavas of Mare Undarum surrounding the dome Condorcet 3 are of Upper Imbrian age, i.e. 3.2–3.8 Ga old (Olson and Wilhelms 1974).

Regarding the dome Mee 1 in comparison with the younger, Eratosthenian edifices M2, M6, and Do2, one might conclude that in the early geologic history of the Moon the conditions in the lunar interior led to large magma reservoirs. On the other hand, the morphometric, rheologic, and feeder dike characteristics of the ancient (older than 3.8 Ga) cryptomare dome Mee 1 and those of various younger mare domes are similar. These findings suggest that the conditions in the upper lunar mantle and the crust did not change fundamentally during the Imbrian period.

### 7.2.8 Gruithuisen Region

The highland domes Gruithuisen  $\gamma$  (G1, located at 40.38° W and 36.43° N) and  $\delta$  (G2, located at 39.42° W and 36.11° N), the Northwest Dome (G3) located nearby at 40.86° W and 36.92° N, and the three Mairan domes situated in the eastern part of Sinus Roris (Fig. 7.53a–b), are described as volcanic edifices by Head and McCord (1978). The Gruithuisen domes (Figs. 1.9a, 7.53a) are known to have large diameters around 20 km, heights of more than 1500 m and very high edifice volumes in excess of  $100 \text{ km}^3$  (Wilson and Head 2003). Their ages are determined by Wagner et al. (2002) to 3.72–3.85 Ga.

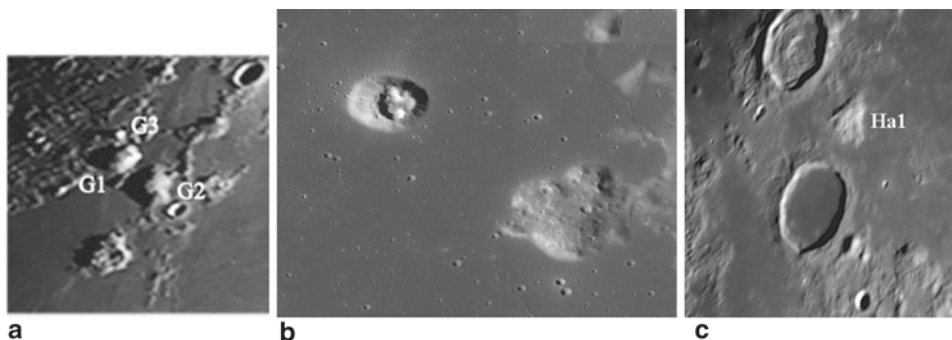


**Fig. 7.53** **a** Telescopic CCD image of the Gruithuisen domes (G1–G3). (Image by C. Wöhler). **b** Section of the global LROC WAC mosaic (NASA/GSFC/Arizona State University) showing the Mairan highland domes. **c** Telescopic image of Mons Hansteen (Ha1). (Image by R. Lena)

Wilson and Head (2003) show that while the eruption processes that formed Gruithuisen  $\delta$  and the nearby Northwest Dome occurred over more than 20 years at low effusion rates between  $6$  and  $50 \text{ m}^3 \text{ s}^{-1}$ , the effusion rate was  $119 \text{ m}^3 \text{ s}^{-1}$  for Gruithuisen  $\gamma$  over a period of 38 years. They furthermore find that the dome-forming lava had very high viscosities between  $10^8$  and  $10^9 \text{ Pa s}$ .

One must be careful when interpreting the flank slope values of the highland domes, since according to Wilson and Head (2003) the domes G1–G3 have been formed during at least two distinct subsequent eruption phases, respectively, a process that may build up steep edifices. They have diameters of  $19.0 \pm 0.4$ ,  $27.0 \pm 0.4$  and  $7.5 \pm 0.4 \text{ km}$ , respectively. According to the DEMs shown in Fig. 1.9, the heights of G1 and G2 correspond to  $1,740 \pm 100 \text{ m}$  and  $2,010 \pm 100 \text{ m}$ , while the height of G3 has been determined to  $1,250 \pm 100 \text{ m}$  based on measurements in the GLD100 topographic map (Scholten et al. 2012, cf. Appendix B for details), resulting in average flank slopes of  $10.4^\circ$ ,  $8.5^\circ$ , and  $18.4^\circ$ . The highland domes form a separate spectral and morphometric group (class G) in the classification scheme introduced in Chap. 5 due to their steep flank slopes, high edifice volumes, and red spectral signatures, suggesting that they have been formed by lava of significantly different composition, as shown by Kusuma et al. (2012), which erupted over a long period of time (Wilson and Head 2003).

For the Gruithuisen and Mairan highland domes, the inferred ratios between the time needed by the magma to ascend to the surface and the characteristic time scale of magma cooling (Chap. 4) are close to 1, such that the eruption temperature of the magma cannot have been much lower than the temperature at the dike source. If the realistic assumption of a magma temperature above the liquidus point at the dike source is made, the role of crystallisation and evolution due to cooling during magma ascent has supposedly not been of high importance for the Gruithuisen and Mairan highland domes. Hence, it is plausible to assume for the magmas that formed these domes a substantially higher Si content than typical of basaltic magma, supporting the idea by Chevrel et al. (1999) of an eruption of



highly viscous non-mare lavas of high Si and low FeO and TiO<sub>2</sub> content in this region. Chevrel et al. (1999) motivate this idea mainly with the strong differences between the spectral characteristics of highland domes and mare surfaces. A more direct evidence of the high Si content of the lavas that formed the Gruithuisen highland domes is provided by Kusuma et al. (2012) based on an analysis of the Christensen spectral feature, which is sensitive to the typical length of silicate molecule chains, using infrared spectral data of the LRO Diviner instrument (Kusuma et al. 2012). The dike dimensions inferred by Wilson and Head (2003) and the crustal thickness data by Wieczorek et al. (2006) indicate an origin of this lava in the lower crust.

### 7.2.9 Mons Hansteen

Mons Hansteen, also known as Hansteen  $\alpha$ , is located at the southwestern border of Oceanus Procellarum. Its spectral properties are similar to those of the Gruithuisen and Mairan highland domes (Hawke et al. 2003). Hawke et al. (2003) propose that Mons Hansteen is a volcanic structure formed by lavas of high viscosity, which is confirmed by Wagner et al. (2010). Accordingly, Mons Hansteen belongs to class G of our dome classification scheme. Its age is determined by Wagner et al. (2010) to 3.65–3.74 Ga.

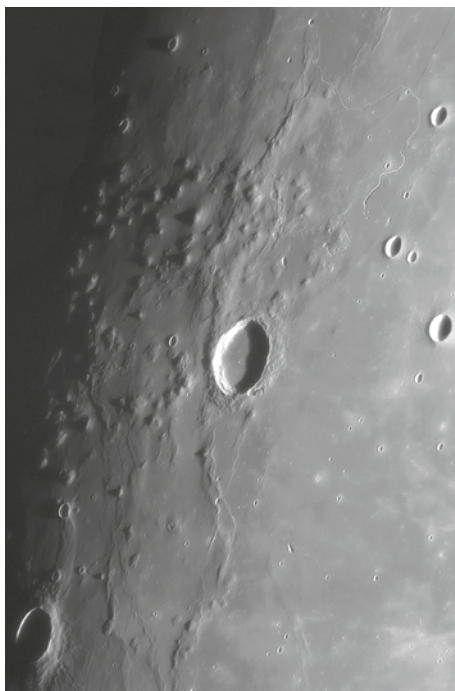
Mons Hansteen (Ha1, Figs. 1.9b, 7.53c) is of roughly triangular shape with a dimension of 29 km (north-south direction) by 27 km (east-west direction). The height of Mons Hansteen determined using the DEM shown in Fig. 1.9 amounts to 1,070 m for its highest part, while the average slope angle corresponds to 4.5°. The average Clementine  $R_{415}/R_{750}$  ratio of the central portion of Mons Hansteen is 0.5970, confirming its spectrally red appearance. Applying the rheologic model described in Sect. 2.5 to Mons Hansteen yields a lava viscosity of the order  $10^8$  Pa s. However, the rough surface texture of Mons Hansteen indicates viscous lava flows (Hawke et al. 2003), such that Mons Hansteen may have been formed during several subsequent effusion events. Hence, the obtained viscosity value is actually an upper bound. A presumably non-monogenetic mode of formation may be responsible for the peculiar shape of Mons Hansteen (cf. also Hawke et al. 2003).

### 7.2.10 Marius Hills

The complex structure of the class D domes Arago  $\alpha$  and  $\beta$  (A2 and A3 in Fig. 1.5d) and the majority of the volcanic edifices in the Marius Hills region (Fig. 1.8 for their localization and Fig. 7.54) indicates that they were probably formed during different subsequent effusion events (cf. Weitz and Head 1999). Clementine UVVIS data reveal that the surfaces of the examined domes consist of spectrally blue mare lavas with  $R_{415}/R_{750}$  ratios between 0.62 and 0.68. This rather broad range of  $R_{415}/R_{750}$  values indicates the presence of several units of different TiO<sub>2</sub> content (Weitz and Head 1999). The observed  $R_{950}/R_{750}$  ratios around 1.02 imply a weak to moderate mafic absorption and an overall high soil maturity.



**Fig. 7.54** Telescopic image of the Marius Hills region. (Image by M. Wirths). The diameter of the crater Marius corresponds to 41 km. The location of the domes is shown in Fig. 1.8



The domes in the Marius Hills region are characterised by flank slopes ranging from  $2^\circ$  to  $9^\circ$  and diameters between 4.5 and 15 km (Table 7.3). The edifice volumes span a broad range between 2 and  $42 \text{ km}^3$ . Marius domes belong to class  $H_1$  as introduced in Chap. 5. The small domes with  $D < 5 \text{ km}$  are assigned to subclass  $H_1$ . They are morphometrically similar to but spectrally bluer than similar domes of class  $E_1$  situated in the Milichius/T. Mayer region. Domes of subclass  $H_2$  with  $D > 5 \text{ km}$  and flank slopes below  $5^\circ$  morphometrically resemble the steep domes of class  $B_1$  situated north of the crater Hortensius and in Mare Undarum, but their irregular shapes also indicate a formation during several effusive episodes. Domes of subclass  $H_3$  have diameters comparable to those of monogenetic class  $B_1$  domes, but their flank slopes are all steeper than  $5^\circ$  and reach values of up to  $9^\circ$ . Such extraordinarily steep flank slopes have not been observed for monogenetic mare domes located in other dome fields. The rheologic model (Sect. 2.5) cannot be applied directly to the non-monogenetic Marius Hills domes as they presumably consist of several superimposed volcanic constructs (Figs. 1.8a–b, 7.54 and 7.55) (Weitz and Head 1999).

For the three example domes Ma23 ( $D = 4.5 \text{ km}$ , slope =  $5.3^\circ$ , subclass  $H_1$ ), Ma17 ( $D = 10.4 \text{ km}$ , slope =  $3.9^\circ$ , subclass  $H_2$ ), and Ma29 ( $D = 7.2 \text{ km}$ , slope =  $9.0^\circ$ , subclass  $H_3$ ), we estimated based on the rheologic model (Sect. 2.5) the lava viscosity, the effusion rate, and the duration of the effusion process, where it was assumed that the volcanic edifice is composed of two layers of a maximum thickness corresponding to half the dome height (Fig. 1.8b). The approximate diameter of the assumed upper layer is inferred from the

**Table 7.3** Morphometric and rheologic properties of the Marius Hills domes

Dome	Longitude (°)	Latitude (°)	Slope (°)	D (km)	h (m)	V (km <sup>3</sup> )	Class
Ma1	−55.53	9.88	5.70	7.8	390	10.7	H <sub>2</sub>
Ma2	−55.26	10.32	5.50	12.1	580	36.6	H <sub>3</sub>
Ma3	−55.81	10.32	2.10	6.4	120	1.9	H <sub>2</sub>
Ma4	−56.15	10.72	3.90	6.1	210	3.7	H <sub>2</sub>
Ma5	−55.96	10.72	3.50	5.9	180	3.4	H <sub>2</sub>
Ma6	−56.83	10.58	3.40	6.1	180	3.7	H <sub>2</sub>
Ma7	−56.67	11.10	2.90	9.2	230	7.6	H <sub>2</sub>
Ma8	−56.61	11.74	3.80	6.4	210	3.0	H <sub>2</sub>
Ma9	−55.68	11.04	2.80	8.1	200	7.6	H <sub>2</sub>
Ma10	−56.37	12.19	4.30	7.5	280	4.0	H <sub>2</sub>
Ma11	−56.60	12.49	4.10	10.9	390	14.8	H <sub>2</sub>
Ma12	−53.88	13.13	3.90	6.4	220	4.2	H <sub>2</sub>
Ma13	−54.45	10.58	5.30	7.8	360	7.0	H <sub>3</sub>
Ma14	−53.73	11.02	2.70	7.5	180	3.8	H <sub>2</sub>
Ma15	−53.35	10.99	3.90	14.2	480	42.2	H <sub>2</sub>
Ma16	−53.14	11.90	2.20	11.2	220	15.6	H <sub>2</sub>
Ma17	−57.44	13.45	3.90	10.4	350	17.0	H <sub>2</sub>
Ma18	−56.90	14.22	5.80	7.9	400	10.1	H <sub>3</sub>
Ma19	−56.09	14.28	5.60	8.5	420	11.3	H <sub>3</sub>
Ma20	−55.70	14.25	3.00	9.7	250	7.6	H <sub>2</sub>
Ma21	−55.18	13.04	3.20	8.9	250	9.0	H <sub>2</sub>
Ma22	−55.11	14.34	4.20	7.3	270	6.3	H <sub>2</sub>
Ma23	−54.73	14.14	5.30	4.5	210	1.9	H <sub>1</sub>
Ma24	−54.44	14.39	3.70	5.8	190	3.2	H <sub>2</sub>
Ma25	−54.20	14.65	5.80	7.5	380	9.0	H <sub>3</sub>
Ma26	−53.60	14.75	8.50	7.1	530	10.4	H <sub>3</sub>
Ma27	−53.65	15.26	6.10	6.5	350	7.3	H <sub>3</sub>
Ma28	−53.25	15.09	4.20	11.5	420	21.8	H <sub>2</sub>
Ma29	−52.97	14.28	9.00	7.2	570	13.1	H <sub>3</sub>
Ma30	−52.94	13.53	8.30	7.4	540	13.5	H <sub>3</sub>

constructed DEM of the dome; it typically corresponds to 70–80 % of the dome diameter. The modelled lava viscosities are always of the same order of magnitude for the lower and the upper dome layer, respectively. They are of the order  $10^6$  Pa s for Ma23 and Ma17 and  $10^7$  Pa s for Ma29, while the effusion rates are always between about 10 and  $100 \text{ m}^3 \text{ s}^{-1}$ . Lava effusion occurred over increasingly long periods of time of about 2, 4, and 10 years for the domes representing subclasses H<sub>1</sub>, H<sub>2</sub>, and H<sub>3</sub>. The modelled magma rise speed (Sect. 4.1) amounts to several  $10^{-6} \text{ m s}^{-1}$  for Ma23 and Ma17 and is lower by a factor of about three for Ma29. The dike width corresponds to 30–50 m for Ma23 and Ma17 and to about 150 m for Ma29.

**Fig. 7.55** DEM of the central part of the Marius Hills region, constructed using the method by Grumpe and Wöhler (2011) based on GLD100 topographic data (Scholten et al. 2012, cf. Appendix B) and M<sup>3</sup> image data. View from southwestern direction. The vertical axis is six times exaggerated. The dome designations are inserted according to Fig. 1.8a



The dike length has similar values between 140 and 190 km for all three domes. As a general result, the inferred rheologic properties and dike dimensions of the Marius domes are comparable to those of monogenetic domes of the classes B<sub>2</sub>, B<sub>1</sub>-E<sub>1</sub>, and the steepest B<sub>1</sub> domes, for subclasses H<sub>1</sub>, H<sub>2</sub>, and H<sub>3</sub>, respectively.

The petrographic mapping technique based on Clementine UVVIS+NIR data (Sect. 3.3) does not reveal a compositional contrast of the Marius domes with respect to each other and to the surrounding mare surface (Table 7.4). Similarly, the absorption wavelength and FWHM of the ferrous absorption trough around 1,000 nm, which we extracted from thermally corrected M<sup>3</sup> spectra, do not show strong differences between the domes and the surrounding surface.

However, the analysis of M<sup>3</sup> data by Besse et al. (2010) reveals that the integrated band depth of the 1,000 nm absorption (IBD1) is lower for many Marius domes than for the surrounding surface, while the integrated band depth of the pyroxene-related absorption trough around 2,000 nm (IBD2) is higher. We observed the same spectral contrasts when analysing thermally corrected M<sup>3</sup> spectra (Fig. 1.8d), where the domes appear as green patches. Besse et al. (2010) suggest that these spectral differences are related to variations in composition between the dome material and the surrounding mare surface due to the high viscosity of the dome-forming lava. However, the complex shape of most Marius Hills domes suggests the presence of individual flow units. Hence, the strongly non-uni-

**Table 7.4** Elemental abundance values (in wt%) of some Marius Hills domes, inferred according to Sect. 3.3

Dome	Fe (%)	Mg (%)	Ca (%)	Al (%)	Ti (%)	O (%)
Ma1	12.6	7.9	8.7	9.5	2.4	43.5
Ma 2	12.8	7.8	8.5	8.7	2.2	43.5
Ma 3	12.8	7.8	9.3	9.4	2.2	43.4
Ma 13	12.6	7.8	9.1	9.3	2.2	43.4
Ma 14	12.8	7.8	8.7	9.1	2.1	43.5
Ma 15	13.0	7.9	8.6	8.9	2.3	43.4
Ma 16	12.9	7.8	8.7	9.1	2.1	43.5
Ma 23	12.3	7.2	9.0	9.5	2.1	43.5
Ma 24	12.5	7.2	9.1	9.5	2.2	43.5
Ma 25	12.6	7.2	9.1	9.5	2.1	43.5
Ma 26	12.2	7.8	8.9	9.6	2.1	43.7
Ma 27	12.2	7.5	9.2	9.6	2.1	43.6
Ma 28	12.5	7.7	8.7	9.3	2.2	43.6
Ma 29	12.8	7.9	8.8	8.9	2.3	43.3
Ma 30	12.6	7.1	9.2	9.9	2.1	43.8

form morphometric properties of the domes are presumably mainly due to differences in magma supply, cooling, and crystallization (cf. Weitz and Head 1999).

### 7.2.11 Mons Rümker

With its diameter of 65 km, the volcanic complex Mons Rümker located in the north-western part of Oceanus Procellarum is the largest contiguous lunar volcanic structure (Figs. 1.6a–b, 7.56, 7.57). The lower central part of Mons Rümker is surrounded by a more elevated ring-shaped structure. Several mare domes are superimposed on the plateau (Smith 1974). Mons Rümker is situated approximately in line with the Marius Hills and the volcanic Aristarchus plateau (Smith 1974).

According to Clementine UVVIS data, the largely uniform surface of Mons Rümker consists of spectrally strongly red mare lava (Table 7.5) (Weitz and Head 1999). The DEM shown in Fig. 7.57 shows that the height of the plateau amounts to about 900 m in its western and northwestern part, 1,100 m in its southern part, and 650 m in its eastern and north-eastern part. The DEM of the western part of Mons Rümker shown in Fig. 1.6b, which has been obtained by shape from shading analysis of an image of the AMIE camera on board the Smart-1 spacecraft, yields similar height values. Six domes are sufficiently well resolved in the telescopic image shown in Fig. 7.57 for morphometric evaluation (Table 7.5). For the domes R3 and R4, the DEM in Fig. 1.6b yields heights of  $275 \pm 20$  m and  $185 \pm 20$  m, respectively, compared to  $240 \pm 20$  m and  $170 \pm 20$  m obtained based on the telescopic CCD image shown in Fig. 7.57. The similar values and overlapping error intervals for these two

**Fig. 7.56** Telescopic CCD image of the Mons Rümker volcanic complex. (Image by J. Phillips)

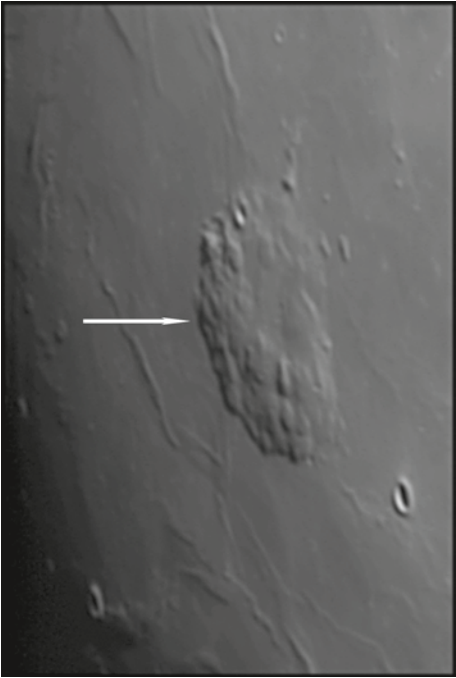


**Fig. 7.57** Section of Lunar Orbiter image IV-163-H2 (*top left*) (NASA/USGS). Telescopic CCD image of Mons Rümker, rectified to perpendicular view (*top right*). (Image by K. C. Pau). The individual domes R1-R6 are marked; DEM of Mons Rümker (*bottom*), derived from the preceding telescopic image viewed from southeastern direction (*top right*). The vertical axis is ten times exaggerated

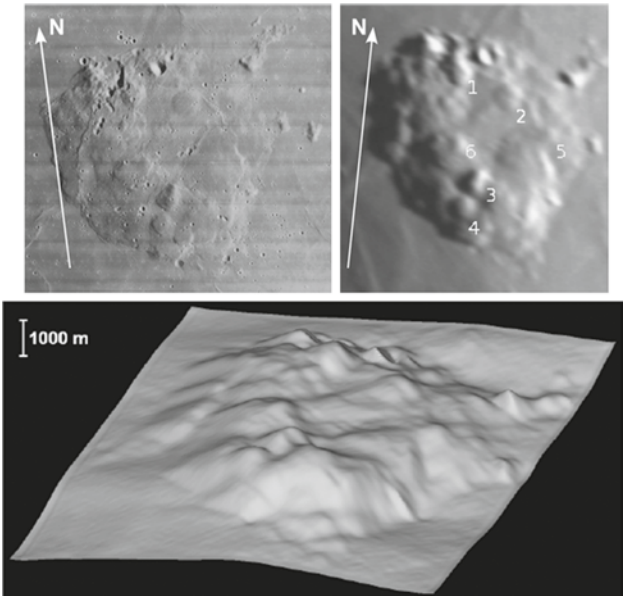


**Table 7.5** Morphometric and rheologic properties of the Rümker domes

Dome	Longi- tude (°)	Latitude (°)	$R_{750}$	$R_{415}/R_{750}$	$R_{950}/R_{750}$	Slope (°)	D (km)	h (m)	V (km <sup>3</sup> )	$\eta$ (Pa s)	E (m <sup>3</sup> s <sup>-1</sup> )	T (years)	U (m s <sup>-1</sup> )	W (m)	L (Km)
R1	-58.80	41.50	0.1127	0.5667	1.0410	2.7	8.4	200	5.7	$2.4 \times 10^6$	61	3.0	$2.4 \times 10^{-5}$	29	88
R2	-58.00	41.30	0.1166	0.5607	1.0305	1.6	9.1	130	4.3	$2.5 \times 10^5$	111	1.2	$1.9 \times 10^{-4}$	11	51
R3	-58.30	40.30	0.1104	0.5643	1.0369	3.0	9.1	240	7.6	$4.8 \times 10^6$	60	4.0	$1.8 \times 10^{-5}$	39	85
R4	-58.00	40.10	0.1124	0.5751	1.0013	2.7	7.3	170	3.7	$1.5 \times 10^6$	55	2.1	$2.5 \times 10^{-5}$	24	89
R5	-57.30	41.00	0.1162	0.5955	0.9718	1.5	5.5	70	0.9	$4.0 \times 10^4$	75	0.4	$5.5 \times 10^{-4}$	6	25
R6	-58.70	40.60	0.1072	0.5622	1.0428	1.7	6.9	100	2.2	$1.4 \times 10^5$	83	0.8	$2.3 \times 10^{-4}$	9	40



domes indicate a good reproducibility of dome height measurements obtained using shape from shading applied to strongly different image data.

A classification of the domes yields that due to their rather small diameters and spectrally red surfaces they belong to classes  $B_1$ , denoting flank slopes steeper than  $2^\circ$ , and  $B_2$ , representing lower slopes. Only the very small dome R5 is similar to the domes M7 encountered in Mare Insularum near T. Mayer (Table 7.5). According to the rheologic model (Sect. 2.5), we obtained viscosity values between  $4 \times 10^4$  Pa s and  $5 \times 10^6$  Pa s, effusion rates between 50 and  $110 \text{ m}^3 \text{ s}^{-1}$ , and durations of the effusion process between 0.4 and 4 years.

If it is assumed that the average dike length of the domes R1–R6 corresponds to the diameter of the Rümker plateau, we obtain (Sect. 4.1) a driving pressure gradient of the ascending magma of  $689 \text{ Pa m}^{-1}$ , where the resulting dike widths correspond to 6–39 m and the magma ascended at low speeds between  $10^{-5}$  and  $10^{-4} \text{ m s}^{-1}$  (Table 7.5). The “default” pressure gradient of  $328 \text{ Pa m}^{-1}$  (Wilson and Head 1996) would result in dike length and width values about twice as high as those listed in Table 7.5 and four times lower values for the magma rise speed.

The rheologic modelling results confirm that the domes were produced by low effusion rates, possibly during the final stage of the eruptions that emplaced the plateau (cf. Weitz and Head 1999). The significant variations across the inferred viscosity values cannot be attributed to compositional differences as the Rümker plateau is spectrally homogeneous. They are more likely caused by different lava eruption temperatures and degrees of crystallization. Under the assumption that the vertical dike extension is similar to the dike length (Head and Wilson 1992; Jackson et al. 1997) and that the crustal thickness in the Rümker region amounts to 50 km (Wieczorek et al. 2006), the dome-forming magma originates from just below the lunar crust.

---

**Abstract**

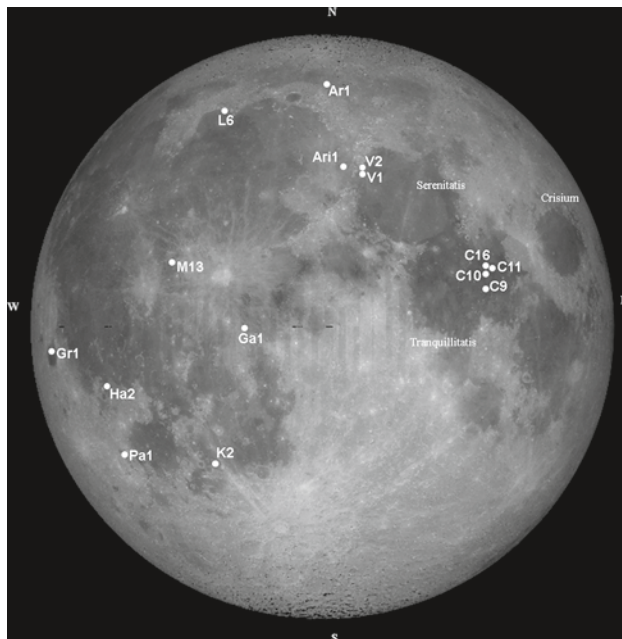
This chapter provides a discussion of the putative lunar intrusive domes, their morphometric properties and the conjunction of the large specimens with linear rilles.

In this chapter we describe the morphometric properties of putative lunar intrusive domes. The flat appearance of these domes and the absence of indicators of flowing lava, such as summit vents or outflow channels, suggest that they were not formed by effusion of lava but by pressurized magma intruding between rock layers and bending upwards the overburden layers (Fig. 8.1).

Clementine multispectral UVVIS imagery indicates that the candidate intrusive domes do not preferentially occur in specific types of mare basalt. The determination of their morphometric properties reveals large dome diameters between 10 and more than 30 km, flank slopes below  $0.9^\circ$ , and volumes ranging from 0.5 to 50 km<sup>3</sup>. Three distinct morphometric classes of candidate intrusive domes have been established. Table 8.1 reports the flank slope, diameter, height, and edifice volume of the candidate intrusive domes examined so far. The diameter vs. flank slope and volume vs. flank slope relations of these domes are illustrated in Fig. 5.4.

The first class, In1, comprises large domes with diameters above 25 km and flank slopes of  $0.2\text{--}0.6^\circ$ , class In2 is made up by smaller and slightly steeper domes with diameters of 10–15 km and flank slopes between  $0.4$  and  $0.9^\circ$ , while domes of class In3 have diameters of 13–20 km and flank slopes below  $0.3^\circ$ . The morphometric properties of classes In2 and In3 domes overlap with those of some classes of lunar effusive domes, but a distinction is possible due to the characteristic non-circularity of the outlines of the domes of classes In2 and In3. A comparison between the candidate intrusive domes and typical domes of classes 5 and 6 as defined by Head and Gifford (1980) reveals that class 6 domes are smaller and display more circular outlines. All candidate intrusive domes are usually not closely associated with or limited by highland terrain but appear as smooth continuations of the mare surface

**Fig. 8.1** Map Lunar map of the putative intrusive domes described in the text. Basemap: Clementine (NASA, <http://photojournal.jpl.nasa.gov/catalog/PIA00302>)



surrounding them, lacking any specific spectral contrast. It is therefore unlikely that they are kipukas. Class 5 domes, which were formed by lava covering an older highland surface (Head and Gifford 1980), have similar diameters as the candidate intrusive domes of classes In2 and In3 but exhibit steeper flank slopes as well as outlines of circular shape for those parts of their boundaries that are not limited by the adjacent highland terrain.

Under the assumption of an intrusive origin of the examined domes, the laccolith model by Kerr and Pollard (1998) has been used to estimate the corresponding geophysical parameters, especially the intrusion depth and the magma pressure (Wöhler and Lena 2009) (Sect. 4.3.2). The morphometric properties of the dome classes In1–In3 have been related to the modelled laccolith parameters (Table 8.1).

According to our modelling results, domes of class In1 are characterised by uppermost basaltic layer thicknesses of 0.2–0.5 km and more, intrusion depths of 2.2–11.4 km, and magma pressures of 18–100 MPa. For the smaller and steeper domes of class In2, the uppermost basaltic layer has a thickness of less than 0.3 km, the magma intruded to shallow depths between 0.4 and 1.1 km while the inferred magma pressures range from 3 to 9.5 MPa. Class In3 domes are similar to those of class In1 with similar thicknesses of the uppermost basaltic layer ranging from 0.6 to 1.0 km, intrusion depths of 1.9–2.5 km, and magma pressures of 15–22 MPa. The comparative numerical modelling of laccolith properties in terms of an elastic plate model, especially their characteristic sizes and thicknesses, under terrestrial and lunar conditions performed by Michaut (2011) is in favour of an intrusive interpretation of large, low, and smooth lunar structures. However, alternative modes of formation are still imaginable.

All domes of class In1 show fractures on their surfaces. These linear rilles were probably formed by the tensional stress fields associated with dikes that ascended to shallow

**Table 8.1** Morphometric properties of candidate intrusive domes of the classes In1–In3 and modeling results for the minimum basaltic layer thickness  $h_1$ , intrusion depth  $d$ , and maximum magma pressure  $p_0$  obtained based on the model by Kerr and Pollard (1998)

Dome	Longitude (°)	Latitude (°)	Slope (°)	D (km)	h (m)	V (km <sup>3</sup> )	$h_1$ (km)	$d$ (km)	$p_0$ (MPa)	Class
K2	–23.82	–28.30	0.15	51 × 34	55	37	1.2	11.4	99.0	In1
Ga1	–14.84	–0.75	0.57	30	140	50	0.28	2.2	17.7	In1
V1	10.20	30.70	0.55	30	130	42	0.27	2.5	19.7	In1
M13	–31.53	11.68	0.41	27.8	100	15	0.50	2.9	23.2	In1
Ar1	0.71	55.71	0.25	33.0	70	22	0.24	3.5	27.7	In1
Gr1	–68.62	–04.45	0.62	36 × 24	160	75	0.7	2.4	19.0	In1
Ari1	05.67	33.28	0.22	54 × 35	85	63	1.1	7.9	66.0	In1
Ha2	–48.20	–10.57	0.52	21 × 16.7	85	12	0.20	1.10	9.5	In2
C11	36.75	11.06	0.70	12.2	75	6.4	0.07	0.50	3.8	In2
C16	32.35	11.95	0.73	16 × 12.5	90	7.0	0.19	0.63	4.9	In2
Pa1	–47.88	–26.63	0.50	13.5	60	4.3	0.12	0.91	7.2	In2
L6	–29.16	47.08	0.70	10	95	1.5	0.10	0.83	4.2	In2
V2	10.26	31.89	0.82	11	80	1.9	0.08	0.38	2.9	In2
Du3	71.30	5.45	0.88	11.7	90	3.0	0.09	0.52	4.1	In2
C9	34.66	7.06	0.13	13.3	15	0.5	0.56	2.5	21.7	In3
C10	35.19	10.00	0.30	19.2	50	10	1.0	1.9	15.3	In3

depths below the surface (Head and Wilson 1996; Wilson and Head 1996, 2002). Linear rilles traversing the summit are detectable on large and low domes located in Grimaldi, near Milichius, Aristillus, Gambart, Archytas, Kies, and on the surface of Valentine dome, termed Gr1 (Fig. 8.6), M13 (Figs. 1.5a and 8.6), Ari1 (Figs. 1.15d and 8.4), Ga1 (Fig. 8.5a–c), Ar1 (Fig. 1.5c), K2 (Figs. 2.8 and 8.2–8.3) and V1 (Figs. 1.13 and 1.15b), respectively. The domes V1, M13 and Ar1 display faults on their surfaces, suggesting that to a limited extent piston-like uplift according to the third phase of laccolith growth (Wichman and Schultz 1996) might have occurred for V1, M13, and Ar1 (Sect. 4.3).

The dome K2 is associated with a linear rille and has a sinuous rille on its surface, the latter clearly indicating an effusion of lava (Figs. 8.2–8.3). Some non-volcanic hills are em-bayed by lavas. Presumably, these hills are part of the underlying rugged basin floor below the mare lavas. Due to the presence of different rilles, the large dome K2 is similar to the well known Valentine dome V1, which shows a sinuous rille and a curvilinear rille on its surface (Fig. 1.13). The sinuous rille can be interpreted as a lava channel, while the curvilinear rille traversing the surface of K2 is likely due to a dike which remained subsurface, applying stress to the surface layers to form the rille. The resulting tensional stress field led to the formation of the southern rille, and the dome was formed in a way similar to a terrestrial laccolith. Although the sinuous rille crossing the surface of K2 (Fig. 8.3) indicates flowing of low-viscosity lava, it is presumably not an outflow channel of K2 as according to LOLA DEM data its end points are both located on the elevation level of the surrounding mare surface; the rille traverses the complete dome surface and does not start on the dome

**Fig. 8.2** Telescopic CCD images of the lunar dome Kies 2 (K2) of possibly intrusive origin. Image by P. Lazzarotti

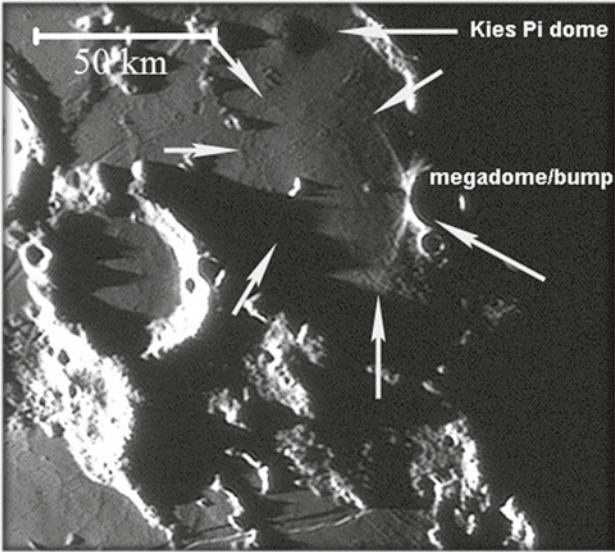
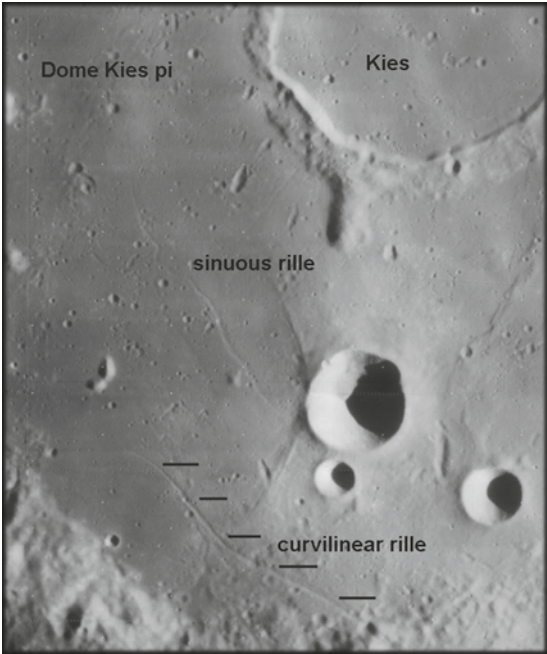


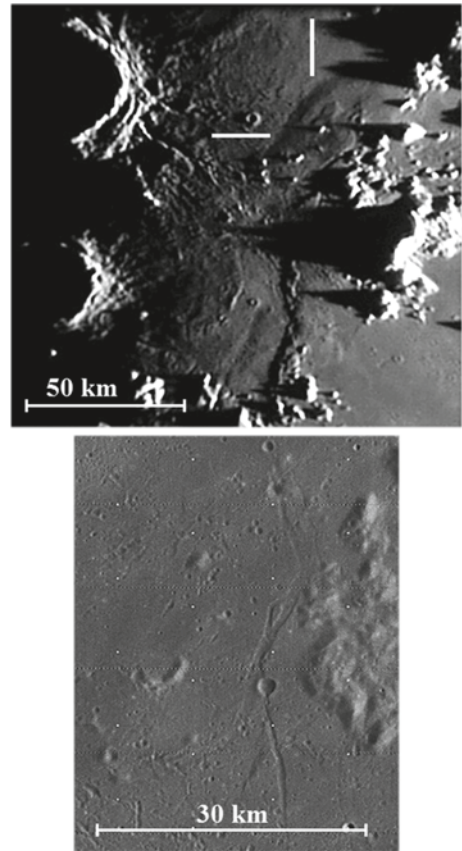
**Fig. 8.3** Lunar Orbiter image IV-125-H1 (NASA/USGS) of K2. Due to the comparably high illumination angle, the dome itself is not visible, but the sinuous rille and the curvilinear rille on its surface are clearly apparent



summit. Hence, the sinuous rille was probably formed prior to K2 during a different phase of volcanism.

The dome Gambart 1 (Ga1) is located in the southern part of Mare Insularum at longitude 14.84° W and latitude 0.75° S and has a diameter of about 30 km. Several individual

**Fig. 8.4** (*top*) Telescopic CCD image of the large dome Ari1 near crater Aristillus. Image by R. Lena; (*bottom*) Lunar Orbiter image IV-110-H1(NASA/USGS) showing the surface of the dome Ari1. A straight rille on the surface of Ari1 is apparent, while sinuous rilles are absent



rilles can be distinguished on its surface (Fig. 8.5a-c). In the northern part of this dome there is a straight rille, likely due to tensional stress consistent with laccolith formation where the pressurized magma beneath the surface not only led to upbowing of the surface rock layers but also to fracturing. Further rilles are visible on the surface of the ridge located nearby in southwestern direction but not on the dome itself.

The large and low class In1 domes V1 and M13 and also the smaller and steeper class In2 dome V2 show small non-volcanic hills on their surfaces. Presumably, these hills are part of the basin floor below the mare lavas. In the case of V1 and V2 (Fig. 1.13), they closely resemble nearby hills belonging to the Serenitatis basin rim just outside the mare region, which are characterised by heights (inferred from shadow length measurements) of not more than a few hundred metres. Accordingly, the hills occurring on the surface of some domes indicate layers of mare basalt only a few hundred metres thick. The exceptionally steep flank slopes of the dome V2 may even be a direct consequence of the fact that both domes formed around a pre-existing non-volcanic hill, as a pre-existing hill in the centre of a laccolith should reduce the tensional stress resulting from the strong bending of the overburden due



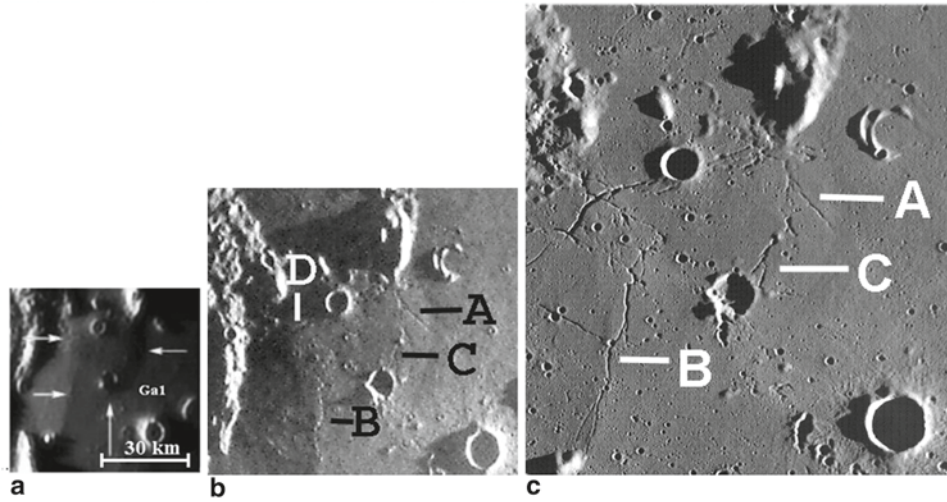
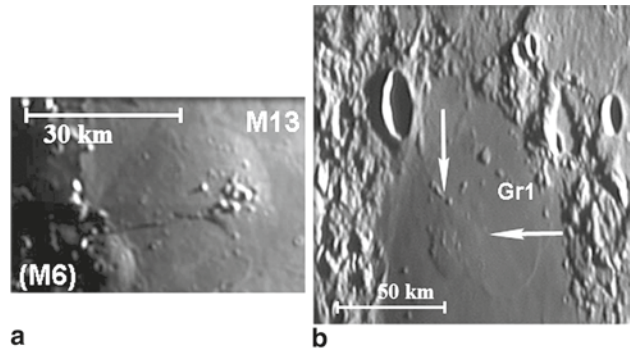


**Fig. 8.5** **a** Telescopic CCD images of the lunar dome Ga1 near the crater Gambart in Mare Insularum. Images by R. Lena. **b** Apollo 12 image AS12-50-7438 (NASA). The letters A-D identify some rilles on the dome Ga1. **c** Section of LROC image WAC M116412029ME showing the dome Ga1 and the rilles (NASA/GSFC/Arizona State University)

**Fig. 8.6** **a** Dome M13 in Mare Insularum. Image by J. Phillips. **b** Dome Gr1 on the floor of Grimaldi. Image by K. C. Pau



to the steep flank slope, thus preventing deep fracturing and subsequent eruption of the pressurized magma. Due to the asymmetric profiles of V1 and V2 (one side of each dome is formed by a fault with a comparably steep slope, while at the opposite side the dome surfaces merge smoothly into the surrounding mare), it appears unlikely that they were formed by lava flowing over pre-existing highland terrain (class 5 by Head and Gifford 1980), since such asymmetric cross-sectional shapes are uncommon for lunar effusive domes.

The dome Ha2 (Figs. 2.4 and 8.7–8.8) shows a similar elongated shape and dimensions comparable to other domes of class In2, like C16 (Figs. 7.6–7.7 and 8.10a), C11, L6, V2

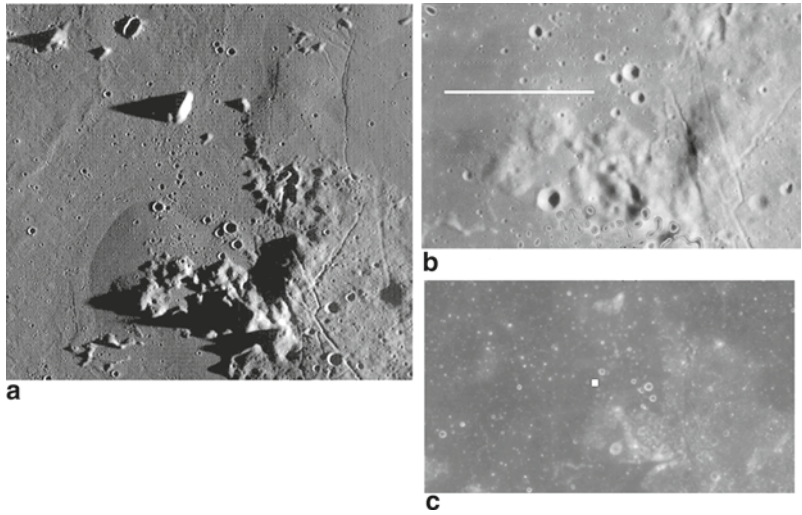


**Fig. 8.7** **a** WAC image M116629324ME (NASA/GSFC/Arizona State University) of the dome Hansteen 2 termed Ha2. **b** Lunar Orbiter image IV-149-H2 of Ha2 (NASA/USGS). Due to the comparably high illumination angle, the dome itself is not clearly visible. The *white line* indicates the location of the cross-sectional profile shown in Fig. 2.4c. **c** Clementine 750 nm image (USGS, <http://www.mapaplanet.org>), including the dome Ha2 marked by a *white square*

**Fig. 8.8** LOLA DEM of the dom Hansteen 2, where a part of the LROC WAC image shown in Fig. 8.7a is used as an overlay

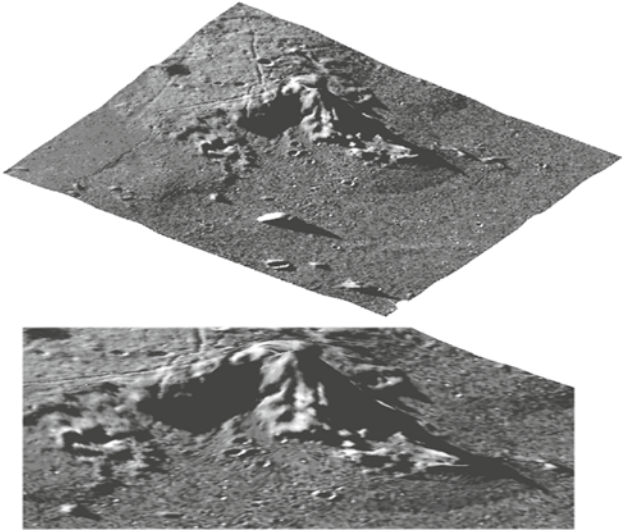


**Fig. 8.9** (*top left*) Tele-  
scopic CCD images of  
the domes V2 of class In2  
located at the western  
border of Mare Serenitatis  
and to the north of the large  
Valentine dome V1 of class  
In1. Image by K. C. Pau;  
(*top right*) The dome L6  
near Sinus Iridum of class  
In2. Image by C. Wöhler;  
(*bottom*) The domes C11 of  
class In2 and C10 of class  
In3 near Rima Cauchy.  
Image by P. Lazzarotti

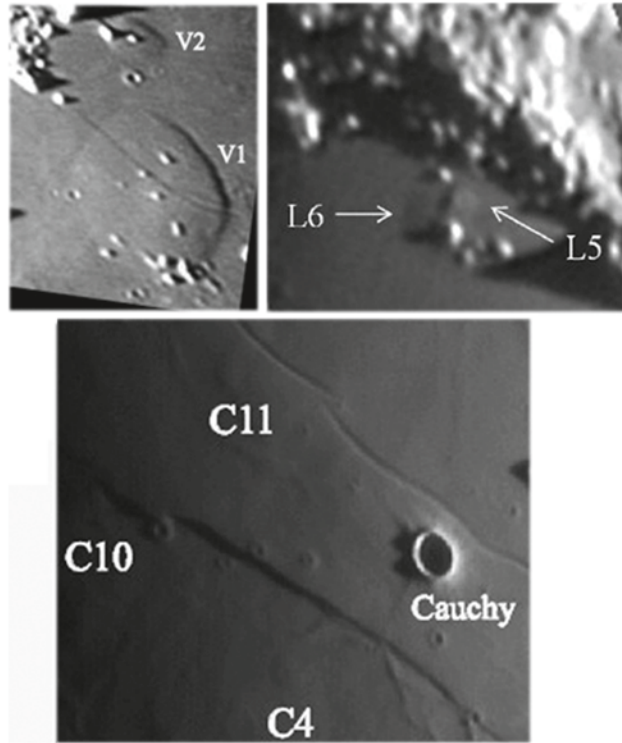


(Fig. 8.9), Pa1 (Fig. 8.10b), and Du3 in Mare Undarum (Fig. 7.30), but with larger diameter and inferred edifice volume. Another candidate intrusive dome is C16, due to its elongated outline (circularity 0.78) and flat summit it has been assigned to class In2. For the dome C16 a minimum thickness of the uppermost mare basalt layer of  $h_1 = 0.19$  km, an intrusion depth of  $d = 0.63$  km and a maximum magma pressure of  $p_0 = 4.9$  MPa was inferred.

The dome Palmieri 1 (Pa1) is another exemplar of class In2 and lies near the crater Palmieri located southwest of Mare Humorum. Its height amounts to  $60 \pm 10$  m, corresponding to an average flank slope of  $0.50^\circ \pm 0.10^\circ$ . Furthermore, Ha2 is characterized by a deeper intrusion ( $d = 1.2$  km) and a higher magma pressure of 9.5 MPa when compared to Pa1, V2, and C16 (Table 8.1). The resulting tensional stress did not result in the formation of crossing rilles, which are characteristic for class In1 with their inferred higher magma pressure of 18–100 MPa.

The morphometric properties of the domes C9 and C10 (Fig. 7.8), which belong to class In3, differ from those of effusive domes of comparable diameter. Their flank slopes are extraordinarily low with slope  $< 0.30^\circ$ , and their outlines are strongly elongated with circularity values of 0.63 and 0.73, respectively. The very low dome C9 is associated with a short linear structure running parallel to Rima Cauchy and Rupes Cauchy, which are in

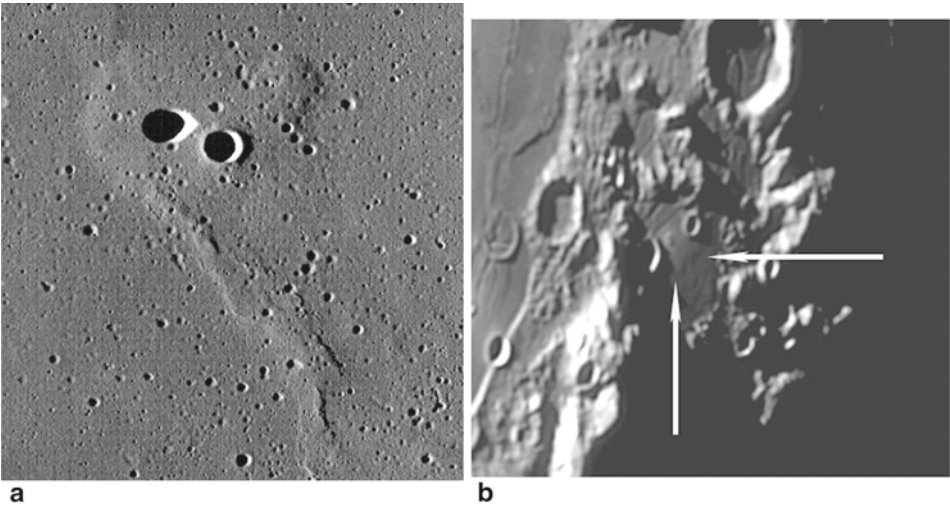


**Fig. 8.10** **a** Section of the LROC image WAC image M117277413ME (NASA/GSFC/Arizona State University), showing the dome C16. Two telescopic images of that dome are shown in Figs. 7.6 and 7.7. **b** Telescopic CCD image of the lunar dome Palmieri 1 (Pa1). Image by J. Phillips

turn oriented radial to the Imbrium basin. The dome C10 is located adjacent to the tectonic fault Rupes Cauchy (Fig. 8.9). The unusual morphometric properties of the class In3 domes along with the presence of tensional features make the occurrence of intrusions at least plausible.

---

**Abstract**

This chapter provides a summary of the book and gives a perspective towards future research activities regarding lunar domes.

This book has started with a description of the volcanic processes that govern the formation of volcanic constructs on the Earth and on the Moon. The shape and morphometric properties of volcanic edifices depend on lava properties such as temperature, chemical composition, volatile content, and pressure, parameters which in turn influence the viscosity and effusion rate of the lava. On the Moon, volatile-rich lava led to the formation of cinder cones and pyroclastic deposits, while basaltic lava of low volatile content formed the extended basaltic mare plains and low domes, the latter probably during later eruption stages characterized by lower lava temperatures and thus higher viscosities.

For determining the morphometric properties of lunar domes, the image-based technique of shape from shading has been described, which relies on an evaluation of image intensities to derive the three-dimensional surface profile. Recently acquired lunar orbital topographic data sets have been discussed, and an approach for constructing topographic maps of high lateral resolution based on the combination of topographic data of relatively low lateral resolution with high-resolution image data has been outlined. The morphometric properties of lunar domes stated in this book were mostly derived using the shape from shading method applied to telescopic CCD images acquired under strongly oblique illumination conditions. Furthermore, several classification schemes for lunar domes have been described.

Subsequently, the spectral characteristics of lunar domes have been discussed. In this context, an overview of the most important lunar minerals has been provided, and state-of-the-art methods for determining the abundances of the key elements and metal oxides of the lunar crust have been described. While lunar mare domes basically share the spectral properties of the surrounding mare surface, a peculiar class of lunar domes, the highland domes, are characterised by exceptionally reddish and bright surfaces. Their spectral be-



haviour together with the measured steep flank slopes has led to the conclusion that they were formed by distinctly non-basaltic lavas of high silica content (cf. Weitz and Head 1999). This supposition has been confirmed recently by the analysis of LRO Diviner infrared spectral data performed by Kusuma et al. (2012).

Furthermore, a geophysical model for estimating the rheologic properties of the dome-forming magma along with the dimensions of the feeder dike has been described. A second model has dealt with lunar laccoliths, magmatic intrusions which are presumably responsible for the formation of several large and exceptionally flat lunar domes. Some of these domes are associated with crustal fractures and faults which might be traces of the laccolith-forming intrusion of pressurized magma between rock layers of the lunar crust.

Based on the morphometric and spectral properties of lunar domes, a classification scheme has been established for both effusive and presumably intrusive domes. These dome classes are strongly correlated with the rheologic properties of the dome-forming magma, the feeder dike dimensions, and with the resulting time scales of magma ascent through the dike and heat conduction from the magma into the surrounding crustal material. For lunar mare domes, the ratio of these time scales has been found to be correlated with the magma viscosity and thus with the dome steepness, leading to the conclusion that the importance of magma evolution processes such as cooling and crystallization increases with increasing steepness of a mare dome. For the highland domes, on the other hand, the time the magma spent in the dike was found to be too short for significant cooling to occur, which is consistent with a formation mechanism based on the eruption of distinctly non-basaltic, highly silicic magma.

The second part of this book has provided detailed descriptions of effusive domes, including bisected domes, and putative intrusive domes across various areas of the lunar nearside. For all these domes, telescopic CCD images taken under oblique illumination have been provided, while some domes (but not all) are also well apparent in recently acquired images of the Lunar Reconnaissance Wide Angle Camera (LROC WAC). As low illumination angles of less than a few degrees are required to unambiguously identify a dome in an image, and because the orbital imaging campaigns did not specifically aim for the acquisition of such images, telescopic CCD images like those routinely taken by advanced amateur astronomers using moderately intricate equipment are still of great value for identifying and confirming lunar domes. The height values inferred from such telescopic images have been found to be generally in surprisingly good correspondence with height values determined based on orbital topographic data sets. Notably, in this context one should be careful when regarding orbital topographic data as “ground truth” when measuring dome heights, since even these recent maps may at places be affected by low lateral resolution or by interpolation artifacts, such that e.g. the actual summit of a dome may be “missed” and as a result the dome height may be underestimated.

An aspect on which future research on lunar domes might concentrate are more detailed spectral studies than those presented in this book, most of which are still based on Clementine multispectral data. The ability of this data set to differentiate between typical dome-forming minerals such as orthopyroxene, clinopyroxene, and olivine is limited due



to low spectral resolution and calibration problems in the near-infrared range. In contrast, the hyperspectral data set acquired by the Moon Mineralogy Mapper ( $M^3$ ) instrument on board the Indian spacecraft Chandrayaan-1 allows for an unambiguous identification of the key minerals of the lunar crust, including different species of pyroxene (Klima et al. 2012), olivine (Wiseman et al. 2012), but also localized deposits of spinel (Dhingra et al. 2011) or nearly pure plagioclase (Cheek et al. 2012). In the Marius Hills region, significant spectral contrasts between the volcanic edifices and the surrounding mare surface have already been found by Besse et al. (2010), which are not detectable in the Clementine data. Future investigations may show whether subtle spectral contrasts between more typical mare domes and the surrounding basaltic plains exist, which might reflect compositional contrasts e.g. due to different degrees of magma evolution.

Another promising aspect of future research activities on lunar domes is the analysis of the complex morphology of presumably non-monogenetic domes such as Arago  $\alpha$  and  $\beta$  or Fracastorius 1. Detailed topographic maps e.g. obtained by a combined analysis of orbital topographic data and LROC WAC and NAC images acquired under strongly oblique illumination may allow to determine the morphometric properties of individual flow structures on the dome surfaces and in turn an estimation of the magma characteristics based on rheologic modeling.

In combination with high-resolution spectral analysis techniques, such investigations might greatly extend our present knowledge of the processes that formed volcanic edifices on the Moon.

---

## Appendix A: Lunar dome images

**Plate I** Telescopic image of the lunar volcanic complex Mons Rümker and the Gruithuisen highland domes. (Image by M. Wirths)



**Plate II** Telescopic image of the lunar volcanic complex Mons Rümker. (Image by M. Wirths)

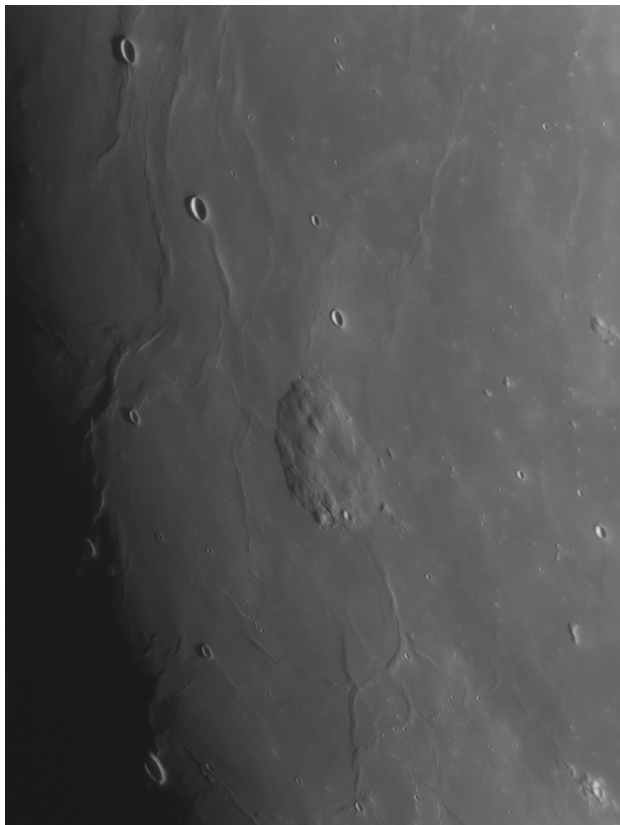


**Plate III** Telescopic image of the large lunar region including Marius hills and the Reiner  $\gamma$  formation. On the *left*, near Cavalerius F, a lunar kipuka is detectable. (Image by M. Wirths)



**Plate IV** Telescopic image of the lunar volcanic region between the craters Tobias Mayer and Hortensius. (Image by J. Phillips)

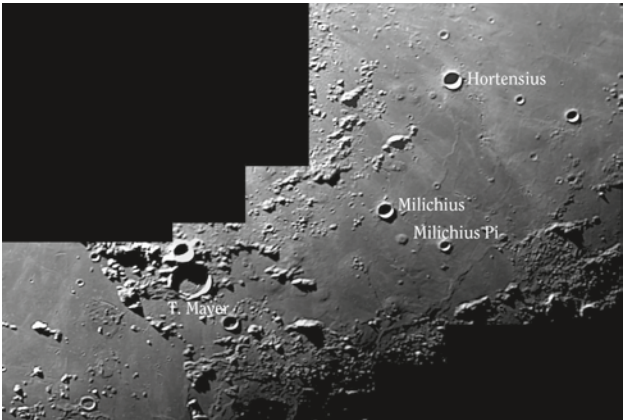


**Plate V** Telescopic image of the lunar region between the Gruithuisen highland domes and Prinz. (Image by P. Lazzarotti)



**Plate VI** Telescopic image of the region between the Mairan highland domes and the Gruithuisen highland domes. (Image by M. Wirths)



**Plate VII** Telescopic image of the dome Kies  $\pi$  near the crater Kies. (Image by J. Phillips)

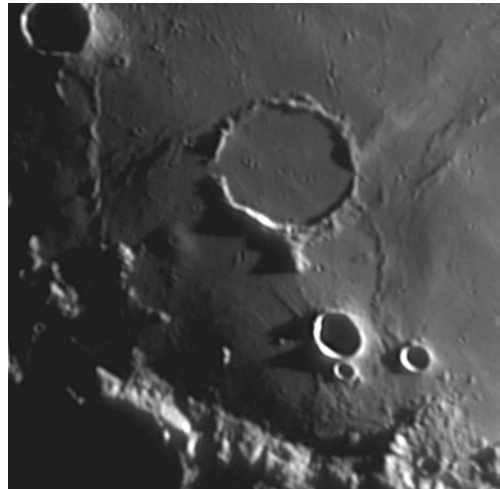


**Plate VIII** Telescopic image of the Valentine dome and its smaller northern neighbor. (Image by J. Phillips)

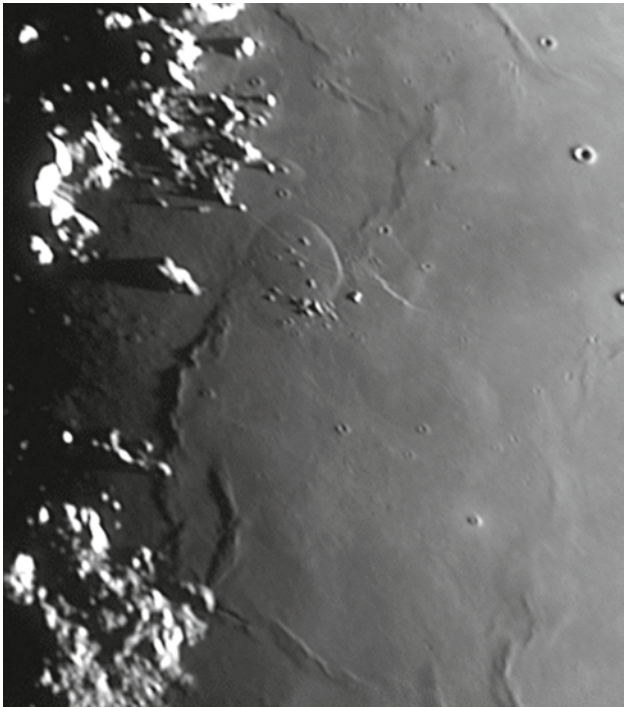


**Plate IX** Telescopic image of the Birt domes. (Image by J. Phillips)

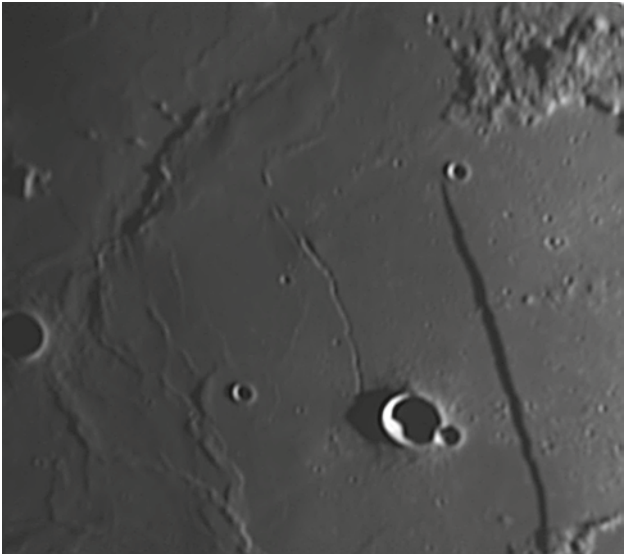




**Plate X** Telescopic image of the region comprising the craters Wallace and Eratosthenes, showing several lunar domes. (Image by K. C. Pau)

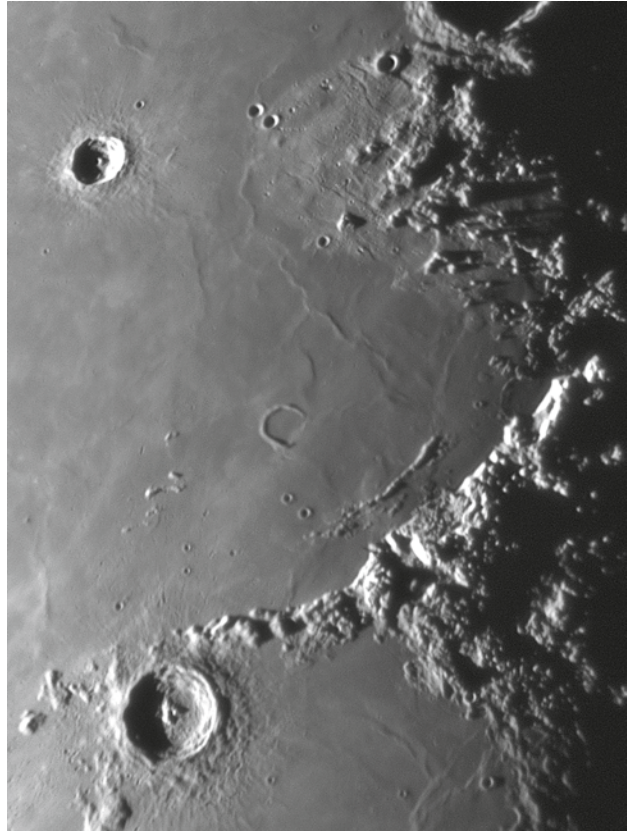


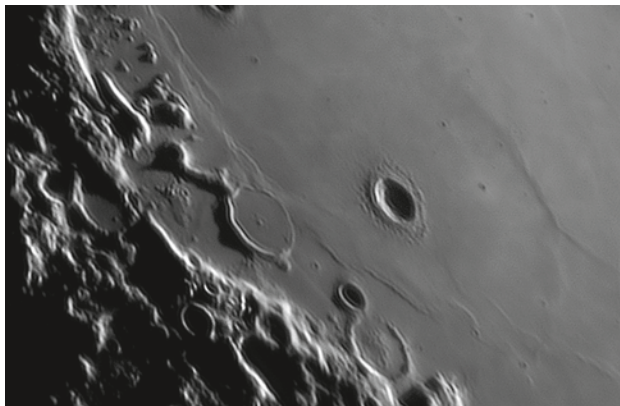
**Plate XI** Telescopic image of the region between the craters Wallace and Eratosthenes, showing several lunar domes. (Image by C. Zannelli)



**Plate XII** Telescopic image of the region including the formation Lamont, the Arago domes, and the crater Carrel (Jansen B). (Image by J. Phillips)



**Plate XIII** Telescopic image of the Yerkes dome situated in Mare Crisium. (Image by R. Lena)



---

## Appendix B: Further Resources

---

### ACT-REACT Quick Map

Scholten et al. (2012) present a nearly global lunar DEM with a grid size of 100 m, the so-called GLD100. This DEM has been constructed based on photogrammetric analysis of LROC WAC image pairs. According to Scholten et al. (2012), the average elevation accuracy of the GLD100 amounts to 20 m, while 10 m accuracy are achieved for the nearside mare regions. The GLD100 yields trustworthy information about the vertical extension of structures of a lateral size of more than 1.5 km. Structures of a lateral extension of less than 300–500 m, which typically display vertical elevation differences of some tens of meters, are usually not apparent in the GLD100 (Scholten et al. 2012). The GLD100 data are accessible at [http://wms.lroc.asu.edu/lroc/global\\_product/100\\_mpp\\_DEM](http://wms.lroc.asu.edu/lroc/global_product/100_mpp_DEM).

We found that many lunar mare domes are apparent in the GLD100. An easy way to access the GLD100 data is the ACT-REACT Quick Map tool<sup>1</sup>. Regarding lunar domes, we found that it is difficult to obtain reliable height values if they are large and flat, i.e. not characterised by a prominent profile, or if the dome outline is not well-defined, as e.g. for V1 and V2 described in Chap. 8.

Plates XIV–XIX display cross-sections of the domes Pe1, M8, and M5 (cf. Chap. 7) generated with the GLD100-based ACT-REACT Quick Map tool. The derived heights correspond to 240, 140, and 78 m, respectively. These results are consistent with the heights of 240, 130, and 80 m inferred from low-sun images using the shape from shading technique described in Chap. 2.

---

<sup>1</sup> <http://target.lroc.asu.edu/da/qmap.html>.

**Plate XIV** Dome Petavius 1 (Pe1) of class C<sub>1</sub>. The cross-sectional profile shown in Plate XV has been extracted along the *gray* line (screenshot from <http://target.lroc.asu.edu/da/qmap.html>)

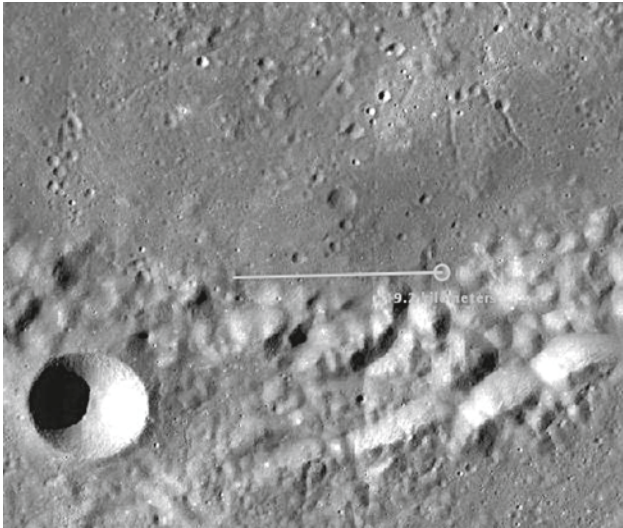


**Plate XV** Cross-sectional profile of Pe1 in east-west direction derived with the ACT-REACT Quick Map tool (cf. also Plate XIV) (screenshot from <http://target.lroc.asu.edu/da/qmap.html>)

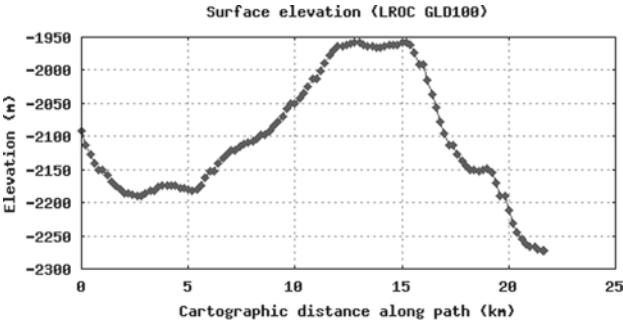


**Plate XVI** Dome M8 of class E<sub>1</sub>. The cross-sectional profile shown in Plate XVII has been extracted along the *gray* line (screenshot from <http://target.lroc.asu.edu/da/qmap.html>)

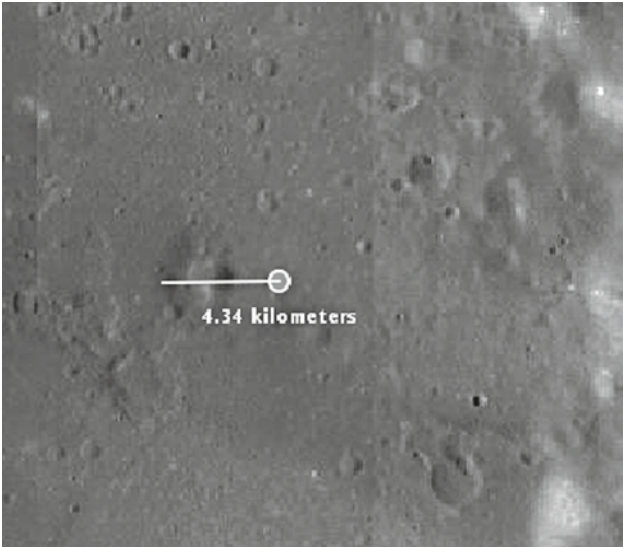




**Plate XVII** Cross-sectional profile of M8 in east-west direction derived with the ACT-REACT Quick Map tool (cf. also Plate XVI) (screenshot from <http://target.lroc.asu.edu/da/qmap.html>)

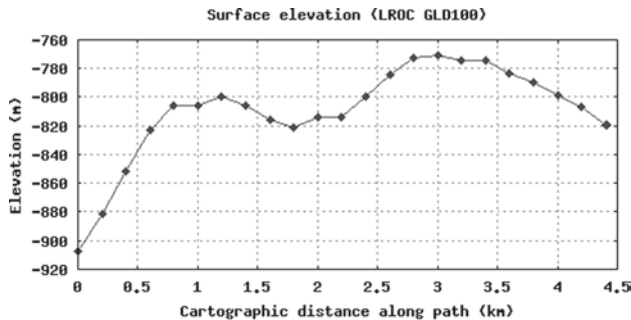


**Plate XVIII** Dome M5 of class C<sub>1</sub>. The cross-sectional profile shown in Plate XIX has been extracted along the *gray* line (screenshot from <http://target.lroc.asu.edu/da/qmap.html>)

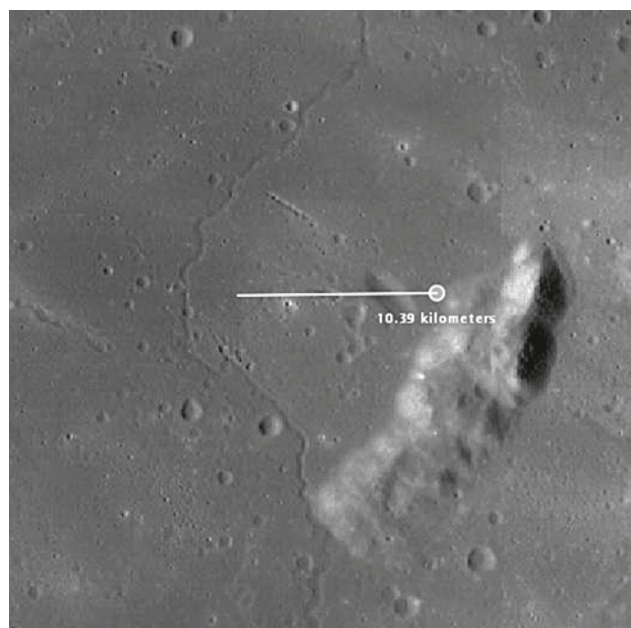
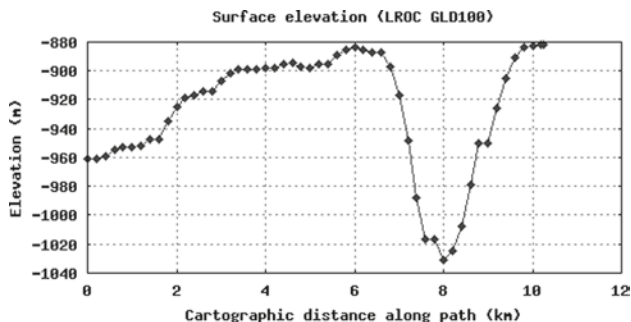


**Plate XIX** Cross-sectional profile of M5 in east-west direction derived with the ACT-REACT Quick Map tool (cf. also Plate XVIII) (screenshot from <http://target.lroc.asu.edu/da/qmap.html>)





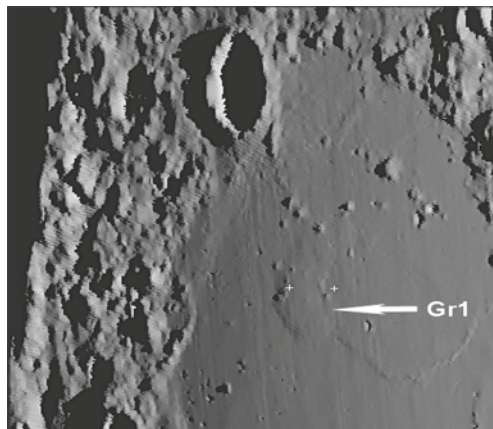
## Lunar Terminator Visualization Tool (LTVT)

The free software “Lunar Terminator Visualization Tool” (LTVT) by Mosher and Bondo (2012) has been designed for performing measurements in lunar images.<sup>2</sup> A calibration procedure assigning points in the image under study to reference points of a Unified Lunar Control Network (ULCN) allows for the accurate determination of selenographic coordinates of image points as well as distances in the image, such as crater diameters or shadow lengths. According to Archinal et al. (2006), a ULCN is a list of reference locations with accurately determined three-dimensional coordinates in a coordinate system with the lunar center at its origin. The ULCN 2005 introduced by Archinal et al. (2006) comprises a number of 272931 reference points.

With the LTVT software, parts of the LOLA DEM can be imported and images can be rendered for given illumination conditions by selecting the following options: (a) “Lunar-Lambert photometric model”, (b) “correct 3D simulation for perspective” and (c) “display elevation as read from current DEM”. Furthermore, contour plots can be generated and elevation values can be read out. For several lunar domes, we obtained dome height measurements using the images rendered with the LTVT software based on the LOLA DEM. These dome heights turned out to be consistent with height measurements computed from low-sun images using the shape from shading technique described in Chap. 2.

Plates XX–XXII show correspondingly obtained data of the dome Grimaldi 1 (Gr1). The derived dome height amounts to 130 m.

**Plate XX** Image rendered based on the LOLA DEM using LTVT for the same illumination conditions as in Fig. 8.6b (solar elevation angle of  $3.1^\circ$ ), assuming a viewpoint on the Earth. The white crosses indicate the positions shown in Plate XXI for which elevation values are extracted



<sup>2</sup> <http://ltvt.wikispaces.com/LTVT>.

**Plate XXI** Image rendered by LTVT based on the LOLA DEM transformed to cylindrical projection. The difference in elevation corresponds to 130 m

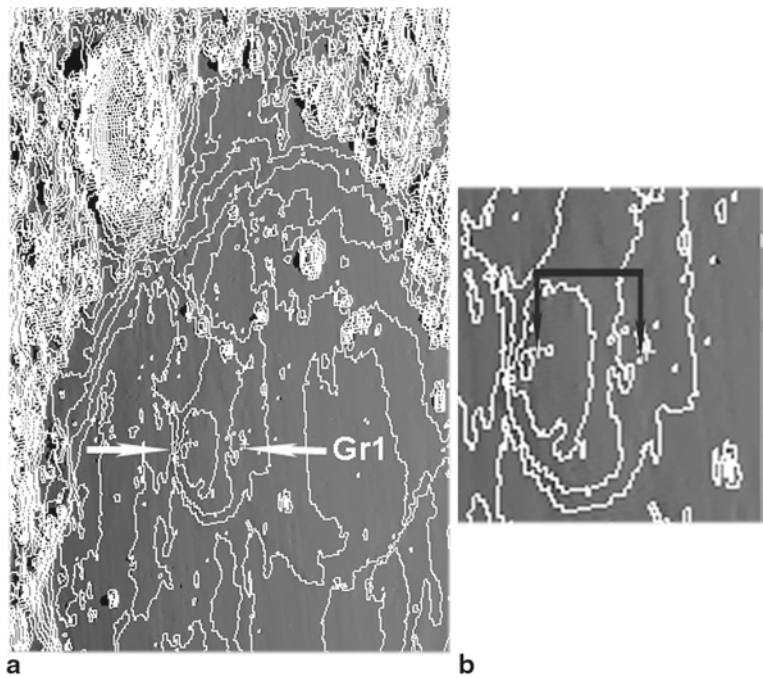
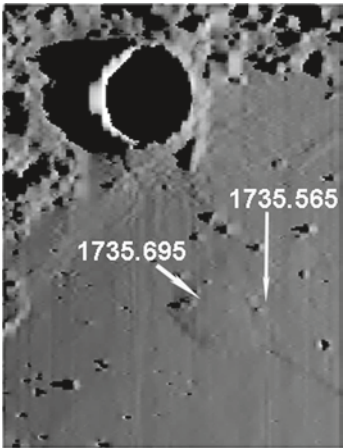


**Plate XXII** **a** Image of the region including the Grimaldi dome shown in Plate XX, rendered image based on the LOLA DEM using LTVT, overlaid by an elevation contour map. The contour interval corresponds to 45 m. **b** Enlarged image section around Gr1

---

## References

- Abels, A.: Impacts in two-layered targets on the Earth: effects of cover thickness on crater morphostructure. Proceedings of 35th Lunar Planetary Science Conference., abstract #1090 (2004)
- Adams, J.B., McCord, T.B.: Remote sensing of lunar surface mineralogy: implication from visible and near infrared reflectivity of Apollo 11 samples. Proceedings of Apollo 11 Lunar Science Conference, 1937–1945 (1970)
- Akima, H.: A new method of interpolation and smooth curve fitting based on local procedures. *J. ACM.* **17**(4), 589–602 (1970)
- Archinal, B.A., Rosiek, M.R., Kirk, R.L., Redding, B.L.: The Unified Lunar Control Network 2005. USGS Open-File Report 2006–1367. <http://pubs.usgs.gov/of/2006/1367/> (2006). Accessed 29 July 2012.
- Arya, A.S., Thangjam, G., Rajasekhar, R.P., Gopala Krishna, B., Kiran Kumar, A.S., Navalgund, R.R.: Morphometric and rheological analysis of an effusive dome in Marius Hills using Chandrayaan-1 TMC data. Proceedings of 42nd Lunar and Planetary Science Conference, abstract #1470 (2011)
- Ashbrook, J.: Dimensions of the Lunar Dome Kies 1. *J. Ass. Lunar Planet. Obs.* **15** (1–2) (1961)
- Basaltic Volcanism Study Project (BVSP). Basaltic volcanism on the terrestrial planets. Pergamon, New York (1981)
- Berezhnoy, A.A., Hasebe, N., Kobayashi, M., Michael, G.G., Okudaira, O., Yamashita, N.: A three end-member model for petrologic analysis of lunar prospector gamma-ray spectrometer data. *Planet. Space Sci.* **53**: 1097–1108 (2005)
- Besse, S., Sunshine, J.M., Pieters, C.M., Petro, N.E., Staid, M., Deepak, D., Head, J.W., Isaacson, P.J., M3 Team.: New observations of the Marius Hills Complex from Moon Mineralogy Mapper (M3). Proceedings of 41st Lunar and Planetary Science Conference, abstract #1361 (2010)
- Blake, S.: Viscoplastic models of lava domes. In: Fink, J. (ed.) *Lava Flows and Domes: Emplacement Mechanisms and Hazard Implications*, IAVCEI Proceedings on Volcanology, vol. 2, pp. 88–128, Springer Verlag, New York (1990)
- Blewett, D.T., Hawke, B.R.: Lunar Basin Ejecta emplacement: evidence from Schiller-Schickard. *Meteoritics.* **28**(3), 325(1993)
- Brungart, D.L.: The origin of lunar domes. MSc. thesis, Air Force Institute of Technology, Wright Patterson Air Force Base, Ohio (1964)
- Burns, R.G., Parkin, K.M., Loeffler, B.M., Leung, I.S., Abu-Eid, R.M.: Further characterization of spectral features attributable to titanium on the moon. Proceedings of 7th Lunar and Planetary Science Conference, 2561–2578 (1976)
- Cadogan, P.H.: Oldest and largest lunar basin? *Nature* 250(5464), 315–316 (1974)

- Carlino, S., Cubellis, E., Luongo, G., Obrizzo, F. On the mechanics of caldera resurgence of Ischia Island (southern Italy). In: Troise, C., De Natale, G., Kilburn, C.R.J. (eds.) *Mechanisms of Activity and Unrest at Large Calderas*, vol. 269: pp. 181–193 Geological Society, London (2006)
- Carrigan, C.R.: Plumbing systems. In: Sigurdsson, H. (ed.) *Encyclopedia of Volcanoes*, pp. 219–235. Academic Press, San Diego (2000)
- Carrigan, C.R., Schubert, G., Eichelberger, J.C.: Thermal and dynamical regimes of single- and two-phase magmatic flow in dikes. *J. Geophys. Res.* **97**(B12), 17377–17392 (1992)
- Charette, M.P., McCord, T.B., Pieters, C., Adams, J.B.: Application of remote spectral reflectance measurements to lunar geology classification and determination of titanium content of lunar soils. *J. Geophys. Res.* **79**(11), 1605–1613 (1974)
- Cheek, L.C., Donaldson Hanna, K.L., Pieters, C.M., Head, J.W., Whitten, J.L. The distribution and mineralogy of anorthosite in the Orientale basin: New perspectives from M3 data. *Proceedings of the 2nd Conference on Lunar Highlands Crust*, abstract #9022 (2012)
- Chevrel, S.D., Pinet, P.C., Head, J.W.: Gruithuisen domes region: a candidate for an extended nonmare volcanism unit on the Moon. *J. Geophys. Res.* **104**(E7), 16515–16529 (1999)
- Davies, M.E., Colvin, T.R., Meyer, D.L., Nelson, S.: The unified lunar control network: 1994 version. *J. Geophys. Res.* **99**(E11), 23211–23214 (1994)
- Davis, P.A., Spudis, P.D.: Petrologic province maps of the lunar highlands derived from orbital geochemical data. *J. Geophys. Res.* **90**, D61–D74 (1985)
- De Hon, R.A.: Thickness of the western mare basalts. *Proceedings of 10th Lunar and Planetary Science Conference*, 2935–2955 (1979)
- Dhingra, D., Pieters, C.M., Boardman, J.W., Head, J.W., Isaacson, P.J., Taylor, L.A., M3 Team.: Theophilus crater: compositional diversity and geological context of Mg-spinel bearing central peaks. *Proceedings of 42nd Lunar Planetary Science Conference*, abstract #2388 (2011)
- Dvorak, J., Phillips, R.J.: Gravity anomaly and structure associated with the Lamont region of the moon. *Proceedings of 10th Lunar and Planetary Science Conference*, 2265–2275 (1979)
- Eliason, E., Isbell, C., Lee, E., Becker, T., Gaddis, L., McEwen, A., Robinson, M.: Mission to the Moon: the Clementine UVVIS global mosaic. *PDS Volumes USANASA PDS CL 4001 4078*. <http://pdsmaps.wr.usgs.gov> (1999). Accessed 20 June 2012
- Fedotov, S.A.: Ascent of basaltic magmas in the crust and the mechanism of basaltic fissure eruptions. *Internat. Geol. Rev.* **20**, 33–48 (1976)
- Gaddis, L.R., Tyburczy, J.A., Hawke, B.R.: Mafic characteristics of lunar pyroclastic deposits. *Proceedings of 31st Lunar and Planetary Science Conference*, abstract #1700 (2001)
- Gaddis, L.R., Staid, M.I., Tyburczy, J.A., Hawke, B.R., Petro, N.E.: Compositional analyses of lunar pyroclastic deposits. *Icarus*. **161**, 262–280 (2003)
- Giguere, T.A., Wilson, L., Hawke, B.R.: Magmatic origin for Rima Hyginus: implications for its feeder dike. *Forty-first Lunar and Planetary Science Conference*, abstract #1129 (2010)
- Gillis-Davis, J.J., Lucey, P.G., Hawke, B.R.: Testing the relation between UV vis color and TiO<sub>2</sub> content of the lunar maria. *Geochimica et Cosmochimica Acta*. **70**(24), 6079–6102 (2006)
- Gómez-Izquierdo, B., Caravantes, G., Dini, A., Rocchi, S.: The laccolithic intrusion of Orciatico (Tuscany). *Geophys. Res. abstracts* **10**, EGU2008-A-02285 (2008)
- Grumpe, A., Wöhler, C.: DEM construction and calibration of hyperspectral image data using pairs of radiance images. *Proceedings of IEEE International Symposium on image and signal processing and analysis, special session on image processing and analysis in Lunar and Planetary Science*, pp. 609–614 (2011)
- Hacker, D.B., Petronis, M.S., Holm, D.K., Geissman, J.W.: Shallow level emplacement mechanisms of the Miocene Iron Axis laccolith group, southwest Utah. *Publications of the Utah Geological Association*, vol. 35, pp. 1–49 (2007)
- Hapke, B.W.: Bidirectional reflectance spectroscopy. 1 Theory. *J. Geophys. Res.* **86**, 3039–3054 (1981)

- Hapke, B.W.: Bidirectional reflectance spectroscopy. 3 Correction for macroscopic roughness. *Icarus*. **59**, 41–59 (1984)
- Hapke, B.W.: Bidirectional reflectance spectroscopy. 4 The extinction coefficient and the opposition effect. *Icarus*. **67**, 264–280 (1986)
- Hapke, B.W.: Bidirectional reflectance spectroscopy. 5 The coherent backscatter opposition effect and anisotropic scattering. *Icarus*. **157**, 523–534 (2002)
- Hawke, B.R., Lawrence, D.J., Blewett, D.T., Lucey, P.G., Smith, G.A., Spudis, P.D., Taylor, G.J.: Hantzen alpha: a volcanic construct in the lunar highlands. *J. Geophys. Res.* **108**(E7), CiteID 5069 (2003). doi: 10.1029/2002JE002013
- Hawke, B.R., Giguere, T.A., Blewett, D.T., Gillis-Davis, J.J., Hagerty, J.J., Lawrence, D.J., Lucey, P.G., Peterson, C.A., Smith, G.A., Spudis, P.D., Taylor, G.J.: Ancient Volcanism in the Schiller-Schickard Region of the Moon. Proceedings of 37th Lunar and Planetary Science Conference, abstract #1516 (2006)
- Hawke, B.R., Giguere, T.A., Blewett, D.T., Campbell, B.A., Gillis-Davis, J.J., Hagerty, J.J., Lawrence, D.J., Lucey, P.G., Peterson, C.A., Smith, G.A., Spudis, P.D., Taylor, G.J.: Remote Sensing Studies of the Schiller-Schickard region of the Moon: Final Results. Proceedings of 38th Lunar and Planetary Science Conference, abstract #1474 (2007)
- Hawke, B.R., Giguere, T.A., Blewett, D.T., Lucey, P.G., Taylor, G.J., Spudis, P.D.: Remote Sensing Studies of Ancient Mare Basalt Deposits. Proceedings of 30th Lunar and Planetary Science Conference, abstract #1956 (1999)
- Head, J.W., Gifford, A.: Lunar mare domes: classification and modes of origin. *Moon Planet.* **22**, 235–257 (1980)
- Head, J.W., McCord, T.B.: Imbrian-age Highland Volcanism on the Moon. The Gruithuisen and Mairan domes. *Science* **199**, 1433–1436 (1978)
- Head, J.W., Wilson, L.: Alphonsus-type dark halo craters: morphology, morphometry and eruption conditions. Proceedings of 10th Lunar and Planetary Science, 2861–2897 (1979)
- Head, J. W., Wilson, L.: Lunar mare volcanism: Stratigraphy, eruption conditions, and the evolution of secondary crusts. *Geochim. Cosmochimica Acta* **56**, 2155–2175 (1992)
- Head, J.W., Wilson, L.: Lunar linear rilles as surface manifestation of dikes: predictions and observations. Proceedings of 27th Lunar and Planetary Science Conference, abstract #519 (1996)
- Herbort, S., Grumpe, A., Wöhler, C.: Reconstruction of non-Lambertian surfaces by fusion of shape from shading and active range scanning. Proceeding of International Conference on Image Processing, pp. 17–20 (2011)
- Hiesinger, H., Head, J.W., Wolf, U., Jaumann, R., Neukum, G.: Ages and stratigraphy of mare basalts in Oceanus Procellarum, mare Nubium, mare Cognitum, and mare Insularum. *J. Geophys. Res.* **108**(E7), 5065–5091 (2003)
- Holt, H.E.: Geologic map of the Purbach quadrangle of the Moon. Geologic Atlas of the Moon I-822 (LAC 95). USGS, Flagstaff (1974)
- Horn, B.K.P.: Height and gradient from shading. *International Journal of Computer Vision* **5**(1), 37–75 (1990)
- Hörz, F., Grieve, R., Heiken, G., Spudis, P., Binder, A.: Lunar surface processes. In: Heiken, G.H., Vaniman, D.T., French, B.M. (eds.) *Lunar Sourcebook*, pp. 61–120. Cambridge University Press, Cambridge (1991)
- Howard, K.A., Carr, M.H., Muehlberger, W.R.: Basalt stratigraphy of southern mare Serenitatis. Apollo 17 Preliminary Science Report, pp. 29–1–29–12. NASA SP-330 (1973)
- Jackson, P.A., Wilson, L., Head, J.W.: The use of magnetic signatures in identifying shallow intrusions on the moon. Proceedings of 28th Lunar and Planetary Science Conference, abstract #1429 (1997)
- Jamieson, H.D., Phillips, J.H.: Lunar dome catalog. *Strolling Astronomer*. **36**(3), 123–129 (1992)

- Johnson, A.M., Pollard, D.D.: Mechanics of growth of some laccolith intrusions in the Henry mountains, Utah. I. Field observations Gilbert's model, physical properties and flow of magma. *Tectonophysics*. **18**, 261–308 (1973)
- Kerr, A.D., Pollard, D.D.: Toward more realistic formulations for the analysis of laccoliths. *J. Structural Geology* **20**(12), 1783–1793 (1998)
- King, T.V.V., Ridley, W.I.: Relation of the spectroscopic reflectance of olivine to mineral chemistry and some remote sensing implications. *J. Geophys. Res.* **92**, 11457–11469 (1987)
- Klima, R.L., Cahill, J.T.S., Hagerty, J., Lawrence, D.: Bullialdus crater: Excavation and exposure of an Mg- or alkali-suite pluton? Proceeding on 2nd Conference on Lunar Highlands Crust, abstract #9017 (2012)
- Koehler, U., Head, J.W., Neukum, G., Wolf, U.: North-polar lunar light plains: ages and compositional observations. Workshop New Views of the Moon II, abstract #8050 (1999)
- Koehler, U., Head, J.W., Neukum, G., Wolf, U.: Lunar light plains in the northern nearside latitudes: latest results on age distributions, surface composition, nature, and possible origin. 31th Lunar and Planetary Science conference, abstract #1822 (2000)
- Kramer, G.Y., Hawke, B.R., Giguere, T.A., Heitman, G., McCord, T.B.: The mare basalts of eastern Frigoris. Proceedings of 40th Lunar and Planetary Science Conference, abstract #2369 (2009)
- Kusuma, K.N., Sebastian, N., Murty, S.V.S.: Geochemical and mineralogical analysis of Gruithuisen region on Moon using M3 and DIVINER images. *Planet. Space Sci.* **67**(1), 46–56 (2012)
- Le Mouelic, S., Langevin, Y., Erard, S.: Discrimination between Olivine and Pyroxene from Clementine NIR data: application to Aristarchus crater. Proceedings of 30th Lunar and Planetary Science Conference, abstract #1098 (1999)
- Le Mouelic, S., Langevin, Y., Erard, S.: Discrimination between maturity and composition of lunar soils from integrated Clementine UV-visible/near-infrared data: application to the Aristarchus Plateau. *J. Geophys. Res.* **105**(E4), 9445–9455 (2000)
- Lena, R., Wöhler, C.: Consolidated Lunar Dome Catalogue <http://digilander.libero.it/iglrgroup/consolidatedlunardomecatalogue.htm> (2011). Accessed 29 July 2012
- Lena, R., Fattinanzi, C., Lottero, F.: Lunar domes and artificial domes: two tools for lunar observers. *Selenology*. **2**(23), 4–10 (2004)
- Lena, R., Pau, K.C., Phillips, J., Fattinanzi, C., Wöhler, C.: Lunar domes: a generic classification of the dome near Valentine located at 10.26°E and 31.89°N. *JBAA*. **116**(1), 34–39 (2006)
- Lena, R., Wöhler, C., Phillips, J., Wirths, M., Bregante, M.T.: Lunar domes in the Doppelmayer region: spectrophotometry, morphometry, rheology and eruption conditions. *Planet. Space Sci.* **55**, 1201–1217 (2007)
- Lena, R., Wöhler, C., Bregante, M.T., Lazzarotti, P., Lammel, S.: Lunar domes in Mare Undarum: spectral and morphometric properties, eruption conditions, and mode of emplacement. *Planet. Space Sci.* **56**, 553–569 (2008)
- Li, L., Mustard, J.F.: Compositional gradients across mare-highland contacts: importance and geological implication of lateral transport. *J. Geophys. Res.* **105**(E8), 20431–20450 (2000)
- Li, L., Mustard, J.F.: On lateral mixing efficiency of lunar regolith. *J. Geophys. Res.* **110**(E11), E11002 (2005)
- Li, L., Mustard, J.F., He, G.: Compositional gradients across mare highland contacts: the importance of lateral mixing. Proceedings of 28th Lunar and Planetary Science Conference, abstract #1724 (1997)
- Lipman, P.W.: Calderas. In: Sigurdsson, H. (ed.) *Encyclopedia of Volcanoes*, pp. 643–662. Academic Press, San Diego (2000)
- Lucchitta, B.K.: Geologic map of the north side of the Moon. *U.S. Geol. Sum. Misc. Invest. Set. Map*, 71062 (1978)



- Lucey, P.G., Blewett, D.T., Jolliff, B.L.: Lunar iron and titanium abundance algorithms based on final processing of Clementine ultraviolet-visible images. *J. Geophys. Res.* **105**(E8), 20297–20306 (2000)
- Martelet, G., Calcagno, P., Gumiaux, C., Truffert, C., Bitri, A., Gapais, D., Brun, J.P.: Integrated 3D geophysical and geological modelling of the Hercynian Suture Zone in the Champtoceaux area (south Brittany, France). *Tectonophysics*. **382**, 117–128 (2004)
- Masursky, H., Colton, G., El-Baz, F.: Apollo over the Moon. NASA SP-362, GPO, Washington (1978)
- Matsunaga, T. et al.: Discoveries on the lithology of lunar crater central peaks by SELENE Spectral Profiler. *Geophys. Res. Lett.* **35**, L23201, (2008). doi: 10.1029/2008GL035868
- Maynard, S.R.: Laccoliths of the Ortiz porphyry belt, Santa Fe County, New Mexico. *New Mexico Geology*. **27**(1), 3–21 (2005)
- McCord, T.B., Charette, M.P., Johnson, T.V., Lebofsky, L.A., Pieters, C., Adams, J.B.: Lunar spectral types. *J. Geophys. Res.* **77**, 1349–1359 (1972)
- McCord, T.B., Adams, J.B.: Progress in optical analysis of lunar surface composition. *The Moon*. **7**, 453–474 (1973)
- McCord, T.B., Pieters, C., Feierberg, M.A.: Multispectral mapping of the lunar surface using ground-based telescopes. *Icarus*. **29**(1), 1–34 (1976)
- McEwen, A.S.: Photometric functions for photoclinometry and other applications. *Icarus*. **92**, 298–311 (1991)
- Melendrez, D.E., Johnson, J.R., Larson, S.M., Singer, R.B.: Remote sensing of potential lunar resources. 2 High spatial resolution mapping of spectral reflectance ratios and implications for nearside mare TiO<sub>2</sub> content. *J. Geophys. Res.* **99**(E3), 5601–5619 (1994)
- Michaut, C.: Dynamics of laccolith intrusions, with applications to the Earth and the Moon. *Proceedings of 41st Lunar and Planetary Science Conference*, abstract #1084 (2010)
- Michaut, C.: Dynamics of magmatic intrusions in the upper crust; theory applications to laccoliths on the Earth and the Moon. *J. Geophys. Res.* **116**, B05205, (2011). doi: 10.1029/2010JB008108
- Mosher, J., Bondo, H.: Lunar Terminator Visualization Tool. <http://ltvt.wikispaces.com/LTVT+Download> (2010). Accessed 29 July 2012.
- Murase, T., McBirney, A.R.: Viscosity of lunar lavas. *Science* **167**, 1491–1493 (1970)
- Nichols, D.J., Young, R.A., Brennan, W.J.: Lunar kipukas as evidence for an extended tectonic and volcanic history of the maria. *Lunar Planet. Sci.* **5**, 550–552 (1974)
- Ollier, C.: *Volcanoes*. Blackwell, New York (1988)
- Olson, A., Wilhelms, D.E.: Geologic map of the Mare Undarum quadrangle of the moon. USGS map I-837. USGS, Flagstaff (1974)
- Peterson, D.W., Tilling, R.I.: Lava flow hazards. In: Sigurdsson, H. (ed.) *Encyclopedia of Volcanoes*, pp. 957–972. Academic Press, San Diego (2000)
- Petrycki, J.A., Wilson, L.: Volcanic features and age relationships associated with lunar Graben. *Proceedings of Lunar Planetary Sciences*, abstract #1335 (1999)
- Piekutowski, A.J.: Cratering mechanisms observed in laboratory-scale high-explosive experiments. In: Roddy, D.J., Pepin, R.O., Merrill, R.B. (eds.) *Impact and Explosion Cratering*, pp. 67–102. Pergamon, New York (1977)
- Pieters, C.M.: Mare basalt types on the front side of the Moon: a summary of spectral reflectance data. *Proceedings of 9th Lunar and Planetary Science*, 2825–2849 (1978)
- Pieters, C.M.: The Moon as a Spectral Calibration Standard Enabled by Lunar Samples: The Clementine Example. *Proc. Workshop New Views of the Moon*, abstract #8025 (1999)
- Pieters, C.M. et al.: The Moon Mineralogy Mapper (M<sup>3</sup>) on Chandrayaan-1. *Current Science* **96**(4), 500–505 (2009)
- Pike, R.J.: Depth/diameter relations of fresh lunar craters: revision from spacecraft data. *Geophys. Res. Lett.* **1**, 291–294 (1974)

- Pike, R.J.: Volcanoes on the inner planets: some preliminary comparisons of gross topography. *Proceedings of 9th Lunar and Planetary Science Conference*, 3239–3273 (1978)
- Pike, R.J., Clow, G.: Revised classification of terrestrial volcanoes and catalogue of topographic dimensions, with new results of edifice volume. *US Geological Survey Open File Report 81-1038* (1981)
- Pollard, D.D., Fletcher, R.C.: *Fundamentals of Structural Geology*. Cambridge University Press, Cambridge (2005)
- Rajmon, D., Spudis, P.: Geology and stratigraphy of mare Fecunditatis. *Proceedings of 21st Lunar and Planetary Science Conference*, abstract #1913 (2000)
- Rajmon, D., Spudis, P.: Distribution and stratigraphy of basaltic units in mare Tranquillitatis. *Proceedings of 32nd Lunar and Planetary Science Conference*, abstract #2156 (2001)
- Robinson, M.S. et al.: Lunar Reconnaissance Orbiter Camera (LROC) instrument overview. *Space Sci. Rev.* **150**, 81–124 (2010)
- Rocchi, S., Dini, A., Farina, F., Innocenti, F., Westerman, D.S.: Intrusive sheets and sheeted intrusions at Elba Island (Italy). *Geophysical Research abstracts*, 10, EGU2008-A02692 (2008)
- Rose, D.E., Spudis, P.D.: Piercing the Clouds: the stratigraphy of mare Nubium. *Proceeding of 31st Lunar and Planetary Science Conference*, abstract #1364 (2000)
- Rosi, M., Papale, P., Lupi, L., Stoppato, M.: *Vulcani*. Mondadori, Milan (1999)
- Rubin, A.S.: Dikes vs. diapirs in viscoelastic rock. *Earth Planet. Sci. Lett.* **199**, 641–659 (1993a)
- Rubin, A.S.: Tensile fracture of rock at high confining pressure: implications for dike propagation. *J. Geophys. Res.* **98**, 15919–15935 (1993b)
- Rubin, A.S.: Propagation of Magma-Filled Cracks. *Ann. Rev. Earth and Planet. Sci.* **23**, 287–336 (1995)
- Rükl, A.: *Mondatlas*, 2nd ed. Verlag Werner Dausien, Hanau (1999)
- Scholten, F., Oberst, J., Matz, K.-D., Roatsch, T., Wählisch, M., Speyerer, E.J., Robinson, M.S.: GLD100: the near-global lunar 100 m raster DTM from LROC WAC stereo image data. *J. Geophys. Res.* **117**(E00H17) (2012). doi: 10.1029/2011JE003926
- Schultz, P.H., Spudis, P.D.: Evidence for ancient mare volcanism. *Lunar Planet. Sci. X*, 2899–2918 (1979)
- Simkin, T., Siebert, L.: Earth's volcanoes and eruptions: an overview. In: Sigurdsson, H. (ed.) *Encyclopedia of Volcanoes*, pp. 249–262. Academic Press, San Diego (2000)
- Smith, E.I.: Rümker Hills: a lunar volcanic dome complex. *The Moon* **10**, 175–181 (1974)
- Smith, D.E. et al.: The lunar orbiter laser altimeter investigation on the lunar reconnaissance orbiter mission. *Space Sci. Review.* **150**(1–4), 209–241 (2010)
- Smrekar, S., Pieters, C.M.: Near-infrared spectroscopy of probable impact melt from three large lunar highland craters. *Icarus* **63**, 442–452 (1985)
- Spera, F.J.: Physical properties of magma. In: Sigurdsson, H. (ed.) *Encyclopedia of Volcanoes*, pp. 171–190. Academic Press, San Diego (2000)
- Spudis, P.: *The Geology of multi-ring impact basins*. Cambridge University Press, Cambridge (1993)
- Spudis, P.D., McGovern, P.J., Kiefer, W.S.: Large shield volcanoes on the Moon. *Proceedings of the 42nd Lunar Planet Science Conference*, abstract #1367 (2011)
- Staid, M.I., Pieters, C.M., Head, J.W.: Mare Tranquillitatis: basalt emplacement history and relation to lunar samples. *J. Geophys. Res.* **101**(E10), 213–227 (1996)
- Tompkins, S., Pieters, C.M., Mustard, J.F., Pinet, P., Chevrel, S.D.: Distribution of materials excavated by the lunar crater Bullialdus and implications for the geologic history of the Nubium region. *Icarus* **110**(2), 261–274 (1994)
- Trang, D., Gillis-Davis, J., Hawke, B., Bussy, D.: The origin of lunar concentric craters, 42nd Lunar and Planetary Science Conference, abstract #1698 (2011)

- Vaniman, D., Dietrich, J., Jeffrey Taylor, G., Heiken, G.: Exploration, samples, and recent concepts of the Moon. In: Heiken, G.H., Vaniman, D.T., French, B.M. (eds.) *Lunar Sourcebook*, pp. 5–26. Cambridge University Press, Cambridge (1991)
- Wagner, R., Head, J.W., Wolf, U., Neukum, G.: Stratigraphic sequence and ages of volcanic units in the Gruithuisen region of the Moon. *J. Geophys. Res.* **107**, E11, 5104, doi:10.1029/2002JE001844 (2002)
- Wagner, R., Head, J.W., Wolf, U., Neukum, G.: Lunar red spots: Stratigraphic sequence and ages of domes and plains in the Hansteen and Helmet regions on the lunar nearside. *J. Geophys. Res.* **115**, E06015, doi:10.1029/2009JE003359 (2010)
- Walker, G. P. L.: Basaltic Volcanoes and Volcanic Systems. In: Sigurdsson, H. (ed.) *Encyclopedia of Volcanoes*, pp. 283–289. Academic Press, San Diego (2000)
- Weitz, C.M., Head, J.W.: Spectral properties of the Marius Hills volcanic complex and implications for the formation of lunar domes and cones. *J. Geophys. Res.* **104**(E8), 18933–18956 (1999)
- Wenker, A.: Geologic map of the near side of the Moon, based on the 1971 Version by Don E. Wilhelms and John F. McCauley. USGS, Flagstaff (1999)
- Westfall, J.: A generic classification of lunar domes. *J. Ass. Lunar Planet. Obs.* **18**(1–2), 15–20 (1964)
- Whitford-Stark, J.L.: The Geology of the lunar mare fecunditatis. *Proceedings of the 17th Lunar Planetary Science Conference*, 940–941 (1986)
- Whitford-Stark, J.L.: The volcanotectonic evolution of Mare Frigoris. *Proceedings of the 20th Lunar Planetary Science Conference*, 175–185 (1990)
- Whitford-Stark, J.L., Head J.W.: The Procellarum volcanic complexes: contrasting styles of volcanism. *Proceedings of the 8th Lunar Planetary Science Conference*, 2705–2724 (1977)
- Wichman, R.W., Schultz, P.H.: Crater-centered laccoliths on the Moon: modeling intrusion depth and magmatic pressure at the crater Taruntius. *Icarus* **122**, 193–199 (1996)
- Wieczorek, M.A., Phillips, R.J.: Potential anomalies on a sphere: Applications to the thickness of the lunar crust. *J. Geophys. Res.* **193**, 1715–1724 (1998)
- Wieczorek, M.A., Zuber, M.T., Phillips, R.J.: The role of magma buoyancy on the eruption of lunar basalts. *Earth Planet. Sci. Lett.* **185**, 71–83 (2001)
- Wieczorek, M.A. et al.: The constitution and structure of the lunar interior. *Rev. Mineralogy Geochemistry* **60**, 221–364 (2006)
- Wilhelms, D.E.: The geologic history of the Moon. USGS Prof. Paper 1348 (1987)
- Wilhelms, D.E., McCauley, J.F.: Geologic map of the near side of the Moon. USGS, Flagstaff, Arizona. USGS Misc. Geol. Inv. Map, I-703 (1971)
- Wilson, L., Head, J.W.: Ascent and eruption of basaltic magma on the Earth and the Moon. *J. Geophys. Res.* **86**, 2971–3001 (1981)
- Wilson, L., Head J.W.: Magma reservoirs and neutral buoyancy zones on Venus: implications for the formation and evolution of volcanic landforms. *Proceedings of 23rd Lunar and Planetary Science Conference*, 1533–1534 (1992)
- Wilson, L., Head, J.W.: Lunar linear rilles as surface manifestations of dikes: theoretical considerations. *Proceedings of 27th Lunar Planet Science Conference*, abstract #1445 (1996)
- Wilson, L., Head, J.W.: Tharsis-radial graben systems as the surface manifestations of plume-related dike intrusion complexes: models and implications. *J. Geophys. Res.* **107**(E8), 5057, (2002). doi: 10.1029/2001JE001593
- Wilson, L., Head, J.W.: Lunar Gruithuisen and Mairan domes: rheology and mode of emplacement. *J. Geophys. Res.* **108**(E2), 5012–5018 (2003)
- Wiseman, S.M., Donaldson Hanna, K.L., Mustard, J.F., Isaacson, P.J., Pieters, C.M., Jolliff, B.L.: Aris-tarchus olivine in context with circum-Imbrium olivine deposits. *Proceedings of 2nd Conference on Lunar Highlands Crust*, abstract #9025 (2012)

- Wöhler, C., Grumpe, A.: Integrated DEM construction and calibration of hyperspectral imagery: a remote sensing perspective. In: Breuß, M., Bruckstein, A., Maragos, P. (eds.) *Innovations for Shape Analysis: Models and Algorithms*. Revised contributions to Dagstuhl Seminar. Mathematics and Visualization. Springer Verlag, Berlin (2013, In Press)
- Wöhler, C., Lena R.: Lunar intrusive domes: morphometric analysis and laccolith modelling. *Icarus*. **204**(2), 381–398 (2009)
- Wöhler, C., Lena, R., Lazzarotti, P., Phillips, J., Wirths, M., Pujic, Z.: A combined spectrophotometric and morphometric study of the lunar mare dome fields near Cauchy, Arago, Hortensius, and Milichius. *Icarus*. **183**(2), 237–264 (2006)
- Wöhler, C., Lena, R., Phillips, J.: Formation of lunar mare domes along crustal fractures: rheologic conditions, dimensions of feeder dikes, and the role of magma evolution. *Icarus*. **189**(2), 279–307 (2007)
- Wöhler, C., Berezhnoy, A., Evans, R.: Estimation of elemental abundances of the lunar Regolith using clementine UVVIS + NIR data. *Planet. Space Sci.* **59**(1), 92–110 (2011)
- Wood, C.A.: Lunar concentric craters. *Proceedings of 9th Lunar and Planetary Science Conferences*, 1264–1266 (1978)
- Wood, C.A.: Monogenetic volcanoes of the terrestrial planets. *Proceedings of 10th Lunar and Planetary Science Conferences*, 2815–2840 (1979)
- Wood, C.A.: Lunar Photo of the Day, March 09, 2006. <http://www.lpod.org/?m=20060309> (2006). Accessed 20 January, 2013.
- Wood, C.A., Andersson, L.: Lunar crater morphometry: new data. *Proceedings of 9th Lunar and Planetary Science Conferences*, 1267–1269 (1978)
- Wu, S.S.C., Doyle, F.J.: Topographic mapping. In: Greeley, R., Batson, R.M. (eds.) *Planetary Mapping*, pp. 169–207. Cambridge University Press, Cambridge (1990)
- Zuber, M.T., Smith, D.E., Lemoine, F.G., Neumann, G.A.: The shape and internal structure of the Moon from the Clementine mission. *Science* **266**, 1839–1843 (1994)

---

# Index

## A

absorption trough, 40, 42–44, 75, 93, 130  
aluminium, 44  
aluminous mare basalts, 47  
andesitic, 14  
Arago, 10, 11, 36, 52, 60, 63, 81, 81ff., 97, 111, 127, 147, 155  
Arago  $\alpha$ , 36, 63, 79, 81, 127, 147  
Arago  $\beta$ , 36, 63, 79, 81, 127, 147  
Archytas, 21, 107, 108, 137  
Archytas G, 19  
Aristarchus plateau, 7, 131  
Aristillus, 21, 137, 139  
Autolycus, 90

## B

basaltic, 3ff., 10, 35, 40, 41, 46, 47, 50, 51, 53, 55, 65, 83, 89, 92, 104, 111, 119, 127, 136, 137, 145ff.  
Birt, 15, 16, 69ff., 78, 153  
bisected dome, 15–17, 69ff.

## C

Capuanus, 10, 12, 27, 33, 116ff.  
Carrel, 79, 83, 155  
Cauchy, 5, 10, 11, 20, 52, 60, 61, 73, 79, 83ff., 107, 111, 116, 142, 143  
central eruption, 4  
Chandrayaan-1, 10, 27, 75, 146  
C. Herschel, 118  
circularity, 23, 64, 91, 99, 118, 135, 142  
classification scheme, 36, 38, 59, 65, 110, 126, 127, 145, 146

Clementine, 8, 14, 39ff., 43ff., 50, 70, 72, 74, 76, 77, 80ff., 86, 88, 89, 91ff., 95ff., 99, 100, 103, 106, 108, 109, 116ff., 123, 125, 127, 130, 131, 135, 136, 141, 146, 147  
clinopyroxene, 5, 146  
concentric crater, 18, 19  
Condorcet, 12, 20, 41, 84, 103ff., 108, 125  
continuum-removed spectrum, 42, 43, 93  
cooling time scale, 52  
crater pit, 5, 6, 9, 120  
Crisium basin, 20, 72, 100, 103, 105  
cryptomaria, 14, 92  
crystallisation, 6, 7, 53, 83, 104, 126

## D

dark mantling deposits, 6  
Darney  $\chi$ , 15, 54  
degassing, 6, 7, 15  
Diana, 88  
dike, 4, 6, 8, 10, 15, 16, 17, 20, 49ff., 69, 72ff., 78, 83, 87ff., 91ff., 95, 98ff., 103ff., 111, 114, 116, 117, 119, 122, 123, 125, 126, 129, 130, 134, 136, 137, 146  
dike length, 15, 50, 52, 72ff., 78, 83, 88, 100, 104, 111, 116, 117, 122, 130, 134  
dike width, 50ff., 72ff., 78, 83, 91, 107, 108, 111, 116, 117, 119, 122, 129, 134  
dome diameter, 23, 27, 51, 86, 92, 121, 129, 135  
dome height, 26ff., 91, 96, 128, 134, 146, 160  
Doppelmayr, 16, 42, 120ff., 125  
Drebbel, 14, 124

**E**

effusion rate, 5, 34, 35, 49, 51, 52, 59, 61, 63, 71, 73, 78, 79, 81, 83, 87ff., 91, 92, 95, 97, 99, 100, 103, 106, 108, 110, 113, 114, 116, 119, 122, 125, 126, 128, 129, 134, 145  
 elastic plate, 55, 136  
 elongated outline, 57, 64, 142  
 elongated summit vent, 20

**F**

fault, 18, 20ff., 54, 56, 57, 63, 69, 83, 137, 140, 143, 146  
 fayalite, 5, 42  
 ferroan anorthosite, 44, 47, 76, 93, 94  
 fissure eruption, 4  
 fissure, 5, 20, 34, 109  
 flank slope angle, 27  
 flank slope, 5, 20, 23, 25, 27, 38, 54, 59ff., 70, 72, 77, 81, 82, 86, 88, 89, 91, 92, 95ff., 103, 104, 106, 109ff., 114ff., 118, 119, 122, 123, 125, 126, 128, 134, 135, 139, 140, 142, 145  
 flexural uplift, 22, 55  
 floor-fractured lunar crater, 21, 101  
 forsterite, 5, 42  
 Fracastorius, 96, 147  
 fracture, 4, 18, 20, 21, 49, 54, 55, 72, 83, 88, 101, 136, 146  
 fracturing, 21, 101, 139, 140

**G**

Gambart, 137, 138, 140  
 Gassendi, 69, 76ff.  
 graben, 5, 6, 15, 16, 83, 89, 120,  
 graben formation, 15, 16  
 Grace, 88  
 Grimaldi, 137, 140, 160, 161  
 Gruithuisen, 5, 10, 14, 35, 42, 46, 51, 53, 61, 63, 125ff., 149, 151, 152

**H**

Hansteen, 10, 14, 21, 26, 46, 126, 127, 141  
 Hansteen  $\alpha$ , 127  
 heat diffusion, 52  
 highland dome, 10, 14, 35, 42, 46, 51, 53, 61, 63, 65, 125ff., 145, 146, 149, 151, 152

Hortensius, 10, 11, 20, 34, 42, 51, 52, 60, 108ff., 128, 151  
 Hyginus, 6, 15, 89

**I**

illumination angle, 29, 121, 138, 141, 146  
 ilmenite, 3, 5, 39  
 integrated band depth, 13, 43, 75, 130  
 intrusion, 3, 15ff., 21, 22, 38, 54, 56, 65, 136, 137, 142, 143, 146  
 intrusive dome, 20ff., 49, 50, 52, 54ff., 63, 64, 83, 103, 107, 111, 119, 135ff., 146  
 intrusive process, 3, 22, 54  
 Isis, 6, 8

**K**

Kies, 31, 115, 137, 138, 152  
 kipuka, 15, 38, 54, 135, 150

**L**

laccolith, 3, 18, 21, 22, 54ff., 64, 136, 137, 139, 146  
 laccolith formation, 21, 54, 139  
 laccolithic intrusion, 54, 56  
 laccolith modelling, 54, 55, 64  
 Lambert model, 29, 30  
 lateral mixing, 14, 15, 40, 42, 47, 89, 104, 125  
 lava, 3ff., 12, 14ff., 18, 34, 35, 38, 41, 46, 49ff., 59ff., 69, 71, 72, 73, 79, 83, 86, 88, 89, 95, 97, 98ff., 103, 104, 106ff., 113ff., 119, 120, 122, 123, 125ff., 134, 135, 137, 139, 140, 145  
 linear graben, 4, 15  
 LOLA DEM, 25, 26, 32, 73, 91, 96, 116, 137, 141, 160, 161  
 lunar cone, 6ff., 20, 40, 44, 61, 63, 65  
 lunar intrusive dome, 20ff., 54, 55, 57, 63, 103, 135ff.  
 lunar-Lambert law, 30, 160  
 Lunar Orbiter, 8, 24, 71, 83, 86, 88, 109, 111, 114, 116, 121, 122, 124, 132, 138, 139, 141  
 Lunar Orbiter Laser Altimeter (LOLA), 24  
 Lunar Prospector Gamma Ray Spectrometer, 44  
 lunar pyroclastic deposit (LPD), 6ff., 42, 101, 103  
 Lunar Reconnaissance Orbiter, 10  
 Lunar Topographic Orthophotomaps, 25



**M**

mafic, 4, 70, 73, 78, 81, 97, 99, 100, 103, 106, 108, 110, 116, 123, 127  
 magma, 3ff., 15, 16, 18ff., 34, 35, 38, 49ff., 55, 56, 63, 65, 71ff., 78, 81, 83, 87, 88, 91ff., 95, 98ff., 103, 104, 106, 108, 116, 117, 119, 122, 123, 125, 126, 129, 131, 134ff., 139, 140, 142, 146, 147  
 magma ocean, 3  
 magma pressure, 7, 49, 50, 55, 56, 65, 74, 117, 136, 137, 142  
 magma rise speed, 49, 51ff., 73, 74, 78, 83, 87, 91, 93, 98ff., 103, 104, 108, 116, 117, 119, 122, 125, 129, 134  
 magmatic intrusion, 18, 19, 38, 56, 146  
 magma viscosity, 6, 50, 51, 78, 91, 92, 100, 103, 125, 146  
 magnesium, 44  
 Mairan, 5, 10, 35, 42, 51, 63, 125ff., 152  
 mare basalt, 5, 14, 15, 35, 44ff., 50, 75, 76, 92ff., 107, 118, 135, 139, 142  
 Mare Cognitum, 15, 54  
 Mare Crisium, 46, 47, 93, 100, 103, 156  
 Mare Fecunditatis, 97, 98  
 Mare Frigoris, 21, 91ff., 97, 107  
 Mare Humorum, 7, 14, 120, 125, 142  
 Mare Imbrium, 10, 21, 88, 90, 105, 118, 119  
 Mare Insularum, 10, 11, 62, 108, 109, 134, 138, 140  
 Mare Nubium, 8, 9, 15, 69, 108, 112, 115  
 Mare Serenitatis, 7, 8, 18, 21, 27, 39, 72, 142  
 Mare Tranquillitatis, 5, 8, 10, 11, 20, 27, 39ff., 43, 51, 52, 61ff., 72, 73, 79, 83, 84, 88, 89, 107, 116, 117  
 Mare Undarum, 10, 12, 20, 41, 51, 72, 84, 93, 103, 104, 108, 125, 128, 142  
 Mare Vaporum, 7, 89  
 Marius Hills, 8, 13, 20, 27, 36, 38, 63, 65, 127, 128, 130, 131, 147, 150, 163  
 Marth, 19  
 Mee, 14, 124, 125  
 Menelaus, 15, 17, 69, 72ff., 78  
 Messier, 97  
 Meton, 91ff.  
 Mg-rich rock, 44ff., 76, 93, 94, 118  
 Milichius, 8, 10, 11, 20, 27, 28, 34, 40, 44, 45, 51, 52, 60, 71, 72, 107, 108, 110ff., 115, 117, 125, 128, 137  
 minimum wavelength, 42, 44  
 mixing, 7, 14, 15, 40ff., 47, 89, 104, 125

monogenetic, 36, 59, 61ff., 65, 127, 128, 130, 147  
 Mons Hansteen, 10, 14, 46, 126, 127  
 Mons Rümker, 10, 12, 20, 131, 132, 149, 150  
 Moon, 3, 4, 6, 8, 10, 12, 14ff., 18, 20, 22, 37, 39, 40, 50, 67, 125, 145ff.  
 multispectral image data, 8, 10, 39

**N**

non-monogenetic, 36, 59, 61, 63, 127, 128, 147

**O**

Oceanus Procellarum, 5, 10, 38, 40, 62, 108, 127, 131  
 olivine, 3, 5, 42ff., 46, 75, 146, 147  
 optical maturity, 40  
 orthopyroxene, 5, 146  
 Osiris, 6, 8  
 outflow channel, 8, 16, 17, 72, 109, 135, 137  
 overburden, 54ff., 135, 139

**P**

Palus Epidemiarum, 116  
 Palus Putredinis, 105  
 Petavius, 10, 12, 101, 102, 158  
 petrographic map, 44ff., 75, 76, 93, 94, 117ff., 130  
 photoclinometry, 24, 26, 28, 29, 96, 100, 116  
 photogrammetric measurements, 25  
 Piccolomini, 14, 95, 100  
 principal component analysis, 60, 61  
 pyroclastic deposit, 6, 12, 89, 101, 145  
 pyroxene, 3, 5, 41ff., 75, 93, 130, 146

**R**

reflectance ratio, 41, 59  
 reflectance spectrum, 39, 41, 42, 75, 89  
 rheologic group, 51ff., 71, 83, 87ff., 95, 98, 107, 117, 125  
 rheologic modelling, 10, 71, 78, 81, 91, 97, 100, 116, 134  
 rheologic properties, 23, 24, 26, 28, 30, 32, 34ff., 38, 49, 51, 61, 63, 69, 73, 78, 79, 83, 84, 107, 112, 116, 117, 129, 130, 133, 146  
 rhyolitic, 5, 14  
 rille, 4, 5, 8, 10, 15ff., 22, 54, 56, 63, 69ff., 71, 72, 74ff., 89, 90, 100, 101, 136ff., 142

Rima Birt, 15, 16, 69, 71  
 Rima Cauchy, 83, 88, 142  
 Rima Menelaus, 15  
 Rupes Altai, 95

## S

shadow length, 25, 27, 96, 121, 139, 160  
 shadow length measurement, 27, 96, 121, 139  
 shape from shading, 12, 24, 28ff., 32, 33, 52,  
 100, 116, 131, 134, 145, 157, 160  
 shield volcano, 3, 5, 20  
 sinuous rille, 6, 8, 10, 20, 101, 137ff.  
 Sinus Iridum, 26, 118, 119, 142  
 spectral parameter, 39, 41, 43, 44, 75  
 spectral ratio image, 41  
 Strombolian eruption, 4, 6, 7

## T

tensional stress, 17, 19, 21, 54, 55, 136, 137, 139,  
 142  
 terrestrial laccolith, 18, 22, 56, 57, 137  
 time scale, 52, 53, 126, 146  
 T. Mayer, 10, 11, 20, 51, 52, 107, 111, 128, 134  
 Tobias Mayer, 42, 71, 72, 108, 109, 111, 112, 151

## U

Unified Lunar Control Network, 23, 160  
 uplift, 21, 22, 55, 56, 101, 137

## V

Valentine dome, 18, 21, 29, 137, 142, 153  
 Vendelinus, 98, 99  
 vent, 4, 5, 7, 9, 14ff., 20, 36, 38, 50, 51, 62, 64,  
 69, 71, 83, 86ff., 96, 101, 102, 105, 111, 114,  
 118, 120, 121, 125, 127, 135, 140  
 vertical mixing, 15  
 vertical pressure gradient, 50, 51, 72, 91  
 viscosity, 5, 6, 18, 34, 35, 49ff., 59, 61, 78, 88, 89,  
 91ff., 95, 100, 103, 106, 108, 110, 111, 113ff.,  
 119, 125, 127, 128, 130, 134, 137, 145, 146  
 volcanic dome, 5, 10  
 volcanic edifice, 3ff., 29, 61, 63, 65, 125, 127,  
 128, 145, 147  
 volcanic eruption, 5, 63  
 volcanic vent, 9  
 vulcanian eruption, 6, 7

## W

Wide Angle Camera, 10, 146

## Y

Yerkes, 100, 103, 156  
 yield strength, 34, 49